Title
High-throughput technologies for the optimization of radiopharmaceuticals using microfluidics

Author
Rios, Alejandra

Publication Date
2022

Peer reviewed|Thesis/dissertation

UNIVERSITY OF CALIFORNIA

Los Angeles

High-throughput technologies for the optimization of radiopharmaceuticals using microfluidics

A dissertation submitted in partial satisfaction of the requirements for the degree Doctor of Philosophy in Physics and Biology in Medicine

by

Alejandra Rios

2022

ABSTRACT OF THE DISSERTATION

High-throughput technologies for the optimization of radiopharmaceuticals using microfluidics

by

Alejandra Rios

Physics and Biology in Medicine

University of California, Los Angeles, 2022

Professor R. Michael van Dam, Chair

The increasing number of positron-emission tomography (PET) tracers being developed to aid drug development and create new diagnostics has led to an increased need for radiosynthesis development and optimization. Current automated radiosynthesizers are designed for production of large clinical batches of radiopharmaceuticals. They are not well suited for reaction optimization or novel radiopharmaceutical development, since each data point involves significant reagent consumption, and contamination of the apparatus requires time for radioactive decay before the next use. Though with some radiosynthesizers it is possible to perform a few sequential radiosyntheses in a day, none allow for parallel radiosyntheses. To address these limitations, I developed a new platform for high-throughput experimentation in radiochemistry. This system contains an array of 4 heaters, each used to heat a chip containing an array of 16 reaction sites (hydrophilic patches) on a small Teflon-coated silicon chip, enabling 64 parallel reactions for the rapid optimization of conditions in any stage of a multi-step radiosynthesis process. As example applications, I studied the syntheses of several ^{18}F-labeled radiopharmaceuticals, performing >800 experiments to explore the influence of parameters

including base type, base amount, precursor amount, solvent, reaction temperature, and reaction time. The experiments were carried out within only 15 experiment days, and the small volume (~10 µL compared to the ~1 mL scale of conventional instruments) consumed ~100x less precursor per datapoint. This new method paves the way for more comprehensive optimization studies in radiochemistry and substantially shortening PET tracer development timelines.

I also developed new methods and technologies to determine the reaction conversion when optimizing radiosynthesis processes. Radio-thin layer chromatography (radio-TLC) is commonly used to analyze purity of radiopharmaceuticals or to determine the reaction conversion. In applications where there are only a few radioactive species, radio-TLC is preferred over radio-high-performance liquid chromatography (radio-HPLC) due to its simplicity and relatively quick analysis time. However, with current radio-TLC methods, it remains cumbersome to analyze a large number of samples during reaction optimization. In a couple of studies, Cerenkov luminescence imaging (CLI) has been used for high-resolution reading TLC plates spotted with a variety of isotopes. We show that this approach can be extended to develop a high-throughput approach for radio-TLC analysis of many samples by spotting multiple samples in adjacent lanes and then separating and reading out all lanes in parallel.

Finally, I worked on techniques to incorporate [^{19}F]fluoride and [^{18}F]fluoride into thioether molecules via electrochemical fluorination. Electrochemical fluorination and radiofluorination was performed under potentiostatic anodic oxidation using various types of electrochemical cells. I incorporated the concept of high throughput experimentation via microfluidics by using 96-ELISA-well plates with printed electrodes for the fast screening of parameters in electrochemistry for the radiofluorination of various thioether molecules, studying variables such as solvents, temperatures and electrolytes for the optimization of electrochemical labeling conditions. The use of high-throughput experimentation in radiochemistry can allow the exploration of various parameters in a fast manner and its combination with microfluidics makes the performance of

various experimental parameters possible due to the minimal use of reagents. Both radiochemistry in droplets and electrochemistry for fluoride labeling in well plates showed the screening and optimization of synthesis parameters that could not be possible with conventional methods, moreover the methods presented in this dissertation can help with the exploration of novel PET tracers for preclinical research that otherwise would be expensive at macroscale.

The dissertation of Alejandra Rios is approved.

Magnus Dahlbom

Peter M. Clark

Keisuke S. Iwamoto

Heather D. Agnew

R. Michael van Dam, Committee Chair

University of California, Los Angeles

2022

Dedicated to my loving and supporting family

TABLE OF CONTENTS

LIST OF FIGURES

LIST OF TABLES

ACKNOWLEDGEMENTS

To start with, I wanted to thank the funding sources that supported my doctoral work: the National Institute of Biomedical Imaging and Bioengineering (R21 EB024243 and T32EB002101), the National Cancer Institute (R21 CA212718, R33 CA240201), and the UCLA Eugene V. Cota Robles Fellowship.

I would like to take this chance to thank all of my fellow lab members in the van Dam lab both past and present. I consider myself incredibly lucky to work alongside and learning from many great people. I want to thank Dr. Jia Wang who has not only been an inspirational microfluidics engineer, but also a great friend. I thank Jia for taking the time to train me to fabricate microfluidic chips, and for sharing her engineering expertise. I would also like to thank Dr. Philip Chao for teaching me to solder and assemble electronics and help me built the high throughput platform for my project. I thank Travis S. Laferriere-Holloway for his help with chemistry questions, the enjoyable project brainstorming conversations, and for being a someone who not only helped me with my research projects but was also extremely supportive and kind friend throughout my journey in my Ph.D. I also thank Yingqing Lu for answering some of my questions and being someone fun to hang out with. I thank Dr. Ksenia Lisova for being such a kind person and helping me during my orientation time at UCLA and being so welcoming when I joined the lab. I thank the awesome undergraduate students Chelsea C. Okoro and Christian de Caro who were a pleasure to work with and who helped with some of the projects. I want to thank Jason Jones for helping me with machining tools. Finally, I am extremely grateful to Dr. R. Michael van Dam for his guidance and mentorship throughout the years of my Ph.D. I thank Dr. van Dam for giving me numerous opportunities to design and perform experiments, present, publish my work, establish collaborations, attend scientific conferences, and communicate with other researchers. I am thankful that as a mentor he gave me space to explore and learn from my mistakes, while always being helpful. Dr. van Dam is an incredible professor who is not only dedicated to his work but

also spends a lot of time with his students, listened to them about their future careers, and provide guidance. Thank you for me teaching work integrity and for being such a patient mentor throughout my Ph.D.

I am also grateful to CNSI cleanroom staff Lorna Tokunaga, Krissy Do and Tony Wright for their help and advice related to fabrication questions. I thank Emily Fitch for her help with the documents and providing detailed answers to any related questions and Karen Lum, Cecilia Canadas and Erika Corrin for their help with purchasing/reimbursements and administrative matters. Moreover, I appreciate the help received from everyone at the Crump Preclinical Imaging Technology Center. Thank you to Dr. Jason Lee for providing in-depth discussion about preclinical image techniques and specific results and lessons on image and data analysis. Thank you to the staff of the UCLA Biomedical Cyclotron facility and Jeffrey Collins for generously providing [^{18}F]fluoride ion for the radiochemistry studies.

I would like to start by thanking the mentors and administration of the Physics and Biology in Medicine program who made me feel welcome from the start of my Ph.D. career at UCLA. I want to thank Dr. Michael McNitt-Gray for his mentorship and support while navigating throughout my Ph.D., for always being there for his students, and providing resources and contacts to help students grow. I thank Reth Im and Alondra Correa Bautista for organizing PBM social events, handling all the administrative paperwork, and answering any of my questions. In addition, I would like to thank Dr. Gregory S. Payne and Dr. Diana Azurdia from the Biosciences program for being both mentors and supportive people during my time at UCLA.

I would like to thank my family who has been supportive throughout my life. My sisters Guadalupe Trujillo, Soledad Loyola, Gabriela Rios, and my brother Enrique Loyola for being understanding and kind. I am eternally grateful to my mother Estela Rios who constantly inspired me with her resilience, kindness, and care for me. I would not be able to be here without my mother’s love and encouragement, I love you very much mom! I also want to thank my father

Everardo Lopez Caloca for being so encouraging and giving me life advice and love. I want to thank my uncle Gregorio Lopez, his wife Maria Bondi, and my cousins Vivian, Paloma, and Gregorio for being so kind and encouraging. I also want to thank my aunt Judith Lopez for her daily texts giving me encouragement for the day. Thank you to my grandparents who taught me compassion and sympathy. I want to thank Adrian L. Gomez who has been a person who always encourage me ever since I met him as an undergraduate at Cal State LA, thank you for being part of my life for so many years. I appreciate you, and your family for being so caring and kind to me.

Lastly, I want to thank my doctoral committee for advising me with my research, study, and helping me to be better in all aspects. Thank you, Dr. Magnus Dahlbom for the engaging and inspiring lectures on the fundamental of nuclear medicine, for the insightful discussions that helped me understand the basic principles and the bigger picture in this field. I want to thank Dr. Peter Clark for having his door open whenever I had questions regarding chemistry or any biochemical question regarding cell culture techniques or protein analysis. I want to thank Dr. Keisuke Iwamoto for teaching me radiobiology and how various biochemical pathways can be affected with radiation. I truly enjoyed his lectures and insightful discussions as well as how much he cares for his students. Dr. Heather Agnew, thank you for allowing me the opportunity to collaborate with you on a peptide labeling project, cell binding assays, and *in vivo* studies. Thank you, Dr. R. Michael van Dam, once again for all his help to me. I'm really thankful for being instructed by him. I have learned so many new techniques, concepts, and expanded my knowledge with the insightful comments and advice that I receive from you all, thank you.

Chapter 2: High-throughput radiochemistry via microdroplets in is a modified version of:
Rios A, Wang J, Chao PH, van Dam RM A novel multi-reaction microdroplet platform for rapid radiochemistry optimization: Application to 18F-Radiolabeling of [^{18}F]Fallypride. *RCS Advances*. 2019;9:20370-20374. As well as Rios A, Laferriere-Holloway TS, Wang J, van Dam RM. Optimization of radiochemical reactions using droplet arrays. *JoVE*. 2021.

Chapter 3: High-throughput radio-TLC analysis is a modified version of:
Wang J, Rios A, Lisova K, Slavik R, Chatziioannou AF, van Dam RM. High-throughput radio-TLC analysis: application to analyze radiopharmaceuticals via Cerenkov luminescence imaging for high-throughput applications. *Nucl. Med. Biol*. 2020;82:41-48.

Chapter 4: Impact of aqueous phases in the analysis of radiopharmaceuticals via radio-TLC is a modified version of:
Laferriere-Holloway TS, Rios A, van Dam RM. Detrimental impact of aqueous phases in 18F-labelled radiopharmaceutical analysis via radio-TLC. *RCS Analy. Meth*. 2022; submitted.

Chapter 5: High-throughput experimentation for optimization of radiopharmaceuticals is a modified version of:
Rios A, Wang J, Laferriere-Holloway TS, Chao PH, De Caro C, Okoro CC, van Dam RM. Microliter-scale reaction arrays for economical, high-throughput experimentation in radiochemistry. *Sci. Rep*. 2022;12:10263.

Chapter 8: Electrochemical fluorination and radiofluorination of methyl(phenylthiol) acetate is a modified version of
Balandeh M, Waldman C, Shirazi D, Gomez AL, Rios A, Allison N, Khan A, Sadeghi S. Electrochemical fluorination and radiofluorination of methyl(phenylthiol)acetate using tetrabutylammonium fluoride (TBAF). *J. Electrochem. Soc*. 2017;164:G99-G103.

Chapter 9: Electrochemical flash fluorination and radiofluorination is a modified version of:
Balandeh M, Rios A, Allison N, Shirazi D, Gomez AL, Rambaran L, Holloway TS, Sadeghi S. Electrochemical flash fluorination and radiofluorination. *Chem. Electro. Chemi.* 2018;5:3353-3356.

Chapter 10: Electrochemical radiofluorination of thioethers is a modified version of:
Allison N, Balandeh M, Holloway TS, Gomez AL, Rios A, Waldmann C, Lebedev A, Sadeghi S. Electrochemical no-carrier added radiofluorination of thioethers. *J. Fluor. Chem.* 2022;257-258:10988.

VITA

EDUCATION

09/2016 - present:	PhD candidate (advanced in 12/2020) in Physics and Biology in Medicine, David Geffen School of Medicine, University of California Los Angeles (UCLA)
09/2014 - 08/2016:	Master of Science in Physics, California State University, Los Angeles (CalState LA)
08/2007 - 05/2016:	Bachelor of Science in Biochemistry, CalState LA
08/2007 - 05/2016:	Bachelor of Science in Biophysics, CalState LA

RESEARCH EXPERIENCE

03/2016 - present:	Graduate student researcher Crump Institute for Molecular Imaging, University of California Los Angeles Department of Molecular and Medical Pharmacology
06/2014 - 05/2016:	Student researcher Department of Chemistry and Biochemistry, California State University, Los Angeles & Department of Engineering and Materials Science, University of Southern California
06/2012 - 05/2014:	Undergraduate student researcher Department of Chemistry and Biochemistry, California State University, Los Angeles & Department of Chemistry and Applied Physics, California Institute of Technology

SELECTED PUBLICATIONS

Alejandra Rios, Travis S. Holloway, Philip H. Chao, Christian De Caro, Chelsea C. Okoro, and R. Michael van Dam. Microliter-scale reaction arrays for economical, high-throughput experimentation in radiochemistry. Scientific Reports 12: 10263, 2022. DOI: 10.1038/s41598-022-14022-2

Alejandra Rios, Travis S. Holloway, Jia Wang, R. Michael van Dam. Optimization of Radiochemical Reactions using Droplet Arrays. J. Vis. Exp. 168: e62056, 2021. DOI: 10.3791/62056

Jia Wang, **Alejandra Rios**, Ksenia Lisova, Roger Slavik, Arion F. Chatziioannou, R. Michael van Dam. High-throughput radio-TLC analysis. *Nuclear Medicine and Biology* 82-83: 41-48, 2020

Alejandra Rios, Jia Wang, Philip H. Chao, R. Michael van Dam. A novel multi-reaction microdroplet platform for rapid radiochemistry optimization. *RSC Advances* 9: 20370-20374, 2019. DOI: 10.1039/C9RA03639C

Allison Nathason, Balandeh Mehrdad, Holloway Travis S, Gomez Adrian L, **Rios Alejandra**, Waldmann Christopher, Lebedev Artem, Sadeghi Saman. Electrochemical no-carrier added radiofluorination of thioethers. *J. Fluor. Chem.* 2022;257-258:10988.

Balandeh Mehrdad, **Rios Alejandra**, Allison Nathanson, Shirazi Daniela, Gomez Adrian L, Rambaran Laura, Holloway Travis S, Sadeghi Saman. Electrochemical flash fluorination and radiofluorination. *Chem. Electro. Chemi.* 2018;5:3353-3356.

Balandeh Mehrdad, Waldman Christopher, Shirazi Daniela, Gomez Adrian L, **Rios Alejandra**, Allison Nathanson, Khan Asad, Sadeghi Saman. Electrochemical fluorination and radiofluorination of methyl(phenylthiol)acetate using tetrabutylammonium fluoride (TBAF). *J. Electrochem. Soc*. 2017;164:G99-G103.

CONFERENCES AND MEETINGS

12/2021: Oral presentation. International Chemical Congress of Pacific Basin Societies (Pacifichem), Virtual Conference

10/2021: Poster presentation. International Conference on Miniaturized Systems for Chemistry and Life Sciences (μTAS) Palm Springs, CA USA

05/2021: Oral presentation. 24th International Symposium of Radiopharmaceutical Sciences (ISRS), Virtual Conference

05/2019: Poster presentation. 23rd International Symposium of Radiopharmaceutical Sciences (ISRS), Beijing, China

09/2018: Poster presentation. 2018 World Molecular Imaging Congress (WMIC), Seattle, USA

09/2018: Poster presentation. International Conference on Miniaturized Systems for Chemistry and Life Sciences (μTAS) Kaohsiung, Taiwan

Chapter 1: Introduction

1.1 Positron emission tomography

Positron emission tomography (PET) is a sensitive non-invasive molecular imaging technique used to visualize molecular interactions and processes in living tissues by tracking the distribution of an administered radiolabeled imaging agent(*1*,*2*). Due to its ability to monitor specific *in vivo* biochemical processes with PET, this imaging technique is widely used as a research tool in fundamental studies of diseases and the development of new drugs and therapies(*3*). Moreover, it is also It is also an indispensable clinical tool for diagnosis and staging of disease, monitoring a patient's response to therapy, and streamlining clinical trials through patient stratification (*1*,*4*–*6*). Approximately 2 million PET scans are conducted in the US every year and even more numerous pre-clinical PET studies are performed routinely(*7*).

A PET radiopharmaceutical (tracer) consists of a biologically active molecule chemically linked with a radioactive positron-emitting isotope. Upon administration of a radiopharmaceutical, it circulates throughout the body, and its concentration in different organs and regions of tissues can be quantitatively imaged during a PET scan. The positrons emitted upon decay rapidly travel through matter losing their energy and annihilate at rest with an electron in the surroundings producing 2 gamma-rays (511 keV) at a nearly 180° angle(*2*). PET scanners rely on coincidence detection of these gamma-rays using a circular ring of scintillation detectors placed around the subject. These coincidence events are then processed and corrected, to map the distribution of the radiopharmaceutical inside the subject, ultimately creating a 3D image (**Figure1.1**). To provide an anatomical reference for the highly sensitive PET signal, PET is commonly used in conjunction with computed tomography (i.e., PET/CT) or magnetic resonance imaging (i.e., PET/MRI). The high sensitivity of PET allows one to obtain detailed images with only picomole to nanomole

amounts of the radiopharmaceutical administered, thus minimizing the possibility of any biological effects caused by the tracer (*8*).

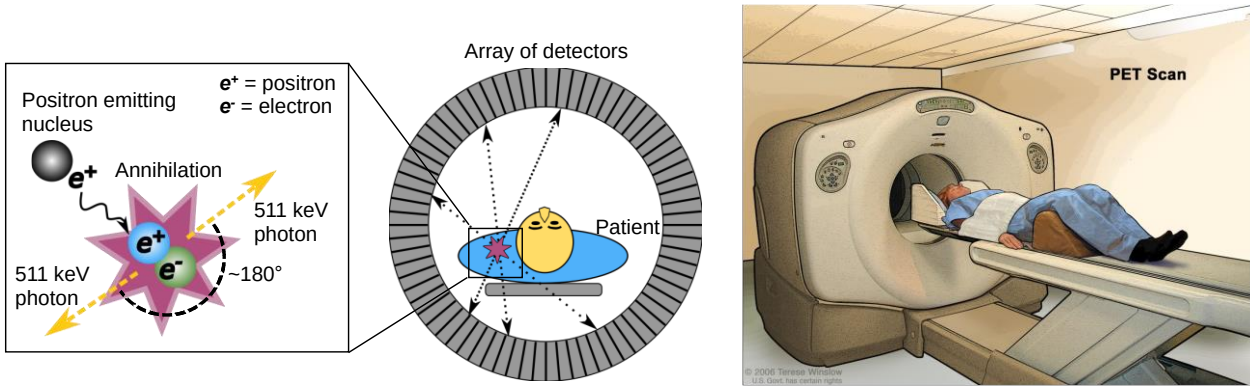

Figure 1. 1 Mechanism of PET imaging.

PET image is formed based on detection of sets of coincident 511 keV photons emitted upon annihilation event after positron decays. Image courtesy of National Cancer Institute.

1.2 Production of fluorine-18

Fluorine-18 has become the most attractive radionuclide for PET tracer development owing to its favorable nuclear and chemical properties, such as high positron emission (96%), short positron range (< 1mm)(*2*). Production of fluorine-18 is achieved in a cyclotron. Due to the 110 min half-life, either the batches of this radioisotope must be ordered from a cyclotron facility and shipped to a radiochemistry facility, or on-site access to a cyclotron is required. There are two main nuclear reactions that produce fluorine-18, that can result in either nucleophilic $[^{18}F]F^-$ or electrophilic $[^{18}F]F_2$ form. The first method $[^{18}O\ (p,n)^{18}F]$ produces aqueous $[^{18}F]F^-$ by bombardment of the oxygen-18 enriched water with 2-15 MeV protons (^1H). The second reaction $[^{20}Ne(d,\alpha)^{18}F]$ involves the bombardment of the high pressure neon gas target with deuterons (*9–11*). However, the method for the electrophilic $[^{18}F]F_2$ require F_2 carrier gas to efficiently recover the produced $[^{18}F]F_2$ after the bombardment. This leads to an important difference between nucleophilic or electrophilic form of fluorine-18 in terms of the resulting molar activity. Molar activity

is defined as a ratio of radioactivity per total number (moles) of the substance and is typically expressed in curie per micromole (Ci/μmol) or gigabecquerel per micromole (GBq/μmol). Thus, the electrophilic form of fluorine-18 is less use in radiochemistry since it will have lower molar activity (< 0.02 Ci/μmol [<0.6 GBq/μmol]) than its electrophilic analogue (typically 2.7 Ci/μmol [100 GBq/μmol]) due to the addition of the carrier in the former (*10*,*11*). A vast majority of fluorine-18 syntheses use nucleophilic [^{18}F]fluoride due to its simpler handling, higher molar activity and widespread availability from commercial nuclear pharmacies and academic medical research centers (*12*).

1.3 Conventional radiosynthesis of the radiopharmaceuticals

Approximately 2 million PET scans are conducted in the US every year and even more numerous pre-clinical PET studies are performed routinely, each requiring a radiopharmaceutical synthesized shortly before the scan(*7*). While the [^{18}F]fluoride half-life is 110 min and provides a moderate timeframe for synthesis and tracer transport, the production time of [^{18}F]fluoride labeled radiopharmaceuticals is preferred to be minimal (<30 min) and contain a minimal number of reaction steps (ideally only 1 or 2) to minimize activity decay. A typical production of a ^{18}F-labeled PET radiopharmaceutical involves: (i) radioisotope production via cyclotron; (ii) radiochemical labeling of a precursor to form the crude radiopharmaceutical compound; (iii) purification to isolate the desired product from excess radioisotope and byproducts of the reaction; (iv) formulation and sterile filtration to deliver a final product suspended in stabilizing; and (v) quality control testing to ensure identity, purity, and safety of the final product for injection (**Figure 1.2**).

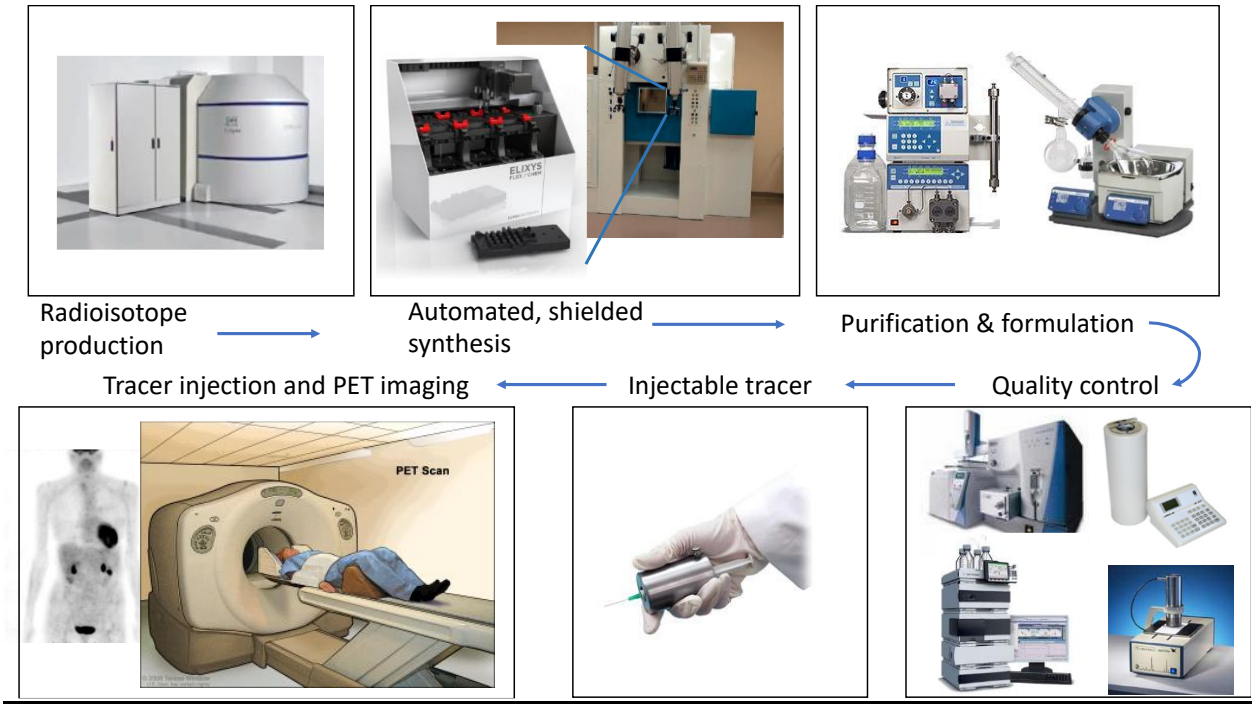

Figure 1. 2 Production flow for fluorine-18-labeled tracers.

Workflow of positron emission tomography (PET) illustrating the conventional equipment to produce PET radiopharmaceuticals.

Typical radiosynthesis of PET radiopharmaceuticals start with the use of nucleophilic [^{18}F]fluoride is initially received in [^{18}O]H_2O from a cyclotron. Because fluorine ion is a strong nucleophile it forms hydrogen bonds with the surrounding water, which makes it unreactive. To remove [^{18}O]H_2O water, [^{18}F]fluoride is trapped using a strong anion-exchange (SAX or QMA) cartridge. Then the trapped [^{18}F]fluoride is eluted into a reaction vial with non-polar solvents with a base and/or phase-transfer catalyst (PTC) such as $TBAHCO_3$ or a combination of K_2CO_3 and Kryptofix 222 (K_{222}). This eluate is then evaporated to remove excess water via azeotropic drying steps (i.e. evaporation in the presence of additional acetonitrile) to ensure complete removal of the water. The use of PTC such as cryptand-counter anion complex K_{222}/K_2CO_3 or tetrabutylammonium cation enhances the fluorine ion solubility and reactivity in organic solvents during the subsequent radiofluorination step. After azeotropic drying, nucleophilic [^{18}F]fluoride is generally incorporated into the precursor molecule either via aliphatic nucleophilic fluorination

(S_N2) into aliphatic positions or aromatic nucleophilic substitution (S_NAr) into aromatic molecules. S_N2 reactions are characterized by fluorine ion binding to the carbon atom of the precursor molecule containing a suitable leaving group (such as a weak base), under basic or neutral conditions in presence of an aprotic solvent (such as acetonitrile, DMF, DMSO). The crude product is then passed through a semi-preparative HPLC to isolate and purify the product, then the product is formulated in an injectable solution for preclinical or clinical use that must pass through quality control before administration.

Generally, to enable a safe and reliable routine PET radiopharmaceutical production, syntheses are carried out using automated radiosynthesizers which are placed inside the shielded fume hoods, known as hot-cells, and are operated remotely often with preprogrammed synthesis sequences. These radiosynthesizers are designed to control the reagent delivery into a reactor, apply heating and gas flow, recover crude synthesis product, and transfer it to perform subsequent purification and formulation with minimal user intervention. In addition, they are designed for relatively large batches of clinical-grade PET radiopharmaceuticals that can provide amounts of sufficient imaging of multiple patients(*13*). Each batch typically consumes 10s of milligrams of expensive precursor and reactions are carried out in milliliter volumes(*14*). The high cost of PET radiopharmaceutical production can be tolerated for clinical diagnostics with commonly used tracers like 2-[^{18}F]fluoro-2-deoxy-D-glucose ([^{18}F]FDG). [^{18}F]FDG to detect abnormal glucose metabolism (e.g., in oncology and neurology)(*15*). In addition, the assessment of abnormalities in glucose metabolism in various organs can be used to aid in the diagnosis of Alzheimer's disease and Parkinson's disease, epilepsy localization, heart disease, detecting inflammatory response related to infectious disease, and studying skeletal muscle (*16–21*). However [^{18}F]FDG cannot differentiate diseases if the patient has multiple disorders.

In recent years there is increasing interest in monitoring other biochemical process using other PET radiopharmaceuticals that can provide more disease-specific information in many cases(*22*). However, the cost is prohibitive for many investigators (making tracers inaccessible) because

there is insufficient demand and coordination of schedules for centralized production and distribution of these compounds, for investigators' focus on preclinical or *in vitro* research(*23*). Preparing a batch of a radiopharmaceutical is expensive due to the high cost of the radiosynthesizer, radiation shielding, reagents, radioisotope, and skilled personnel. Furthermore, most radiosynthesizers are designed for only one or a few consecutive radiosyntheses per day, thus limiting the number of radiopharmaceuticals produced per day(*24*). To increase accessibility to diverse PET tracers, and to facilitate the production of novel tracers for early studies, advances are needed in radiosynthesis technology that make it possible to produce smaller batches on demand at an affordable cost.

1.4 Use of microfluidics in radiosynthesis of PET radiopharmaceuticals

Production of PET radiopharmaceuticals require sophisticated equipment and large radiochemistry facilities, making each radiopharmaceutical batch very costly. Typically, these automated synthesis modules are optimized to work with large quantities of the radioisotope (e.g. an entire [^{18}F]fluoride batch from cyclotron) and, because the apparatus becomes contaminated after use, are limited to producing one tracer per day. Furthermore, large radiopharmaceutical production facilities are built around a cyclotron and contain hot-cells, various analytical equipment and radiation shielding for individual equipment units and radiation handling areas. Such highly specialized labs cost millions of dollars to set up and few hundreds of thousands of dollars to maintain yearly (*25*). Recent technological advancements in PET radiopharmaceutical production have the potential to revolutionize the field and make PET more accessible, versatile and cost-efficient for both clinical use and research. The miniaturization of PET production makes it possible to create efficient systems compatible with different levels of the radioactivity for synthesis of a variety of radiopharmaceuticals on demand. In recent years, there has been significant development of microfluidic devices to perform radiochemical synthesis (*26*,*27*).

1.4.1 Advantages of microfluidics

Microfluidic techniques can reduce the infrastructure and equipment needed by the reduction of footprint of the radiosynthesizer and reduction in the shielding, unlike conventional equipment, compact micro-radiosynthesizers could be moved out of centralized radiopharmacies and instead be located directly in clinics. Microfluidic technologies have been increasingly used in radiochemistry to capitalize on several advantages over conventional systems(*26*,*28*,*29*). Systems based on 1-10 µL reaction volumes (*30*–*32*), have shown significant reduction of reagent volumes and consumption of expensive precursor by 2-3 orders of magnitude, as well as short reaction times. These reductions lead to lower costs, faster heating and evaporation steps, simpler and shorter downstream purification, an overall “greener” chemistry process(*24*), and higher molar activity of the produced tracers(*33*). and higher molar activity of the produced tracers(*33*). High molar activity is possible due to the reduction of fluorine-19 contamination from reagents and other sources (*33*). Importantly, this high molar activity can be achieved even when producing only small batches of a PET tracer; in contrast, conventional systems require the production of large amounts of tracer to achieve satisfactory molar activity(*33*). High molar radioactivity is especially important in early tracer development and preclinical research due to the small amounts needed, and to enable injection of sufficient activity (to achieve high signal-to-noise ratio image) without inducing pharmacologic effects. For example, small animals are generally injected with much higher concentrations of the tracer per mass of the animal compared to humans to achieve sufficient signal in the small voxel size of small animal scanners (*34*,*35*). Another advantage of microvolume radiosynthesis is that the purification of crude product can be simply carried out using analytical-scale (as opposed to semi-preparative scale) radio-high-performance liquid chromatography (radio-HPLC), because of greatly reduced quantities of reagents and small volume (10s of microliter) of crude product. Analytical-scale chromatography generally enables much quicker purification (shorter retention times), and the pure product is

collected in a much smaller volume, simplifying the downstream process of formulating the tracer into an injectable solution(*24*).

1.4.2 Microfluidic in radiochemical synthesis

In general, there are two major types of microfluidic radiosynthesizers based on the mode of production: ones based on continuous flow microfluidics, and others based on batch micro-reactors. The flow-based microfluidic radiosynthesizers allows one to perform radiolabeling reactions continuously as the mixed reagents flow inside a heated channel or capillary. The benefits of this technique are uniformity of the reaction conditions due to efficient mixing and a very high surface-to-volume ratio, permitting efficient heat transfer throughout the reaction volume and rapid synthesis (*36*–*38*). Flow-based radiosynthesizers, such as commercially available Advion NanoTek, has been used to synthesize fluorine-18 labeled tracers as well as the tracers labeled with carbon-11, nitrogen-13 and various radiometals (*29*,*39*–*42*). Some of these devices are capable of using 10s of microliters of the reagents to perform low-starting activity optimization syntheses. To perform synthesis with larger quantities of radioisotope either requires a corresponding increase of the precursor volume or instead requires the preconcentration of radioactivity prior to the synthesis (*43*–*45*).

In the simplest batch reactors, parts of the conventional apparatus are miniaturized to a small scale, using on-chip valves, micro pumps and tiny reaction chambers or miniature conical vials. A few groups have demonstrated successful implementations of small-scale batch production by using micro-vials with 5-20 µL volumes for synthesis of [^{18}F]FET (*46*), custom PEEK/pDCPD 50 µL reactor with integrated microvalves for clinically-used batches of [^{18}F]fallypride (*47*), and integrated PDMS chip with 0.1 mL reaction chamber with externally-controlled valves for [^{18}F]fallypride synthesis (*48*). The application of microliter droplet manipulation in radiopharmaceutical synthesis have gained a lot of interest in the past several years, and a few droplet-based approaches have been developed (*49*,*50*).

Our group recently pioneered a microfluidic platform (**Figure 1.3**), in which reactions are performed at an even smaller scale (i.e. 1-10 µL) in droplets confined in surface-tension traps patterned on a surface(*31*). Under these conditions, droplet reactions typically have yields comparable to conventional methods but allow shorter synthesis time and up to ~100x lower reagent consumption per reaction(*49*,*51*,*52*).

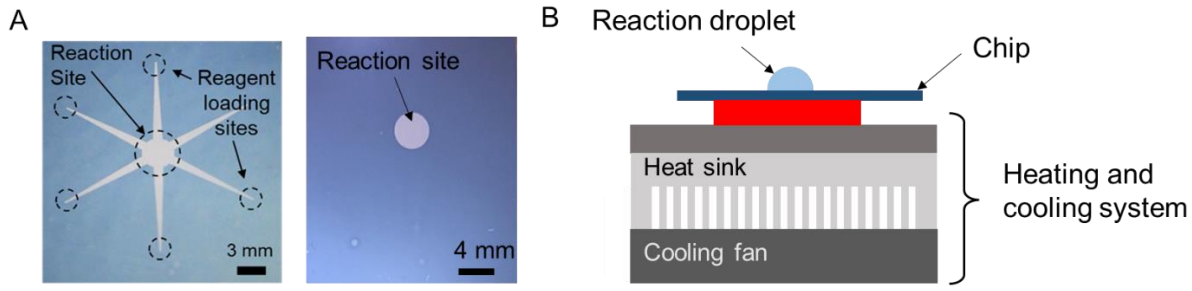

Figure 1. 3 Droplet platforms using surface tension traps on Teflon coated silicon chips.

Various patterned chips for droplet radiochemistry. A) Star shape for the delivery of reagents using an automated platform and a single spot chip design were used to perform a single reaction. B) Reaction platform that contains a cooling fan and heater where a single chip can be place to perform radiochemistry using microdroplet chips.

Current automated radiosynthesizers are design to produce large clinical batches of radiopharmaceuticals. They are not suited for reaction optimization or novel radiopharmaceutical development, since each data point involves significant reagent consumption, and contamination of the apparatus requires time for each radioactive decay before the next use. By lowering the reagent cost of each synthesis, low-volume microfluidic synthesizers make it more practical to perform more detailed optimization studies. Further benefits can be achieved by performing multiple experiments from a single batch of radioisotope in a single day. For example, microfluidic flow chemistry radiosynthesizers operating in “discovery mode” can sequentially perform dozens of reactions, each using only 10s of µL reaction volume(*53*). Several groups have shown that dozens of small-scale radiochemical reactions can be sequentially performed using flow-chemistry capillary reactor platforms with crude products collected and analyzed offline(*45*,*53*–

55). Another microfluidic platform used a polydimethylsiloxane (PDMS) microfluidic chip to prepare ultra-small batches (~100 nL each)(*56*,*57*). Small-volume vial-based reactions have also been used for optimization(*58*) and enable a wider range of parameters to be studied. Recently, Laube *et al.* reported the use of multi-vial heating blocks to perform up to ~50 radiofluorinations per day, each involving drying a small aliquot of [^{18}F]fluoride eluted from a QMA cartridge, followed by reaction at the 25-50 µL scale(*59*). While demonstrating parallelism and low reagent consumption, this technique required significant manual handling of vials, including installation and removal of vial caps. In addition, it is well known that the detailed heating characteristics of the system are essential to consider(*60*).

To increase throughput, we created chips with multiple reaction sites for performing up to 16 droplet-based syntheses in parallel and a platform that would allow the mounting of four chips to allow the variation of temperature and reaction times in parallel (*24*,*61*). The high throughput platform allowed the performance of 64 simultaneous reactions in one day, and the disposable chips could allow the performance of more reactions, since no decontamination procedure is necessary. **Figure 1.4** shows some of the droplet reactors developed for the performance of radiochemistry reactions.

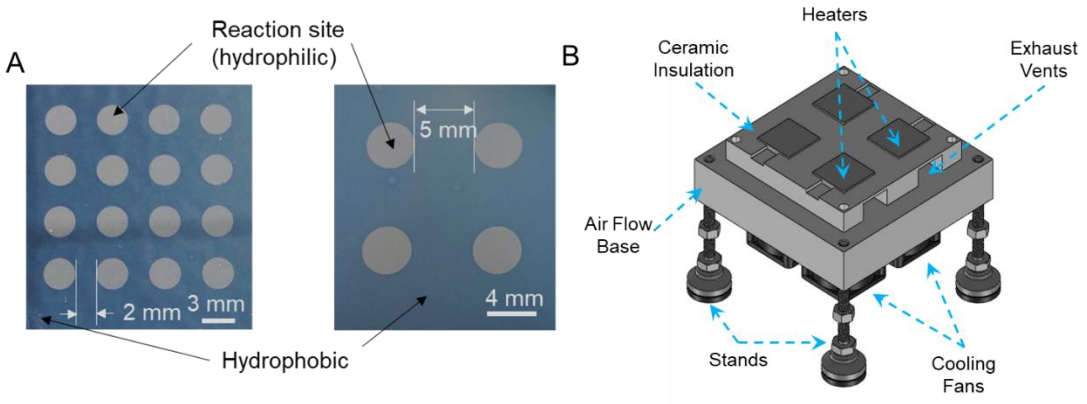

Figure 1. 4 Droplet platforms using surface tension traps on Teflon coated silicon chips for high throughput optimization.

Various patterned chips for droplet radiochemistry. A) 16 spot and 4 spot reaction chips for the performance of high throughput experimentation and parameter optimization of radiopharmaceuticals. B) High throughput platform with four heaters that allows the exploration of up to 64 different optimization conditions.

1.4.3 Scaling up to clinical doses

Of particular note, after optimization under low activity conditions, larger scale production (e.g. one or a few clinical doses) can be achieved under identical conditions using an automated droplet-based radiosynthesizer(*62*,*63*) by a simple increase of starting activity.

1.5 Focus of dissertation (summary)

The increase interest in the development of new radiopharmaceuticals (tracers) for PET imaging in preclinical and clinical research requires the need for the development of cutting-edge methods of tracer production to make research more accessible and affordable. As discussed above, low-cost microfluidic methods can be used for efficient dose-on-demand tracer production in both a clinical and pre-clinical setting, as well as in radiochemistry-related research. In addition to the reduction on reagent consumption, the droplet-based technologies can achieve comparable or better yields compared to conventional methods, reduction in synthesis time, higher molar activity, faster purification, and compact system size. While the translation of the microfluidic technology for routine use in clinical PET diagnostics will take significant effort to optimize and validate the microfluidic systems, the technology can be readily applied for preclinical use and supply researchers with diverse PET radiopharmaceuticals.

To make use of these platforms for tracer production, it is necessary to adapt synthesis protocols from conventional systems (macroscale) to the microscale reaction format, or to initially develop the synthesis directly in droplet format. Both of these scenarios involve the need to optimize reaction conditions, and the majority of my dissertation focuses on novel radiochemistry optimization methods and applications.

Chapter 2 was the development of a high-throughput microdroplet platform that would allow the fast optimization of the radiopharmaceutical [^{18}F]Fallypride with the use of silicon Teflon

coated chip that has multiple hydrophilic reaction sites (2 x 2 array or 4 x 4 array) surrounded by hydrophobic surface. We characterized the uniformity of reaction sites and cross-contamination. As a proof of concept, an optimization study of [^{18}F]Fallypride was carried out on the multi-reaction microfluidic chips. The cost of the optimization process was significantly lower than for conventional setups since the amount of precursor consumed per reaction is extremely small (e.g. ~84 µg per data point compared to 4 mg per data point in conventional reactions), and many reactions can be carried out using the same batch of radioisotope.

To aid on the fast examination of multiple samples produced via high-throughput microdroplet chip, radio TLC analysis was applied for the analysis of collected crude products after synthesis instead of radio-HPLC analysis. In **Chapter 3**, we show the use of a new approach that can be extended to develop a high-throughput approach for radio-TLC analysis of many samples via use of Cerenkov luminescence imaging (CLI). TLC plates can be spotted with multiple samples for a fast reading and capture of product separation after the spotted samples are developed by placing the spotted TLC on a mobile phase. Furthermore, in **Chapter 4** we study the effects of water as a mobile phase on silica plates for radio TLC sample separation. The use of silica plates as TLC plates for spotting crude samples is widely used since [^{18}F]fluoride is retained at the origin and the radiolabeled radiopharmaceutical is separated by the mobile phase during development since the 18-F radiolabeled molecule is more organic. While the use of water is commonly used in various reports, too much water can affect the analysis of 18-F radiopharmaceuticals due to modification on silica, altering sample migration.

In **Chapter 5**, we look at the development of a throughput and flexible system that can allow further increase on radiosynthesis reactions by introducing an array of four independent heaters, enabling operation of 4 chips in parallel, giving the opportunity of performing 64 reactions in parallel. To explore the capabilities of this platform, radiosyntheses of four different neuroimaging ^{18}F-labeled radiopharmaceuticals ([^{18}F]Flumazenil, [^{18}F]PBR06, [^{18}F]Fallypride, and

[^{18}F]FEPPA), performing >800 experiments to explore the influence of parameters including base type, base amount, precursor amount, solvent, reaction temperature, and reaction time.

^{18}F-labeled radiopharmaceutical production via droplet-based methods have successfully been used for preclinical imaging, demonstrating sufficient quantity and concertation of each batch for multiple mouse or rat injections(*31*,*64*,*65*), but generally, activity scales are much lower than those reported of macroscale synthesis(*14*). If the final product activity could be increased in droplet-based radiosynthesizers, their applications could be further expanded to produce clinically-relevant amounts of radiopharmaceuticals. However, previous work has shown a decrease in overall product formation when starting activity increases(*61*–*63*). In **Chapter 6**, we explore the possible causes on product decrease with the increase of starting activity. The increase of contaminants introduced on the reaction from the activity source was tacked by the introduction of ion exchange resins for the capture of metal cations. Furthermore, a baseless method for the elution of activity from basic anion exchange resin is explored to prevent decomposition of product during the reaction.

Open chip reactions explained in the previous chapters showed the rapid optimization for radiopharmaceuticals since various experiments can be conducted in parallel. On the other hand, a limitation of this approach is that the open droplet format had significant volatile losses for some syntheses. While volatile losses were very low for [^{18}F]PBR06, [^{18}F]Fallypride, and [^{18}F]FEPPA in droplet format (as well as many other tracers(*31,51,64*)), losses were significant for [^{18}F]Flumazenil and were found to occur during the radiofluorination step. In contrast, in macroscale systems, the reactor is usually closed for the duration of the reaction, and losses during this step are generally likely to be lower. In **Chapter 7** we focus on the exploration of various methods to allow the radiosynthesis of the [^{18}F]Flumazenil with close reactors using microvolumes to minimize the volatility losses and reduce the hazard that it presents, while retaining the benefits of low precursor and fast reaction times.

Chapters 8-10 look at the application of electrochemistry for the introduction of nucleophilic [^{18}F]fluoride to electron rich molecules, such as thioethers. The projects discuss in these chapters are work that took place in Dr. Saman Sadegui's laboratory for three years where the focus was the exploration of novel techniques for radiolabeling small molecules. Electrochemistry is gaining prominence as a versatile tool in organic synthesis and electrochemical fluorination of organic compounds can be a powerful alternative technique for direct fluorination. Thus, the application of electrochemistry in radiolabeling is showed promise as a tool that can aid on the direct radiolabeling of electron rich molecules. In **Chapter 11**, we look at the introduction of high-throughput experimentation and microfluidics in electrochemistry and showed similar results on the radiolabeling of thioether molecules with conventional methods discusses in Chapters 8-10. Furthermore, the high-throughput method allowed the exploration and implementation of various reaction parameters in parallel. Finally, I conclude this dissertation with **Chapter 12**, where the future directions of these microfluidic-based new technologies is discussed.

Chapter 2: High-throughput radiochemistry vial microdroplets

2.1 Introduction

Most of positron emission tomography (PET) tracers available for preclinical and clinical research are produced using commercial macroscale radiosynthesizers(*66–68*). These automated devices enable the consistent production of tracers while protecting the operator from radiation. Most systems are designed for production of relatively large batches, which can be divided up among many end users to share the production cost. While this approach is suitable for commonly used tracers, like [^{18}F]FDG, the systems can be wasteful for production of smaller batches of tracers (e.g. less common tracers, or novel tracers in development). Reaction volumes are typically in the ~1 mL range with needed amounts of expensive precursors in the range of 1s – 10s of mg, and the systems must be operated in specialized facilities (hot cells) to provide radiation protection.

To develop a new tracer or synthesize the existing tracers on different systems, optimization of synthesis protocols is needed to achieve sufficient and consistent yield. Using macroscale radiosynthesizers for new tracer development, is a cumbersome and tedious process as the apparatus generally becomes contaminated after use and one must wait for radioactive decay (e.g. overnight) before beginning the next experiment, limiting the experimental throughput. Performing optimization studies over weeks or months has significant costs, including labor, facilities, multiple batches of radionuclide, as well as the high amount of precursor needed per reaction. These challenges can hinder the development of new tracers and limits the progress of research relying on those tracers.

Recently, Zhang *et al.* reported a high-throughput technique for optimization of ^{18}F-radiosyntheses(*69*) that avoids the use of radioactivity, thus allowing multiple syntheses to be

carried out back to back on the radiosynthesizer without worry of radioactive contamination of the apparatus. Syntheses are performed starting with levels of [^{19}F]fluoride (in the form of KF) that are comparable to what would be expected in an actual radiosynthesis (using [^{18}F]fluoride), and reaction yield is determined by detecting species of interest in the crude reaction mixture with very high sensitivity using liquid chromatography/tandem mass spectrometry (LC-MS/MS). Reasonable correlation of yields between the non-radioactive approach and conventional radiosynthesis were reported for two PET tracers, [^{18}F]Fallypride and [^{18}F]MDL100907(*69*). While enabling optimization to be carried out in a shorter time and reducing radionuclide costs, this technique relies on a very expensive instrument that is not commonly found in radiochemistry laboratories. Furthermore, the optimization remains somewhat labor intensive as reactions are carried out serially.

In recent years, microfluidic radiochemistry has drawn increasing attention due to several advantages over radiochemistry performed in conventional radiosynthesizers(*29*,*70*). Several microfluidic platforms have demonstrated reactions in very small volumes with short synthesis times (*29–31*,*47*,*71*,*72*), yet can produce tracers in comparable radiochemical yield to conventional approaches. As a result of the small volume, consumption of expensive reagents (e.g. precursors, peptides, proteins…) can be up to two orders of magnitude less(*30*), purification can be simplified and accelerated, and high molar activity of the tracer can be achieved, even when using only a small amount of radioactivity(*33*). All these factors contribute to significant reductions in the cost of radiosynthesis, which will have particular impact when only small batches are needed.

Leveraging the benefits of microfluidic radiochemistry, Pascali *et al.* reported an optimization protocol for ^{18}F-radiosyntheses using a flow-based microfluidic device (Nanotek, Advion , Ithaca, NY, USA). Operating in a back-to-back experiment mode, optimization of the radiofluorination step (reaction temperature, residence time and reagent ratio) could be completed in only 5–10

experimental days, which is significantly shorter than the time typically required for optimization on conventional systems.

Inspired by these advances, we developed a high throughput radiochemistry optimization platform, adapted from droplet-based microdroplet reactors developed by our group (*31*), where multiple reactions can be performed in parallel instead of sequentially. This approach uses a microfluidic chip that contains an array of reaction sites (either 2x2 or 4x4) for performing simultaneous droplet-based radiosyntheses. This approach has considerable advantages: (i) reactions are performed in parallel, with up to 16 reactions (different conditions and/or replicates) completed in the time taken to perform 1 reaction; (ii) each reaction uses only a tiny amount of reagents (typically 10s of µg), reducing the cost of optimization and enables optimization even in early stage development when precursor is scarce; (iii) the droplet-based microdroplet reactor uses low-cost analytical radiochemistry techniques and does not require significant new instrumentation. Furthermore, the platform significantly relieves the radiochemist from tedious and repetitive work typically required if using traditional synthesis means. As a proof of concept, we optimize the synthesis of [^{18}F]fallypride, a PET tracer used to study diseases associated with the dopaminergic system such as Parkinson's, Huntington's, and Alzheimer's diseases(*73*–*75*). To assess the suitability of this approach, we performed experiments to measure cross-contamination from one site to another and to measure the consistency of radiochemical processes among different reaction sites. Finally, extensive sets of varied reaction conditions (e.g. base amount, volume of precursor, and precursor concentration) were performed with each to map out the parameter space and ultimately maximize the yield. By having 16 reaction sites, we could perform analysis of 8 different reaction conditions while using 2 replicates per condition to assess repeatability, all within a single day.

2.2 Materials and Methods

2.2.1 Materials

Teflon AF 2400 (1% solids) solution was purchased from Chemours (Wilmington, DE, USA). Positive photoresist (MEGAPOSIT SPR 220-7.0) and developer (MEGAPOSIT MF-26A) were purchased from MicroChem (Westborough, MA, USA). Additional solvents and chemicals used for microfluidic chip fabrication, including methanol (MeOH, Cleanroom LP grade), acetone (Cleanroom LP grade) and isopropanol (IPA, Cleanroom LP grade) were purchased from KMG Chemicals (Fort Worth, TX, USA).

Anhydrous methanol (MeOH, 99.8%), anhydrous acetonitrile (MeCN, 99.8%), 2,3-dimethyl-2-butanol (thexyl alcohol, 98%), ammonium formate (NH_4HCO_2, 97%) and trimethylamine (TEA, 99%) were purchased from Sigma-Aldrich (St. Louis, MO, USA). Tetrabutylammounium bicarbonate ($TBAHCO_3$, 75mM), tosyl fallypride (fallypride precursor, >90%) and fallypride (reference standard for [^{18}F]fallypride, >95%) were purchased from ABX Advanced Biochemical Compounds (Radeberg, Germany). DI water was obtained from a Milli-Q water purification system (EMD Millipore Corporation, Berlin, Germany). No-carrier-added [^{18}F]fluoride in [^{18}O]H_2O was obtained from the UCLA Ahmanson Biomedical Cyclotron Facility.

2.2.2 Multi-reaction microdroplet chips

The multi-reaction microfluidic chips were fabricated utilizing the standard lithographic processes reported previously(*31*,*76*). In short, batches of muti-reaction microdroplet chips were fabricated from 4” silicon wafers. The silicon wafers were placed on a spin-coater chuck and 3 mL of Teflon AF 2400 solution was poured at the center of the wafer and coated at 1000 rpm for 30 s (500 rpm/s ramp). Solidification of the coating was ensured by placing the wafer on a 160 °C hotplate for 10 min and then transfer to a 245 °C hotplate for 10 min. Annealing of the coating was performed by placing the coated wafers in a high-temperature (HTCR 6 28, Carbolite) at 340 °C for 3.5 h under nitrogen atmosphere, followed by cooling to 70 °C at a 10 °C/min ramp. Then,

Teflon coated silicon wafers were placed on spin-coated and 2 mL of 2 mL of positive photoresist (SPR 220-7) at the center of the wafer using a transfer pipet, and then perform coating at 3000 rpm for 30 s (1000 rpm/s ramp). Solidification of the photoresist was conducted by soft bake of the wafer on a 115 °C hotplate for 3 min. A photomask with the chip pattern was used in a mask aligner (MA6, Karl Suss), and perform a 14 s exposure at 12 mW/cm^2 lamp intensity and 356 nm wavelength in hard contact mode. Excess photoresist was removed by using photoresist developer solution (MF-26A) in a glass container for 3 min with slight agitation to develop the exposed pattern and rinsed with DI water for 3 min. The next step was to edge away the exposed Teflon regions via 30 s exposure to oxygen plasma (Oxford80 Plus RIE) at 100 mTorr pressure, 200 W power and 50 sccm oxygen flow. Finally, the wafers were then cut to each individual chop and each individual chip was submerged in acetone for 1 min to remove photoresist, then isopropanol for 1 min. Finally, dry each chip with a nitrogen gun. **Figure 2.1** demonstrated the photolithography method for the fabrication of the microdroplet chips.

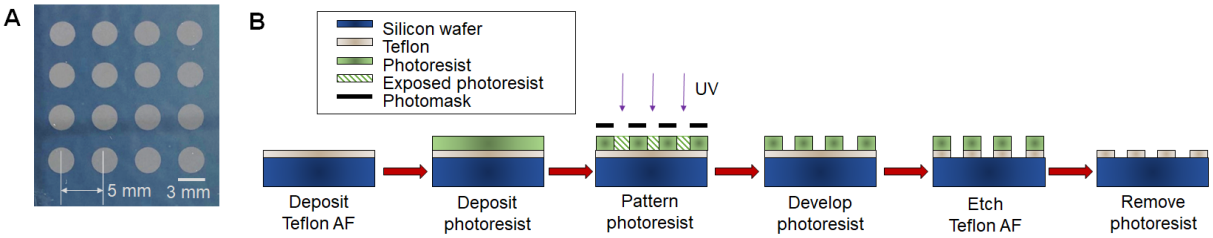

Figure 2. 1 Photolithography process for multi-reaction microdroplet chip fabrication

(A) Photograph of multi-reaction microdroplet chip with 4x4 array of reaction sites. The chip consists of Teflon-coated silicon with circular regions of Teflon etched away to create the hydrophilic reaction sites. (B) Schematic of fabrication procedure. A silicon wafer is spin-coated with Teflon AF 2400 solution and baked to solidify the coating. Next, photoresist is spin-coated, and patterned via photolithography to produce an etch mask. Photoresist is developed with photoresist developing solution. The exposed Teflon is then removed via dry etching with oxygen plasma. The wafer is diced into individual chips and photoresist is stripped.

The 4-spot chip (25.0 x 27.5 mm^2) comprises a hydrophobic Teflon surface with four circular hydrophilic reaction sites (4 mm diameter) positioned in 2 x 2 array with 5 mm space between adjacent reaction sites (9 mm center to center). The 16-spot chips (25.0 x 27.5 mm^2) have sixteen circular hydrophilic reaction sites (3 mm diameter) positioned in a 4 x 4 array with 2 mm space in

between (5 mm center to center). The reagents were manually loaded on the hydrophilic reaction site and retained within it during reaction processes due to the preferred wettability compared to the surrounding hydrophobic (Teflon AF) surface. Each reaction site was designed for performing an individual synthesis.

The chip was affixed to a temperature control platform, which was previously described(*31*). The chips and overall setup are shown in **Figure 2.2.**

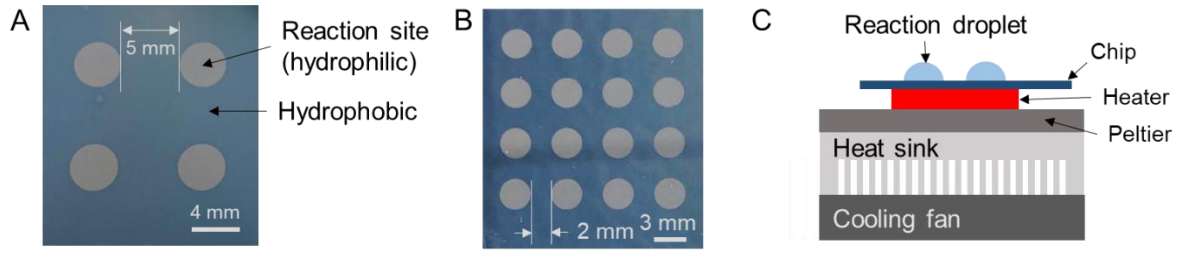

Figure 2. 2 The microdroplet chips and overall setup.

Photograph of the 4-spot microfluidic chip. Diameter of each reaction site is 4 mm and the pitch is 9 mm. (B) Photograph of the 16-spot microfluidic chip. Diameter of each reaction site is 3 mm and the pitch is 5 mm. (C) Schematic of the side view of the experimental setup for performing parallel radiosyntheses on the multi-spot microfluidic chip.

2.2.3 Synthesis and optimization on the chip

[^{18}F]fallypride was synthesized using a modified version of a previously described droplet synthesis protocol (*31*). Briefly, a [^{18}F]fluoride stock solution (30 mM $TBAHCO_3$; 4 mCi; 148 MBq) was prepared by mixing with $TBAHCO_3$ with [^{18}F]fluoride/[^{18}O]H_2O and diluting with DI water up to 150 µL. An 8 µL droplet of this stock solution was loaded to each of the desired spot(s) on a 2 x 2 or a 4 x 4 multi-reaction chip and dried for 1 min at 105 °C. Next, a 6 µL solution of fallypride precursor (39 mM in 1:1 v/v mixture of thexyl alcohol and MeCN) was added, mixed with the dried residue at the desired spot(s), and allowed to react for 7 min at 110 °C. Crude [^{18}F]fallypride product was collected from the desired spot(s) on the chip, with 60 µL of 90% MeOH and 10% DI water.

Variation of individual parameters ($TBAHCO_3$ concentration, volume of precursor solution, and precursor concentration) was carried out with at least n=2 replicates each to determine their

influence on fluorination efficiency and crude radiochemical yield (RCY). Volume of precursor was varied from 2 to 8 µL, $TBAHCO_3$ concentration was varied from 0.95 to 60 mM, and precursor concentration ranged from 0.6 to 77 mM.

2.2.4 Analytical methods

The activity distribution on the chips at three different stages of [^{18}F]fallypride synthesis (after drying of fluoride, after fluorination, and after collection) were analyzed using Cerenkov imaging as previously described(*31*,*77*). Briefly, chips were placed in a home-built light-tight box(*77*), covered with a transparent substrate, and Cerenkov light was detected by a scientific cooled camera (QSI 540, Quantum Scientific Imaging, Poplarville, MS, USA) equipped with a 50 mm lens (Nikkor, Nikon, Tokyo, Japan). The temperature of the camera was maintained at -10°C for dark current reduction and the field of view of the system was 50 x 50 mm^2. Exposure time was 5 min and raw images were corrected as previously described(*77*), followed by background subtraction and decay correction to the starting time of the first image. The images were then analyzed by drawing regions of interest (ROIs) using custom-written MATLAB software. (One of the ROIs, drawn in an area that did not contain radioactive sample, was used for background subtraction.)

Moreover, performance of synthesis was evaluated by analyzing the collection efficiency and fluorination efficiency to obtain the crude radiochemical yield (crude RCY). Radioactivity measurements were made using a calibrated dose calibrator (CRC-25R, Capintec, Florham Park, NJ, USA). Activity on chip was measured when adding an 8 µL droplet mixture of $TBAHCO_3$ with [^{18}F]fluoride/[^{18}O]H_2O to the first reaction site and subsequent measurements were performed after adding activity to each reaction site on the chip. Subtraction and decay correction to the first measurement on the chip was performed to calculate the starting activity on each reaction site. Collection efficiency was determined by dividing the activity of the collected crude sample (decay corrected) by the starting activity in the reaction site Fluorination efficiency was analyzed using radio-TLC. The crude sample was spotted (1 µL) onto a silica gel 60 F_{254} plate (Merck KGaA,

Darmstadt, Germany), and developed with 60% MeCN in 25 mM NH_4HCO_2 with 1% TEA (v/v). To accelerate analysis, radio-TLC plates were spotted with multiple samples (up to 8 at 0.5 mm pitch) before developing. After separation, a glass microscope slide (76.2 mm x 50.8 mm, 1 mm thick) was placed over the multi-sample plates and were read out using Cerenkov imaging (5 min exposure)(*78*) using the same method as for imaging the microfluidic chips. To determine the fluoride conversion, ROIs were drawn on the final corrected image to enclose the radioactive regions/spots. Each ROI was integrated, and then the fraction of the integrated signal in that ROI (divided by the sum of integrated signal in all ROIs corresponding to the particular sample) was computed. Finally, crude RCY was determined by multiplying the collection efficiency by the fluorination efficiency.

Analytical radio-HPLC was performed using a Smartline HPLC system (Knauer, Berlin, Germany) equipped with a degasser (Model 5050), pump (Model 1000), a UV (254nm) detector (Eckert & Ziegler, Berlin, Germany) and a gamma-radiation detector and counter (B-FC- 4100 and BFC-1000; Bioscan, Inc., Poway, CA, USA). Separation was performed using a C18 column (Kinetex, 250 x 4.6 mm, 5 µm, Phenomenex, Torrance, CA, USA). The mobile phase was 60% MeCN in 25 mM NH_4HCO_2 with 1% TEA (v/v) and flow rate was 1.5 mL/min. The retention time of fallypride was 4.5 min. The crude [^{18}F]fallypride mixture collected from the chip was mixed with fallypride (reference standard) and manually injected into the HPLC system for confirmation of radiochemical identity. Examples of chromatograms of crude [^{18}F]fallypride were shown in **Figure 2.8**.

2.3 Results and discussion

The chips were installed on top of a heater such that the temperature was the same at all reaction sites (confirmed with thermal imaging, data not shown). Syntheses were carried out in parallel, with the whole chip (i.e. whole array of sites) heated or cooled simultaneously after adding

the relevant reagent to all reaction sites (**Figure 2.3**). After completion of reactions, crude reaction products were collected independently from each reaction site for analysis.

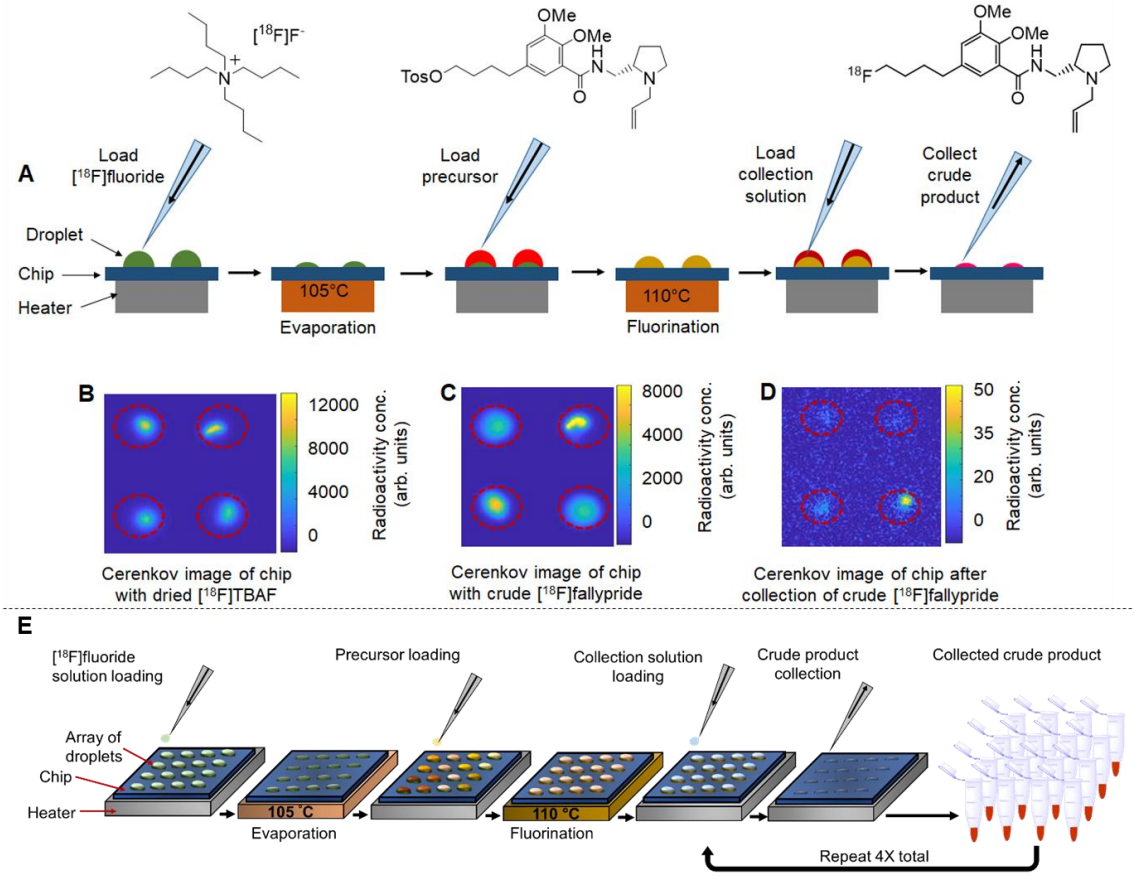

Figure 2. 3 Parallel synthesis of [18F]Fallypride using the multi-reaction platform

Up to 4 reactions can be performed in parallel on 2 x 2 array chips and up to 16 reactions can be performed in parallel on 4 x 4 array chips. (A) Schematic of the multi-step radiochemical synthesis of [^{18}F]fallypride in micro-droplets. First, at each site, an 8 µL droplet of [^{18}F]fluoride (~3.7 MBq) mixed with $TBAHCO_3$ (240 nmol) was added and then dried at 105 °C for 1 min. Then, a 6 µL droplet of tosyl-fallypride precursor (39 mM) was added and reacted for 7 min at 110 °C. Finally, 20 µL collection solution (90:10 v/v MeOH:water) was loaded on the reaction site to dissolve resulting compounds and the mixed droplet was collected from the chip. Each site was collected for independent analysis via 3 repeats of the collection process. (B) Cerenkov image showing the distribution of radioactivity on a 2x2 chip of the parallel synthesis after the evaporation of 8 µL droplets of [^{18}F]fluoride mixed with $TBAHCO_3$. (C) Cerenkov image showing the distribution of radioactivity on a 2x2 chip of crude [^{18}F]fallypride after the fluorination of tosyl-fallypride with [^{18}F]fluoride. (D) Cerenkov image showing the distribution of the residual radioactivity on a 2x2 chip after the collection of crude [^{18}F]fallypride. The Cerenkov brightness is decay-corrected to a common timepoint for all images. (E) Experimental procedure for performing 16 parallel syntheses using a 4 x 4 array chip.

Evaluation of synthesis performance was achieved by analyzing the collection efficiency and fluorination efficiency to calculate the crude radiochemical yield (crude RCY). Collection efficiency was determined by dividing the activity of the collected crude sample (decay corrected) from the starting activity in the reaction site. Fluorination efficiency was analyzed via radio-TLC or radio-HPLC.

2.3.1 Cross-contamination tests

We first assessed the independence of each reaction site by performing droplet radiochemical syntheses of [^{18}F]fallypride at some sites on the chip while other sites were left “blank” (no [^{18}F]fluoride added, but otherwise synthesis steps still carried out). Cerenkov luminescence imaging of the chip surface(*31*,*77*) was used to quantify any cross-contamination of radioactive species to the blank sites at different stages of the synthesis process. In one experiment on a 2x2 chip, 1 of 4 sites was used to perform the first step of [^{18}F]fallypride synthesis (i.e., drying of solution containing [^{18}F]fluoride and $TBAHCO_3$ to form the [^{18}F]TBAF complex), and Cerenkov images taken afterwards (see **Appendix, Figure 2.5A**) revealed negligible signal in the blank sites, i.e. activity level was <0.3-0.6% of the activity at the non-blank site suggesting no cross-contamination of radioactivity. In another experiment on a 2x2 chip, 3 of 4 sites were used to perform the complete synthesis of [^{18}F]Fallypride while a mock synthesis (no [^{18}F]fluoride) was performed at the remaining site. In this case, Cerenkov images taken afterwards (see **Appendix, Figure 2.5A**) also showed negligible radioactive contamination of the blank site, i.e. activity level was<0.4 % of the activity at the non-blank sites. Similarly, no significant cross-contamination was observed on 4x4 chips either, despite the closer spacing of these reaction sites. Quantitation of Cerenkov images (see **Appendix, Figure 2.6A** and **Figure 2.6B**) showed the amount of contamination in blank spots to be <1.4% of the average activity in non-blank spots. Overall, these results suggest that the parallel reactions can be considered independent.

2.3.2 Reproducibility tests

Next, we assessed the reproducibility at different reaction sites by performing replicates of syntheses using multiple reaction sites on a single chip. In a set of experiments on 2x2 chips, we performed drying of the [^{18}F]TBAF complex and subsequent fluorination of tosyl-fallypride on all sites (see **Appendix, Table 2.1**) and found the crude radiochemical yield (crude RCY) to be 88 ± 1 % (n=4), indicating excellent reproducibility from site to site. Similar reproducibility was found for an experiment on a 4x4 chip, in which syntheses on half of the sites were carried out with a $TBAHCO_3$ amount of 240 nmol, and the other half were carried out with 7 nmol (see **Appendix, Table 2.2**). The crude RCYs were measured to be 85 ± 2% (n=8) and 38 ± 4% (n=8) for the two conditions, respectively, the low standard deviation across each condition indicates excellent site-to-site reproducibility. In later experiments (described below), we discovered that the yield is highly sensitive to the amount of base at the low-base condition and thus the higher variability in crude RCY of those reactions is expected.

2.3.3Optimization studies

To demonstrate the utility of the platform, we then leveraged the parallel reactions to perform an extensive, fine-grained optimization of several [^{18}F]fallypride synthesis parameters, each data point with multiple replicates. The initial syntheses were performed using the reaction conditions adapted from Wang *et al.*(*31*) to gather baseline performance. In short, a [^{18}F]fluoride stock solution was prepared by combining [^{18}F]fluoride/[^{18}O]H_2O (150 µL, ~200 MBq; 5.5 mCi) with 30 nmol of $TBAHCO_3$. An 8 µL droplet of the mixture was added to each reaction site and dried at 105°C for 1 min, then a 4 µL droplet of tosyl-fallypride precursor (77 mM) in a mixture of MeCN and thexyl alcohol (1:1, v/v) was added in each reaction site, and the chip was heated to 110°C for 7 min to carry out the fluorination step. Collection of the crude reaction product at each site was carried out by repeating the following steps 3 times: adding 20 µL of a mixture of MeOH and DI water (9:1, v/v) and collecting the resulting mixture from the chip (total of 60 µL). In repeated experiments under identical conditions, we observed high variability of crude RCY from 8-84%,

suggesting the reactions were either highly sensitive to certain conditions (e.g. reagent amount) or to a variable we had not accounted for.

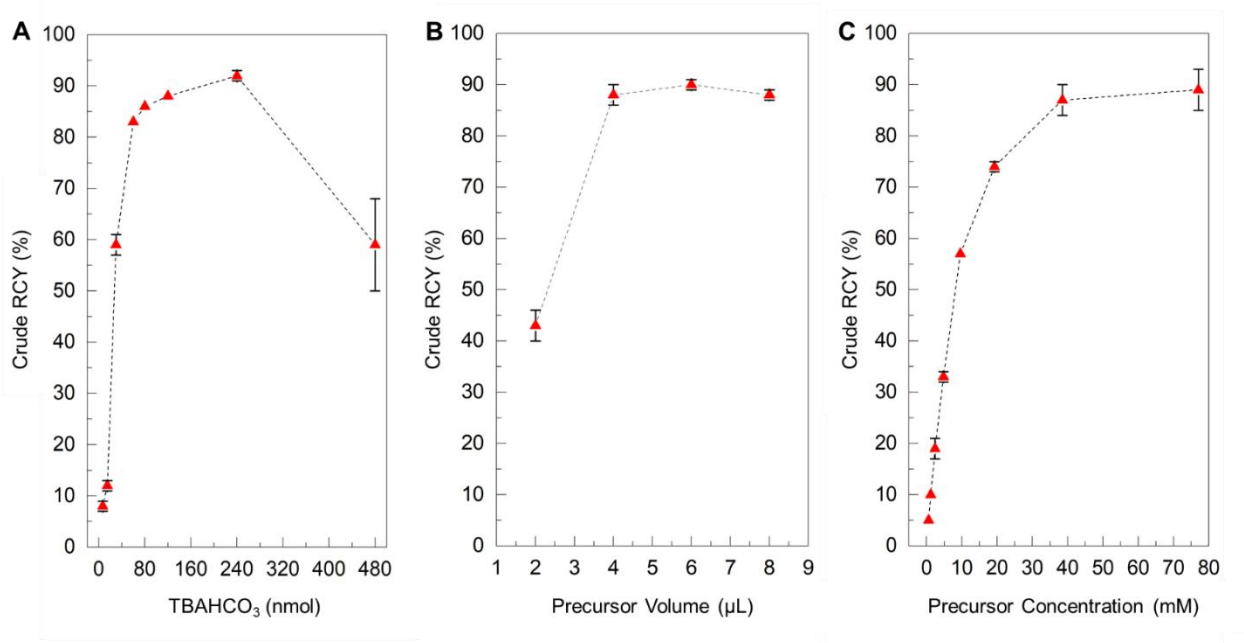

Figure 2. 4 Influence of reaction parameters on the platform of the microdroplet synthesis of [18F]Fallypride, explored using the high-throughput platform

(A) Effect of concentration of base solution. Reaction volume: 4 µL. Precursor solution concentration: 77 mM. The optimal value was taken as 240 nmol of $TBAHCO_3$, giving a crude RCY of 92±1% (n=2). (B) Effect of volume of precursor solution. Base amount: 240 nmol. Precursor solution concentration: 77 mM. The optimal value was taken as 6 µL, giving a crude RCY of 90±1% (n=4). (C) Effect of concentration of the precursor solution. Base amount: 240 nmol. Precursor solution volume: 6 µL. The optimal value was taken as 39 mM, giving a crude RCY of 87±3% (n=2).

We first explored the impact of the amount of $TBAHCO_3$ in the reaction (**Figure 2.4A**, and **Appendix, Table 2.3**). Standard deviations of data points were small, and the yield showed a clear dependence on the amount of base. From nearly zero yield at low base amount, the yield sharply rises to ~86% at 80 nmol base, where it remains relatively stable, and then falls off again with higher base amounts. The highest yield (92 ± 1%, n=2) was obtained at 240 nmol. The very high sensitivity to base at 30 nmol may suggest why high variability was observed under the original synthesis conditions: a small variation in the amount of base (e.g. due to pipetting error when adding the [^{18}F]fluoride/$TBAHCO_3$ solution) could result in large variation in yield. The

relatively low slope in the 80-240 nmol range suggests the yield would be fairly immune to pipetting errors.

We next examined the effect of fluorination reaction volume on yield, using 240 nmol of $TBAHCO_3$ in the initial [^{18}F]fluoride/$TBAHCO_3$ droplet and 77 mM concentration of precursor solution (**Figure 2.4B**, and **Appendix, Table 2.4**). The crude RCY yield showed a strong dependence on reaction volume, rising from a moderate value (43 ± 3%, n= 4) for a 2 µL reaction to nearly 100% for volumes of 4, 6, and 8 µL. Based on visual observations, we suspect that the smaller volumes are not sufficient to fully wet the reaction site and thus some of the dried [^{18}F]TBAF residue remaining after the drying step does not get dissolved into the reaction droplet. We chose a reaction volume of 6 µL for subsequent experiments as in that region the flat slope of the graph indicates an insensitivity to errors in precursor droplet volume.

Finally, we explored the influence of precursor concentration, when using 240 nmol of $TBAHCO_3$ and a 6 µL fluorination reaction volume (**Figure 2.4C**, and **Appendix, Table 2.5**). Crude RCY was near zero for low precursor concentrations, increasing rapidly with precursor concentration, and reaching a plateau with near 100% yield above ~40 mM. At the optimal conditions (240 nmol $TBAHCO_3$, 6 µL reaction volume, and 39 mM precursor concentration), the fluorination efficiency was 96.0 ± 0.5 % (n=2) and the crude RCY was very high, namely 87 ± 3 % (n=2).

The optimized reaction conditions found using our multi-reaction microfluidic chip provided higher and more consistent crude RCY compared to previous reports using microscale platforms(*48*,*79–81*). For example, 84 ± 7 % (n=6) was reported for droplet-based reactions on an EWOD chip(*79*) and 64 ± 6 % (n=4) was reported for droplet-based reactions on a chip using a passive droplet transport mechanism(*31*). Furthermore, we were able to perform 16 syntheses within only 90 min (starting from the loading of [^{18}F]fluoride/$TBAHCO_3$ mixture, up to the end of collection process. On other microscale platforms, the time for a single synthesis run was, e.g., 31 min(*79*) or 25 min(*31*), which would require ~500 min [8.3 h] or ~400 min [6.7 h] to perform 16

experiments. The time savings using the multi-reaction chip are a direct result of performing many of the steps (e.g. drying step and fluorination step) at all reaction sites in parallel.

Interestingly, we observed the formation of a side-product on the TLC chromatogram when the molar ratio of base to precursor exceeded 1.0. (This observation seems to be consistent withMoon *et al.* who reported that the usage of high base concentration (either K_{222}/K_2CO_3 or $TBAHCO_3$) led to low radiochemical yield and unidentified radio-impurities (*82*).) We found no detectable side product as long as the molar ratio of base to precursor remained < 1.0 (as shown in the **Appendix, Figure 2.7**). This finding might be applicable to synthesis of [^{18}F]fallypride, or other base-sensitive tracers in other setups to help choose an appropriate precursor amount depending on the amount of base needed to elute [^{18}F]fluoride from the QMA cartridge.

2.4 Conclusion

Using the reaction array chips, the synthesis conditions could be rapidly optimized, and the optimization could be performed with fine granularity while including replicates of each data point. Using the 2x2 reaction chips, it was possible to run 16 experiments per day at low activity levels, allowing the full optimization study reported here (20 conditions, n=2 each) to be completed in 3 days. By using 4x4 reaction chips that we started developing near the end of this study, it would be practical to complete this study in even shorter time. Further increase in throughput could be accomplished by operating multiple heaters (and multiple chips) in parallel.

Though in this study we examined the effect of reaction volume and reagent concentrations, one could also study variables such as reaction temperature or time, by using multiple heaters, or by running multiple chips sequentially on the same heater.

An important aspect of high-throughput reaction optimization is the ability to rapidly analyze all of the collected reaction mixtures. To accomplish this, we developed an optimized TLC separation method with short separation length (35mm), and spotted multiple samples (1.0 µL each, 1.0 mm pitch) that could be separated and read out in parallel using CLI(*77*).

Due to limitations of conventional radiochemistry systems that allow only one or a small number of reactions per day, one typically explores only a small range of the potential parameter space and results are often reported with no repeats (n=1). Compared to such approaches, our high-throughput droplet radiosynthesis platform makes it practical to perform more comprehensive and robust studies of radiosynthesis conditions, potentially enabling new insights on parameters that influence product yield and side-product formation, or on what choice of parameter values leads to a robust synthesis (i.e. insensitivity to small variations in variables). Furthermore, since the amount of precursor consumed per reaction is extremely small (e.g. ~84 µg per data point compared to 4 mg per data point in conventional reactions), and many reactions can be carried out using the same batch of radioisotope, the cost of the optimization process can be significantly lower than for conventional setups. The low precursor consumption may be especially useful in the early development of novel tracers when only a small amount of precursor may be available.

Due to success in synthesizing other tracers on this and similar microfluidic platforms (*31*,*65*,*79*), we expect this platform to be applicable to the development and optimization of a wide range of PET tracers and other radiopharmaceuticals. In other work, we have shown the ability to increase the scale of droplet-based reactions by pre-concentrating the radioisotope(*83*), providing a route to immediately transition from low-activity optimization runs to high-activity production runs using the exact same microfluidic reaction geometry and synthesis process. Thus, microdroplet reactions are not only a useful tool during the optimization phase, but also can produce sufficient quantity of tracers for preclinical or even clinical studies.

In summary, we have developed a general platform and strategy for the rapid optimization of PET tracer syntheses and demonstrates efficient translation of macroscale synthesis procedures to microscale syntheses by using a novel multi-reaction microfluidic chip that allows analysis of performance of up to 16 parallel reactions. Contamination tests confirmed the independence of

reaction sites and reproducibility of reactions was demonstrated by performing replicate syntheses.

2.5 Appendix

2.5.1 Cross-contamination and repeatability studies

To investigate the cross contamination between adjacent reaction sites, Cerenkov luminescence imaging (CLI) was employed to image the activity distribution on the chip after performing drying of [^{18}F]fluoride/TBAHCO$_3$ or fluorination in different patterns of reaction sites. In an initial test of 2x2 chips, an 8 µL droplet of [^{18}F]fluoride/TBAHCO$_3$ solution (~1.8MBq; 3.8 mM) was loaded on 1 of 4 reaction sites, 8 µL droplets of TBAHCO$_3$ solution (3.8 mM) were loaded on the remaining reaction sites, and all spots were dried simultaneously at 105 °C for 30 s, followed by CLI imaging (**Figure 2.5A**). Suspecting that steps with more volatile organic solvent could increase cross-contamination, we also performed investigations during the fluorination reaction. On a 2x2 chip, 3 of 4 sites were loaded with 8 µL of [^{18}F]fluoride/TBAHCO$_3$ (~1.8 MBq; 3.8 mM), while one was loaded with just TBAHCO$_3$ solution (no [^{18}F]fluoride). After the drying step, 6 µL of 39 mM precursor solution was added to all reaction sites, and fluorination was carried out in parallel, followed by CLI imaging (**Figure 2.5B**).

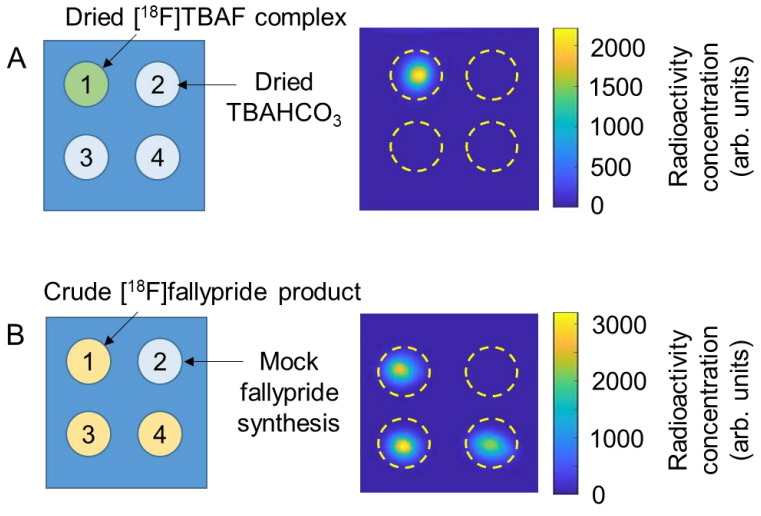

Figure 2. 5 Cross-contamination tests using 2x2 chips

(A) (Left) Schematic of an experiment to test cross-contamination during drying of [^{18}F]TBAF complex. (Right) Cerenkov image of the chip after the drying step. (B) (Left) Schematic of experiment to test cross-contamination during synthesis of [^{18}F]fallypride. (Right) Cerenkov image of the chip after the fluorination step.

To assess the reproducibility at different reaction sites, syntheses of [^{18}F]fallypride were performed in parallel at multiple sites of the same chip. In a set of experiments on 2x2 chips, we performed drying of the [^{18}F]TBAF complex and subsequent fluorination of tosyl-fallypride on all sites. The crude product was collected from each site and analyzed (**Table 2.1**).

Table 2. 1 Performance of [18F]Fallypride synthesis on 4 sites on a 2x2 reaction chip

Reactions were carried out with 240 nmol of TBAHCO3, 39 mM of precursor, and 6 µL of precursor solution loaded on each reaction site. High reproducibility is evident.

Performance measure	Reaction site 1	Reaction site 2	Reaction site 3	Reaction site 4	Average ± std dev (n=4)
Collection efficiency (%)	91	92	93	91	92 ± 1
Fluorination efficiency (%)	97	93	94	95	95 ± 2
Crude RCY (%)	89	86	88	87	88 ± 1

We also tested the 4x4 chips to determine if the closer spacing had an impact on cross-contamination. Two experiments were performed with different solution loading patterns. One pattern was made by loading an 8 µL droplet of [^{18}F]fluoride solution (~ 3.6 MBq) on the reaction sites at the four corners of the 4 x 4 array, and another pattern was made by loading an 8 µL droplet of [^{18}F]fluoride solution on alternating reaction sites. The remaining reaction sites were each filled with an 8 µL droplet of DI water. Then, the chips were dried at 100 °C for 1 min, followed by CLI imaging (**Figure 2.6A** and **Figure 2.6B**, respectively).

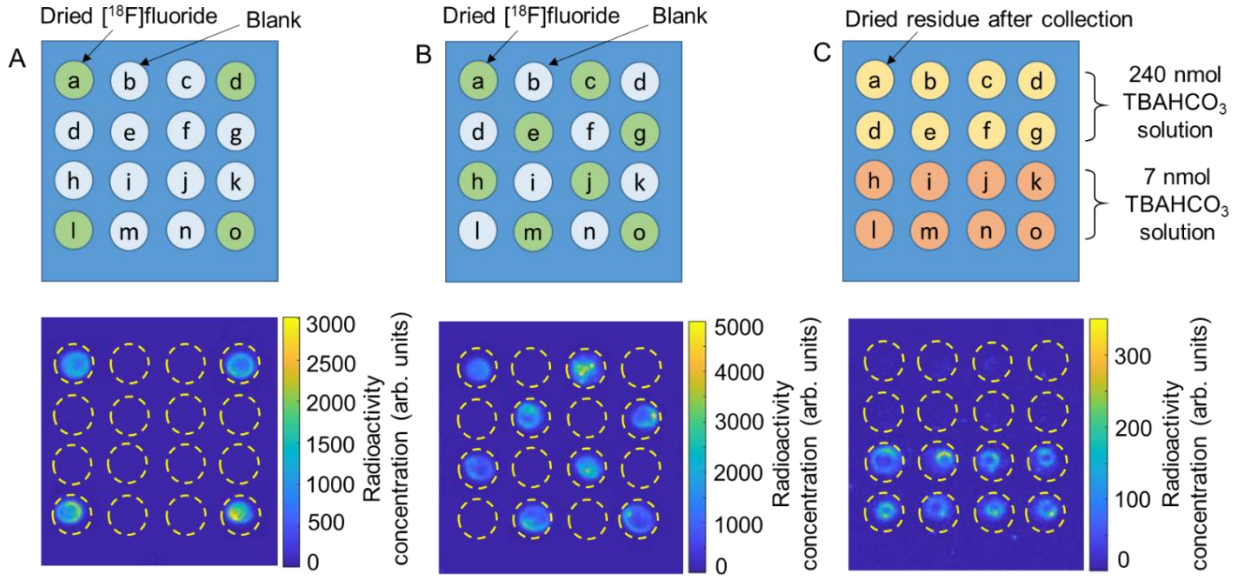

Figure 2. 6 Cross-contamination and repeatability tests using 4x4 chips

(A) (Top) Schematic of an experiment with a pattern of loaded and blank reaction sites. (Bottom) Cerenkov image of the chip after drying. (B) (Top) Schematic of an experiment with a different pattern of loaded and blank reaction sites. (Bottom) Cerenkov image of the chip after drying. (C) (Top) Schematic of experiment to test repeatability during synthesis of [^{18}F]Fallypride (240 nmol $TBAHCO_3$ amount for top two rows and 7 nmol $TBAHCO_3$ amount for bottom two rows). (Bottom) Cerenkov image of the chip after the collection step.

To assess repeatability on the 4x4 chip, we loaded 8 µL of two different concentrations of [^{18}F]fluoride/$TBAHCO_3$ solution: ~3.6 MBq [^{18}F]fluoride and 30 mM [240 nmol] $TBAHCO_3$ in the first 2 rows and ~3.6 MBq [^{18}F]fluoride and 0.9 mM [7 nmol] $TBAHCO_3$ in the second two rows. After the drying step was performed, 6 µL of 39 mM precursor was added to all reaction sites and the fluorination reaction was performed by heating the whole chip. The crude products were collected and analyzed (**Table 2.2**) and a CLI image of the chip after sample collection was obtained (**Figure 2.6C**).

Table 2. 2 Synthesis performance from 16 sites on a 4x4 reaction chip using two different base concentrations (n=8 each) corresponding to Figure 2.6C

For all reactions, precursor concentration was 39 mM, and volume of precursor solution was 6 µL. $TBAHCO_3$ amount was 240 nmol in the reactions of rows 1 and 2 on the chip, and 7 nmol in rows 3 and 4. High reproducibility is evident. The higher variability in rows 3 and 4 may be caused by the higher sensitivity to salt concentration under this condition.

	Performance measure	Column 1	Column 2	Column 3	Column 4	Average ± std dev (n=4)
Row 1	Collection efficiency (%)	93	92	94	94	93±1
	Fluorination efficiency (%)	93	92	93	90	92±1
	Crude RCY (%)	87	84	87	84	86±2
Row 2	Collection efficiency (%)	92	95	92	93	93±2
	Fluorination efficiency (%)	89	91	91	89	90±1
	Crude RCY (%)	81	86	84	83	84±2
Row 3	Collection efficiency (%)	92	84	89	88	89±3
	Fluorination efficiency (%)	50	41	41	40	43±5
	Crude RCY (%)	46	35	36	35	38±5
Row 4	Collection efficiency (%)	91	86	88	95	90±4
	Fluorination efficiency (%)	41	45	39	44	42±3
	Crude RCY (%)	37	39	34	42	38±3

2.5.2 Optimization results

This section contains all the raw data that was used to generate the plots in **Figure 2.4**. Experiments to compare the effects of amount of base, precursor solution volume, and precursor solution concentration are summarized in **Table 2.3, Table 2.4,** and **Table 2.5,** respectively.

Table 2. 3 Details of syntheses to evaluate influence of base amount on the synthesis of [18F]fallypride

Reactions were carried out with 77 mM of precursor, 4 µL of precursor solution, and base amount in an 8 µL droplet as indicated. Each condition was replicated n=2 times.

Base amount (nmol)	Collection efficiency %	Fluorination efficiency %	Crude RCY %
480	94 ± 1	63 ± 11	59 ± 9
240	94 ± 1	98.9 ± 0.2	92 ± 1
120	93 ± 1	96 ± 1	88.3 ± 0.3
80	92 ± 1	94 ± 1	86.0 ± 0.2
60	91 ± 3	92 ± 2	83.1 ± 0.5
30	90.4 ± 0.1	65 ± 2	59 ± 2
15	91 ± 2	13 ± 1	12 ± 1
7	88 ± 1	9 ± 1	8 ± 1

Table 2. 4 Details of syntheses to evaluate the influence of precursor solution volume on the synthesis of [18F]fallypride.

Reactions were carried out with 240 nmol of $TBAHCO_3$ in an 8 µL droplet with [^{18}F]fluoride, 77 mM of precursor, and volume of precursor solution as indicated. Each condition was replicated n=2 times.

Precursor solution volume (µL)	Collection efficiency %	Fluorination efficiency %	Crude RCY %
2	87 ± 4	51 ± 7	43 ± 3
4	92 ± 1	96 ± 1	88 ± 2
6	92 ± 1	98 ± 1	90 ± 1
8	92 ± 1	96 ± 1	88 ± 1

Table 2. 5 Details of syntheses to evaluate influence of precursor concentration on the synthesis of [18F]fallypride.

Reactions were carried out with 240 nmol $TBAHCO_3$ in an 8 µL droplet with [^{18}F]fluoride, 6µL of precursor solution, and precursor concentration as indicated. Each condition was replicated n=2 times.

Precursor concentration (mM)	Collection efficiency %	Fluorination efficiency %	Crude RCY %
77	92 ± 2	97 ± 2	89 ± 4
38.5	91 ± 2	96.0 ± 0.5	87 ± 3
19.3	91.1 ± 0.5	81.1 ± 0.3	74 ± 1
9.6	91 ± 1	63 ± 1	57.0 ± 0.5
4.8	89 ± 1	37 ± 1	33 ± 1
2.4	88 ± 2	22 ± 2	19 ± 2
1.2	82 ± 1	13 ± 1	10.4 ± 0.1
0.6	82 ± 4	7 ± 1	5.1 ± 0.5

The data in **Figure 2.7** shows the correlation between base: precursor ratio and the appearance of radioactive side-products in the crude product.

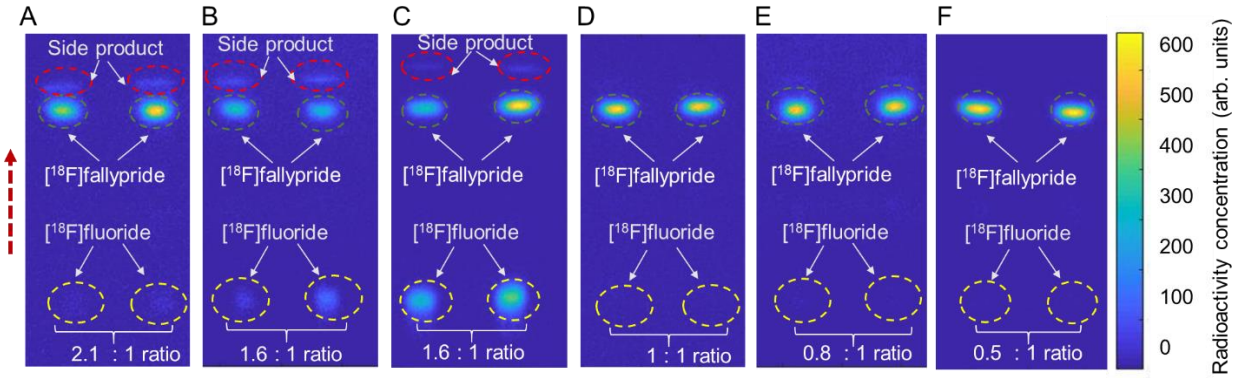

Figure 2. 7 Correlation of amount of side-product with the base:precursor ratio in microdroplet synthesis of [18F]fallypride

(A) Cerenkov luminescence image of developed TLC plate spotted with 1 µL each of 2 crude [^{18}F]fallypride samples, performed with 240 nmol $TBAHCO_3$ and 110 nmol of precursor (6 µL droplet of 19 mM solution). (B) Developed TLC plate spotted with 1 µL each of 2 crude [^{18}F]fallypride samples, performed with 480 nmol $TBAHCO_3$ and 310 nmol of precursor (4 µL droplet of 77 mM solution) (C) Developed TLC plate spotted with 1 µL each of 2 crude [^{18}F]fallypride samples, performed with 240 nmol $TBAHCO_3$ and 154 nmol of precursor (2 µL droplet of 77 mM solution). (D) Developed TLC plate spotted with 1 µL each of 2 crude [^{18}F]fallypride samples, performed with 240 nmol $TBAHCO_3$ and 230 nmol of precursor (6 µL

droplet of 39 mM solution). (E) Developed TLC plate spotted with 1 µL each of 2 crude [^{18}F]fallypride samples, performed with 240 nmol $TBAHCO_3$ and 310 nmol of precursor (4 µL droplet of 77 mM solution). (F) Developed TLC plate spotted with 1 µL each of 2 crude [^{18}F]fallypride samples, performed with 240 nmol $TBAHCO_3$ and 460 nmol of precursor (6 µL droplet of 77 mM solution). The dashed circles represent the ROIs for analysis. The dashed arrow represents the direction of solvent flow during developing.

2.5.3HPLC chromatogram of crude [^{18}F]Fallypride

Radiochemical purity of the crude sample was determined using analytical-scale radio HPLC (**Figure 2.8**). Due to the low reagent mass, the chromatogram is very clean. The absence of impurities near the [^{18}F]fallypride peak suggests that purification via analytical-scale radio-HPLC should be straightforward.

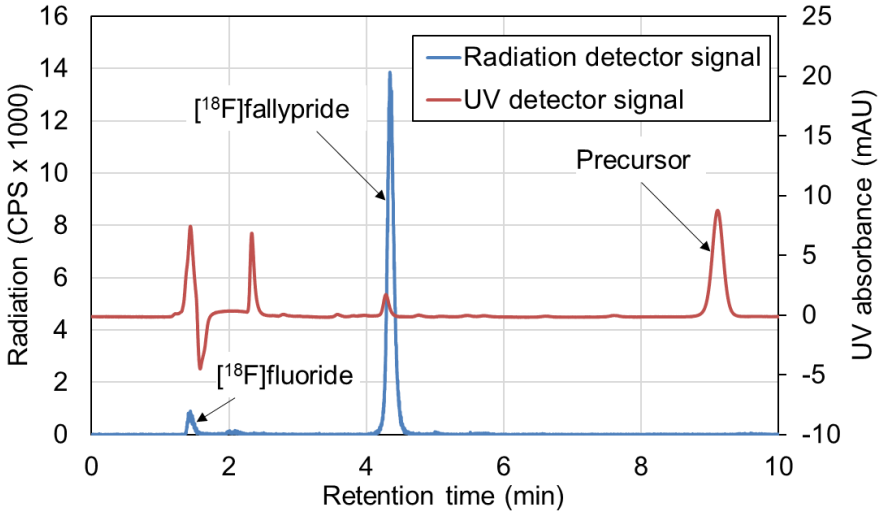

Figure 2. 8 Example of analytical radio-HPLC chromatogram showing the crude [18F]fallypride product synthesized on the microfluidic chip

Non- radioactive fallypride reference standard was injected together with the crude product to confirm the identity of [^{18}F]fallypride.

Chapter 3: High-throughput radio-TLC analysis

3.1 Introduction

Thin layer chromatography (TLC) is a technique used to separate the chemical components of a mixture to identify its composition. This method was first used for the separation of alkaloids present in extracts from medicinal herbs(*84*). Now TLC has multiple uses ranging from analysis of purity and yield in chemical synthesis(*85*,*86*), separation of phospholipids in biological assays(*87*), and, in conjunction with a radiation detector, analysis of radiopharmaceuticals used for positron emission tomography (PET)(*31*,*88*,*89*), single-photo emission computed tomography (SPECT)(*90*,*91*), or targeted radiotherapy(*92*,*93*). In particular, radio-TLC is useful as a means to measure the conversion of radionuclide incorporation into the target radioactive product during synthesis development and optimization: its use is further extend as a quality control (QC) testing of the final formulated radiopharmaceutical to ensure radiochemical purity and radiochemical identity(*94*) before administering to patients. Radio-high-performance liquid chromatography (radio-HPLC) is another chromatography technique for QC testing, and is particularly useful when distinct separation of multiple compounds is needed. However, in many radiopharmaceutical analysis applications, radio-TLC is sufficient and is preferred over radio-HPLC due to its simplicity, quantitative accuracy (e.g. retention of fluoride-18 on the HPLC column affects the quantitative accuracy of radio-HPLC)(*95*), relatively short measurement time(*96*), and low need for maintenance.

Generally, a small amount of the sample is spotted near one end of the TLC plate, and then the edge of the plate is immersed in a solvent to “develop” the TLC plate. As the solvent flows up the TLC plate due to capillary action, the sample is separated into multiple spots each corresponding to a chemical component of the sample. After developing, the plate is dried and analyzed. Typically, a developed silica TLC plate will be analyzed using a radio-TLC scanner, in which a radiation detector is moved along the plate to obtain measurements of emitted radiation

as a function of distance along the plate, which can then be expressed as a chromatogram. Most radio-TLC scanners (e.g. AR-2000, Eckert & Ziegler) use gas-based radiation detectors that are sensitive to gamma radiation as well as beta particles. Downsides of such systems are high cost, and the requirement for continuous supply of gas as well as periodic calibrations. Other radio-TLC scanners (e.g. miniGITA, Raytest) are based on crystal scintillators and photodiodes that do not require a gas supply but are also expensive. Sometimes, different detectors can be installed depending on the radionuclides of interest, and collimators can be added to improve spatial resolution of gamma detection (at the expense of sensitivity). Typically, the TLC plates used are 60 - 100 mm long and typically take 10 - 30 min to develop. The length of the TLC plate is needed both to achieve adequate chemical separation and provide enough readout resolution. The scanning time depends on activity level, but typically 1-3 min is sufficient to analyze the TLC plate(*97*,*98*).

Our laboratory is developing high-throughput radiolabeling methods for optimization of synthesis conditions or preparation of compound libraries, resulting in the need to perform significant numbers of TLC separations and analyze the resulting TLC plates, requiring significant time for development and scanning.

Though some scanners, e.g. AR-2000, have space to install multiple TLC plates which can be scanned automatically in sequence, the overall analysis time still remains long(*99*). To reduce the readout time, we have looked into alternative approaches for readout of TLC plates. Other than scanning detectors, several techniques have been used to more efficiently read radio-TLC plates. One such technique is electronic autoradiography. Such systems, e.g. Instant Imager (Canberra Packard) have a large-area multiwire proportional counter detector, on which multiple radio-TLC plates can be imaged simultaneously. While shown to be convenient, accurate, and able to image a wide range of isotopes (Tc-99m, I-124, F-18, Cu-64, C-11)(*100*,*101*), the readout system is far more expensive than other approaches(*97*,*102*). Radio-TLC plates have also been imaged in a more cumbersome two-step process by first exposing a phosphor screen that is subsequently

scanned with a phosphor imaging system(*103*) (e.g. Perkin Elmer Cyclone Plus). Additional types of detectors have been used for simultaneous readout at multiple positions along a TLC plate thus avoiding the need for scanning. For example, using a 64x1 array of scintillator crystals above a photodiode array, Jeon *et al.* quantified samples spotted at multiple locations with different radioisotopes (Tc-99m, F-18) and found excellent agreement with an AR-2000 scanner (*98*). In another example, Maneuski *et al.* used a pixelated solid-state Timepix silicon detector to obtain a 2D image of a partial radio-TLC plate spotted with an unspecified ^{18}F-containing compound (*104*); however the detector size is small and multiple detectors would be needed to image a full radio-TLC plate or multiple plates, resulting in a high instrument cost.

A more scalable approach is Cerenkov luminescence imaging (CLI) in which radiation is detected indirectly via Cerenkov light emission, and the overall detection area can be scaled with a suitable optical system rather than larger detector. CLI-based detection of compounds containing a wide variety of radionuclides has been demonstrated, including H-3, C-11, C-14, F-18, P-32, Cu-64, Ga-68, I-124,and I-131. Originally reported as a method to observe radioactivity in microfluidic chips (*105*,*106*), CLI is also used for *in vivo* optical imaging (*107*,*108*), intraoperative imaging (*109*,*110*), and has been reported for readout of radio-TLC plates (*111*). One of the attractive features is that this technique can be used for imaging of β^- particles (mostly involved in therapeutic applications in cancer), which do not emit gamma rays (as occurs after positron emission) and thus are not easily imaged by systems based on gamma detection (*107*).

Park *et al.* reported a proof-of-concept demonstration in 2011, showing the possibility to use a commercial small-animal luminescence imaging system (IVIS 200, Caliper Life Sciences) to perform CLI of a developed radio-TLC plate spotted with an unspecific mixture of ^{131}I-containing compounds(*111*). The quantified percentage of luminescence in each of four ROIs compared favorably to the analysis using a conventional radio-TLC scanner (AR-2000). Furthermore, the CLI approach augmented the resolution between separated species and the imaging could be performed rapidly (1 min). Using a custom-built optical imaging system, Spinelli *et al.* later showed

that the imaging time of radio-TLC plates with spotted samples of [^{68}Ga]Ga-DOTANOC (7 kBq) could be reduced (compared to CLI) by placing the plates in contact with a phosphor-containing intensifying screen (*112*). Recently, Ha *et al.* investigated the effect of different types of TLC plates (differing backing materials, stationary phase type and thickness, and addition of fluorescent indicator) by placing multiple spots of various radioisotope solutions (e.g. H-3, P-32, I-124, and I-131) on TLC plates, imaging these plates directly and quantifying relative intensity between spotting locations(*113*), showing the possibility to significantly increase the CLI signal and sensitivity. An interesting feature of this work was a demonstration that multiple radio-TLC plates (16) could be positioned within the large field of view of the small animal scanner (IVIS Spectrum or IVIS Lumina II, Caliper) for simultaneous imaging, and thus speeding the readout when multiple plates are analyzed. However, the high cost (an order of magnitude higher than a conventional radio-TLC scanner) and large size of the small animal scanners may not be practical for many radiochemistry laboratories.

Though demonstrating the potential for high-throughput readout of radio-TLC plates, Ha *et al.* did not perform developing of the TLC plates (i.e. did not perform sample separations). It can be assumed that this step would be very time-consuming and cumbersome for a large number of TLC plates, and that this time and effort would dominate the overall radio-TLC analysis process.

In this chapter, we tackle this missing step and we show a practical approach for the complete analysis of radio-TLC plates (both separation and readout) in a high-throughput, time- and labor-efficient manner. This was accomplished by leveraging the high resolution of CLI and optimizing the sample volume to enable multiple samples to be spotted close together on the same TLC plate. All samples could then be rapidly developed in parallel (leveraging the high imaging resolution to enable very short separation distances) and then read out simultaneously using a compact, low-cost Cerenkov imaging system. We demonstrate high-throughput radio-TLC analysis of complex mixtures of ^{18}F-labeled and ^{177}Lu-labeled radiopharmaceuticals including (S)-N-((1-Allyl-2-pyrrrolidinyl)methyl)-5-(3-[^{18}F]fluoropropyl)-2,3-dimethoxybenzamide

([^{18}F]fallypride), [^{18}F]fluoroethyl-tyrosine ([^{18}F]FET) and [^{177}Lu]Lu-PSMA-617 for assessment of radiochemical purity or reaction conversion. Interestingly, the Cerenkov imaging readout clearly showed small peaks that were not discernable with a conventional radio-TLC scanner (miniGITA), was able to identify anomalies in the spotting/separation process that also would not be apparent when using a conventional scanner and resulted in superior accuracy and precision compared with conventional radio-TLC scanning.

3.2 Methods

3.2.1 Preparation and developing of radio-TLC

Samples of crude radiopharmaceuticals were deposited with a micropipettor 15 mm from the edge of the TLC plate. Deposited volume was 1.0 µL unless otherwise specified. Typically, 4 samples were spotted on each 50 mm x 60 mm TLC plate along the 50 mm edge at 1 cm spacing so that 4 “lanes” would be formed during development. We also performed spotting of 8 samples at 0.5 cm spacing on 50 mm x 35 mm TLC plates. For mock TLC plates, we spotted with [^{18}F]fluoride/[^{18}O]H_2O at multiple points on the TLC plate and then immediately dried the plate (i.e. no developing was performed).

[^{18}F]Fallypride samples (synthesized according to **Figure 3.7**) were deposited onto silica gel 60 F_{254} sheets (aluminum backing) and developed with 60% MeCN in 25 mM NH_4HCO_2 with 1% TEA (v/v). The solvent front took ~8 min to travel 55 mm (i.e. 35 mm separation distance), or ~2.5 min to travel 30 mm (i.e. 15 mm separation distance).

Samples of [^{18}F]FET and the fluorinated intermediate (see **Figure 3.7**) were spotted onto silica gel 60 F_{254} sheets (aluminum backing) and developed with a 80:20 (v/v) mixture of MeCN and DI water. The solvent front took ~9 min to travel 55 mm (i.e. 35 mm separation distance). In some cases, single samples were spotted onto longer TLC plates (Baker-flex silica gel IB-F sheets, 25 mm x 75 mm, plastic backing) to allow increased separation distance. In these cases, the solvent front took ~20 min to travel 70 mm (i.e. 55 mm separation distance).

Samples of [^{177}Lu]Lu-PSMA-617 were spotted onto RP-18 silica gel 60 F_{254} sheets (aluminum backing) and developed with a 75:25 (v:v) mixture of MeOH and DI water with 0.1% TFA. After developing, the plates were dried at room temperature.

To estimate radioactivity of deposited samples, measurements of radioactivity to estimate radioactivity concentration of samples were performed with a calibrated dose calibrator (CRC-25PET, Capintec, Florham Park, NJ, USA).

3.2.2 Analysis of TLC plates by Cerenkov luminescence imaging

After drying, the plates were imaged for 5 min with a previously-described home-built setup(*114*), with minor modifications to support radio-TLC plates instead of microfluidic chips. Briefly, the radio-TLC plate was placed in a light-tight chamber, covered with a transparent substrate, and Cerenkov light was detected by a scientific cooled camera (QSI 540, Quantum Scientific Imaging, Poplarville, MS) equipped with a 50 mm lens (Nikkor, Nikon, Tokyo, Japan). The temperature of the camera was maintained at -10°C for dark current reduction. The field of view was 50 x 50 mm^2.

The raw image comprised an array of values (analog-to-digital units; ADUs) corresponding to detected light at each pixel location. Using custom-written MATLAB software, images were first processed with three corrections as previously described(*77*), including CCD dark current and bias level correction, lens vignetting and CCD pixel nonuniformity correction, and 3 x 3 median filtering. In addition, we performed background subtraction by selecting an area of the image not containing radioactive sample, computing the average pixel value, and subtracting this average from the pixel values across the whole image. Regions of interest (ROIs) were drawn on this final corrected image to enclose the radioactive regions/spots. Each ROI was integrated, and then the fraction of the integrated signal in that ROI (divided by the sum of integrated signal in all ROIs) was computed.

3.2.3 Analysis of TLC plates via radio-TLC scanner

TLC plates were scanned with a miniGITA TLC scanner (Elysia-Raytest; Straubenhardt, Germany) for 3 min, and the resulting chromatograms were analyzed by GINA-STAR software (Elysia-Raytest). Specifically, the software allowed identification of peaks and integrating the area under the curve (AUC) for each peak. The fraction of total AUC contained within each peak was then computed.

Prior to radio-TLC scanner analysis, TLC plates containing multiple samples of radiopharmaceuticals were first cut into individual “lanes”, each lane corresponding to a single separated sample.

3.3 Results and Discussion

3.3.1 High-throughput radio-TLC analysis

Recently we have developed droplet-based platforms to perform multiple radiochemical reactions simultaneously that can be used for exploration of reaction parameters and/or to increase the number of replicates of each reaction. Such studies require a means for high-throughput sample analysis. A previously-described home-built Cerenkov imaging setup(*77*) with minor modifications to support radio-TLC plates instead of microfluidic chips (**Figure 3.1**) was used to image the radio-TLC plates. The field of view was 50 mm x 50 mm. When using 5 min acquisitions, the corresponding limit of detection (LOD) and limit of quantification (LOQ) were determined to be 0.8 kBq/µL and 2.4 kBq/µL, respectively, for 1 µL spots of fluoride-18 (**Figure 3.8, Figure 3.9**), and the linear range extended up to 21.3 MBq (**Figure 3.11**). The LOD could be further reduced by replacing the glass cover with a scintillator (**Figure 3.10**).

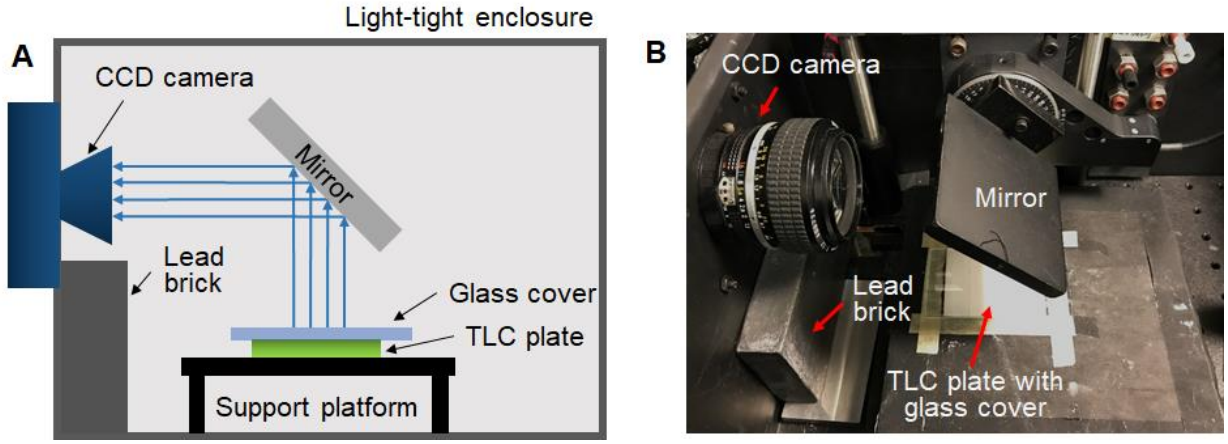

Figure 3. 1 Cerenkov luminescence imaging setup within the light-tight enclosure.

(A) Schematic. (B) Photograph

As an initial demonstration of high-throughput analysis, replicates of both [^{18}F]fallypride (**Appendix**) and [^{18}F]FET samples were studied. Two replicates of a sample of the crude intermediate product (collected after fluorination of the FET precursor) were spotted on the left half of the plate and two replicates of a sample of the crude [^{18}F]FET product (collected after the subsequent hydrolysis step) were spotted on the right side. The CL image of the developed TLC plate (35 mm separation distance; silica gel 60 F_{254}) is shown in **Figure 3.2A**. At the same time, each sample was also spotted on an additional, longer TLC plate (55 mm separation distance; silica gel IB-F), developed, and scanned with the radio-TLC scanner (sample chromatograms in **Figure 3.2B** and **Figure 3.2C**). The greater separation resolution of CLI was readily apparent: a low-abundance side product (6 ± 0% of activity, n=2) was easily visible in the CL images (showing 3 distinct regions for both samples), but was not clearly discernable or quantifiable using the radio-TLC scanner software (showing only 2 peaks for each sample). For the pair of samples of the fluorinated intermediate, percentages of [^{18}F]fluoride, impurity and intermediate determined from the CL image were 27 ± 0 % (n=2), 4 ± 0 % (n=2) and 68 ± 0 % (n=2), respectively. Using the miniGITA scanner after cutting the TLC plate into individual “lanes”, the percentages of [^{18}F]fluoride and intermediate for one “lane” were 32% and 68%, respectively. For the pair of samples of the crude [^{18}F]FET product, percentages of [^{18}F]fluoride, [^{18}F]FET and impurity from

the CL image were 15 ± 0 % (n=2), 79 ± 0 % (n=2) and 6 ± 0 % (n=2), respectively. In the analysis from the miniGITA scanner, the percentages of [^{18}F]fluoride and [^{18}F]FET were 19% and 81%, respectively. Aside from the cleaner separation and better resolution, the CLI-based method also had the benefit of faster analysis. The total imaging time for the whole plate (5 min) is independent of the number of samples, while additional scanning time is needed for each strip cut from the radio-TLC plate (4 x 3 min = 12 min).

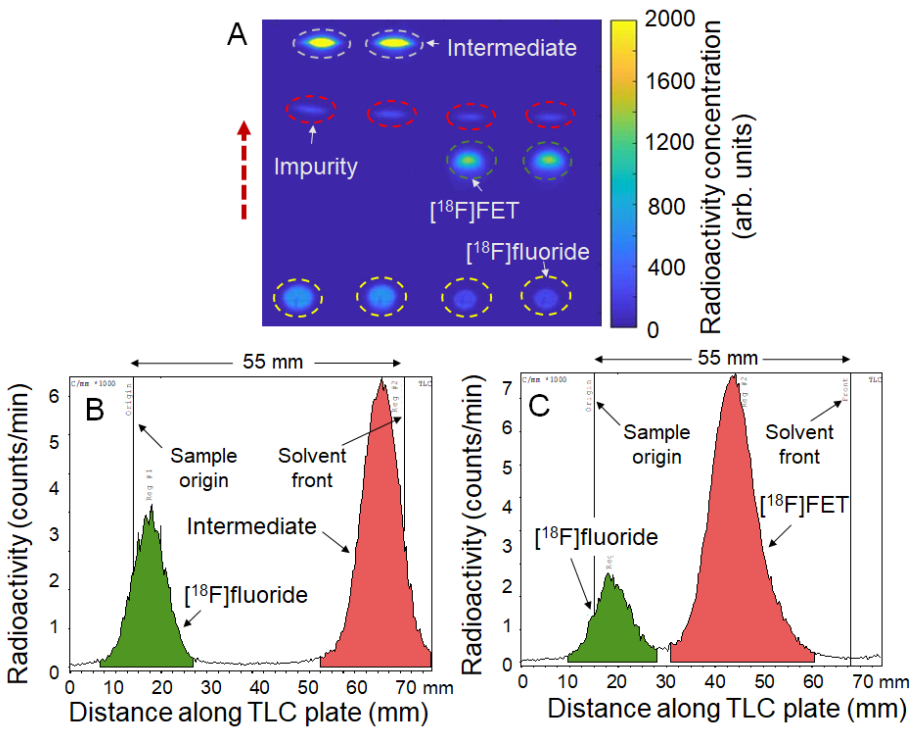

Figure 3. 2 High-throughput analysis of [18F]FET samples

(A) Cerenkov image of developed TLC plate spotted with two replicates of crude fluorination product (1 µL each) and two replicates of crude hydrolysis product (1 µL each). The dashed circles indicate the ROIs used for analysis. The dashed arrow indicates the direction of solvent movement during developing. (B) Example chromatogram obtained with the radio-TLC scanner spotted with crude fluorination product. (C) Example chromatogram from radio-TLC scan of crude hydrolysis product. Note that for B and C, the samples were spotted onto a different TLC plate and separation performed over 55 mm instead of 35 mm (in the Cerenkov image) to try to enhance separation between the species, but the low-abundance impurity could not be discerned.

3.3.2 Increasing sample throughput

To further increase the number of samples that can be analyzed simultaneously, one option would be to redesign the optical system (including lens) to achieve a larger field of view. Then, a

TLC plate (wider than 50 mm) with more spots (“lanes”) could be developed and imaged without increasing the overall analysis time (i.e. without increasing the developing time or readout time). Such an approach would result in a reduction in the number of pixels per imaged spot, however, potentially increasing the noise level slightly and decreasing sensitivity.

Alternatively, the size of the radio-TLC plates could be further reduced to allow multiple plates to fit within the field of view. Due to the excellent separation in the Cerenkov images, we hypothesized that the separation length could be even further reduced. **Figure 3.3A** shows the separation of 4 crude samples of [^{18}F]fallypride, with a separation distance of only 15 mm. The radio-TLC plate (silica gel 60 F_{254}) cut to 50 mm x 35 mm size was spotted with two 1 µL droplets and two 0.5 µL droplets at 1 cm spacing along the long edge of the plate, 15 mm from this edge. After developing, the resulting CLI images showed clear separation of the spots, allowing accurate quantification. The fluorination efficiency obtained with the CLI-based analysis for 1 µL spot size was 76 ± 0 % (n=2), and for 0.5 µL spot size was 74 ± 1 % (n=2). To compare with the radio-TLC scanner, each TLC plate was cut into four lanes. The resulting chromatograms showed 78% conversion for 1 µL spot size and 74% for 0.5 µL spot size, but, notably, the peaks exhibited very significant overlap (**Figure 3.3B**), which we show, below, can introduce significant errors and uncertainties into the analysis. To further increase the throughput, 8 samples from a batch of crude [^{18}F]Fallypride were spotted (0.5 µL droplet size) on the TLC plate at 5 mm spacing and separated for 15 mm as well (**Figure 3.3C**). The fluorination efficiency obtained with the CLI-based analysis appears to be consistent (73 ± 1 %, n=8). In another experiment, 2 different batches (n=4 replicates each batch) of crude [^{18}F]fallypride were analyzed, enabling fluorination efficiency to be easily determined for each (**Figure 3.3D**). In addition to being able to fit a larger number of samples in the CLI system field of view, the plate could be developed more quickly (i.e. 2.5 min for the 15 mm separation distance vs. 8 min for 35 mm separation). Though not demonstrated here, readout throughput could be further increased by placing 2 of these TLC plates within the field of view of the CLI system.

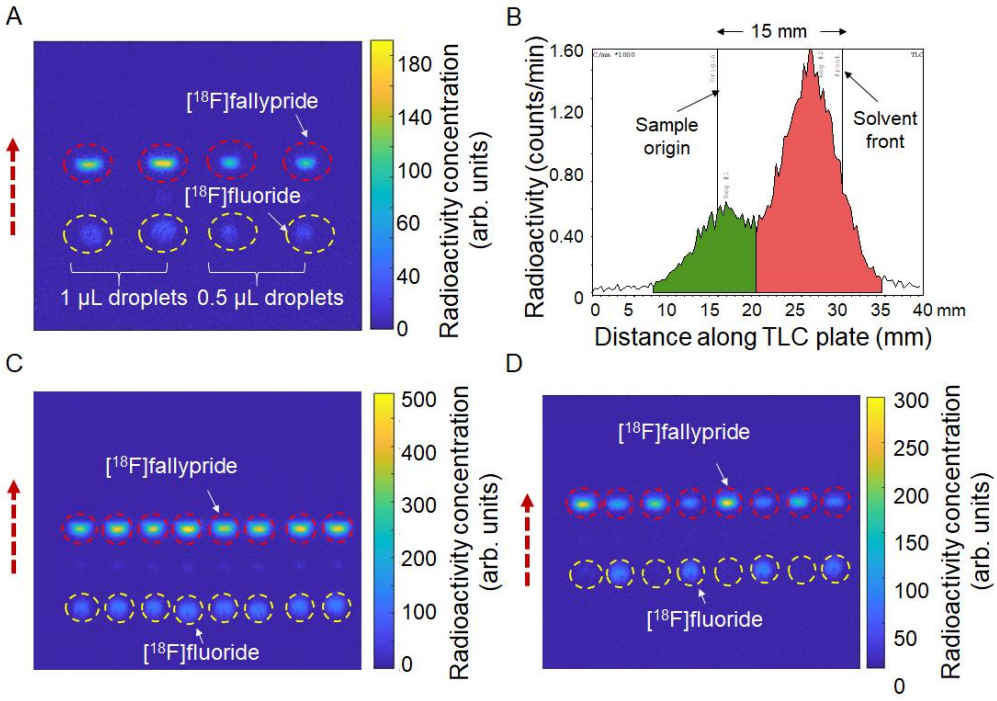

Figure 3. 3 High-throughput analysis of crude [18F]fallypride samples.

(A) Cerenkov image of developed TLC plate spotted with 4 replicates (two 1.0 µL and two 0.5 µL) of the same crude reaction mixture using only 15 mm separation distance. (B) One example chromatogram obtained from the 0.5 µL sample in (A) using the radio-TLC scanner. The TLC plate was first imaged with the CLI based scanner and then was cut into 4 "lanes" each of which was scanned separately with miniGITA scanner. (C) Cerenkov image of developed TLC plate spotted with 8 replicates (0.5 µL) of another batch of crude [^{18}F]fallypride. The dashed circles represent the ROIs for analysis. The dashed arrow represents the direction of solvent flow during developing. (D) Cerenkov image of developed TLC plate spotted with 8 droplets (0.5 µL) sampled from 8 different batches of crude [^{18}F]fallypride reacted under different sets of conditions (n=4 replicates each of two different sets of conditions, spotted in alternating pattern).The dashed circles highlight the ROIs for the 8 samples. The dashed arrow represents the direction of solvent flow during developing.

3.3.3 Comparison of readout via CLI versus a radio-TLC scanner

In a systematic analysis, we found the accuracy and precision of CLI-based analysis to be higher than analysis using commercial radio-TLC scanner software (miniGITA), especially for closely spaced peaks and unequal activity distribution (**Appendix**). The results of gamma counting (taken as ground truth; calibration curve in **Figure 3.13**) and analysis via CLI and radio-TLC scanner are summarized in **Figure 3.14** and **Table 3.1.**

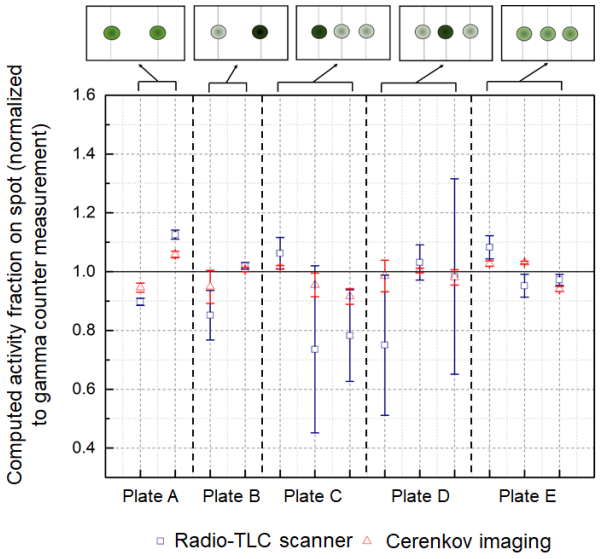

Figure 3. 4 Radio-TLC readout performance comparison of radio-TLC scanner and Cerenkov luminescence of the plates.

The data points show the average activity fraction in each spot (averaged over the analysis performed by n=8 participants) normalized by the activity fraction determined by gamma counting. The error bars show the relative standard deviations. The black dashed vertical lines separate the data from each of the five radio-TLC plates. Cartoons of the activity distribution are shown at the top of the graph (darker green spots represent higher activity level). Raw data was presented in **Table 3.1**.

3.3.4 Assessing quality of the TLC spotting and developments

One notable advantage of the Cerenkov imaging readout technique versus radio-TLC scanner readout is the ability to see a high-resolution 2D image of the final separation. This can be used to monitor the quality of the spotting and developing process. For example, compared to a normal separation (**Figure 3.5A**), we have been able to observe problems such as the splitting of single spots into multiple regions due to incomplete drying of the sample before developing (**Figure 3.5B**), poor separation as a result of large spot size (**Figure 3.5C**), and non-linear separation path due to accidentally introducing an additional source (droplet) of liquid at the side of the radio-TLC plate during developing (**Figure 3.5D**). It should also be possible to detect problems such as double-spotting, or inadvertent contamination of the plate during spotting or subsequent handling. This feedback provides increased information to ensure accurate readout of a given radio-TLC plate or to determine when a TLC (sample spotting and separation) should be re-run.

While not implemented in this study, the CLI readout can be improved by using the same camera to take a bright-field image of the radio-TLC plate (including markings on the TLC plate of sample origin and solvent front) and superimposing the CL image. For example, in the work of Ha *et al.*(*113*), such superposition allowed confirmation of the multiple positions where samples were spotted on each TLC plate. An example using our setup, showing both the sample origin and solvent front from the brightfield image (e.g. to compute R_f values), is shown in the **Appendix**.

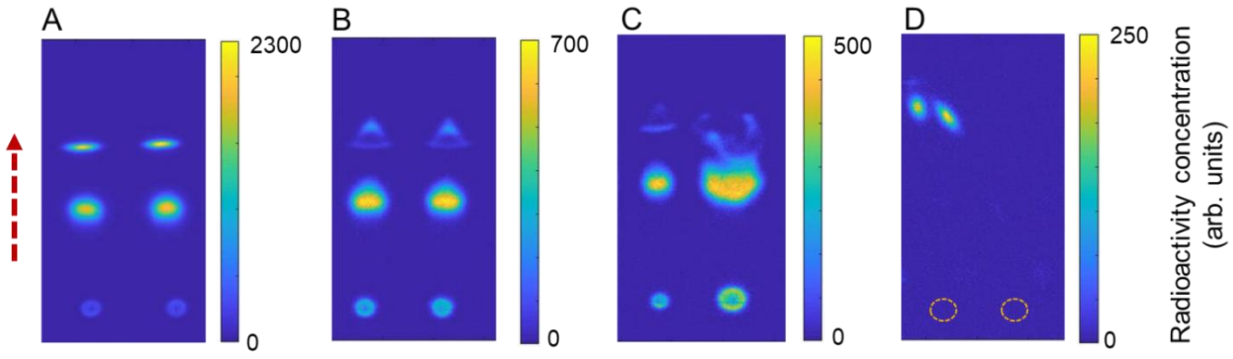

Figure 3. 5 Assessing quality of the TLC spotting and developing process.

(A) Cerenkov image of developed plate after spotting of two replicates (1 µL) each of crude [^{18}F]FET product. This image indicates a normal spotting and developing process. (B) Separation artifacts visible in most distant spots when the plate was not completely dried prior to developing. (C) Separation artifacts due to a combination of incomplete drying as well as abnormally large sample volume (right spot 2.0 µL). (D) Separation artifacts arising from liquid contamination at the right edge of the TLC plate during developing, causing the main solvent flow to be deflected to the left. The TLC plate in this case was spotted, at the positions marked with dash circles, with two replicates (1 µL each) of crude [^{18}F]fallypride product.

3.3.5 Radiochemical purity measurements of [^{177}Lu]-PSMA-617 via CLI

To explore the application of CLI-based radio-TLC analysis to additional isotopes, labeling yield of [^{177}Lu]Lu-PSMA-617 was measured as a function of reaction time by sampling 2 µL crude product (925 kBq/µL) at different time points and spotting on a TLC plate (silica gel 60 RP-18 F_{254}, aluminum backing). The results of CLI analysis in **Figure 3.6** suggest that high labeling efficiency (99%) can be achieved in just 10 min, rather than the typical 30 min timeframe used(*114*).

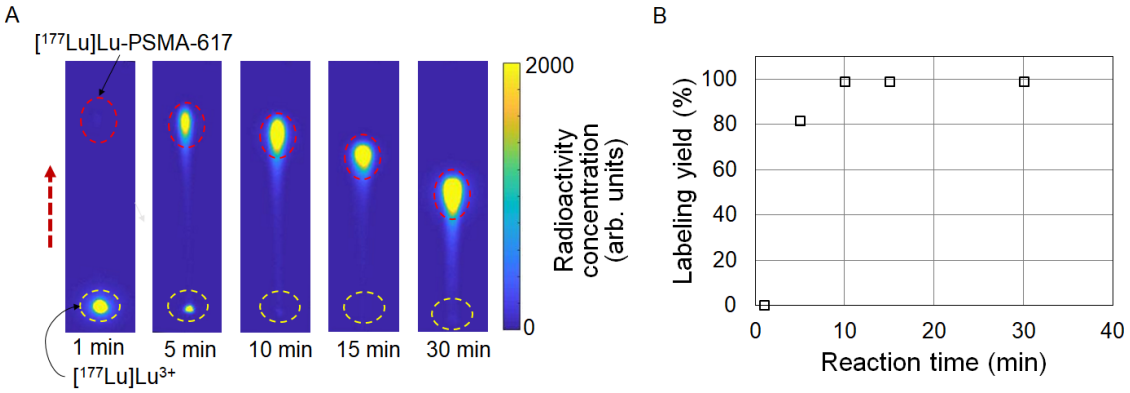

Figure 3. 6 CLI-based analysis of crude [177Lu]Lu-PSMA-617 samples (β--emitter).

(A) Cerenkov image of developed TLC plates spotted with droplets (2 µL) of the crude reaction mixture sampled at different reaction times. In this demonstration, each TLC plate was developed individually, resulting in variable separation distances, but multiple plates were imaged together. The dashed circles represent the ROIs for analysis. The dashed arrow represents the direction of solvent flow during developing. (B) Graph of radiolabeling yields as a function of reaction time.

3.4 Conclusion

Cerenkov imaging in combination with parallel developing of multiple samples on a single TLC plate proved to be a practical method for rapid, high-throughput radio-TLC analysis. Compared with the miniGITA radio-TLC scanner, the CLI-based imaging method provided significantly higher resolution, the ability to image multiple samples in parallel (rather than requiring sequential scanning), and the ability to detect and quantify low-abundance impurities that were not discernable with radio-TLC scanning. The bulk of time and effort savings were realized by spotting multiple samples onto a single TLC plate and developing the multiple samples in parallel prior to imaging, rather than spotting the developing separate TLC plates individually. Furthermore, by leveraging the high resolution of CLI, a much smaller separation distance could be used while still resolving each region of radioactivity, further reducing the time needed for developing the samples. The shorter separation distance in turn can facilitate increased throughput by enabling more TLC plates to be imaged within the field of view; alternatively, the optical system could be redesigned to increase the field of view, thus allowing more spots to be imaged without increasing the system cost or imaging time.

Quantitative accuracy of the CLI-based readout was found to be higher compared to analysis via the radio-TLC scanner software, and relative uncertainty was lower. This was especially true when chromatograms contained overlapping peaks and/or small peaks. Furthermore, CLI-based analysis enabled detection of quality issues in the spotting or development processes.

CLI imaging of TLC plates has broad application for the analysis of radiotracers labeled with radionuclides that are positron emitters (F-18, Cu-64, Zr-89, I-124) used for PET imaging (*31*,*115*) and radiopharmaceuticals labeled with beta emitters (e.g., I-131, Lu-177)(*116–118*). Though we demonstrated the analysis of ^{18}F-labeled compounds and ^{177}Lu-labeled peptide, this approach could also be used for the analysis of radiopharmaceuticals labeled with alpha emitters (e.g. Ac-225, Bi-213), with applications in targeted radiotherapeutics(*119*,*120*). Previous reports have shown detectable Cerenkov emission from such radionuclides(*120*,*121*), likely due to emissions from daughter isotopes (*119*). In addition to high-throughput analysis applications, the rapid separation and readout of radio-TLC plates by the method described here could be especially useful in conjunction with very short-lived isotopes such as C-11 (half-life 20.4 min).

3.5 Appendix

3.5.1Materials

Methanol (MeOH), 2,3-dimethyl-2-butanol (thexyl alcohol; 98%), trifluoroacetic acid (TFA, 99%), ethanol (EtOH, 99.5%), anhydrous acetonitrile (MeCN, 99.8%), and 1 N hydrochloric acid (HCl) were purchased from Sigma-Aldrich. Sodium acetate was purchased from Alfa Aesar. Tetrabutylammounium bicarbonate ($TBAHCO_3$, 75 mM), (S)-2,3-dimethoxy-5-[3-[[(4-methylphenyl)-sulfonyl]oxy]-propyl]-N-[[1-(2-propenyl)-2-pyrrolidinyl]methyl]-benzamide (Fallypride precursor), O-(2-[^{18}F]Fluoroethyl)-L-tyrosine (FET precursor) and PSMA-617 were purchased from ABX Advanced Biochemical Compounds (Radeberg, Germany). Unmodified and RP-18 modified silica gel 60 F_{254} sheets (aluminum backing; 50 mm x 200 mm) were purchased from Merck KGaA (Darmstadt, Germany) and were cut into 50 mm x 60 mm pieces for use. -Baker-flex silica gel IB-F sheets (plastic backing; 25 mm x 75 mm) were obtained from Fisher Scientific

(Hampton, NH, USA). Sheets of organic scintillator BC-400 (1 mm and 3 mm thicknesses) were purchased from Saint-Gobain (Karnataka, India). Glass microscope slides (76.2 mm x 50.8 mm, 1 mm thick) were obtained from C&A Scientific (Manassas, VA, USA). DI water was obtained from a Milli-Q water purification system (EMD Millipore Corporation, Berlin, Germany). No-carrier-added [^{18}F]fluoride in [^{18}O]H_2O was obtained from the UCLA Ahmanson Biomedical Cyclotron. No-carrier-added [^{177}Lu]$LuCl_3$ was obtained from Isotope Technologies Munich and Spectron MRC LLC.

3.5.2 Sample of [^{18}F]Fallypride

Crude [^{18}F]fallypride was obtained from a microdroplet synthesis (**Figure 3.7**) previously reported (*31*). Briefly, from a 50 µL [^{18}F]fluoride stock solution (1 mCi; 3.75 mM $TBAHCO_3$), an 8 µL droplet was deposited on the chip and dried for 1 min at 105 ^{o}C. Next, a 4 µL solution of fallypride precursor (77 mM in 1:1 v/v mixture of thexyl alcohol and MeCN) was added, mixed with the dried residue, and allowed to react for 7 min at 110 ^{o}C. Crude [^{18}F]fallypride product was collected from the chip with 60 µL of 90% MeOH and 10% DI water.

3.5.3 Samples of [^{18}F]FET

The microdroplet synthesis of [^{18}F]FET (**Figure 3.7**) was adapted from the method of Hamacher and Coenen(*122*) and Bourdier *et al.*(*123*). A 1.5 µL droplet of 9.8 mM $TBAHCO_3$ solution and 10 µL of [^{18}F]fluoride/[^{18}O]H_2O (1-7 mCi) were loaded on a chip and dried for 1 min at 105 ^{o}C. Next, 10 µL of FET precursor (5 mM in 1:1 v/v mixture of thexyl alcohol and MeCN) was added and reacted with the dried [^{18}F]TBAF residue for 5 min at 80 ^{o}C. Finally, 10 µL of 1 N HCl was added to hydrolyze the intermediate at 90 °C for 3 min, and the crude product was collected using 40 µL of a 1:1 (v/v) mixture of EtOH and DI water. When needed, samples of the fluorinated intermediated were collected using 90:10 (v/v) mixture of MeOH and DI water.

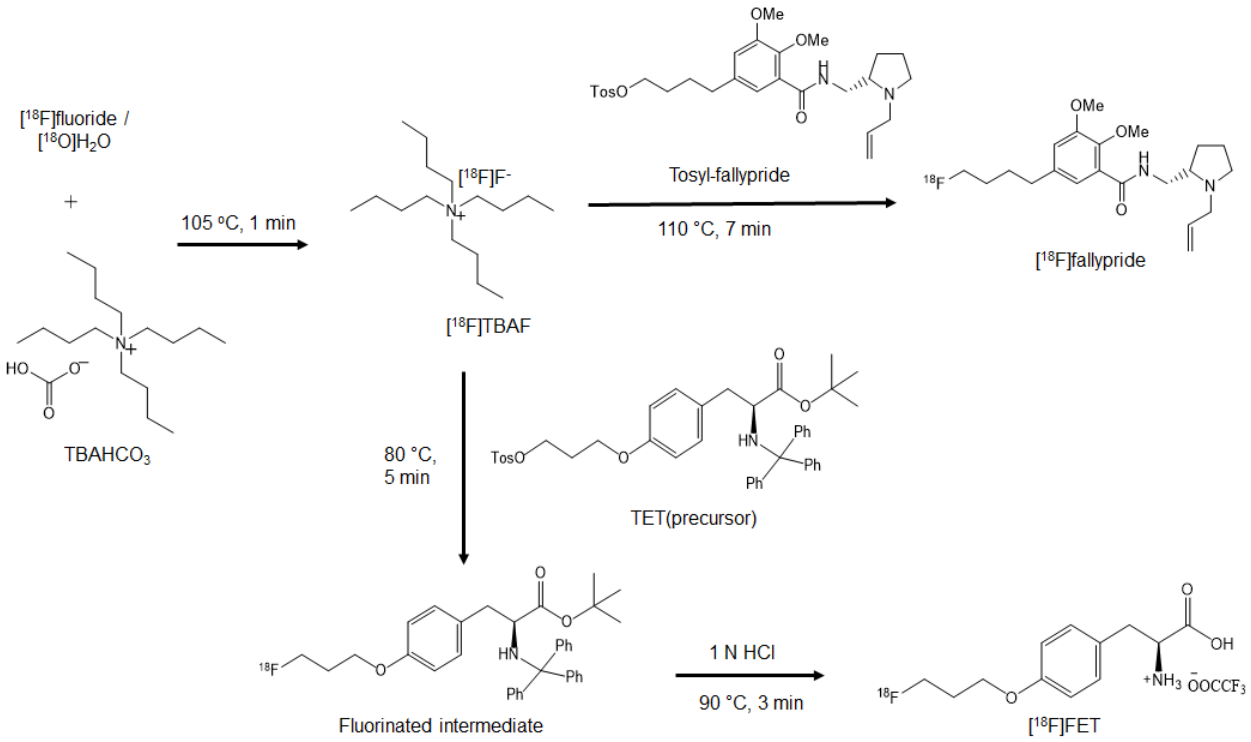

Figure 3. 7 Radiosyntheses of [18F]fallypride and [18F]FET.

For both compounds, [^{18}F]fluoride in [^{18}O]H_2O is first dried and activated. To synthesize [^{18}F]fallypride, the dried residue is reacted with tosyl-fallypride, and to synthesize [^{18}F]FET, the dried residue is first reacted with O-(2-[^{18}F]Fluoroethyl)-L-tyrosine (precursor TET) and then the resulting intermediate undergoes a deprotection reaction.

3.5.4 Samples of [^{177}Lu]Lu-PSMA-617

PSMA-617 was added to a solution of [^{177}Lu]$LuCl_3$ (84 MBq/nmol precursor) in 0.4M sodium acetate buffer, pH 4.8, containing dihydroxybenzoic acid (10 mg/mL). The mixture was heated to 95°C in a dry heating block.

Multiple samples for Cerenkov analysis were obtained by opening the reaction vial and sampling the reaction mixture at different timepoints.

3.5.5 Detection range

3.5.5.1 Methods

To determine the limit of detection (LOD) of the CLI setup for 5 min acquisitions, samples containing different amounts of radioactivity were spotted and analyzed. Based on the recent report by Ha *et al.* (*113*), we used TLC plates containing a fluorescent dopant to maximize the Cerenkov brightness and thus the sensitivity. Radioactivity of the original mixture of

[^{18}F]fluoride/[^{18}O]H_2O and DI water, measured with a dose calibrator, was 88.8 kBq/µL. A series of 1:1 (v/v) dilutions was created and spotted across two TLC plates. Each plate had five of the dilutions, each spotted with n=4 replicates at 1 cm intervals for a total of 20 spots per TLC plate. 1 µL was deposited for each spot. The plates were dried and a glass slide was placed over top during imaging. For each spot on the same TLC plate, the deposited activity was estimated and decay-corrected to the start-time of plate imaging. For each TLC plate, decay-correction was performed to the start-time of imaging of that TLC plate.

A circular ROI (consisting of 4250 pixels) was drawn around each deposited droplet and the total integrated signal calculated for each from the corrected image. To determine the background noise level, 8 ROIs of the same size were drawn in the blank region of the image and the integrated signal (i.e. total ADUs) computed for each. Since background subtraction has been performed, the integrated signal for each ROI was expected to be close to zero. The noise level was determined by calculating the standard deviation of the integrated signal for the 8 ROIs. The LOD was then taken as the point where a plot of the integrated ADU as a function of activity crossed 3x the noise level.

The maximum detectable activity was determined by a similar procedure using a dilution series of higher activity spots (radioactivity of the original mixture was 20.7 MBq/µL). After processing Cerenkov images, the integrated signal versus radioactivity was fit to a straight line and the maximum detectable activity was defined where the data points deviated from the line. We expected this would occur when spots contain a significant number of saturated pixels.

3.5.5.2 Results

Sample images from the dilution series are shown in **Figure 3.8.** (The full set of data is shown in the **Figure 3.9**) From the background ROIs (-1300 ± 1300, n=8), we determined the noise level to be 1300 ADU. After linear fitting of the integrated ADU as a function of activity (**Figure 3.8**), the corresponding LOD was determined to be 0.8 kBq (intersection with 3x noise level).

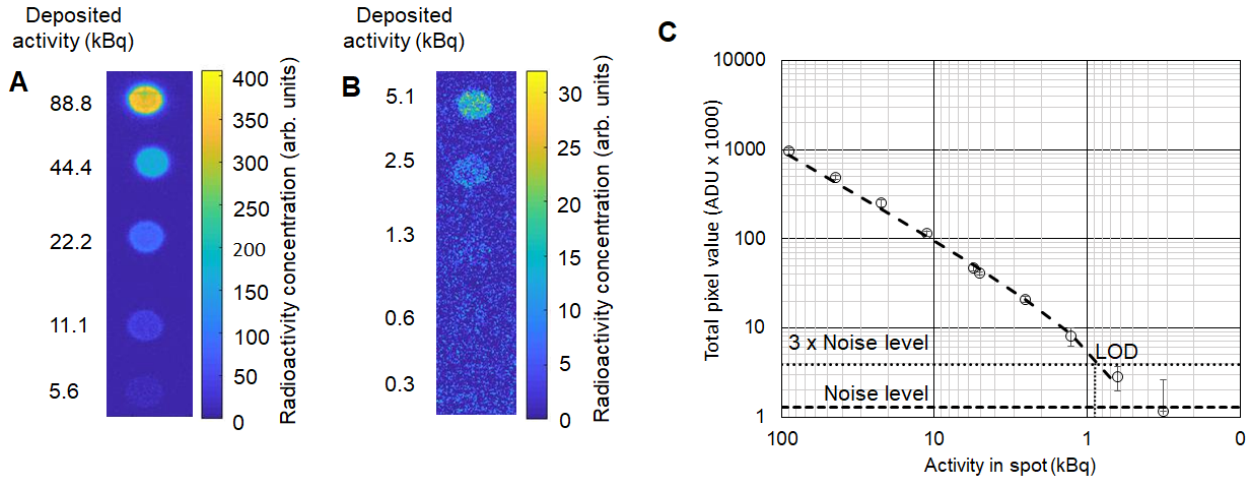

Figure 3. 8 Evaluation of limit of detection (LOD) of the Cerenkov luminescence approach.

(A-B) A dilution series of [^{18}F]fluoride solution was deposited (1 µL each spot) on two TLC plates and imaged. Each spot was replicated n=4 times but only one representative of each dilution is shown. (C) Integrated signal was plotted as a function of deposited activity. A weighted linear least squares fit was performed to determine the minimum detectable activity (R^2=0.99998). Note that the linear fit appears non-linear on the log-log plot due to the non-zero intercept. The non-zero intercept arises as the background subtraction procedure is not perfect. Note that, if needed, the LOD can be easily modified as described in the text.

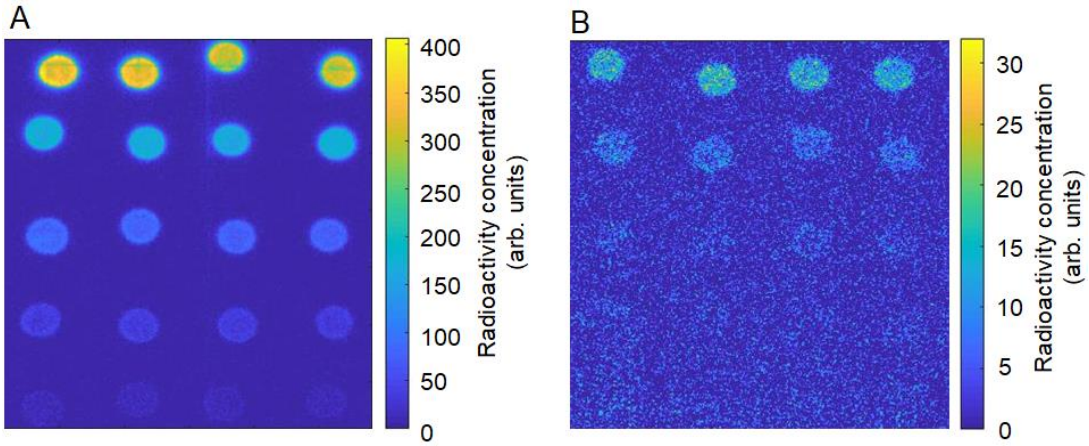

Figure 3. 9 Full set of Cerenkov images used for determination of limit of detection.

The limit of quantification (LOQ) was 2.4 kBq. To reliably quantify the proportion of activity in different spots resulting from a real TLC separation process, the initially deposited sample activity must be sufficient that the amount of activity in each spot after the separation process is above the LOQ. In general, the greater the activity in the initial sample, the more accurate quantification

of low-activity spots (i.e. low-abundance species) after developing. For example, spotting a 37 kBq sample would allow species with abundance as low as ~10% to be quantified. Spotting a 370 or 3700 kBq sample would allow species with abundance as low as ~1% or ~0.1% to be quantified, respectively.

It should be mentioned that increasing the sample volume is typically not a desirable way to increase the activity level. Instead one can use a different cover plate. For example, by replacing the cover glass (1 mm thick) with an organic BC-400 scintillator (1 mm thick), light output was increased significantly, and the LOD could be improved (**Figure 3.10**). Light output of the plate with the 1 mm thick and 3 mm thick scintillators are comparable since the positrons travel less than ~ 1 mm in plastic. Note that the spots on TLC plates covered with the scintillators appear to be blurrier than the glass cover; we believe this is due to a slight shift in focal plane. If needed, the sensitivity could be further boosted by imaging for a longer period of time (detection limit improves as the square root of acquisition time), or potentially by choosing a thicker TLC plate or adding a liquid scintillator spray as demonstrated by Ha *et al.*(*113*).

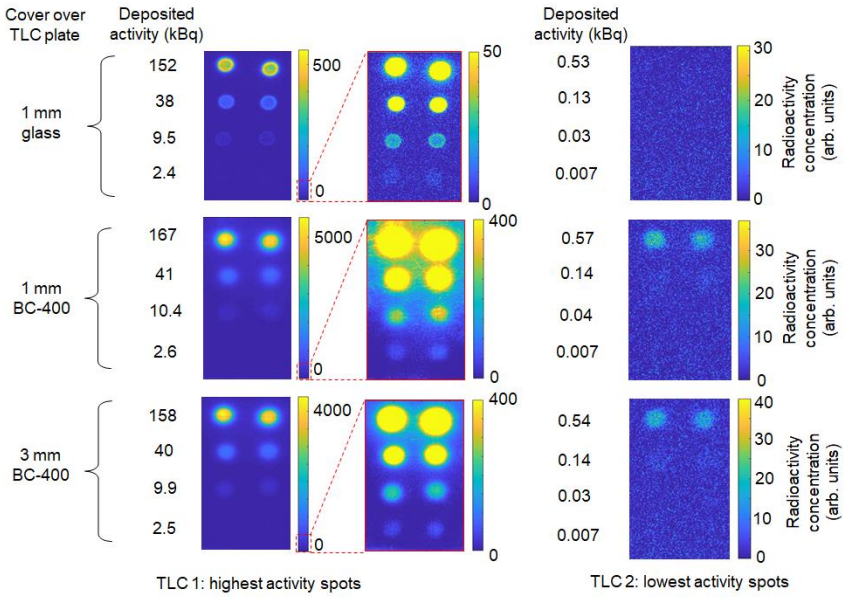

Figure 3. 10 Improvement of detection limit by varying the cover over the TLC plate (glass or BC-400 scintillator).

For each case, two TLC plates were prepared, each spotted with n=2 replicates of 4 different concentrations of [^{18}F]fluoride solution (1 µL each). The left side of the image represents the higher activity samples (shown with two different ranges of the color scale), and the right side of the image represents the lower activity samples.

For higher activity levels, pixels in the image can become saturated and the integrated ROI underestimates the actual activity level. The maximum detectable activity of the CLI setup was determined to be 21300 kBq, the interception of the linear fit and theoretical limit **(Figure 3.11)**. If higher activity samples need to be analyzed, saturation can be avoided by reducing the imaging time (i.e. signal will be reduced in proportion to the reduction in acquisition time), or reducing the lens aperture. Alternatively, the signal can be reduced by using a thinner or lower refractive index material as a cover during imaging.

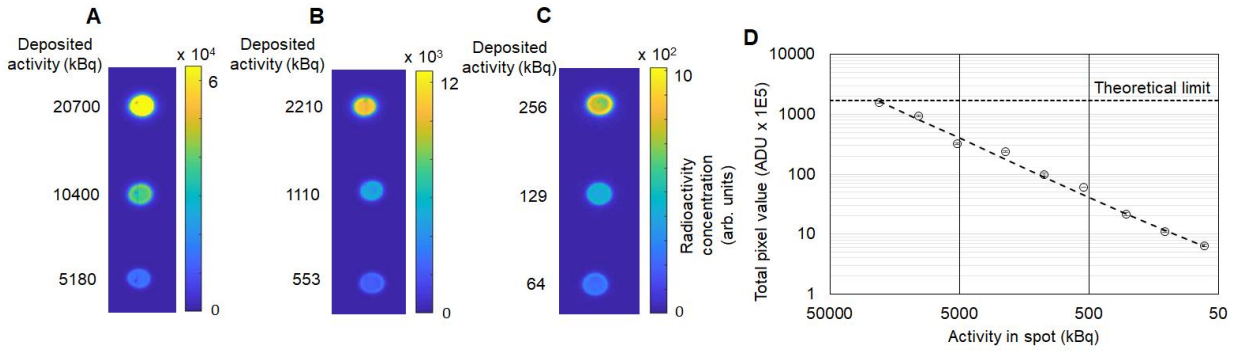

Figure 3. 11 Analysis of maximum detectable activity.

A dilution series of [^{18}F]fluoride solutions was prepared and spotted (1 µL each) onto radio-TLC plates. An initial stock solution with concentration 20700 kBq/µL was prepared. (A) The first plate contained samples of 20700 kBq, 10400 kBq, and 5180 kBq (top to bottom). (B) The second plate contained samples of 2210 kBq, 1110 kBq, and 553 kBq. (C) The third plate contained samples of 256 kBq, 129 kBq, and 64 kBq. All values were decay-corrected to the start time of imaging. (D) The data are plotted (n=2 each point) and weighted linear least squares fit was performed (R^2= 0.99996) to determine the linear range. Theoretical limit is determined by multiplying the number of pixels in the ROI (2604) by the maximum possible pixel value from CCD camera (2^{16} = 65536). Note that the limit, if needed, can be easily modified as described in the text.

3.5.6 Repeatability test

As an initial demonstration of high-throughput analysis to study replicate samples, we deposited four droplets of the same crude [^{18}F]fallypride product on a single TLC plate (silica gel 60 F_{254}), developed the plate to separate all samples simultaneously (separation distance 35 mm), and then performed CLI imaging of the whole plate. **Figure 3.12** shows the resulting CLI image,

as well as a representative chromatogram from a conventional radio-TLC scanner (obtained after cutting the TLC plate into individual lanes, each corresponding to one separated sample). The fluorination efficiency obtained with the CLI-based analysis (88 ± 1 %, n=4) compared favorably with the analysis using the radio-TLC scanner software (90 ± 0 %, n=4).

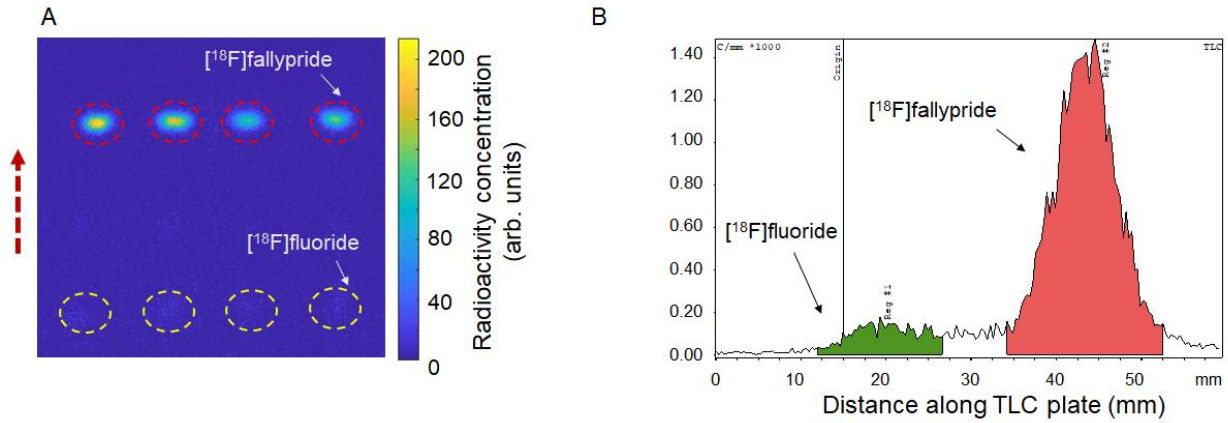

Figure 3. 12 High-throughput analysis of crude [18F]fallypride samples.

(A) Cerenkov image of developed TLC plate spotted with 4 replicates (1 µL each) of the same crude reaction mixture using a separation distance of 35 mm. The dashed circles represent the ROIs for analysis. The dashed arrow represents the direction of solvent flow during developing. (B) One example chromatogram obtained using the radio-TLC scanner. To scan the TLC plate, it was cut into 4 strips after Cerenkov imaging was performed.

3.5.7 Comparison of radio-TLC analysis methods

3.5.7.1 Methods

Three methods of reading and analyzing the TLC plates were compared. Solutions comprising [^{18}F]fluoride/[^{18}O]H_2O and DI water were prepared in different activity concentrations ranging from ~17 kBq/µL to ~148 kBq/µL. Droplets of the same or different concentrations were spotted on the TLC plate to test the detection performance at different peak ratios. Five different TLC plates were prepared by depositing 1 µL droplets with activities in the following ratios: (1) 50:50 (two droplets of 37 kBq/µL each), (2) 10:90 (droplets of ~17 kBq/µL and ~148 kBq/µL, respectively), (3) 80:10:10 (droplets of ~148, ~17, and ~17 kBq/µL, respectively), (4) 10:80:10 (droiplets of ~17, ~148, and ~17 kBq/µL, respectively), and (5) 33:33:33 (three droplets of 37 kBq/µL each). For

cases with two radioactive spots, the distance between spot centers was 35 mm, and for cases with three spots, the distance was 17.5 mm. Plates were dried after spotting but not developed.

Cerenkov images and radio-TLC scans were obtained as described above. As a reference point, and to account for possible errors in preparing stock solutions and pipetting, the activity in the spots was also measured with an automatic well-type gamma counter (WIZARD 3” 1480, Perkin Elmer, Waltham, MA, USA). The TLC plates were cut with scissors at the midpoint between expected spot locations (2 halves for plates with 2 samples and 3 thirds for plates with 3 samples). Individual pieces of TLC plates were placed in 20 mL HDPE scintillation vials from Thermo Fisher Scientific (Pittsburg, Pennsylvania, USA) and the activity was counted for 1 min. For each original TLC plate, the radioactivity distribution of a single spot was expressed as a fraction of the total radioactivity (sum of radioactivity of all spots on the plate).

A calibration curve was separately generated to ensure all measurements were within the linear range of the gamma counter. The calibration curve was generated by preparing a dilution series of [^{18}F]fluoride/[^{18}O]H_2O solution in Eppendorf tubes. A stock solution was prepared with concentration 2590 kBq/mL, and then a 2x dilution series was created by preparing mixtures of 500 µL of DI water with 500 µL of the previous dilution. Samples were measured in a gamma counter for 1 min counting time and decay-corrected to the measurement time of the first sample. The relationship was found to be linear up to ~300 kBq (**Figure 3.13**). For higher activity samples, the counter reached saturation.

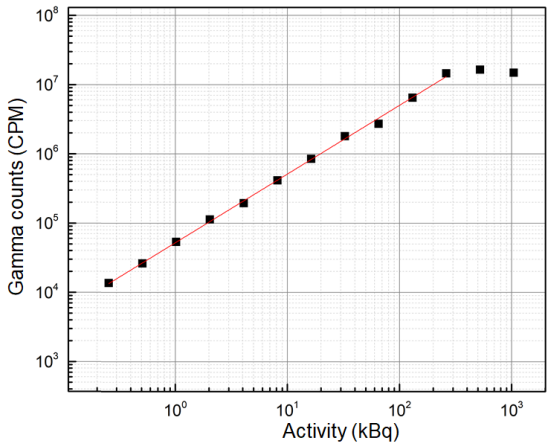

Figure 3. 13 Calibration of gamma counter to determine linear range.

A linear least square fit of the linear part of the curve was performed (R^2=0.9987).

To compare readout methods (CLI and miniGITA scanner), a survey was made that requested participants (experienced operators of radio-TLC scanners; n=8) to analyze the chromatograms obtained with the miniGITA scanner and the CLI images without knowing the deposited percentages on each of the 5 sample plates. The average percentage was computed for each spot/method (across all participants) and the relative error was determined by using the gamma counter as a reference. This was done by subtracting the percentage as measured by the gamma counter and dividing the result by the gamma counter percentage. The relative uncertainty for a particular spot/method was calculated as the standard deviation of percentages (across all participants) divided by the average of percentages computed above.

3.5.7.2 Results

To systematically compare the performance of CLI readout to a conventional radio-TLC scanner and to determine the influence of overlapping peaks, five mock radio-TLC plates were prepared by spotting with different patterns of activity (**Figure 3.14**), and n=8 participants (with experience in radio-TLC scanner operation and analysis of chromatograms) were asked to analyze the resulting data. The results of gamma counting (taken as ground truth; calibration curve is **Figure 3.13**) and analysis via CLI and radio-TLC scanner are summarized in **Table 3.1** and **Figure 3.4** of the chapter**.**

For all plates, the CLI images showed well-separated spots and participants could readily draw ROIs that accurately contained the activity of each spot. In contrast, the radio-TLC scanner, not equipped with a collimator, showed wide peaks that overlapped in many of the plates. In all cases, the CLI-based results were in better agreement with gamma counter values (lower relative error) compared to the radio-TLC scanner-based results.

For analysis of the chromatograms from the radio-TLC scanner, we observed that participants used two different methods for integrating the area under the curve (AUC). In “Method 1”, the area under each peak is integrated down to zero signal level. In “Method 2”, a baseline is first drawn joining the left and right sides of each peak, and the AUC is computed for the area between the curve and the baseline. The varied analysis method introduced variation (higher relative uncertainty) into the radio-TLC scanner results, and the Method 2 analysis led to especially large errors in certain cases (i.e. for small peaks). For samples containing only 2 spots separated by 35 mm (plates A and B), the peaks showed minimal overlap and the AUC could be accurately computed by the radio-TLC scanner software. Results were in reasonable agreement with the gamma counter values, though error and uncertainty were higher than for CLI-based analysis, likely due to variation in where participants defined the edges of each peak and the mixture of integration methods. When the spots had very different activity levels (plate B), the relative uncertainty was significantly higher for the lower activity spot. This trend was observed both for the CLI and radio-TLC scanner methods (6% relative uncertainty in the lower activity spot vs 1% in the higher activity spot for CLI; 10% vs 1% for radio-TLC scanner). In addition, the activity in the smaller peak tended to be underestimated (-5% relative error for CLI; -15% for radio-TLC scanner) while the large peak tended to be slightly overestimated.

These phenomena were exaggerated for the TLC plates with three radioactive spots, where the corresponding peaks in the chromatogram were overlapping (plates C and D). Using CLI, the smallest spots were underestimated up to -8%, while using the radio-TLC scanner, the smallest peaks were underestimated up to -26%. In these cases, relative uncertainties were lower for CLI

(<5%) but were quite high (20-39%) for radio-TLC-based analysis. The higher activity spots in samples C and D were quantified more accurately and precisely by both methods, though the relative accuracy and precision were significantly higher for the CLI-based method. For plate E, with more equal activity distribution among spots, the results were similar to plate A, despite the overlap observed in the radio-TLC chromatograms.

Overall, the relative uncertainty was much lower for CLI-based analysis compared to radio-TLC scanner software analysis. When analyzing radio-TLC plates containing regions of unequal radioactivity, CLI-based analysis showed improved quantitative accuracy. Because overlapping peaks are often observed in radio-TLC samples in our laboratory and in the literature, it is likely that many studies contain non-trivial quantitation errors. Such errors could be minimized by switching to a CLI-based readout method, or alternatively by modifying the radio-TLC scanner to reduce the overlap (e.g. using a collimator on the detector head to decrease peak widths at the expense of reduced sensitivity, or increasing the length of the radio-TLC plates to increase separation between peaks at the expense of longer development times).

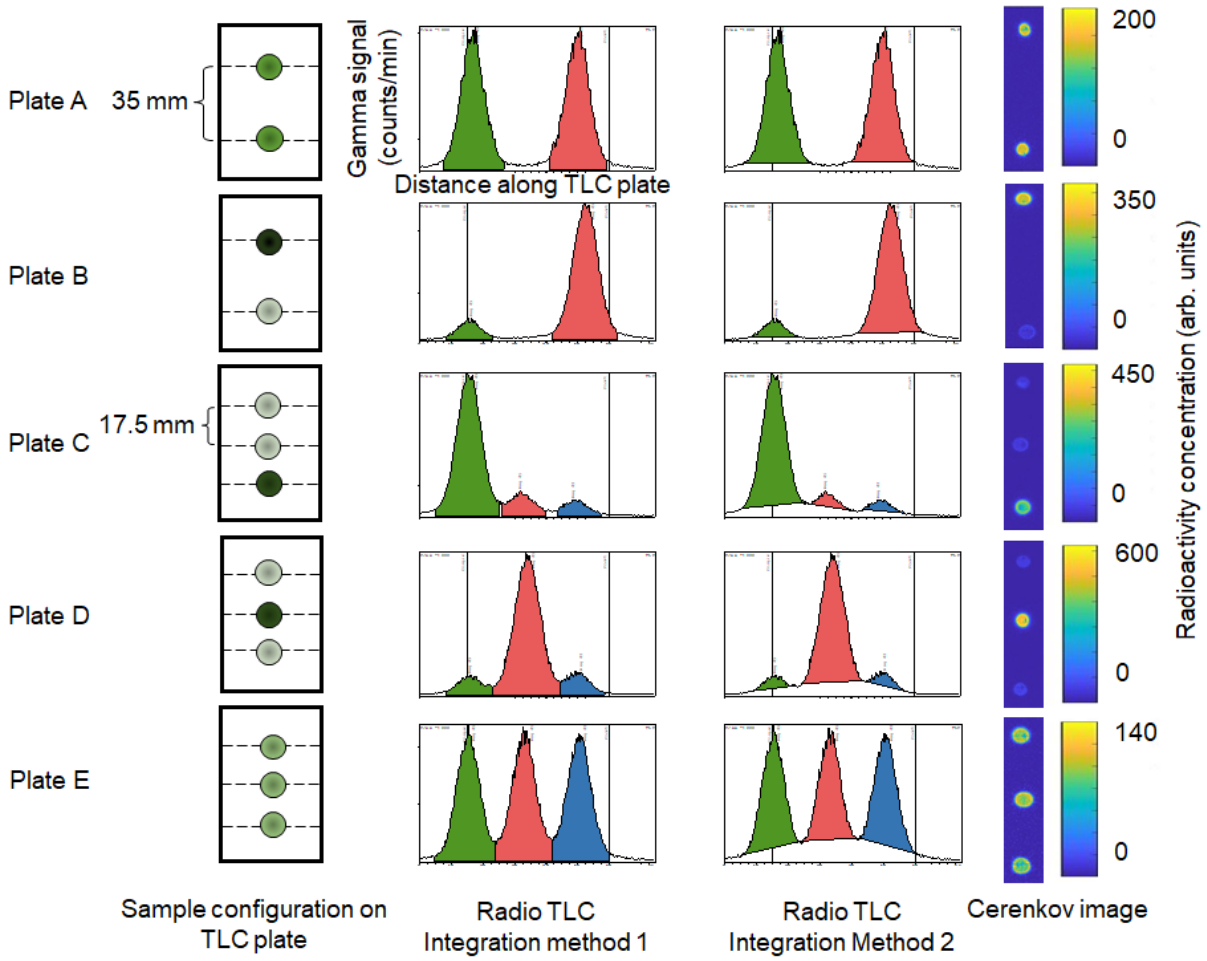

Figure 3. 14 Comparison of analysis via radio-TLC scanner software and Cerenkov luminescence imaging approach for five specially prepared radio-TLC plates.

The first column depicts a cartoon of the arrangement of [^{18}F]fluoride solution samples (1 µL each but different concentrations) on the radio-TLC plate. The darkness of each spot represents the amount of radioactivity. Note that the radio-TLC scanning direction is from bottom to top. The intended radioactivity distributions (bottom to top) were: 50:50 (Plate A), 10:90 (Plate B), 80:10:10 (Plate C), 10:80:10 (Plate D), and 33:33:33 (Plate E). The second and third columns show radio-chromatograms obtained from a radio-TLC scanner. The columns depict the same radio-chromatograms, but use two different methods of integrating the peaks. Finally, the fourth column shows a Cerenkov luminescence image of the same plate.

Table 3. 1 Comparison of analyses using radio-TLC scanner software and CLI-based approach for the five TLC plates of Figure 3.14.

For each plate, the spots are listed in the order they would be encountered by the scanner (i.e. bottom to top in Figure 3.14). Values for radio-TLC scanner and CLI-based analysis are derived from n=8 analyses of the same plate and are normalized to the measurements from the gamma counter. n=1 for the gamma counter measurements.

	Gamma counter	Conventional radio-TLC scanner			Cerenkov luminescence imaging (CLI)		
Plate	**Fraction of activity in each spot (%)**	**Fraction of activity in each spot (average ± std. dev. %)**	**Relative error (%)**	**Relative uncertainty (%)**	**Fraction of activity in each spot (average ± std. dev. %)**	**Relative error (%)**	**Relative uncertainty (%)**
A	55.1	49.4 ± 0.7	-10	1	52.1 ± 0.9	-5	2
	44.9	50.6 ± 0.7	13	1	47.5 ± 0.5	6	1
B	11.7	9.9 ± 1.0	-15	10	11.1 ± 0.7	-5	6
	88.3	90.1 ± 1.0	2	1	88.9 ± 0.7	1	1
C	80.0	85.0 ± 4.3	6	5	81.2 ± 0.5	2	1
	11.1	8.2 ± 3.2	-26	39	10.6 ± 0.4	-4	4
	8.8	6.9 ± 1.4	-22	20	8.1 ± 0.2	-8	3
D	9.8	7.4 ± 2.3	-25	32	9.7 ± 0.5	-1	5
	82.2	84.8 ± 4.9	3	6	82.5 ± 0.7	0	1
	7.9	7.8 ± 2.6	-1	34	7.8 ± 0.2	-2	3
E	31.4	34.0 ± 1.3	8	4	32.3 ± 0.3	3	1
	34.1	32.5 ± 1.3	-5	4	35.2 ± 0.2	3	0
	34.5	33.5 ± 0.6	-3	2	32.4 ± 0.3	-6	1

3.5.8 Superposition of bright-field and CLI images

In some cases, it may be useful to superimpose the CLI image onto a brightfield image of the radio-TLC plate. For example, the brightfield image could shows markings on the TLC plate of spotting locations and solvent front to help quantify R_f values and identify radioactive species. An example of a superimposed image of a developed TLC plate is shown in **Figure 3.15**.

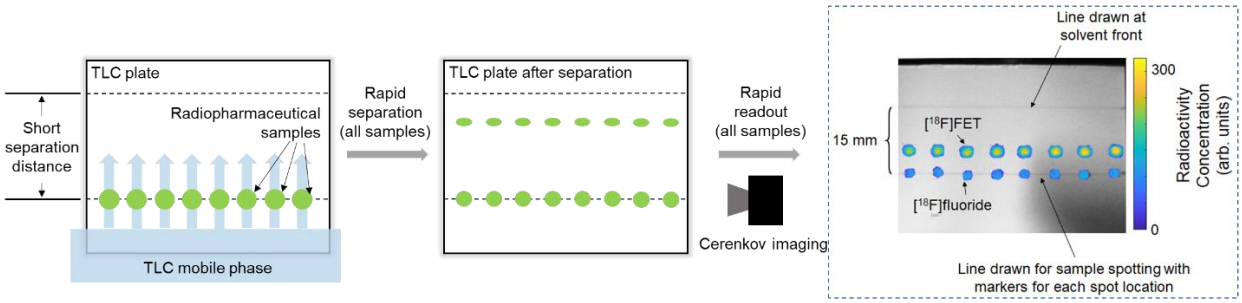

Figure 3. 15 An example image obtained by superimposing the Cerenkov luminescence signal (false color) over a brightfield image (greyscale).

Eight replicate samples (0.5 μL each) of crude [^{18}F]FET were spotted on a single TLC plate with 5 mm pitch and then separated in parallel. The separation distance was 15 mm.

Chapter 4: Impact of aqueous phases in the analysis of radiopharmaceuticals via radio-TLC

4.1 Introduction

Positron-emission tomography (PET) is a non-invasive molecular imaging technique that harnesses radiopharmaceuticals to quantify biochemical processes *in vivo*. The radiopharmaceutical (or tracer) is a bioactive molecule labelled with a short-lived positron-emitting radionuclide. The most commonly used radionuclide is fluorine-18 due to its favorable physical and chemical properties(*10*,*124*). Currently, most PET scans measure glucose metabolism with the radiopharmaceutical 2-[^{18}F]fluoro-2-deoxy-D-glucose ([^{18}F]FDG) to diagnose a myriad of diseases. However, additional types of scans may become more prevalent as several new PET tracers that are more specifically targeted to disease phenotypes have recently garnered clinical approval, including those targeting amyloid plaques (Neuraceq, Amyvid, Vizamyl), dysfunctional tau protein (Tauvid), prostate cancer (Axumin, Pylarify), and Parkinson's disease ([^{18}F]FDOPA)(*125*). The list of new ^{18}F-labeled tracers under development also grows with the discovery of new biological targets and therapeutic strategies(*126*).

The successful development and production of PET tracers rely on analytical techniques such as radio-high performance liquid chromatography (radio-HPLC) and radio-thin layer chromatography (radio-TLC) to assess radiochemical conversion (during radiosynthesis development) or radiochemical purity (during quality control testing of tracers produced for clinical use). A shortcoming of radio-HPLC, however, is the propensity for retention of free [^{18}F]fluoride in the column (i.e., not reaching the detectors), which can lead to the underestimation of this species in the output chromatogram(*95*). In contrast, radio-TLC does not suffer from this issue as the entirety of the TLC plate is scanned.

When using typical silica TLC plates to separate ^{18}F-labelled mixtures, [^{18}F]fluoride is usually sequestered near the origin through strong interaction with surface silanol groups, and the mobile

phase moves the radiopharmaceutical away from the origin. The stationary phase, silica gel (polysilicic acid), is well known in the literature to possess the ability for acidic hydrogen bonding, basic hydrogen bonding, and dipolar interactions with analytes(*127*), and the mobile phase plays an important role in modulating these interactions. The reported mobile phases vary widely in literature, even for analysis of the same compound (**Table 4.1**), and we noted with interest that many studies use water as a polar mobile phase additive to enhance the migration of polar radiopharmaceutical compounds.

Table 4. 1 Mobile phases reported in the literature for silica-based TLC separation of various radiopharmaceuticals.

Radiopharmaceutical	Aqueous Mobile Phase	Non-Aqueous Mobile Phase
[^{18}F]Fallypride	(60:40 MeCN: 25 mM NH_4HCO_2, 1% TEA)(*33*,*128*), (95:5 MeCN:H_2O)(*129*), (90:10 MeCN:H_2O)(*81*)	(10:90 MeOH:DCM)(*130*), (50:50 MeOH:EtOAc, 1% TEA)(*131*)
[^{18}F]FET	(80:20 MeCN:H_2O)(*63*,*128*), (67:16.5:16.5 MeCN:MeOH:H_2O)(*132*)	(90:10 MeOH:AcOH)(*133*), (67:33 Hexanes:EtOAc)(*134*)
[^{18}F]FBB	(90:10 MeCN:H_2O)(*135*)	NR
[^{18}F]FDOPA	(95:5 MeCN:H_2O)(*136*), (67:16.5:16.5 MeCN:MeOH:H_2O)(*137*)	(90:10 DCM:EtOAc)(*138*), (40:60 EtOAc:Et_2O)(*139*)
[^{18}F]FEPPA	NR	(8:10:92 MeOH:Hexanes:EtOAc)(*140*)
[^{18}F]FPEB	NR	(95:5 EtOAc:EtOH)(*141*)
[^{18}F]FLT	(95:5 MeCN:H_2O)(*142*,*143*)	(90:10 DCM:MeOH)(*144*)
[^{18}F]FMZ	(80:15:5 EtOAc:EtOH:H_2O)(*145*,*146*)	(80:20 EtOAc:EtOH)(*147*)
[^{18}F]FMISO	NR	(95:5 MeOH:NH_4)(*143*), (MeOH)(*148*)
[^{18}F]FNB	(60:40 MeCN:H_2O)(*14*)	NR
[^{18}F]FBA	(95:5 MeCN:H_2O)(*14*)	(67:33 Hexanes:EtOAc)(*149*)
[^{18}F]DFA	(95:5 MeCN:H_2O)(*14*)	NR
[^{18}F]AlF-2-AMPDA-HB	(75:25 MeCN:H_2O)(*150*)	NR
[^{18}F]AlF-NOTA-HL	(50:50 MeCN:H_2O)(*151*)	NR
[^{18}F]FTP	(20:80 MeOH: 1M NH_4OAc)(*152*)	NR
[^{18}F]Altanserin	(80:20 MeCN:H_2O)(*153*)	NR
[^{18}F]MPPF	(90:10 MeCN:H_2O)(*154*)	NR

NR = Not Reported

However, a drawback of using water is that it can alter the stationary phase itself through direct interactions of the water with surface silanol groups of the TLC plate. These modifications can disrupt the possible intermolecular interactions of the surface silanol groups, impeding plate-

analyte interactions and adversely affecting chromatographic behavior(*155*). In fact, under some conditions, the [^{18}F]fluoride-silica interaction can be disrupted, leading to the movement of free radionuclide away from the origin, which could lead to confusion and ambiguities in the analysis of ^{18}F-radiopharmaceuticals if the TLC method is not carefully validated. We use systematic studies with different aqueous compositions to illustrate the potential detrimental impacts of using mobile phases with significant aqueous component on the radio-TLC analysis of tracers labeled with [^{18}F]fluoride and argue that the effects could also apply to tracers labelled with other radionuclides.

4.2 Materials and Methods

4.2.1Materials

All reagents and solvents were obtained from commercial suppliers. Acetonitrile (MeCN; anhydrous, 99.8%), methanol (MeOH; anhydrous, 99.8%), water (H_2O; suitable for ion chromatography), 2,3-dimethyl-2-butanol (thexyl alcohol; anhydrous, 98%), N-methyl-2-pyrrolidone (NMP; anhydrous, 99.5%), 4,7,13,16,21,24-hexaoxa-1,10-diazabicyclo[8.8.8]hexacosane (K_{222}; 98%), and potassium carbonate (K_2CO_3; 99.995%), were purchased from Sigma-Aldrich (St. Louis, MO, USA). Tetrabutylammonium bicarbonate ($TBAHCO_3$; 75mM in ethanol), (2*S*)-*O*-(2′-tosyloxyethyl)-*N*-trityl-tyrosine-tert-butyl ester (TET ; precursor for [^{18}F]FET, >95%), *O*-2-fluoroethyl-L-tyrosine (FET-HCl; reference standard, >95%), ethyl-5-methyl-8-nitro-6-oxo-5,6-dihydro-4H-benzo[f]imidazo[1,5-a][1,4]diazepine-3-carboxylate (nitromazenil; precursor for [^{18}F]Flumazenil, >97%), Flumazenil (FMZ; reference standard, >99%), (S)-2,3-dimethoxy-5-[3-[[(4-methylphenyl)-sulfonyl]oxy]-propyl]-N-[[1-(2-propenyl)-2-pyrrolidinyl]methyl]-benzamide ([^{18}F]Fallypride precursor, >90%), Fallypride (reference standard, >95%), were purchased from ABX Advanced Biochemical Compounds (Radeberg, Germany). Silica gel 60 F_{254} sheets (aluminum backing, 5 cm x 20 cm) were purchased from Merck KGaA

(Darmstadt, Germany). Glass microscope slides (76.2 mm x 50.8 mm, 1 mm thick) were obtained from C&A Scientific (Manassas, VA, USA).

4.2.2 Preparation of samples of [^{18}F]fluoride and complexes

To illustrate the impact of aqueous mobile phases on the migration of [^{18}F]fluoride, several samples were prepared. [^{18}F]fluoride samples were prepared by diluting [^{18}F]fluoride/[^{18}O]H_2O with ion chromatography-grade water to a concentration of 0.75-1.1 MBq/µL. [^{18}F]KF/K_{222} samples were prepared by adding K_2CO_3 (0.5 mg, 3.6 µmol) and K_{222} (5 mg, 13.3 µmol) to a volume of 0.5 mL of ion chromatography grade water spiked with [^{18}F]fluoride, yielding a 0.75-1.1 MBq/µL solution with 7.2 mM K_2CO_3 and 26.2 mM K_{222}. [^{18}F]TBAF samples were prepared by adding $TBAHCO_3$ (75 mM; 1.2 µL, 0.7 µmol) to 99 µL of ion chromatography grade water spiked with [^{18}F]fluoride to yield a 0.75-1.1 MBq/µL solution with 7.2 mM $TBAHCO_3$.

4.2.3 Preparation of samples of [^{18}F]fluoride labeled radiopharmaceuticals

To prepare mixed samples of radiotracers and [^{18}F]fluoride, several radiopharmaceuticals were prepared using droplet radiochemistry methods on Teflon-coated silicon surface-tension trap chips as previously described[8]; except that optimal reaction conditions were altered to increase the amount of [^{18}F]fluoride in the crude reaction mixture.

Mixtures of [^{18}F]FET-intermediate/[^{18}F]TBAF were prepared by depositing an 8 µL droplet of [^{18}F]fluoride/[^{18}O]H_2O (70-90 MBq [1.9-2.5 mCi]; mixed with 240 nmol of $TBAHCO_3$) and drying at 105 °C for 1 min. Then, the fluorination step was performed by adding a 10 µL droplet containing 80 nmol of FET precursor dissolved in thexyl alcohol:MeCN (1:1; v/v) to the dried [^{18}F]fluoride residue and reacting at 90 °C for 5 min. The crude product was collected by dispensing 10 µL of MeCN to the reaction site and aspirating the volume. This process was repeated 6x for 60 µL of collected crude product.

Mixtures of [^{18}F]FMZ/[^{18}F]TBAF were prepared similarly, except that the fluorination step was performed by adding an 8 µL droplet containing 280 nmol of FMZ precursor dissolved in NMP to the dried [^{18}F]fluoride residue and reacting at 200 °C for 0.5 min.

Mixtures of [^{18}F]Fallypride/[^{18}F]TBAF were prepared similarly, except that (i) the initial [^{18}F]fluoride droplet contained 480 nmol of $TBAHCO_3$, and the fluorination step was performed by adding a 6 µL droplet containing 234 nmol of Fallypride precursor dissolved in thexyl alcohol:MeCN (1:1; v/v) to the dried [^{18}F]fluoride residue and reacting at 110 °C for 1 min.

Stock solutions of non-radioactive reference standards were prepared at 20 mM concentration. 5 mg of Fallypride standard was added to 685 µL of MeOH. 5 mg of FMZ standard was added to 825 µL of MeOH. 5 mg of FET standard was added to 1100 µL of MeOH.

4.2.4 TLC spotting, developing, and readout

TLC plates were cut (6 cm long x 3 cm wide), then marked with a pencil at 1 cm (origin line) and 5 cm (development line) from the bottom edge. 1 µL of the relevant sample was applied to the plate via a micro-pipette. In cases where radiopharmaceutical solutions were separated, an adjacent lane on the plate was spotted with the corresponding reference standard. The sample spots were then dried under a gentle stream of nitrogen for 1 min. Spotting was repeated on multiple plates to compare the effect of different mobile phases containing MeCN with different amounts of H_2O (all compositions expressed as v/v). After developing, plates were dried under a gentle stream of nitrogen for 3 min.

To better visualize the location of phase transfer catalysts ($TBAHCO_3$ and K_2CO_3/K_{222}), some plates were stained after developing by exposure for 1 min to a mixture of iodine crystals and silica gel in a sealable container(*156*).

Plates were visualized via Cerenkov luminescence imaging (CLI) as previously described(*33*,*128*). Briefly, the radio-TLC plate was positioned inside a light-tight chamber, then the plate was covered with a glass microscope slide. The Cerenkov light emission was detected by a cooled (-10 °C) scientific camera (QSI 540, Quantum Scientific Imaging, Poplarville, MS,

USA) equipped with a 50 mm F/1.2 lens (Nikkor, Nikon, Tokyo, Japan) for a 60 s exposure. In addition to previously described corrections, background subtraction was further performed by selecting a small region of the image (approximate size 20 pixels) not containing any radioactive species, computing the average pixel intensity, and subtracting this average from the entire image.

After CLI imaging, the glass microscope slide was removed, and a UV lamp installed inside the light-tight chamber was illuminated while acquiring another image of the plate (7 ms exposure time). This enabled visualization of chemical species on the plate (which appear as darker bands due to indicator present on the TLC plate), as well as capturing an image of pencil markings and iodine-stained bands on the plate.

4.2.5 Analysis of TLC plates

A MATLAB program (MathWorks, Natick, MA, USA) was written to generate TLC chromatograms and display TLC plate images. The user is first prompted to select the CLI image to be analyzed, followed by a corresponding darkfield image, and corrections are applied as previously described(*77*). The program then asks the user to select a corresponding UV image, followed by selecting a flat field correction UV image (taken in advance with a blank TLC plate installed). The UV image is corrected in a similar fashion (i.e., dividing by the flat field correction image and applying 3x3 median filtering), and the user can further adjust brightness and contrast for viewing. The CLI image is then redisplayed, and the user is asked to draw a line to define the width of the widest radioactivity band, which is used as the lane width. The UV image is then redisplayed, and the user is asked to draw a line from the bottom of the TLC plate to the solvent front. The program then generates an average line profile along the lane, taking the pixel intensities versus distance from the CLI image along the user-defined centerline and averaging with adjacent lines automatically generated at 1-pixel intervals along the entirety of the selected lane width. The program displays the final averaged line profile (chromatogram), the corrected CLI image, and the UV image.

The chromatogram was then exported and loaded in OriginPro (OrignLab, Northampton, MA, USA) to normalize the chromatograms to the highest intensity and plot groups of chromatograms. To compute the percentage of each species in a chromatogram, OriginPro was used to find the area under each band (peak) after fitting to a sum of Gaussian curves and then dividing the area corresponding to a particular band by the sum of areas for all bands.

4.3 Results

Samples of [^{18}F]fluoride (with and without phase transfer catalysts) and various crude radiopharmaceuticals with different polarities were prepared and separated on silica TLC plates with different aqueous mobile phase compositions to illustrate the effect of water on the mobilization of different species and the potential pitfalls in analysis.

4.3.1 Effect of aqueous mobile phases on migration of [^{18}F]fluoride

Samples of [^{18}F]fluoride/[^{18}O]H_2O were initially spotted on TLC plates and developed under mobile phases of increasing aqueous composition (**Figure 4.1**). When the water content is low, [^{18}F]fluoride remains at the origin as expected. For ≥40% water, free [^{18}F]fluoride begins migrating away from the origin. Notably, and with great potential for ambiguity in the radio-TLC analysis of radiopharmaceuticals, two distinct bands of radioactivity are observed when using a mobile phase with ≥50% water. For ≥80% water composition, there is again only a single band observed, but it is located at the solvent front, near where the radiopharmaceutical species would be expected.

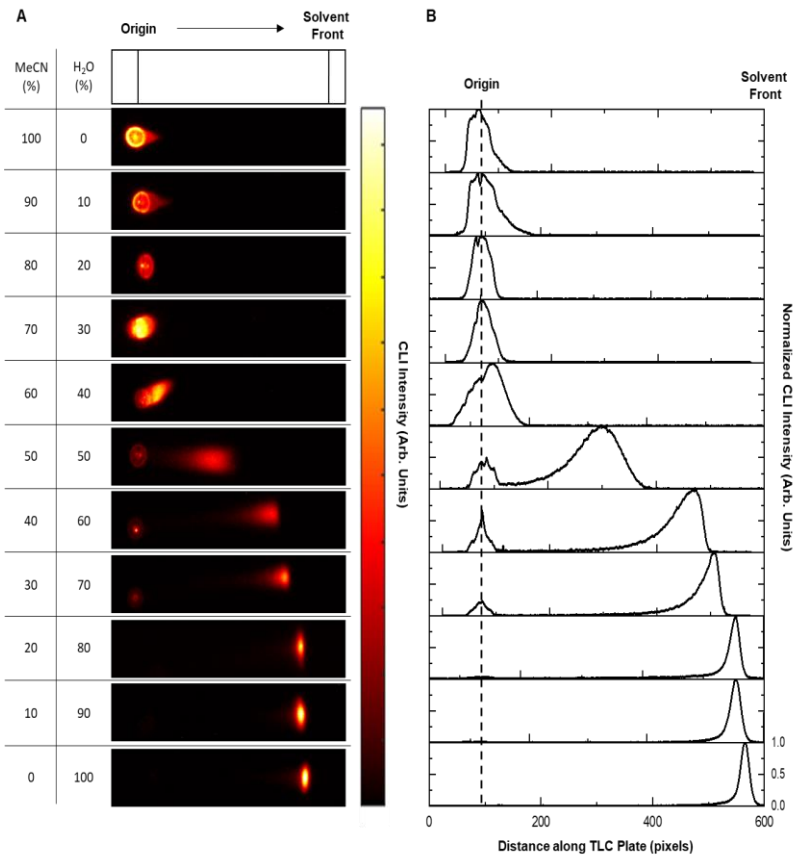

Figure 4. 1 Impact of water composition in aqueous mobile phases (MeCN:H2O) on the migration of [18F]fluoride.

(A) CLI images of TLC plates. (B) TLC chromatograms generated from the CLI images.

Recognizing that phase transfer catalysts are typically used in ^{18}F-radiosyntheses, the behavior of complexed [^{18}F]fluoride was also investigated. **Figure 4.2** shows the effects of water on the movement of [^{18}F]TBAF (i.e., [^{18}F]fluoride in the presence of $TBHACO_3$). The overall trend is similar to free [^{18}F]fluoride, though there are increased signs of chromatographic fronting and band widening for some mobile phase compositions. This fronting may be explained because [^{18}F]fluoride and the phase transfer catalyst interact with one another yet have different migration behavior (**Figure 4.2A**). The migration of [^{18}F]KF/K_{222} (i.e., [^{18}F]fluoride in the presence of K_2CO_3 and K_{222}) was also explored (**Figure 4.6**) and shown to behave similarly to [^{18}F]TBAF.

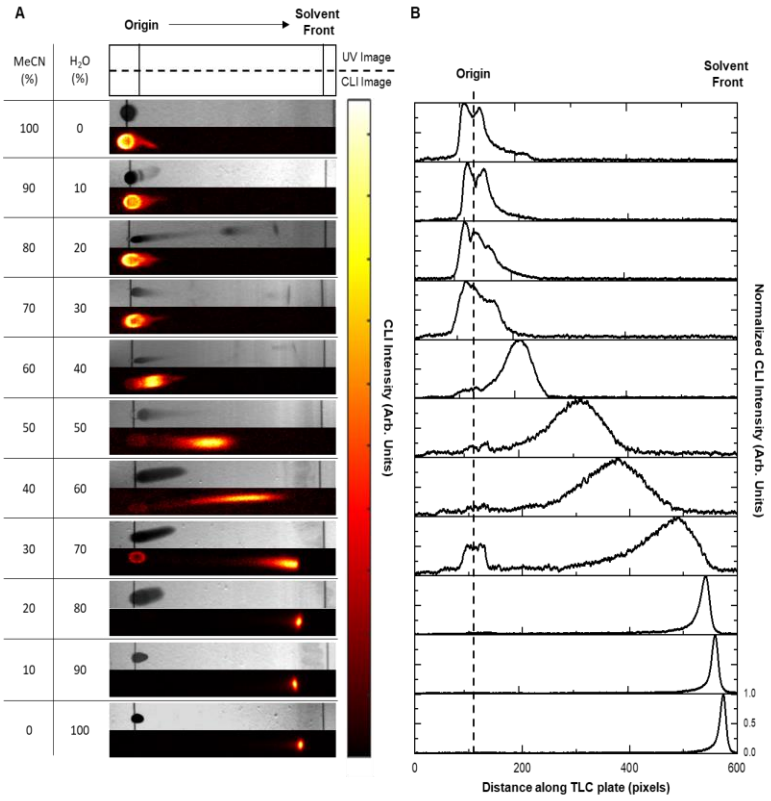

Figure 4. 2 The effect of aqueous mobile phases (MeCN:H2O) on the migration of [18F]TBAF.

(A) For each mobile phase composition, two images are shown: a UV image of the TLC plate stained with I_2 to visualize $TBAHCO_3$ (top), and a CLI image of a TLC plate spotted with [^{18}F]TBAF (bottom). (B) Normalized TLC chromatograms generated from the CLI images. The Supplementary Information contains an additional figure showing the migration of samples of [^{18}F]KF/K_{222}.

4.3.2 Effects of aqueous mobile phases on the analysis of [^{18}F]Fallypride

Noting the effects that water composition had on the chromatographic behavior of [^{18}F]fluoride and its complexes, the effect of aqueous mobile phases on the chromatographic behavior of crude [^{18}F]Fallypride samples (containing unreacted [^{18}F]TBAF) was investigated (**Figure 4.3**). Interestingly, while [^{18}F]Fallypride is non-polar (cLogP = 3.3), using a mobile phase of 100% MeCN did not lead to migration away from the origin, and the [^{18}F]TBAF and [^{18}F]Fallypride bands could not be resolved. Increasing the water content to ≥20% caused the migration of [^{18}F]Fallypride toward the solvent front and allowed the bands to be resolved. However, for ≥40%

water, there was decreased migration of [^{18}F]Fallypride (and further increased mobilization of [^{18}F]TBAF), and at 50% water, there was a significant overlap of the two species. Further addition of water (≥60%) led to a reversal in the order of the bands.

Under most TLC analyses performed, the radioactivity at the origin is generally assumed to be the free radionuclide and the migrated species as the intermediate or product. Without careful assessment and validation of which bands correspond to which species, the overlapped or reversed results under the moderate or high proportion of water could introduce significant ambiguity and errors during analysis (**Figure 4.7**).

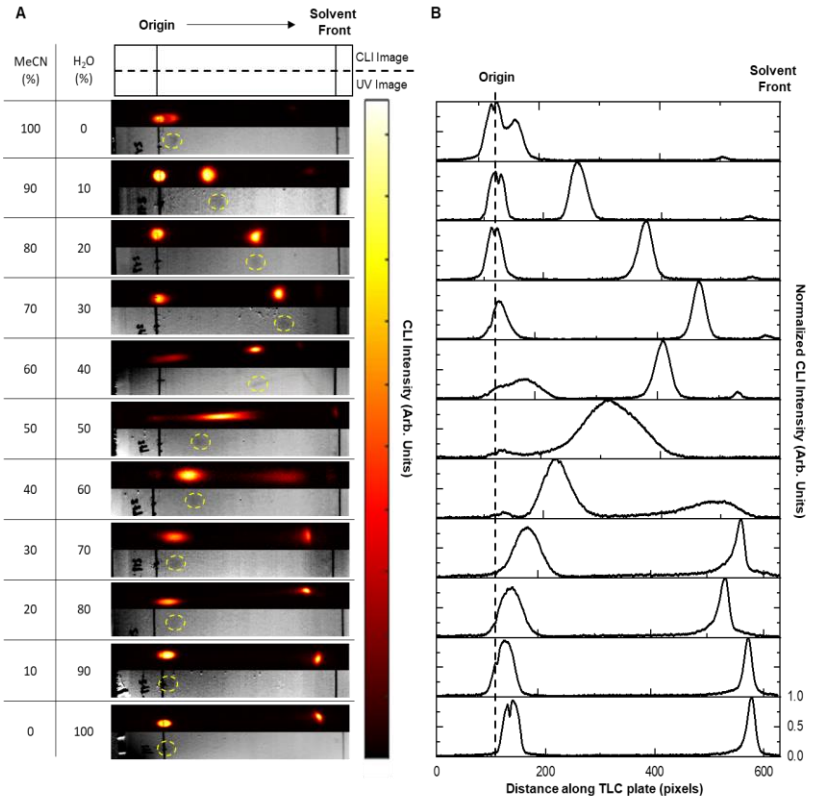

Figure 4. 3 Impact of water composition in aqueous mobile phases (MeCN:H2O) on the migration of [18F]Fallypride.

(A) Images of TLC plates. For each mobile phase composition, a CLI image of the TLC plate spotted with crude [^{18}F]Fallpyride is shown (top), along with a UV image of an adjacent lane spotted with Fallypride standard (bottom). The Fallypride standard band is enclosed with a yellow dashed line for clarity. (B) Normalized TLC chromatograms generated from the CLI images.

4.3.3 Effects of aqueous mobile phases on the analysis of [^{18}F]Flumazenil

The effects of water composition were further investigated using samples of a more polar compound, [^{18}F]FMZ (cLogP = 1.0), containing [^{18}F]TBAF (**Figure 4**). Though [^{18}F]FMZ is more polar than [^{18}F]Fallypride, the use of 100% MeCN led to the complete separation of [^{18}F]FMZ (near the solvent front) from [^{18}F]TBAF (at the origin). For ≥40% water, the [^{18}F]TBAF band begins to migrate away from the origin and split into two distinct radioactive bands, and for ≥60% water, mobilization of [^{18}F]FMZ begins to be adversely impacted. Significant overlap of the bands was observed using a 70% water mobile phase. Mobile phases with higher water content resulted in the migration of [^{18}F]TBAF to the solvent front, and [^{18}F]FMZ remained close to the origin. As mentioned previously, improper assumptions about the band locations could lead to significant misinterpretation of results (**Figure 4.8**).

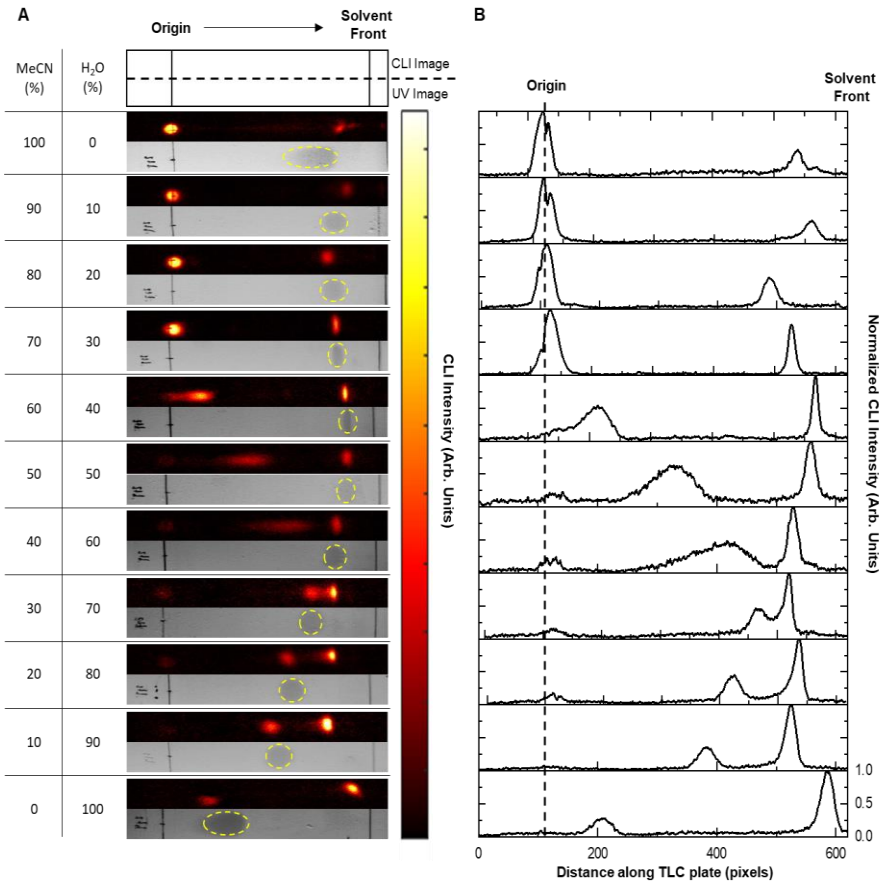

Figure 4. 4 Impact of water composition in aqueous mobile phases (MeCN:H2O) on the migration of [18F]FMZ.

(A) Images of TLC plates. For each mobile phase composition, a CLI image of the TLC plate spotted with crude [^{18}F]FMZ is shown (top), along with a UV image of an adjacent lane spotted with FMZ reference standard (bottom). The FMZ standard band is enclosed with a yellow dashed line for clarity. (B) Normalized TLC chromatograms generated from the CLI images.

4.3.4 Effect of aqueous mobile phases on the analysis of [^{18}F]FET-intermediate

Next, the impact of aqueous mobile phases was assessed for crude mixtures of [^{18}F]FET-intermediate (cLogP = 3.9) containing [^{18}F]TBAF. Spotting of FET reference standard (cLogP = -0.9) in an adjacent lane allowed visualization of the impact of mobile phase composition on the analysis of 3 species (i.e., [^{18}F]TBAF, [^{18}F]FET-intermediate, and FET). With 100% MeCN, both [^{18}F]TBAF and FET remain at the origin, while the non-polar [^{18}F]FET-intermediate moves with the solvent front (**Figure 4.5**). With ≥10% water, FET begins to move away from the origin, and with ≥40% water, [^{18}F]TBAF moves away from the origin, travelling close to FET. Interestingly, using ≥60% water impairs the mobility of the [^{18}F]FET-intermediate, which ends up closer to the origin with increasing water content, while [^{18}F]TBAF and FET remain overlapped at the solvent front. **Figure 4.9** shows the potential for the erroneous determination of radiochemical yield if the bands were improperly identified.

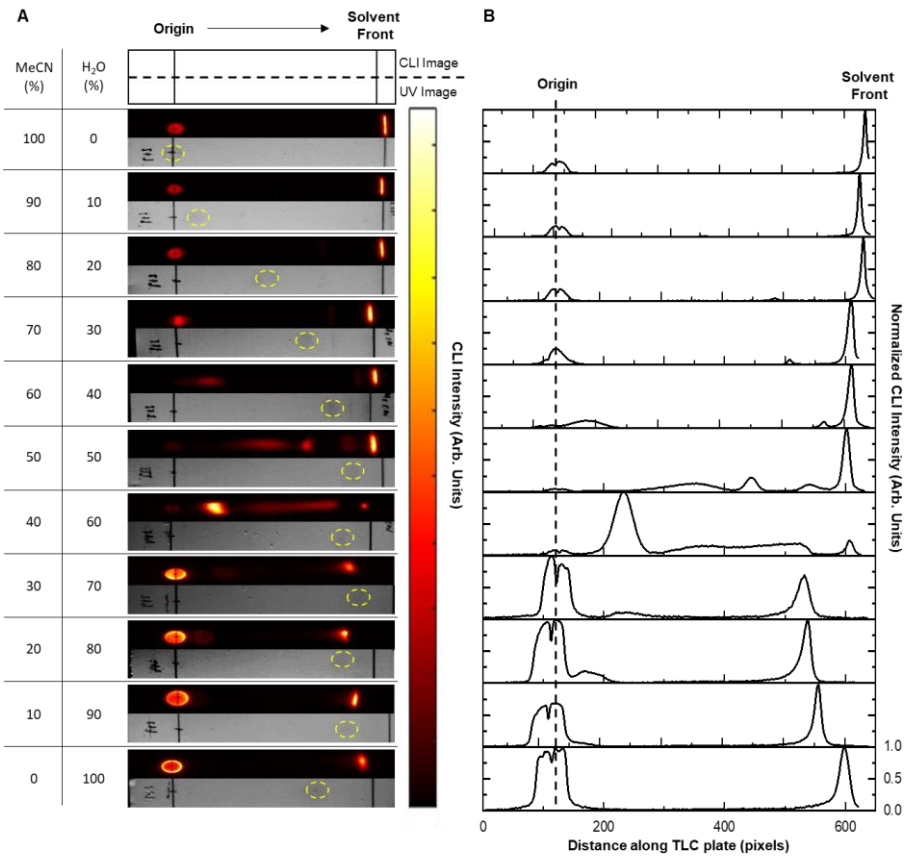

Figure 4. 5 Impact of water composition in aqueous mobile phases (MeCN:H2O) on the migration of [18F]FET-intermediate and FET.

(A) Images of TLC plates. For each mobile phase composition, a CLI image of the TLC plate spotted with crude [^{18}F]FET-intermediate is shown (top), along with a UV image of an adjacent lane spotted with FET reference standard (bottom). The FET standard band is enclosed with a yellow dashed line for clarity. (B) Normalized TLC chromatograms generated from the CLI images.

4.3.5 Discussion

These findings underscore water's complex role in chromatographic selectivity and highlight two major concerns about using water as a mobile phase additive for radiopharmaceutical analysis on silica TLC plates. Firstly, the use of increasing amounts of water leads to a decreasing ability of the silica TLC plate to sequester [^{18}F]fluoride (and [^{18}F]fluoride complexes) at the origin, as well as the possibility that the [^{18}F]fluoride can form multiple bands when using a certain range of mobile phase compositions. Secondly, the water content can greatly affect the migration of the radiopharmaceutical species. Evidently, water plays a more important role in TLC plate selectivity

than as a purely polar additive to affect analyte retention. These effects can lead to overlap of bands at moderate water content and reversal of expected band positions at high water content, potentially leading to ambiguous or inaccurate determination of radiochemical compositions if TLC methods are not carefully validated.

A possible explanation for the first observation could be that water can convert silanol groups (Si-OH; isoelectric point ~2-3) to silanolate ($Si\text{-}O^-$) groups(*157*). While silanol groups can act as weak ion exchangers and bind anionic [^{18}F]fluoride, silanolate groups do not possess this ion exchange capacity(*158*), potentially explaining the inability of the silica plates to sequester [^{18}F]fluoride at the origin when using mobile phases with moderate to high water percentages. This change in the TLC plate may also explain the reduced migration of polar radiopharmaceuticals for mobile phases with high water content, i.e., modification of the silanol groups could lead to greater analyte affinity.

Interestingly, the water content of the mobile phase also appears to strongly influence the migration of cationic radionuclides like [^{68}Ga]Ga^{3+} on silica TLC plates. In a recent publication, researchers studied the effects of various mobile phases in the analysis of a ^{68}Ga-labeled radiopharmaceutical(*159*), finding that with a 50% aqueous mobile phase, [^{68}Ga]Ga^{3+} remains at the baseline, but for 100% aqueous mobile phases, [^{68}Ga]Ga^{3+} migrated with the solvent front. This trend of mobilization for cationic species also appears to be true for other radionuclides like [^{64}Cu]Cu^{2+}, which have also been shown to move with the solvent front when using purely aqueous mobile phases(*160*), and it is possible that similar effects could be possible for other charged radionuclides (e.g., Sc-47, Zr-89, I-124, Lu-177, Ac-225).

4.4 Conclusion

Via systematic studies of different TLC mobile phase compositions and different ^{18}F-labelled radiopharmaceuticals, we investigated the potential pitfalls of using water-containing mobile phases in TLC analysis of radiopharmaceuticals on silica TLC plates. Aqueous mobile phases

with ≥30% water composition led to the migration of [^{18}F]fluoride (or complexes) away from the origin, with higher water content (~50%), leading to the splitting of the [^{18}F]fluoride band, and further increase of water content pushing [^{18}F]fluoride to the solvent front. Secondarily, it was found that moderate amounts of water could hinder the migration of the radiopharmaceutical and even cause overlap with the [^{18}F]fluoride band. While water is often used as a polar mobile phase additive in radiochemical analysis, the observations in this work highlight that water has, in fact, a more complex role in chromatographic selectivity, and care is needed in radio-TLC interpretation when using mobile phases containing significant amounts of water. To avoid these complex effects, we are exploring facile methodologies for purely organic mobile phase optimization that can efficiently separate radiopharmaceuticals from radionuclides.

4.5 Appendix

Further effects observed with different percentages of water added to a mobile phase composition for the development of radiopharmaceuticals.

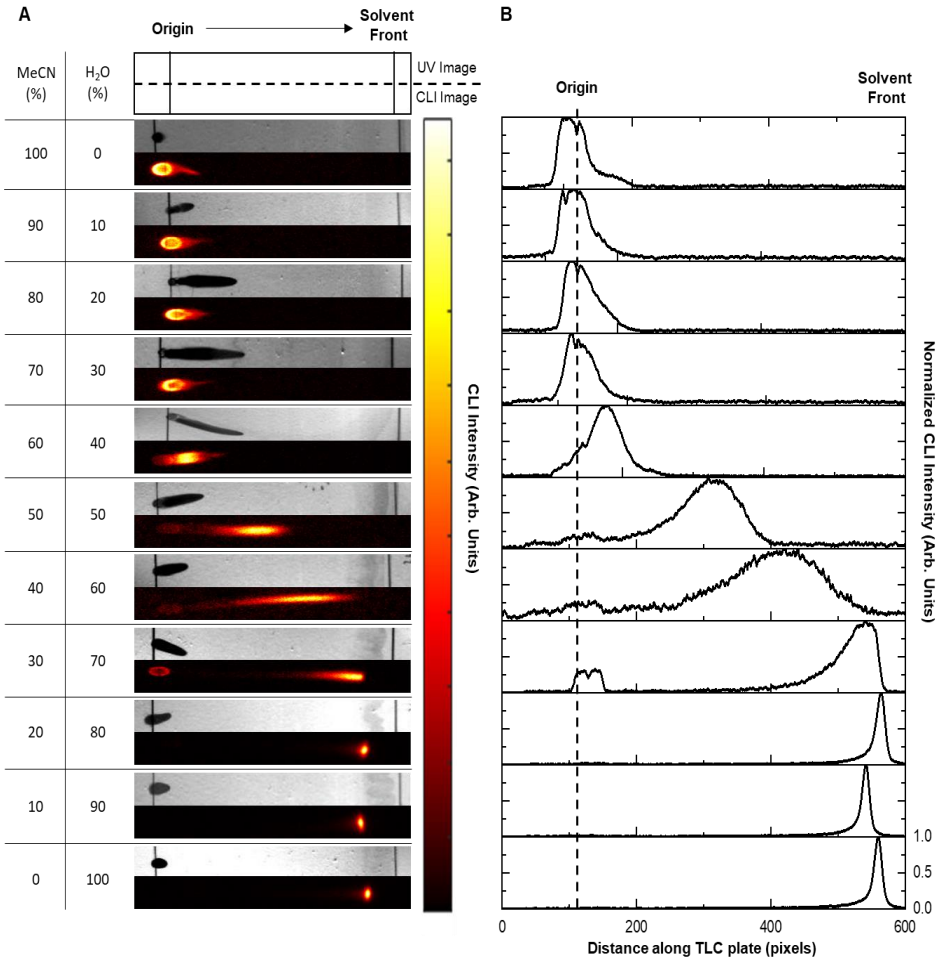

Figure 4. 6 The effect of aqueous mobile phases (MeCN:H2O) on the migration of [18F]KF/K222.

(A) For each mobile phase composition, two images are shown: a UV image of the TLC plate spotted with K_2CO_3/K_{222} and stained with I_2 (top) and a CLI image of a TLC plate spotted with $[^{18}F]KF/K_{222}$ (middle). (B) TLC chromatograms generated from the CLI images.

A

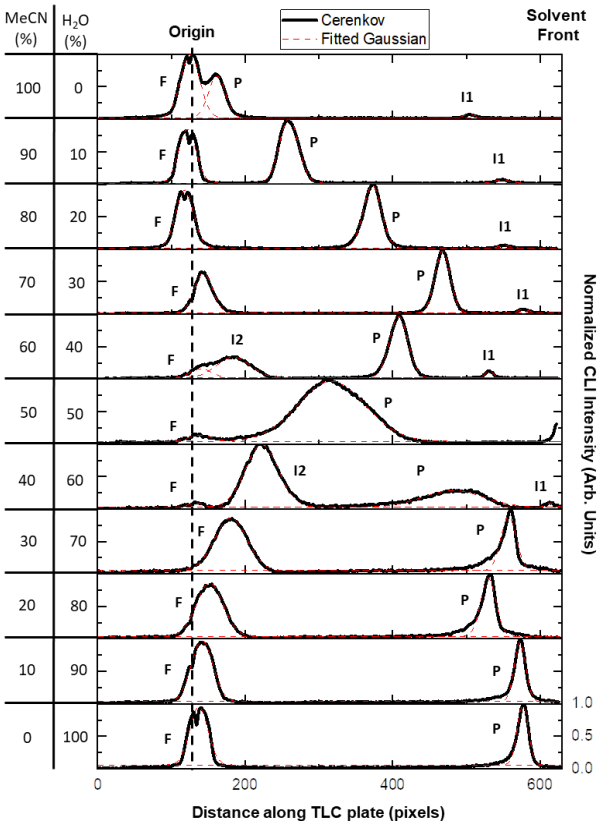

B

[18F]fluoride (%)	Impurity (%)	[18F]Fallypride (%)
62	2	36
42	2	56
43	1	56
42	2	56
9	33, 3	55
3	0	96
2	65, 1	32
62	0	38
62	0	38
62	0	38
62	0	38

Figure 4. 7 The adverse impact of water-containing mobile phases in the naive calculation of fluorination efficiency for [18F]Fallypride.

(A) Chromatograms of samples of [^{18}F]Fallypride/[^{18}F]TBAF separated under different compositions of MeCN:H_2O mobile phases replicated from Figure 3. Chromatograms are annotated with the following naive assignment of bands: F ([^{18}F]fluoride, assumed at origin), P (radiopharmaceutical product, confirmed with the spotting of Fallypride standard); I_i (additional band(s), naively assumed to be impurities). (B) Computed proportion of each species based on naive assumptions. The actual proportions of [^{18}F]TBAF and [^{18}F]Fallypride in the samples were 44% and 56%, respectively.

A

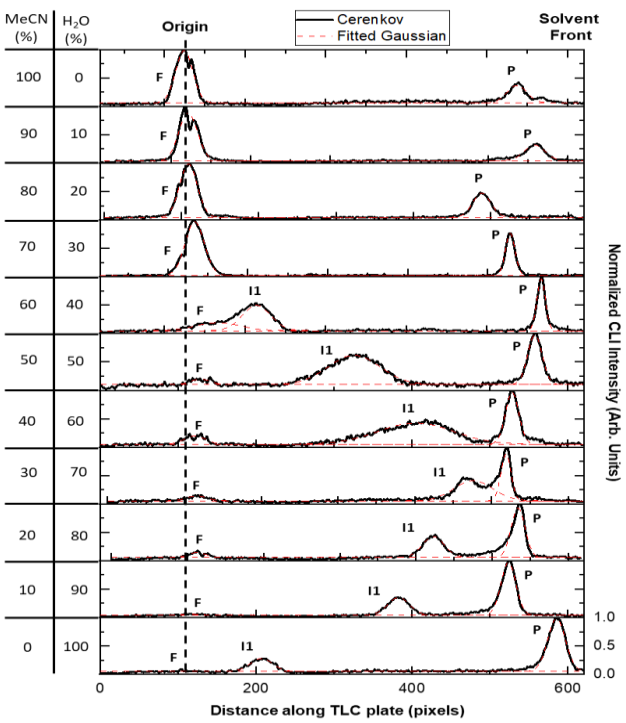

B

[18F]fluoride (%)	Impurity (%)	[18F]FMZ (%)
72	0	28
73	0	27
70	0	30
72	0	28
23	48	29
5	65	30
7	65	28
7	58	35
7	37	56
2	32	66
0	24	76

Figure 4. 8 The adverse impact of water-containing mobile phases in the naive calculation of fluorination efficiency for [18F]Flumazenil.

(A) Chromatograms of samples of [^{18}F]FMZ/[^{18}F]TBAF separated under different compositions of MeCN:H_2O mobile phases replicated from Figure 4. Chromatograms are annotated with the naive assignment of bands: F ([^{18}F]fluoride, assumed at origin), P (radiopharmaceutical product, confirmed with the spotting of FMZ standard); I_i (additional band(s), naively assumed to be impurities). (B) The computed proportion of species is based on naive assumptions. The actual proportions of [^{18}F]TBAF and [^{18}F]Fallypride in the samples were 72% and 28%, respectively.

A

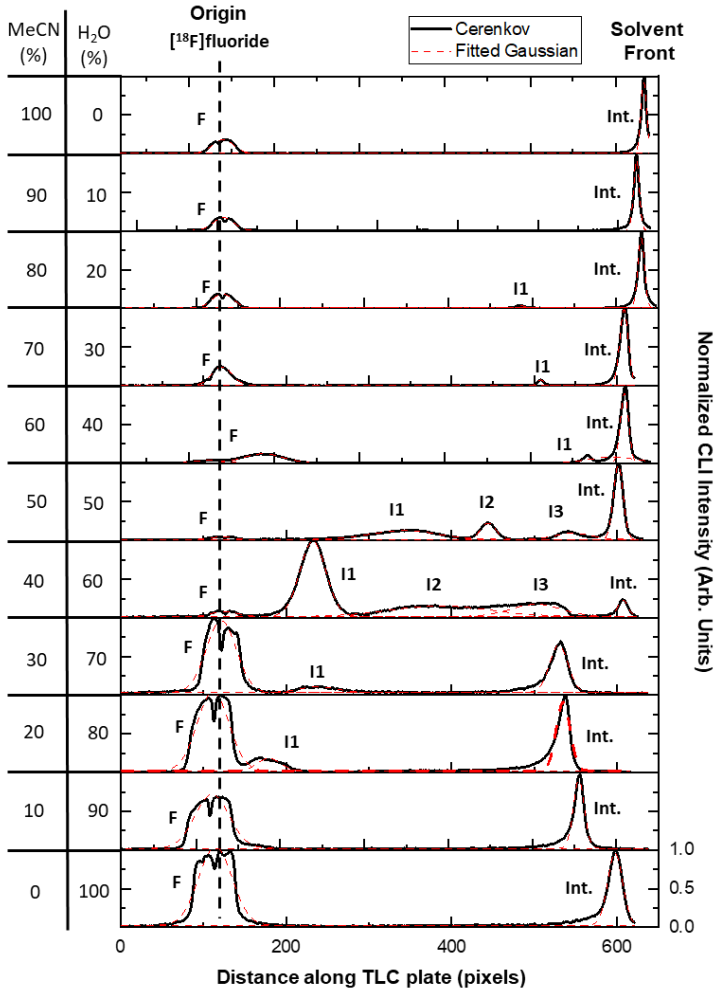

B

[18F]fluoride (%)	Impurity (%)	[18F]FET-Intermediate (%)
39	0	61
39	0	61
38	3	59
35	4	61
6	29, 21	45
3	32, 13, 12	40
3	50, 27, 16	4
67	6	27
67	8	26
71	0	29
71	0	29

Figure 4. 9 The adverse impact of water-containing mobile phases in the naive calculation of fluorination efficiency for [18F]FET-intermediate.

(A) Chromatograms of samples of [^{18}F]FET-intermediate/[^{18}F]TBAF separated under different compositions of MeCN:H_2O mobile phases replicated from Figure 5. Chromatograms are annotated with the naive assignment of bands: F ([^{18}F]fluoride, assumed at origin), P (radiopharmaceutical product, assumed at solvent front); I_i (additional band(s), naively assumed to be impurities). (B) The computed proportion of species is based on naive assumptions. The actual proportions of [^{18}F]TBAF and [^{18}F]FET-intermediate in the samples were 39% and 61%, respectively.

Chapter 5: High-throughput experimentation for the optimization of radiopharmaceuticals

5.1 Introduction

The field of molecular imaging has created positron emission tomography (PET) and single-photon emission computed tomography (SPECT)(*2*)for the visualization and quantification of biochemical processes in living subjects. The use of biologically active molecules tagged with short-lived radionuclides enables such imaging to be performed non-invasively at the whole-body level. PET is used in a wide range of research in small animals and humans to help understand disease pathways(*161,162*), measure pharmacokinetics, confirm the biological effects of new therapeutic compounds(*163,164*), monitor disease progression, or monitor the response to treatment(*165–167*). Common radioisotopes used in PET include C-11 ($t_{1/2}$ = 20.4 min), F-18 ($t_{1/2}$ = 109.8 min), and Ga-68 ($t_{1/2}$ = 67.7 min), among others.

Radiopharmaceuticals are typically prepared using automated synthesizers to limit radiation exposure to personnel and improve reproducibility(*43*). Preparing a batch of a radiopharmaceutical is expensive due to the high cost of the radiosynthesizer, radiation shielding, reagents, radioisotope, and skilled personnel. These costs are greatly multiplied for optimization studies, which require many syntheses to be performed under different conditions. Furthermore, most radiosynthesizers are designed for only one or a few consecutive radiosyntheses per day, thus optimization studies can take weeks or months which further increase labor cost, resource usage, and radioisotope cost.

Recently, multiple approaches have been described to significantly improve the throughput of radiochemistry experiments. Zhang *et al.* performed reactions without radioactivity but mimicked the ultra-low concentrations associated with radionuclides, and leveraged the high sensitivity of LC-MS/MS analysis to assess product yield(*69*). While avoiding the use of radioactivity increased

the throughput of experiments, the reliance on conventional reaction volumes still consumed significant time and reagents to obtain each data point. As an alternative, microfluidic platforms and miniaturized radiochemistry techniques provide promising avenues to increase throughput while minimizing reagent consumption(*26,29,33,168*) by borrowing concepts from high-throughput experimentation in organic chemistry(*169–171*). Several groups have shown that dozens of small-scale radiochemical reactions (i.e. 10s of µL each, compared to the ~0.5 – 2.0 mL used in conventional setups) can be sequentially performed using flow-chemistry capillary reactor platforms with crude products collected and analyzed offline(*45,53–55*). While parameters like temperature and reagent flow rates can be readily studied in a high-throughput manner, others, such as reaction solvent or the conditions for the drying/activation of the [^{18}F]fluoride, cannot. Another optimization platform used a polydimethylsiloxane (PDMS) microfluidic chip to prepare ultra-small batches (~100 nL each) for screening of aqueous protein radiolabeling conditions but was limited to varying reagent ratios and pH(*56,57*).

Small-volume vial-based reactions have also been used for optimization(*58*) and enable a wider range of parameters to be studied. Recently, Laube *et al.* reported the use of multi-vial heating blocks to perform up to ~50 radiofluorinations per day, each involving drying a small aliquot of [^{18}F]fluoride eluted from a QMA cartridge, followed by reaction at the 25-50 µL scale(*59*). While demonstrating parallelism and low reagent consumption, this technique required significant manual handling of vials, including installation and removal of vial caps. In addition, it is well known that the detailed heating characteristics of the system are essential to consider(*60*), and after optimization in small vials the conditions may have to be adapted to a conventional synthesizer for routine automated production.

Our group recently pioneered a microfluidic platform, in which reactions are performed at an even smaller scale (i.e. 1-10 µL) in droplets confined in surface-tension traps patterned on a surface(*32*(p)). Under these conditions, droplet reactions typically have yields comparable to

conventional methods but allow shorter synthesis time and up to ~100x lower reagent consumption per reaction(*49,51,52*). Of particular note, after optimization under low activity conditions, larger scale production (e.g. one or a few clinical doses) can be achieved under identical conditions using an automated droplet-based radiosynthesizer(*62,63*) by a simple increase of starting activity. To increase throughput, we created chips with multiple reaction sites for performing up to 16 droplet-based syntheses in parallel, all with the same reaction temperature and time but with varying volumes or concentrations of reagents(*24*). A preliminary study showed the possibility of optimizing several parameters in the synthesis of [^{18}F]Fallypride, including the amount of base, precursor concentration, and droplet reaction volume. In this paper, throughput and flexibility are further increased by introducing an array of 4 independent heaters, enabling operation of 4 chips in parallel. This improved platform allows the parallel exploration of additional reaction variables (reaction temperature and time) that cannot be conveniently studied with a single chip at a time

5.2 Materials and reagent preparation

5.2.1 Materials

Anhydrous N,N-dimethylformamide (DMF, 99.8%) purchased from Fisher Scientific, anhydrous dimethyl sulfoxide (DMSO, ≥99.9%), anhydrous acetonitrile (MeCN, 99.8%), 2,3-dimethyl-2-butanol (thexyl alcohol,98%), 4,7,13,16,21,24-hexaoxa-1,10-diazabicyclo[8.8.8]hexacosane (K_{222}, 98%), triethylamine (TEA, 99%), trifluoroacetic acid (TFA, >99%), tetrahydrofluran (THF, >99.9%, inhibitor-free), hexanes (95%), dichloromethane (DCM, >99.8%), acetone (99.5%), ammonium formate (NH_4HCO_2: 97%) N-methyl-2-pyrrolidone (NMP, 99.5% anhydrous), 1,3-dimethyl-3,4,5,6-tetrahydro-2(1H)-pyrimidinone (DMPU, 98%), ethylene glycol (99.8%) and potassium carbonate (K_2CO_3, 99.995%) were purchased from Sigma-Aldrich (St. Louis, MO, USA). n-butanol (nBuOH, 99%) was purchased from Alfa Aesar (Ward Hill, MA, USA). Tetrabutylammonium bicarbonate ($TBAHCO_3$, 75mM in ethanol), ethyl-5-methyl-8-nitro-6-oxo-

5,6-dihydro-4*H*-benzo[f]imidazo[1,5-*a*][1,4]diazepine-3-carboxylate (nitromazenil; precursor for [^{18}F]Flumazenil, > 97%) and Flumazenil (reference standard, >99%), 2-((2,5-dimethoxybenzyl)(2-phenoxyphenyl)amino)-2-oxoethyl-4-methylbenzenesulfonate ([^{18}F]PBR06 precursor, >95%), 2-fluoro-N-(2-methoxy-5-methoxybenzyl)-N-(2-phenoxyphenyl)acetamide (reference standard for [^{18}F]PBR06, >95%), (*S*)-2,3-dimethoxy-5-[3-[[4-methylphenyl)-sulfonyl]oxy]-propyl]-N-[[1-(2-propenyl)-2-pyrrolidinyl]methyl]benzamide (Fallypride precursor, >90%), Fallypride (reference standard, >95%), 2-(2-((*N*-4-phenoxypyridin-3-yl)acetamido)methyl)phenoxy)ethyl-4-methylbenzenesulfonate ([^{18}F]FEPPA precursor, >90%), and *N*-[[2-(2-fluoroethoxy)phenyl]methyl]-*N*-(4-phenoxypyridin-3-yl)acetamide (reference standard for [^{18}F]FEPPA, >95%) were purchased from ABX Advanced Biochemical Compounds (Radeberg, Germany). DI water was obtained from a Milli-Q water purification system (EMD Millipore Corporation, Berlin, Germany). No-carrier-added [^{18}F]fluoride in [^{18}O]H_2O was obtained from the UCLA Ahmanson Biomedical Cyclotron Facility and Crump Cyclotron Facility.

1% Teflon AF 2400 solution was purchased from Chemours. Positive photoresist (MEGAPOSIT SPR 220-7.0) and developer (MEGAPOSIT MF-26A) were purchased from MicroChem (Westborough, USA). Additional solvents and chemicals used for microfluidic chip fabrication, including methanol (MeOH, Cleanroom LP grade), acetone (Cleanroom LP grade), isopropanol (IPA, Cleanroom LP grade), sulfuric acid (96%, Cleanroom MB grade) and hydrogen peroxide (30%, Cleanroom LP grade), were purchased from KMG Chemicals (Fort Worth, USA).

5.2.2 Reagent preparation

The following stock solutions were prepared daily to carry out droplet reactions. The [^{18}F]fluoride stock solution contained either 60 mM $TBAHCO_3$ and 1.8 MBq/μL (48 μCi/μL) of [^{18}F]fluoride in water (i.e. for [^{18}F]Flumazenil, [^{18}F]PBR06, [^{18}F]Fallypride, and [^{18}F]FEPPA), or 60 mM of K_{222} with 30 mM of K_2CO_3 and 1.8 MBq/μL (48 μCi/μL) of [^{18}F]fluoride in water (i.e. for [^{18}F]Flumazenil and [^{18}F]PBR06), or 60 mM of K_{222} with 30 mM of Cs_2CO_3 and 1.8 MBq/μL (48 μCi/μL) of [^{18}F]fluoride in water (i.e. for [^{18}F]Flumazenil). [^{18}F]Flumazenil precursor stock solution

contained 70 mM precursor in either DMSO, DMF, NMP, DMPU, or ethylene glycol. [^{18}F]PBR06 precursor stock solution contained 70 mM precursor in either DMSO or a 1:1 v/v mixture of thexyl alcohol and MeCN. [^{18}F]Fallypride stock solution contained 77 mM of precursor in a 1:1 v/v mixture of thexyl alcohol and MeCN. [^{18}F]FEPPA stock solution contained 30 mM of precursor in a 1:1 v/v mixture of thexyl alcohol and MeCN. For [^{18}F]Flumazenil, the collection stock solution was a 2:1 v/v mixture of reaction solvent and water when using DMSO or DMF as the reaction solvent, or a 9:1 v/v mixture of MeOH and H_2O collection stock solution when using NMP, DMPU, or ethylene glycol as the reaction solvent. For [^{18}F]PBR06, [^{18}F]Fallypride, and [^{18}F]FEPPA, the collection stock solution was a 9:1 v/v mixture of MeOH and H_2O.

5.3 Analytical methods

5.3.1 Analysis of reaction performance

Radioactivity measurements were made using a calibrated dose calibrator (CRC-25R, Capintec, Florham Park, NJ, USA). To calculate the starting activity on each reaction site, we measured the activity on the chip after loading the initial [^{18}F]fluoride solution to each individual spot (via dose calibrator) and subtracted the previous measurement of chip activity. All measurements were decay-corrected to a common timepoint. Collection efficiency was determined by dividing the activity of the collected crude sample from an individual spot by the starting activity used in that same reaction site (corrected for decay). Fluorination efficiency was analyzed using radio-TLC. Crude radiochemical yield (crude RCY) was calculated by multiplying the collection efficiency by the fluorination efficiency. The total residual activity left on the chip was measured by placing the chip in a dose calibrator after collection of the crude products from each reaction site. To compute the residual activity left on the chip at each individual reaction site, the activity distribution on the chips was first determined via Cerenkov imaging(*24,31,77*). For Cerenkov imaging, a glass microscope slide (76.2 mm x 50.8 mm, 1 mm thick; C&A Scientific; Manassas, VA, USA) was placed on top of the chip, and the acquisition time was 5 min. Raw images were corrected as previously described(*128*). Residual activity for a particular reaction site

on the chip was computed with the aid of a custom region-of-interest (ROI) analysis software written in MATLAB (MathWorks, Natick, MA). For each reaction site, an ROI was drawn and the integrated Cerenkov signal was computed from the image. To quantify the amount of residual activity at a particular reaction site, the corresponding ROI integrated signal was divided by the sum of integrated signal for all ROIs and multiple by the measured total residual radioactivity on the chip. This value could then be expressed as a fraction of starting radioactivity by dividing the residual activity for a particular reaction site by the starting activity used at that particular reaction site (correcting for decay).

5.3.2 Thin-layer chromatography

Performing 64 simultaneous reactions presents a significant challenge for analysis. Typical methods of spotting one sample per TLC plate for typically used TLC plates lengths and conditions require 2-7 min per sample separation and readout and cannot be practically scaled to 64 samples. To accelerate the analysis, TLC plates (silica gel 60 F254; Merck KGaA, Darmstadt, Germany) were spotted with multiple samples (8 samples at 0.5 mm pitch), with all samples separated in parallel and read out simultaneously via Cerenkov imaging using methods we have previously reported(*128*). Briefly, 8 samples (0.5 µL each) were spotted onto a 50 mm x 60 mm (W x L) TLC plate, with adjacent spots separated by 5 mm. Developed TLC plates were read out by covering the TLC plate with a scintillator plate (50 mm x 35 mm, 1 mm thick, BC-400, Saint-Gobain, OH, USA) or a glass microscope slide (76.2 mm x 50.8 mm, 1 mm thick, A&C Scientific) to obtain images of the emitted light. The solvent front took ~2 min to travel 45 mm (corresponding to 30 mm separation distance). The mobile phase to separate the [^{18}F]Flumazenil crude sample was 100% MeCN, for [^{18}F]PBR06 crude samples 13:10:24:54 (v/v) dichloromethane:chloroform:acetone:hexanes as the mobile phase, for [^{18}F]FEPPA crude samples 25.6:37.5:36.5:0.4 (v/v) nBuOH:THF:hexanes:TEA as the mobile phase, and [^{18}F]Fallypride crude samples were separated using 60% MeCN in 25 mM HN_4HCO_2 with 1% TEA

(v/v), as previously reported(*24*). More information on R_f values and TLC separation studies can be found in **Appendix**, under the radio-TLC methods.

5.3.3High-performance liquid chromatography (HPLC)

Analytical radio-HPLC was used to identify the product of each synthesis (via co-injection with reference standard) and to isolate pure products to confirm the R_f value of the product bands in radio-TLC. The radio-HPLC system setup comprised a Smartline HPLC system (Knauer, Berlin, Germany) equipped with a degasser (Model 5050), pump (Model 1000), UV detector (254 nm; Eckert & Ziegler, Berlin, Germany) and gamma-radiation detector, and counter (B-FC- 4100 and BFC-1000; Bioscan, Inc., Poway, CA, USA). All HPLC separations used a C_{18} Gemini column (Kinetex, 250 x 4.6 mm, 5 µm, Phenomenex, Torrance, CA, USA). Using a mobile phase of 3:1 H_2O:MeCN with 0.1% TFA (v/v) and a flow rate of 1.0 mL/min, the retention time of [^{18}F]Flumazenil was 11 min. For [^{18}F]PBR06, the retention time was 8 min using a mobile phase of 60:40 (v/v) MeCN:20 mM sodium phosphate buffer (pH = 5.8) with a flow rate of 1.5 mL/min. [^{18}F]Fallypride samples were separated with a mobile phase of 60% MeCN in 25 mM HN_4HCO_2 with 1% TEA (v/v) and a flow rate of 1.5 mL/min resulting in a retention time of 4.5 min. [^{18}F]FEPPA samples were separated with a mobile phase of 70:30 v/v H_2O:EtOH with 0.1% H_3PO_4 at 0.8 mL/min, giving a retention time of 15.5 min.

5.4 Results

5.4.1 Platform design

Arrays of reactions were performed in droplet format on 25.0 x 27.5 mm^2 Teflon-coated silicon "chips" (**Figure 5.1**). Each reaction was confined to a 3 mm diameter circular hydrophilic site (made by etching away the Teflon coating) that acts as a surface tension trap. Details of the chip fabrication have been previously reported(*24*) and shown in **Chapter 2**.

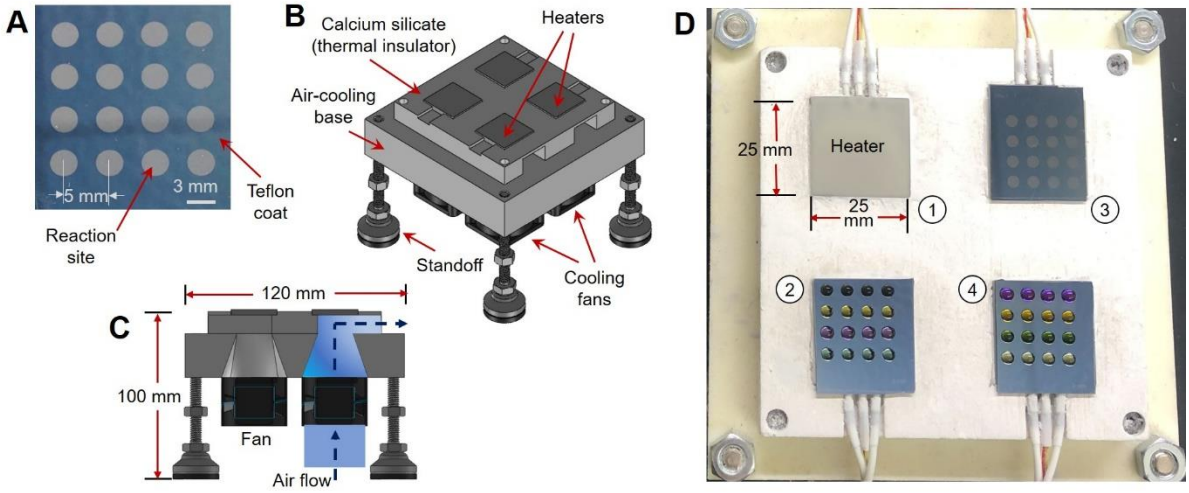

Figure 5. 1 High-throughput reaction apparatus.

(A) Photograph of multi-reaction chip. (B) CAD model showing platform components. (C) Cross-section view of the multi-heater platform showing the path of forced-air cooling. (D) Photograph of the platform (from above) with multi-reaction chips installed.

Multiple chips were operated in parallel using a custom-built four-heater platform (**Figure 5.1B-D**). To provide radiation protection, the platform was operated inside a hot cell, but the control system could be placed outside to minimize the footprint. The platform comprised four 25 mm ceramic heaters glued with epoxy on top of a thermally insulating frame CNC-machined from a calcium silicate composite, which was in turn affixed atop of a 3D-printed nylon piece to direct cooling air to each heater from a set of four 36 mm 12V DC fans (**Appendix** and **Figure 5.8**). Thermal simulations were performed to determine an appropriate heater spacing to avoid thermal crosstalk from neighboring heaters (**Appendix** and **Figure 5.9 - 5.12**). The chips were affixed to the heaters with a thin layer of thermal paste.

Each heater (and fan) was independently controlled, enabling the set of reactions on each multi-reaction chip to be performed at a unique temperature or duration (**Figure 5.8**). For each heater, the signal from the integrated K-type thermocouple was amplified and connected to an analog input of a data acquisition module (DAQ). Heaters were powered with 120VAC switched by a solid-state relay driven by a digital output of the DAQ using an on-off controller implemented in LabView (National Instruments). After the desired heating time, forced-air cooling was activated using a digital output of the DAQ to power the corresponding fan via a Darlington driver circuit.

After calibrating the heaters, temperature stability was assessed by monitoring the integrated thermocouple with respect to time (**Figure 5.13**). At each setpoint tested, heating took only ~5 s, and temperature exhibited <1 °C fluctuation once stabilized (**Table 5.2**). Forced-air cooling to 30 °C took ~3 min from 140 °C, ~2.5 min from 100 °C, and ~1.2 min from 50 °C. In addition, spatial temperature distribution of each heater was visualized via thermal imaging. All heaters exhibited uniform surface temperature (**Figures 5.14, 5.15,** and **Table 5.3**), except near the edges (where deviation >2% from the mean was observed). In all cases, the extent of this unusable region was limited to <1.5 mm on each edge of the heater. Thus, the multi-reaction chips were designed with a 2.4 mm unused boundary, ensuring that all 16 reaction sites were entirely located within the uniform portion of the heater surface (**Figure 5.16**)(*24*). A previous study confirmed the consistency of reactions at different sites on the chip and the negligible degree of cross-contamination from one site to another(*24*). With the platform, up to 64 radiochemical syntheses could be performed in parallel, each reaction using ~100x less reagents than conventional approaches. Because all steps, including [^{18}F]fluoride drying, are performed on-chip, the conditions used in any part of the synthesis can be explored in a high-throughput fashion.

5.4.2 Synthesis optimization

We used this new platform to perform extensive studies of the syntheses of several clinically relevant PET tracers: [^{18}F]Flumazenil ([^{18}F]FMZ), [^{18}F]PBR06, [^{18}F]Fallypride, and [^{18}F]FEPPA.

For each radiopharmaceutical, an extensive set of experiments was performed to compare the influence of different reaction conditions related to [^{18}F]fluoride drying and the radiofluorination reaction. Our goals were to better understand the influence of various reaction parameters and to develop efficient microscale synthesis protocols for these tracers. Initial droplet reaction conditions were determined essentially by reducing volumes ~100x from conventional macroscale protocols. In general, experiments were performed in batches of 64 simultaneous reactions (4 chips x 16 reactions each), exploring 16 different conditions, each with n=4 replicates.

Figure 5.2 illustrates the synthesis scheme for each tracer and the generalized process for one set of 16 reactions. At each site, an 8 µL droplet of [^{18}F]fluoride stock solution ([^{18}F]fluoride mixed with the desired amount and type of base and phase-transfer catalyst) is added to the reaction site and dried. (Though drying parameters to eliminate residual water could also be studied, drying was performed for 1 min at 105 °C in all experiments.) Next, 8 µL of precursor solution (6 µL for [^{18}F]Fallypride) with the desired concentration and reaction solvent is added to the dried residue and reacted at elevated temperature for the desired time. Reaction volume could also be studied as a parameter but was not explored here. After the reaction is complete, crude product is collected. Though collecting parameters could be optimized to minimize residual activity on the chip, we performed product collection in all cases by dispensing 10 µL of collection solution to the reaction site and aspirating the volume and repeating these steps 4x for a total of 40 µL of collected crude product. The reaction performance was determined by measuring both the conversion of [^{18}F]fluoride to product via radio-TLC, as well as the recovered activity from each reaction (compared to starting activity, i.e. collection efficiency) to determine an overall crude radiochemical yield (RCY). TLC analysis was performed using recently reported multi-lane methods with 8 samples per plate(*128*).

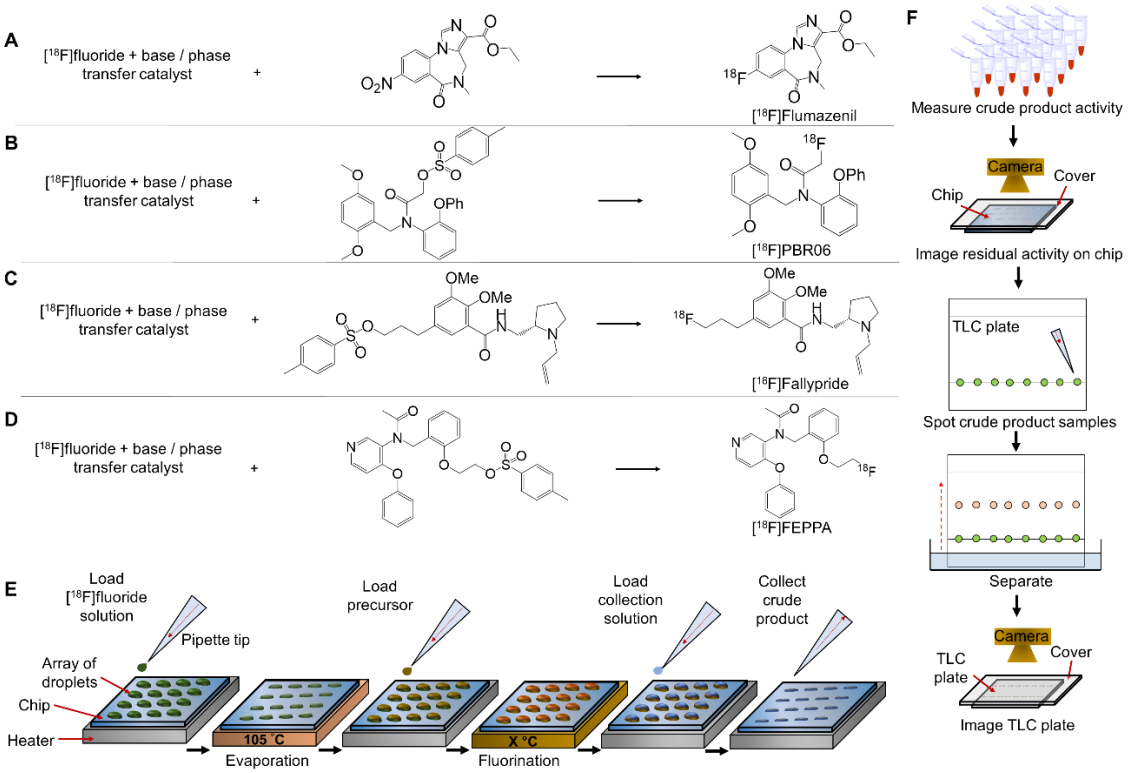

Figure 5. 2 Optimization process.

(A) Scheme for the radiosynthesis of [^{18}F]Flumazenil. (B) Synthesis of [^{18}F]PBR06. (C) Synthesis of [^{18}F]Fallypride. (D) Synthesis of [^{18}F]FEPPA. (E) Experimental procedure for performing parallel radiosyntheses using a (4x4) multi-reaction microdroplet chip. Concentrations, solvents, and volumes can be varied from site to site, and temperature and heating time can be varied from chip to chip. (F) Procedure for reaction performance analysis. Activities of collected crude samples are measured using a dose calibrator and compared with starting activity to determine collection efficiency. Residual activity on chip is analyzed via Cerenkov imaging. Crude samples are analyzed via radio-TLC to determine the fluorination efficiency.

5.4.3 Optimization of [^{18}F]Flumazenil

[^{18}F]Flumazenil is used to quantify changes in the density of $GABA_A$ receptors associated with Alzheimer's disease, Schizophrenia, neuronal plasticity, and sensory processes(*172*). We focused on the route from the commercially-available nitromazenil precursor(*45,145,146,173–175*), for which reported isolated yields are in the range of 8 to 30%(*145,146,173–175*). Though other synthesis routes have led to higher yields, they were not pursued here due to the lack of commercial availability of the diaryliodonium tosylate precursor(*176*) or the very low molar activity (0.37 GBq/μmol [0.01 Ci/μmol]) of the isotopic exchange method(*147*). Previous optimization studies using macroscale and flow chemistry approaches (**Table 5.1**) have typically compared

just a couple of values for parameters studied and often with few if any replicates(*45,145,146,173–175*).

Table 5. 1 Summary of parameters and conditions tested in reports of optimization of [18F]Flumazenil using nitromazenil as precursor in microscale and macroscale platforms.

	This work	**Wong et al(*45*). (2012)**	**Nasirzadeh et al(*146*). (2016)**	**Mandap et al(*173*). (2009)**	**Massaweh et al(*174*). (2009)**	**Ryzhikov et al(*175*). (2005)**
Synthesizer type	Microscale (droplet format)	Microscale (flow format)	Macroscale	Macroscale (microwave)	Macroscale	Macroscale
Solvents	DMSO, DMF, NMP, DMPU, ethylene glycol	DMSO, DMF, MeCN	DMF	DMSO, DMF, MeCN	DMF	DMSO, DMF
Reaction times (min)	0.5, 1, 2, 3, 4, 5, 6, 7	2.5	15, 30	2, 5, 10	30	15, 30
Temperatures (°C)	100, 120, 140, 160, 180, 200, 220, 240	110, 120, 130, 140, 160	150	90, 140, 160, 180, 200*	160	130, 160
Base types	$TBAHCO_3$, K_{222} / K_2CO_3, K_{222} / Cs_2CO_3	K_{222} / $KHCO_3$	K_{222} / K_2CO_3	K_{222} / K_2CO_3	K_{222} / K_2CO_3	K_{222} / K_2CO_3
Base amounts (nmol)	480, 320, 240, 160, 80, 40, 20, 10 and 240/120	2850 / 2590	25000 / 12000	12000 / 6000[#]	2800/ 1200	25000 / 12000[+]
Precursor amounts (nmol)	560, 400, 280, 160, 80, 40, 20, 10	1500	24220, 12000, 5100, 3030	24000, 15000, 12000, 51000, 3000	18000, 21000	6000, 12000, 13000, 13000, 19000, 24000, 25000, 25000, 25400, 36000
Total number of different conditions tested	85	13	3	19	1	14
Total number of experiments performed	335	13	23	52	15	14

[#]Not reported but the amount of K_{222} was computed based on the amount of precursor and an indicated precursor to K_{222} / K_2CO_3 molar ratio of 0.5:1. Ratio of K_{222} to K_2CO_3 needed to calculate K_2CO_3 was inferred from a paper they referenced(*177*)

‡Based on 1:1 precursor to K_{222} / K_2CO_3 molar ratio. Note: different volumes of solvent were used as an additional parameter (0.5, 1.0, 1.5, and 2.0 mL)
*In the microwave reactor, the pressure was also varied (0, 100, and 200 kPa).

Leveraging the increased throughput of our platform, we performed a series of experiments to explore more comprehensive ranges of each parameter with finer granularity (typically 8 values each) and more replicates. Parameters explored included: (i) reaction temperature, (ii) amount of base, (iii) amount of precursor, (iv) reaction time, (v) reaction solvent, and (vi) type of base and phase-transfer catalyst. Full details and results for each set of experiments can be found in **Appendix** on the [^{18}F]Flumazenil section. Since most literature reported the use of the solvents N,N-dimethylformamide (DMF) and dimethyl sulfoxide (DMSO)(*45,173*), the studies we performed for parameters i – iv were carried out using each of these solvents. As an example of how each experiment was set up, **Figure 5.3** shows how four chips were used to explore reaction temperature. The figure also shows the images of residual radioactivity on the chips after synthesis, and the Cerenkov images of the TLC plates used to evaluate conversion.

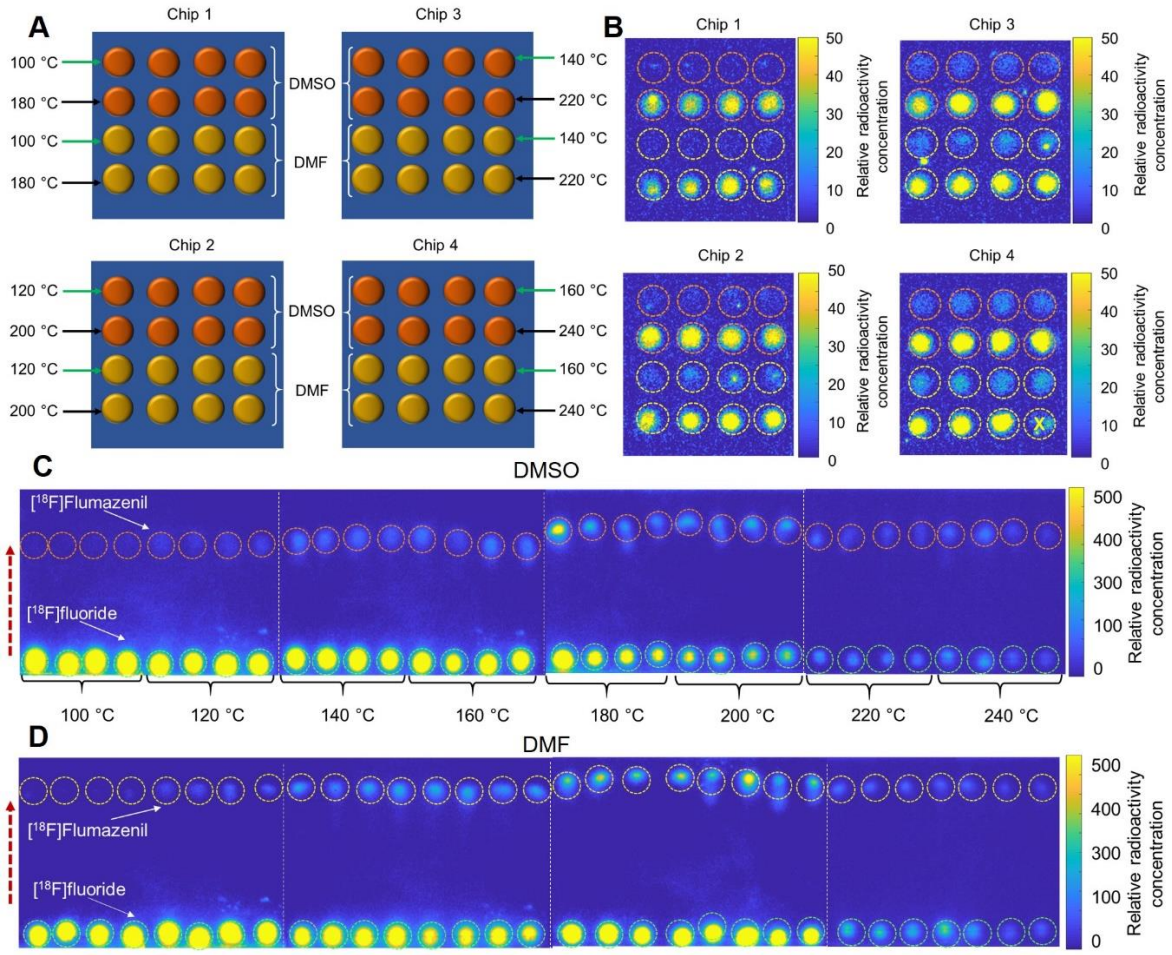

Figure 5. 3 Experimental set up for one batch of experiments that explored the influence of reaction temperature (8 values) and solvent (2 types) for the synthesis of [18F]Flumazenil.

(A) Assignment of 64 reaction sites. Half of the reaction sites were used first to explore 4 different temperatures in the first set of 32 simultaneous reactions. Then the other half of the sites were used for the remaining 4 temperatures. (B) Cerenkov images show the distribution of the residual activity on each chip after collecting the crude products. Radioactivity signal is decay-corrected to a common timepoint for all images. The reaction marked with an "X" was not analyzed (by mistake the precursor droplet was not added to reaction site). (C) Cerenkov images of developed TLC plates (each containing 8 samples) for reactions that used DMSO as the reaction solvent. (D) Separated crude samples using DMF as the reaction solvent. Dashed circles indicate the ROIs used for analysis. The dashed red arrow indicates the direction of solvent movement during development. White dotted lines represent the boundary of each multi-sample plate.

The resulting performance calculations for each condition are tabulated in **Appendix Table 5.4** and the performance is plotted in **Figure 5.4A**. The fluorination efficiency increased strongly with temperature. However, unlike other droplet-based reactions, volatile losses during the

fluorination reaction, as well as residual activity stuck to the chip after collection, led to declining collection efficiency with increasing temperature. (Generally, the amount of volatile loss dominated and was about 15 - 10x higher than the residual loss.) The resulting crude RCY exhibited a peaking behavior with a maximum of 13.5 ± 0.6 (n=4) at 200 °C (with DMF). Consistent with these trends, Wong *et al.* found temperature of a flow reactor to be an essential factor with fluorination efficiency increasing from ~0% at 120 °C to ~20% at 160 °C using DMF as the solvent, and from ~0% to ~5% using DMSO(*45*). Mandap *et al.*, using a microwave reactor, also found that fluorination efficiency increased substantially with temperature to a maximum value and then declining somewhat at higher temperatures(*173*).

We should point out that typically only the radiofluorination efficiency (as determined by radio-HPLC or radio-TLC) and/or radiochemical yield is reported in optimization experiments, making it difficult to make detailed comparisons with droplet reactions. Reporting only radiofluorination efficiency can be misleading as many potential losses (e.g. volatile losses or residual activity stuck on vials or tubing, which can be significant(*129*)) are not accounted for. Reporting only radiochemical yield accounts for losses, but all the losses (from various synthesis steps or purification) are lumped together. Significant discrepancies have been reported between radiochemical conversional and radiochemical yield for [^{18}F]Flumazenil(*145,146,174*). For example, Vaulina *et al.* observed fluorination efficiency (TLC) of 25% but obtained only a 2% isolated yield after HPLC purification and SPE formulation, or 9% after SPE-based purification/formulation(*145*). Massaweh *et al.* found that despite a fluorination efficiency (TLC) of 27-35%, isolated yield was only 2-5% (*175*), though it improved to 15-20% after mobile phase optimization(*174*). While these discrepancies may reflect high losses during the purification/formulation step(*145*), these reports do not contain sufficient details or data to rule out other losses (e.g. residual activity on reaction vessel or tubing, volatile losses, etc.)

The temperature was fixed at 200 °C for subsequent experiments. With increasing base amount (**Figure 5.4B**), we observed the fluorination efficiency to increase from near zero and plateau at a maximum value when base amount reached ~150-200 nmol. Collection efficiency exhibited an inverse behavior, and the overall crude RCY for DMF (the higher performing solvent) exhibited a sharp increase and then plateau starting at ~160 nmol of base. 240 nmol (where the crude RCY was only marginally lower) was selected as the optimal amount to provide robustness against pipetting errors. Study of increasing precursor amount (**Figure 5.4C**) showed rapid increases up to ~80 nmol and then a plateau, for fluorination efficiency, collection efficiency and crude RCY. The highest crude RCY (with DMF, the higher performing solvent) occurred at a precursor amount of 280 nmol, which was selected as the optimal condition. The strong impact of precursor amount below the plateau is consistent with Mandap *et al.*, who reported low fluorination efficiency (<3%, n = 1) for 1 mg of precursor in DMF at 160°C, and high values (~30%) with 2-8 mg of precursor. Ryzhikov *et al.* also found marked differences in fluorination efficiency in pairwise comparisons of precursor amounts(*175*). Unfortunately, the reaction volume is given as a range in both papers, making it impossible to compare the concentration values. In many reactions, the ratio of base to precursor is a relevant parameter and we thus plotted the reaction performance as a function of this ratio in **Figure 5.24**. Ratios in the range ~1-3 gave the highest crude RCY, with a rapid drop for lower ratio values and a gradual drop for higher values. When exploring increasing reaction time (**Figure 5.4D**), fluorination efficiency exhibited a gradual increase and the collection efficiency exhibited an inverse trend (mostly due to volatile activity loss). The resulting crude RCY in DMF (the better performing solvent) exhibited a decrease with time, with a maximum of 15.4 ± 0.9% (n = 4) for a 0.5 min reaction. Though reaction time has not been extensively studied in the literature, longer times seemed to improve the synthesis performance in closed reactors. Ryzhikov *et al.* observed an increase in fluorination efficiency from 39% (n = 1) to 80% (n = 1) when increasing the time from 15 to 30 min(*175*).

Considering the high volatile losses at high temperatures and longer reaction times, we explored additional high boiling point reaction solvents (**Figure 5.4E**), including N-methyl-2-pyrrolidone (NMP), 1,3-dimethyl-3,4,5,6-tetrahydro-2(1H)-pyrimidinone (DMPU), and ethylene glycol, which have been used in other radiosyntheses(*178,179*). Fluorination efficiency and crude RCY were significantly improved using NMP compared to DMF. As a final test we compared the influence of the type of base and phase-transfer catalyst (**Figure 5.4F**) in the reaction solvents DMF, DMSO, and NMP. The best combination was NMP with $TBAHCO_3$; much lower performance was observed with K_{222}/K_2CO_3 and K_{222}/Cs_2CO_3. The optimized conditions (NMP reaction solvent, 240 nmol base ($TBAHCO_3$), and 280 nmol precursor in an 8 µL droplet at 200 °C for 0.5 min) resulted in fluorination efficiency of 37.5 ± 0.8 (n = 4), collection efficiency of 51 ± 1 (n = 4) and crude RCY of 19.1 ± 0.6% (n = 4). Purification via analytical HPLC (**Figure 5.50**) for a batch that had a crude RCY of 18.0% gave an isolated yield of 11.6% (n = 1). Further optimization of purification may lead to modest improvements but was not investigated. Notably, the droplet-based synthesis could achieve useful isolated yields that are only slightly below the isolated yields reported by others (**Table 5.12**) while offering multiple advantages, including completion within only ~35 min (20 min for synthesis and HPLC purification, with an estimated ~15 min needed for formulation(*64*)) instead of 55-80 min (*173–175*), and 100x reduced precursor consumption(*173–175*).

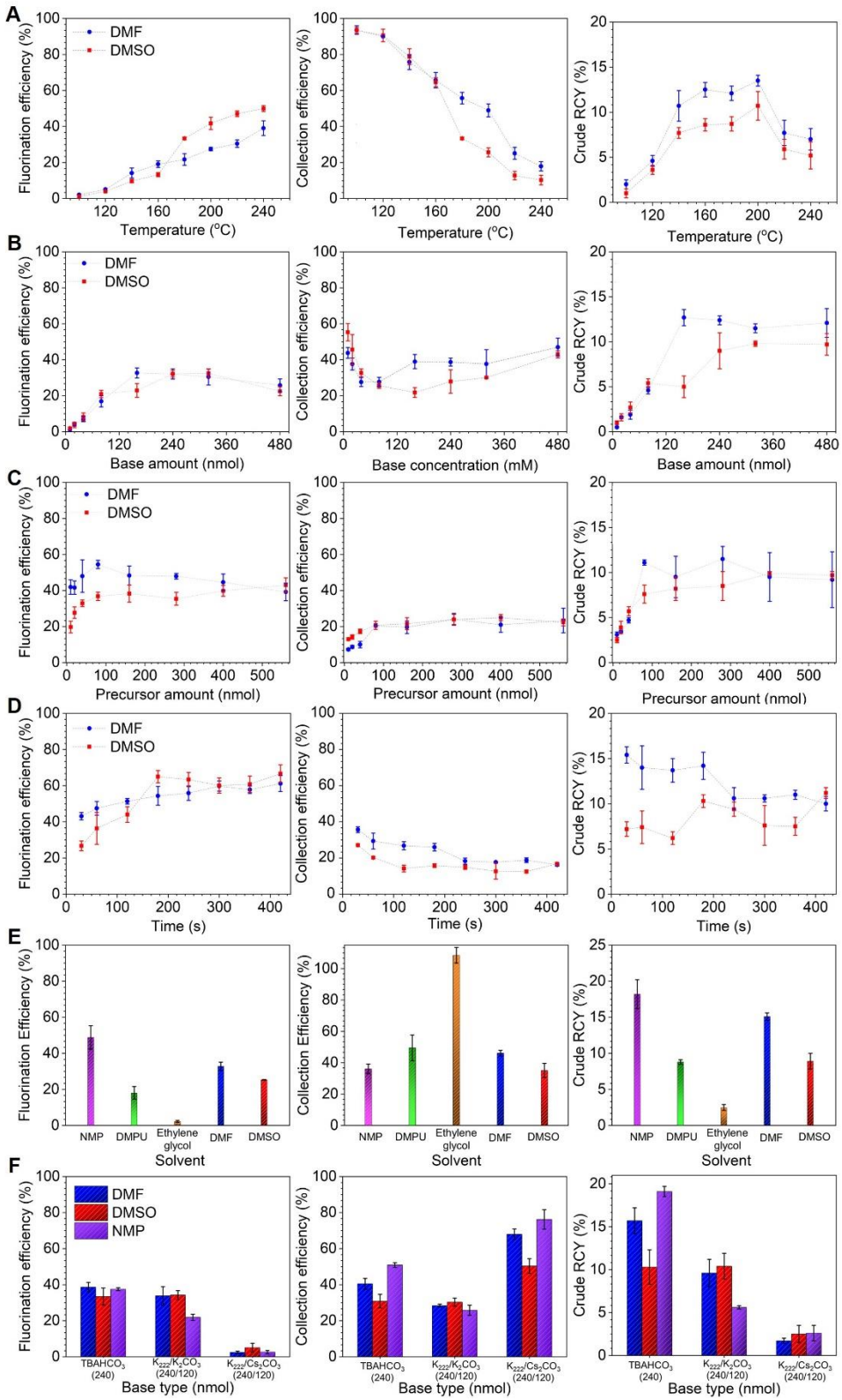

Figure 5. 4 Influence of reaction parameters on the performance of the microdroplet radiosynthesis of [18F]Flumazenil.

For each parameter, influence on fluorination efficiency, collection efficiency, and crude RCY are plotted individually. (A) Effect of temperature (and solvent). Precursor amount: 280 nmol. Reaction volume: 8 µL. Base amount: 480 nmol. Reaction time: 2 min. (B) Effect of amount of base (and solvent). Precursor amount: 280 nmol. Reaction volume: 8 µL. Reaction temperature: 200 °C. Reaction time: 2 min. (C) Effect of precursor concentration (and solvent). Reaction volume: 8 µL. Base amount: 240 nmol. Reaction time: 2 min. Reaction temperature 200 °C. (D) Effect of reaction time (and solvent). Precursor amount: 280 nmol. Reaction volume: 8 µL. Base amount: 240 nmol. Reaction temperature: 200 °C. (E) Effect of reaction solvent. Precursor amount: 280 nmol. Reaction volume: 8 µL. Base amount: 240 nmol. Reaction temperature: 200 °C. Reaction time: 0.5 min. (F) Effect of the base type (and solvent). Precursor amount: 280 nmol. Reaction volume: 8 µL. Base amount: 240 nmol. Reaction temperature: 200 °C. Reaction time: 0.5 min.

5.4.4 Optimization of [^{18}F]PBR06 radiosynthesis

To demonstrate versatility of the high-throughput approach, we next used the platform to perform an optimization of the radiosynthesis of [^{18}F]PBR06. This tracer detects microglial activation by targeting the translocator protein (TSPO) and is used for monitoring treatment response in Huntington's disease(*180*), imaging neuroinflammation, and monitoring tumor progression(*181*). Using the commercially-available tosylate precursor for the radiosynthesis, isolated yields of [^{18}F]PBR06 in the range 30-60% have been reported in literature(*181*,*182*); however, to our knowledge, no studies have been reported on the influence of different reaction conditions on the radiosynthesis performance.

Full details of all parameters we explored (precursor amount, base amount, temperature, reaction time, and type of base / phase transfer catalyst) are included in the **Appendix** on the [^{18}F]PBR06 section. Similarly to [^{18}F]Flumazenil, studies of each parameter were performed in the following two different reaction solvents: DMSO (commonly reported in literature(*181*,*182*)), and a 1:1 (v/v) mixture of thexyl alcohol and MeCN (used in aliphatic radiofluorinations of other tosylate precursors(*24*)). In the study of precursor amount (**Figure 5.5A**), reactions in the mixed solvent showed a rapidly increasing fluorination efficiency with increasing precursor amount, reaching a plateau of ~100% at ~100-200 nmol of precursor, and the collection efficiency was consistently high. The resulting crude RCY increased rapidly as precursor amount was increased, reaching a plateau of 91 ± 4% (n = 4) at 160 nmol of precursor. Interestingly, for reactions performed in DMSO, the trends were similar for precursor amounts below ~100-200 nmol precursor, but for

higher precursor amounts, the fluorination efficiency, collection efficiency, and crude RCY showed gradual to moderate decrease instead of leveling off. Still, the maximum crude RCY using DMSO (86 ± 6%, n = 4) was similar to that obtained using the mixed solvent.

In the studies of base amount (**Figure 5.5B**), fluorination efficiency, collection efficiency, and crude RCY were relatively unaffected, showing only modest reductions when the amount of base was lower than ~150 nmol. The crude RCY was maximal at 240 nmol of base. In the study of reaction temperature (**Figure 5.5C**), the fluorination efficiency was relatively independent of temperature when using the mixed reaction solvent. When using DMSO, the fluorination was highest from 90 – 130 °C. Collection efficiency was consistently high across all temperatures (and for both solvents), and the crude RCY mirrored the fluorination efficiency**.** A temperature of 100 °C was selected. The reaction time (**Figure 5.5D**) had almost no impact, with high crude RCY in all cases except for DMSO at 0.5 min, where the crude RCY was substantially lower. Finally, we found no significant difference when using $TBAHCO_3$ compared to the typically reported phase transfer catalyst K_{222}/K_2CO_3 when using the mixed solvent; however, when using DMSO as the reaction solvent, the fluorination efficiency and crude RCY were slightly lower when using K_{222}/K_2CO_3 compared to $TBAHCO_3$ (**Figure 5.5E**). The results for DMSO were lower overall due to the suboptimal reaction time used in this comparison.

Overall, the optimal conditions (240 nmol of $TBAHCO_3$, 160 nmol of precursor in 8 µL of thexyl alcohol: MeCN (1:1 v/v), 100 °C, 0.5 min) gave a fluorination efficiency of 97.4 ± 0.2% (n = 4) and crude RCY of 94 ± 2% (n = 4). Compared to conventional methods (**Table 5.19**), our optimal conditions were significantly quicker (0.5 vs 15 min reaction time)(*181*) and milder (100 vs 140 °C)(*181*). We performed purification via analytical-scale radio-HPLC (**Figure 5.51**) and obtained an isolated yield of 75.8 % (n=1). Though we did not perform formulation to determine the overall RCY, this compares favorably with the overall RCY values (30-60%) reported in literature(*181*,*182*), consumed 10-30x less precursor(*181*,*182*), and was a shorter synthesis

process (~35min, i.e. 20 min for synthesis and HPLC purification, plus an estimated ~15 min needed for formulation(*64*)), compared to 50 min reported in literature(*182*).

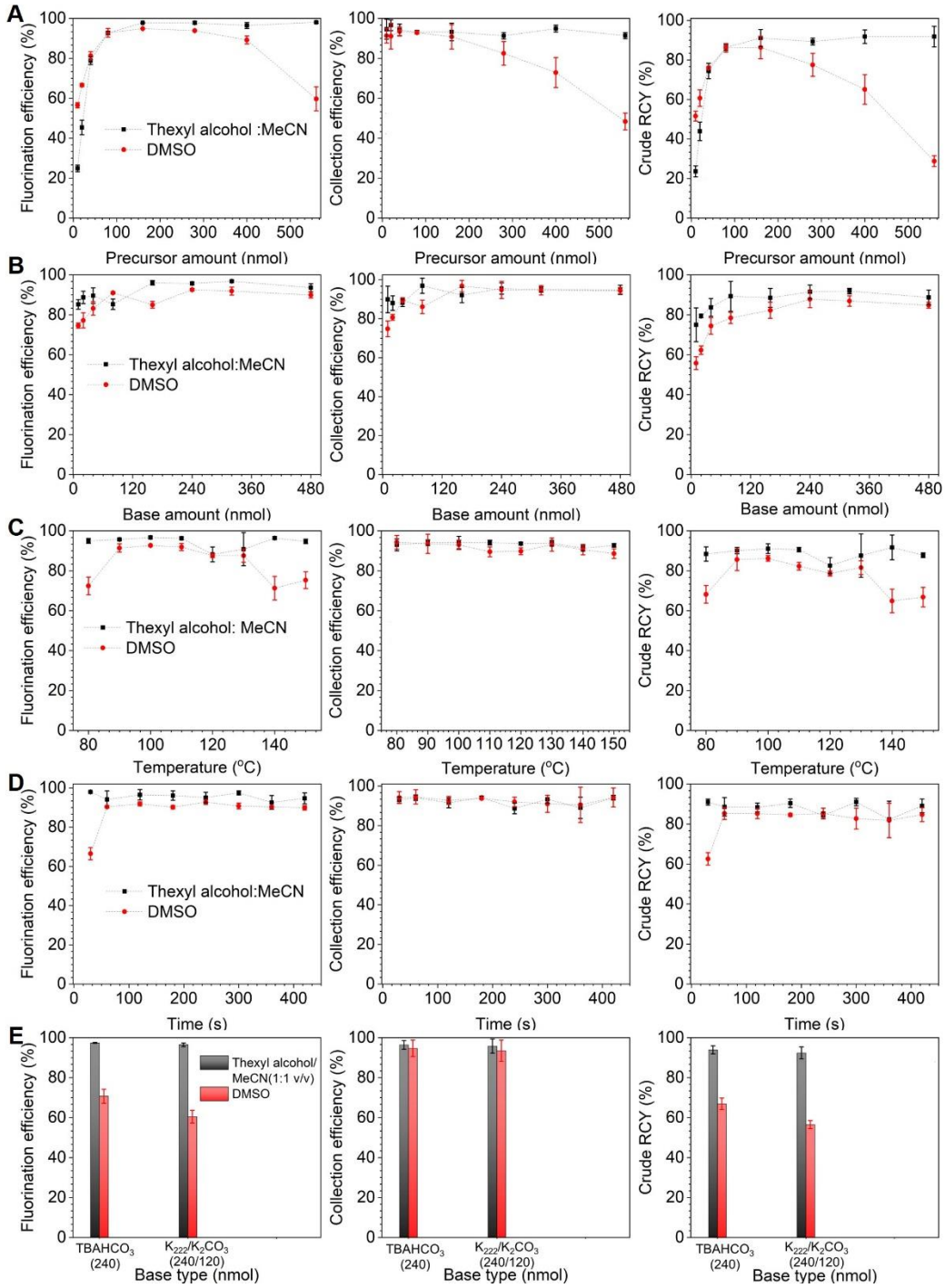

Figure 5. 5 Influence of reaction parameters on the performance of the microdroplet radiosynthesis of [18F]PBR06.

For each parameter, influence on fluorination efficiency, collection efficiency, and crude RCY are plotted individually. (A) Effect of precursor concentration (and solvent). Reaction volume: 8 µL. Base amount: 240 nmol. Reaction time: 5 min. Reaction temperature 100 °C. (B) Effect of amount of base (and solvent). Precursor amount: 160 nmol. Reaction volume: 8 µL. Reaction temperature: 100 °C. Reaction time: 5 min. (C) Effect of temperature (and solvent). Precursor amount: 160 nmol. Reaction volume: 8 µL. Base amount: 240 nmol. Reaction time: 5 min. (D) Effect of reaction time (and solvent). Precursor amount: 160 nmol. Reaction volume: 8 µL. Base amount: 240 nmol. Reaction temperature: 100 °C. (E) Effect of the base type. Precursor amount: 160 nmol. Reaction volume: 8 µL. Base amount: 240 nmol. Reaction temperature: 100 °C. Reaction time: 0.5 min.

5.4.5 Optimization of [^{18}F]Fallypride radiosynthesis

[^{18}F]Fallypride is used to study diseases associated with the dopaminergic system, such as Parkinson's, Huntington's, and Alzheimer's diseases(*74,75*). We previously performed a preliminary study of the droplet synthesis of [^{18}F]Fallypride from the tosylate precursor exploring the impact of the base amount, precursor amount, and reaction volume(*24*). However, with only a single heater operating a single chip, reaction temperature and time could not previously be studied conveniently. Using the expanded capabilities of the multi-heater platform described here, we studied the impact of temperature and reaction time in combination with precursor concentration. Full details are in **Appendix** under the [^{18}F]Fallypride section. As a function of increasing precursor concentration, the fluorination efficiency and crude RCY exhibit a rapid increase from near zero and reach a plateau, while the collection efficiency is consistently high. Surprisingly, nearly identical behavior was observed for reaction temperatures of 95, 110, and 125 °C; but at 80 °C it was evident that a higher precursor concentration was needed to achieve the maximal fluorination efficiency and crude RCY (**Figure 5.6A**). Maximum crude RCY occurred at 110 °C and 39 mM precursor. When examining the combined effect of precursor concentration and reaction time (**Figure 5.6B**), the impact of reaction time was nearly negligible, only leading to discernable differences when the precursor concentration was below ~20 mM. The highest crude RCY (93 ± 5%, n = 2) was obtained when running the reaction at 110 °C for 1.0 min, 240 nmol of $TBAHCO_3$, and 39 mM precursor in 6 µL of thexyl alcohol: MeCN (1:1 v/v). After purification by analytical HPLC (**Figure 5.52**) the isolated yield was 74% (n = 1). The ability to perform a kinetic

study like this in one set of simultaneous experiments is a significant advantage compared to the typical lengthy series of sequential studies with conventional instruments or microfluidic flow chemistry systems(*183–185*). This approach likely also provides more reliable reaction times and temperatures than when repeatedly cooling and opening a single reaction to extract samples at different timepoints(*186*).

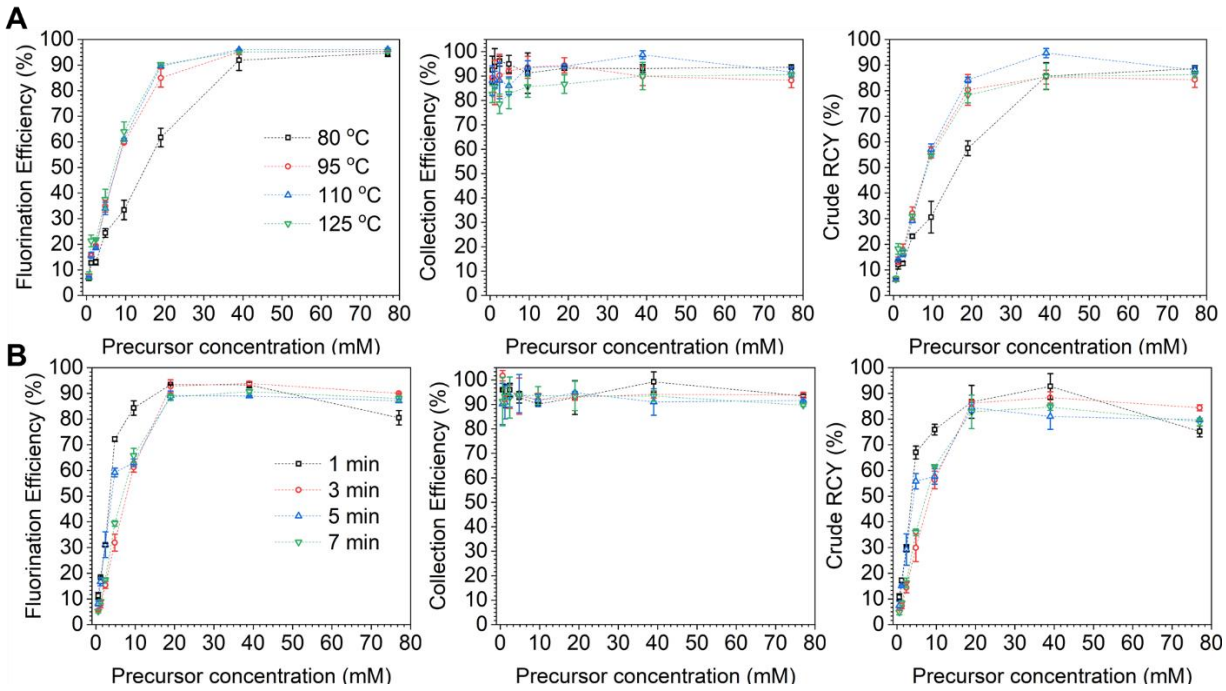

Figure 5. 6 Influence of temperature and reaction time on [18F]Fallypride production.

(A) Investigation of [^{18}F]Fallypride synthesis performance reaction performance as a function of reaction temperature and precursor concentration. Reaction volume: 6 µL. Base amount: 240 nmol. Reaction time: 7 min. Reaction solvent: thexyl alcohol and MeCN (1:1 v/v) (B) Investigation of reaction performance as a function of reaction time and precursor concentration. Reaction volume: 6 µL. Base amount: 240 nmol. Temperature: 110°C. Reaction solvent: thexyl alcohol and MeCN (1:1 v/v).

5.4.6 Optimization of [^{18}F]FEPPA radiosynthesis

As a final example, we performed a very limited optimization of the synthesis of [^{18}F]FEPPA, a radiopharmaceutical that has been used in several pre-clinical and clinical settings in recent years(*187–191*) to look at the overexpression of TSPO, which is known to be associated with a variety of neurodegenerative disorders. With the aid of the high-throughput platform to explore the influence of temperature (**Appendix**), we translated the synthesis into droplet format to

leverage the advantages of small-volume reactions. We started with conditions similar to past droplet studies for other tracers using tosylate precursors. Since literature reports include a range of 9 to 45 mM precursor concentration(*187–189,192*), we chose an initial value of 30 mM. As a function of increasing temperature (**Figure 5.7**), the fluorination efficiency was ~10% at 60 °C and sharply increased to reach a plateau after 90 °C. The collection efficiency was consistently high at all temperatures, and the resulting crude RCY showed a similar trend to the fluorination efficiency. The highest crude RCY (77 ± 2%, n = 4) was observed at a temperature of 110 °C for 2.0 min, 30 mM precursor in 8 µL of thexyl alcohol: MeCN (1:1 v/v) solvent and 240 nmol of base ($TBAHCO_3$). Compared to literature methods (**Table 5.23**), the reaction time is shorter (2 min vs 10 min(*187–189,192*)), the droplet reaction consumes 40-50x less precursor, and the overall synthesis is shorter and has higher yield(*187–189,192*). A batch was purified by analytical-scale HPLC (**Figure 5.53**) and the collected fraction was diluted (1:3, v/v) with 9 mM $NaHCO_3$ to produce an isotonic solution appropriate for injection containing 440 MBq [12 mCi], sufficient for multiple preclinical studies. The overall 30 min synthesis had an RCY of 67% (n = 1).

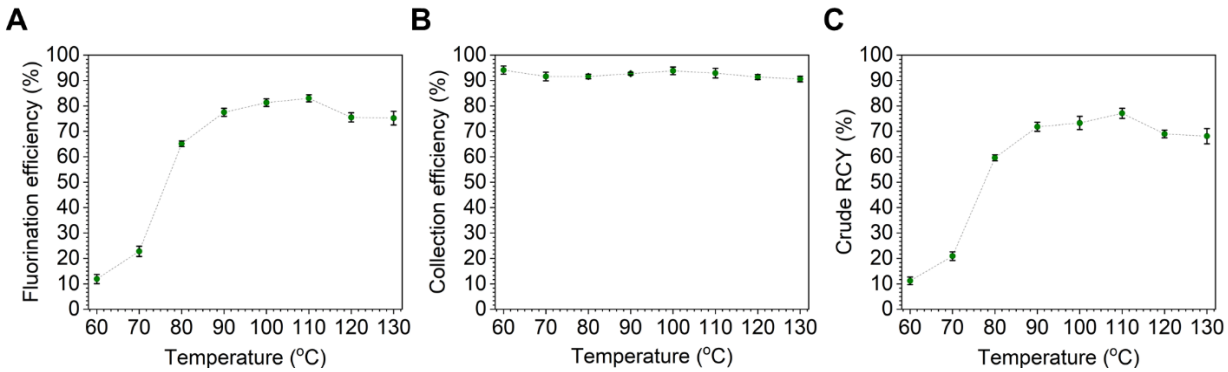

Figure 5. 7 Effect of temperature on the performance of [18F]FEPPA synthesis. Reaction volume: 8 µL. Base amount: 240 nmol. Precursor amount: 240 nmol. Reaction time: 2 min. Reaction solvent: thexyl alcohol and MeCN (1:1 v/v).

(A) Effect on fluorination efficiency. (B) Effect on collection efficiency. (C) Effect on crude RCY.

5.4.7 Clinical-scale radiosynthesis

The optimization experiments in this work were performed with ~14 MBq [0.38 mCi], where each reaction often yielded enough product for multiple mouse scans(*193,194*). Nevertheless, we wanted to explore whether one of the optimized compounds ([^{18}F]PBR06) could be scaled to clinically-relevant levels without changing any reaction conditions other than the amount of starting radioactivity. We've previously reported that significant scale-up is possible for [^{18}F]Fallypride (7.2 GBq demonstrated)(*62*), as well as O-2-[^{18}F]fluoroethyl-L-tyrosine ([^{18}F]FET) and [^{18}F]Florbetaben (up to 0.8 GBq demonstrated for each)(*63*). Experiments with increasing starting activity up to 3.2 GBq (86 mCi) are described and shown in the **Figure 5.54**. While the crude RCY showed a slight reduction as starting activity increased due to a decrease in fluorination efficiency, the final quantities after purification and formulation would still be sufficient for several clinical doses.

These results reinforce the ability to optimize small-scale reactions in a high-throughput fashion using the platform described here, and then scale up the starting activity to increase the output of a droplet radiosynthesis. In fact, the starting activity itself could be varied as a reaction parameter and studied with high throughput using the platform described in this paper. Studies are currently underway in our laboratory to explore in more detail how scale-up influences the performance.

5.4.8 Comparison to other optimization approaches

With the platform presented here for performing parallel radiosyntheses in droplet format, we were able to rapidly and conveniently study the influence of various reaction parameters to obtain a detailed map of conditions that influence the synthesis performance. Each radiopharmaceutical synthesis could be extensively investigated (100s of data points) in a few days, requiring only a few batches of radioisotope. In total, for the four example compounds, 820 experiments were completed in 15 experiment days, with an average of 55 reactions per day. While the maximum number of experiments completed in a single day was 64, it is probably feasible to increase this

number to ~96. The limiting factor is the tedious manual adding of reagents, collecting crude products, and performing TLC analysis. An automated platform for high-throughput experimentation is currently being developed, which could address these issues and perhaps increase reaction throughput further while also reducing radiation exposure and the chance for human error(*195*). Performing many reactions per day saves on total time (and thus labor and other costs) for optimization and requires far fewer batches of radioisotope, significantly reducing radioisotope production and/or purchase and shipping costs. Importantly, since day-to-day variation such as radioisotope quality or reagent preparation can sometimes also affect results(*196*), reducing the total number of experimental days (and radioisotope batches) also reduces the confounding effects of this variability. Furthermore, using small-scale droplet reactions (i.e., 6-8 µL) compared to conventional reactors (0.5-2.0 mL), reagent usage per datapoint was reduced by ~10-100x. The total amount of precursor consumed was only 30 mg for 355 data points for [^{18}F]Flumazenil, 20 mg for 296 data points for [^{18}F]PBR06, 6 mg for 128 data points for [^{18}F]Fallypride, and 4 mg for 32 data points for [^{18}F]FEPPA. These amounts are equivalent to just 12 macroscale reactions for [^{18}F]Flumazenil (5 mg each), 6-7 for [^{18}F]PBR06 (3 mg each), 3 for [^{18}F]Fallypride (2 mg each), and one for [^{18}F]FEPPA. Moreover, the amount of product activity in some cases is sufficient for *in vitro* or pre-clinical *in vivo* imaging studies. This could be a tremendous advantage for new radiotracer development where the precursor is in short supply. The droplet platform allows the possibility of performing both optimization and initial preliminary biological studies in the shortest time using only a few mg of precursor.

Aside from conventional radiosynthesizers, rapid and economical optimizations have also been performed using continuous-flow microfluidic platforms. Small boluses of reagents (10s of µL) are reacted sequentially under different conditions(*53,197*) (up to 25 experiments per day have been reported(*153*)). While convenient for studying the influence of residence time, reactant concentrations and ratios (via changes in relative flow rates), and reaction temperature, varying

other conditions (e.g. solvent) is cumbersome, requiring manual intervention and cleaning procedures for each change. In addition, some aspects (e.g. [^{18}F]fluoride drying conditions) cannot be explored in a high-throughput fashion since they are performed outside the flow-chemistry workflow. Droplet reactors are suitable for studying all of these variables and can perform reactions in parallel rather than sequentially. An additional advantage of optimization using droplet reactions is that the multi-heater platform is compact (120 x 120 x 100 mm^3), allowing operation in a small part of a hot cell or mini-cell. Its low weight (~900 g) makes the system portable and easy to move in and out of a hot cell and occupies space only when optimization efforts are needed. In contrast, conventional radiosynthesizers and flow chemistry systems are typically much larger and integrated into infrastructure (gases, vacuum) and cannot easily be moved.

A unique feature of the open microdroplet system is the convenience of visualizing and quantifying the radioactivity distribution on the chip surface via Cerenkov imaging at different stages of the synthesis process. This information enables a more comprehensive assessment of the performance of each step. While some macroscale systems include radiation detectors near reaction vessels and cartridges that enable straightforward activity measurements on these components to help pinpoint losses(*129*), other systems require removing / disassembling components to make activity measurements, which may be infeasible or inconvenient and increases radiation exposure. In comparison, this data can be readily gathered in parallel for many reactions at once in our high-throughput approach, saving significant time, reducing radiation exposure, and reducing the chance for errors.

On the other hand, a limitation of this approach is that the open droplet format had significant volatile losses for some syntheses. While volatile losses were very low for [^{18}F]PBR06, [^{18}F]Fallypride, and [^{18}F]FEPPA in droplet format (as well as many other tracers(*31,51,64*)), losses were significant for [^{18}F]Flumazenil and were found to occur during the radiofluorination step. In

contrast, in macroscale systems, the reactor is usually closed for the duration of the reaction, and losses during this step are generally likely to be lower. Of course, both droplet systems and conventional systems can exhibit volatile losses at other stages of the radiosynthesis process, such as during solvent evaporation steps. Despite the volatile loss, meaningful and repeatable experiments could still be performed. Moreover, the isolated yield for [^{18}F]Flumazenil (which had substantial volatile loss) was only slightly below the range of isolated yields (before formulation) reported by others, suggesting that loss of the volatile species was not very detrimental to the overall reaction performance, or perhaps that the reaction loss was offset by other improvements (e.g. perhaps the use of an analytical instead of semi-preparative HPLC column reduced the degree of purification loss). Of course, the volatile losses present a hazard that needs to be mitigated by operation of the system within an appropriate hot cell.

While studies here were performed using a one variable at a time (OVAT) method, further optimization efficiency improvements might be achieved by integrating concepts like the design of experiments (DoE)(*196*) and reaction modeling. In addition to the reactions optimized here, the droplet format is compatible with other ^{18}F-labeled radiopharmaceuticals(*51,52,64,65*). It can likely be used with other isotopes, including radiometals. Although designed for operation in a radiochemistry laboratory, the platform could possibly also be used for reagent-economical optimization of a wide range of chemical reactions outside the field of radiochemistry. Recently, several new platforms and techniques have been reported for performing screening of organic reactions in volumes of 1.5 –100 µL(*169,170*), and our platform could provide an enhanced ability to vary reaction temperatures and times for different simultaneous reactions.

5.5 Conclusion

In this work, we have developed a platform for radiosynthesis optimization relying on droplet-based reaction arrays that enables many reactions (up to 64) to be performed in parallel, each with minimal reagent consumption. Combined with high-throughput analysis methods(*128*), it is

practical to perform hundreds of experiments in a matter of days. While similar in throughput to flow-chemistry-based optimization methods(*198*), this platform allows studies of all stages of the synthesis process, including [^{18}F]fluoride drying/activation, and it has been shown in previous work that the chips are also compatible with optimization of reactions having at least 2 synthetic steps(*52,64*). It also allows reaction solvent and reagent amounts to be readily varied without the constraints of flow-based systems. Finally, product amounts can be scaled up after optimization by varying the starting activity.

As examples, we used the platform to perform the rapid optimization of the production of [^{18}F]Flumazenil, [^{18}F]PBR06, [^{18}F]Fallypride, and [^{18}F]FEPPA from their commercially-available precursors. Using the platform, a series of syntheses using different conditions (85 for [^{18}F]Flumazenil, 74 for [^{18}F]PBR06, 64 for [^{18}F]Fallypride, and 8 for [^{18}F]FEPPA), spanning 6 different reaction parameters, were performed. Replicate studies were performed for each condition and the small standard deviation computed for each set of replicates indicated that the platform has high reproducibility. For [^{18}F]Flumazenil, the observed trends were comparable to optimization studies performed using conventional radiosynthesizers. For other tracers there is limited optimization data in the literature.

This platform conveniently brings the power and efficiencies of high-throughput experimentation to the field of radiochemistry. It could find use in: (i) rapid refinement and optimization of radiosynthesis protocols for existing or novel radiopharmaceuticals, (ii) translation of known macroscale protocols into droplet format, and (iii) studies of novel labeling methods. The high throughput platform allows exploration of many more reaction conditions within the available parameter space, which can potentially lead to discovery of favorable reaction conditions that might not otherwise be attempted with conventional methods due to time, cost, and low throughput. The small amount of precursor required for each reaction is a crucial advantage, particularly in the early stages of novel radiopharmaceutical development where only a small

amount of the starting material may be available; the high-throughput platform enables the development of syntheses within a short timeframe at low cost.

5.6 Appendix

5.6.1 Multi-heater platform

The platform was assembled as described in the manuscript from the following components: ceramic heaters (Ultramic CER-1-01-00093, Watlow, St. Louis, MO, USA), , epoxy glue (JB weld, Sulphur Springs, TX, USA), calcium silicate thermal insulation material (McMaster-Carr; Atlanta, GA), 3D-printed nylon piece (Fictiv Inc., San Francisco, CA, USA), DC fans (Sanyo Denki model 9GV3612G301), thermocouple amplifier board (AD8495 Breakout Board, Adafruit, New York, NY, USA), data acquisition module (DAQ; NI USB-6003, National Instruments, Austin, TX, USA), and solid-state relay (SSR, Model 240D05, Sensata-Crydom). Thermal paste (OT-201-2, OMEGA, Norwalk, CT, USA) was used to enhance thermal conductivity between the heaters and the multi-reaction chips.

Figure 5.8 shows a photograph of the entire platform composed of the high-throughput microdroplet apparatus and a separate control box (250 mm x 204 mm x 200 mm) that can be placed outside the shielding or hot cell. CAD models of the platform will be provided upon request.

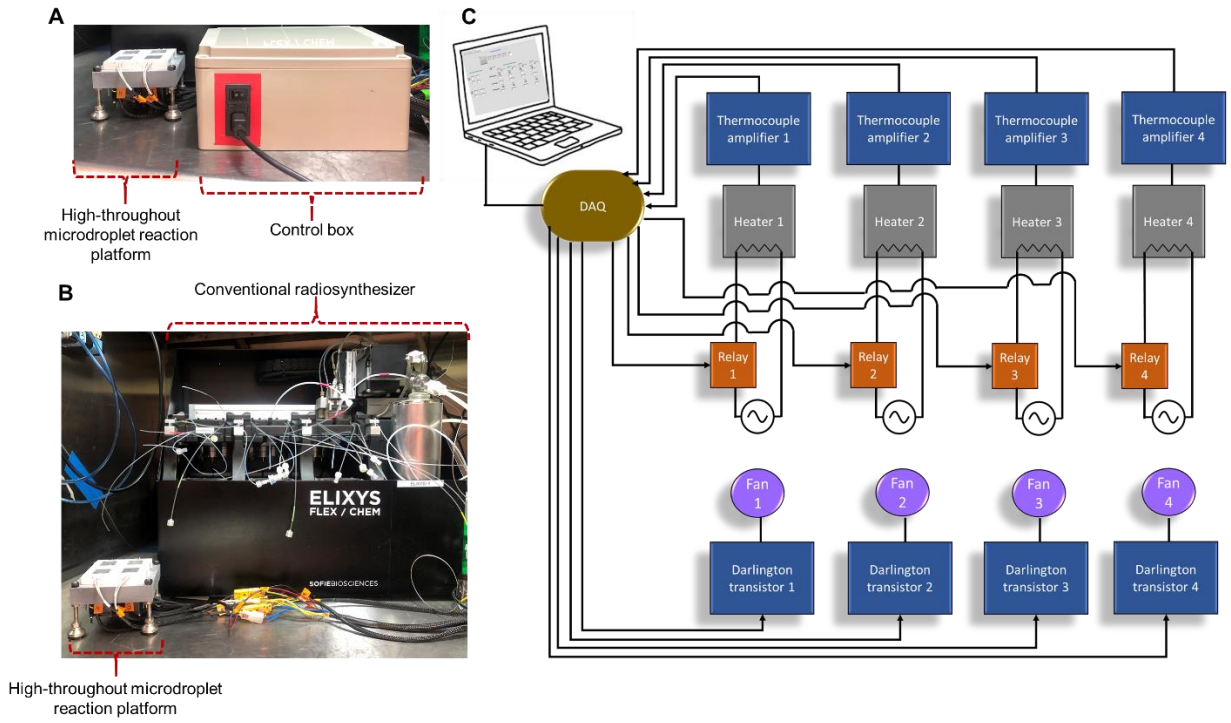

Figure 5. 8 High-throughput microdroplet reaction platform

(A) Photograph of fully assembled high-throughput apparatus with control box inside a hot cell. (B) Photograph with control box located outside the cell to illustrate the small system footprint compared to a conventional radiosynthesizer (ELIXYS, Sofie, Inc., Culver City, CA, USA). C) Electronic wiring diagram of the high-throughput platform.

5.6.2 Thermal simulations

To prevent thermal crosstalk between heaters (i.e., one heater affecting the temperature of a neighboring heater), the heaters were mounted to a frame made of thermally insulating material. Two different types of thermal insulation were explored: Thermo-12 Gold (Johns Manville, Brunswick, GA, USA) and Firetemp – X (Johns Manville). We chose to use Firetemp-X as it could be readily machined, in contrast to Thermo-12 Gold, which we found too flaky and fibrous. To understand if the spacing of the heaters (19.3 mm gap) was enough to prevent thermal crosstalk, thermal modeling was performed on a simplified CAD model of the platform using Solidworks (Dassault Systems, Vélizy-Villacoublay France) with the Solidworks Simulation add-in. The model includes the thermal insulation frame and the heaters. The heaters were modeled as aluminum nitride blocks having a thermal conductivity of 285 W/m-K. The frame was modeled as Firetemp–X; according to manufacturer specifications, the thermal conductivity of this material depends on

operating temperature, so we chose a value of 0.094 W/m-K, which corresponds to an estimated operating temperature range of 60-150°C. The model included a thin layer (200 μm) of JB Weld epoxy between the heaters and insulating material, with thermal conductivity of 0.2 W/m-K. A thermal resistivity value of the interface between the heater and the insulation was set to be 0.001 m^2K/W. This value is derived from both the thermal conductivity of the epoxy and the contact area (allowing for heat transfer) of the heater and insulating material. Bulk ambient temperature and starting temperatures in the model were set to 298 K, and the convective coefficient for stagnant air was modeled as 25 W/m^2-K. A convection boundary condition using the convective coefficient listed above was applied to all outward-facing surfaces. Each heater was defined to have a heater power of 150 W. A high-quality mesh was applied to the model resulting in 17239 nodes and 9796 total elements.

A simple steady-state thermal simulation was performed to analyze the overall temperature distribution of the construct with each of the four heaters set to different temperatures. The resulting temperature distribution from the simulation can be seen in **Figure 5.9.**

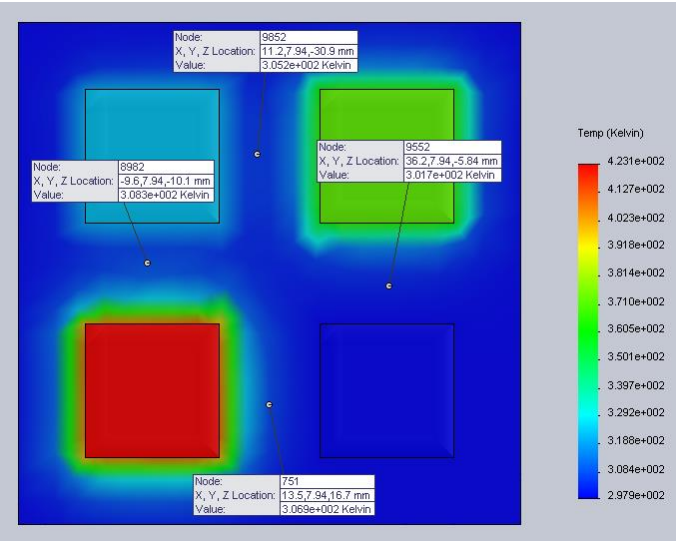

Figure 5. 9 Temperature influence from heater to heater.

Steady-state temperature distribution of the four-square heaters mounted in the insulating construct, with setpoints of 323, 373, 298, and 423 K (clockwise, starting at top left). The annotated probe points represent approximate midpoints between adjacent heaters.

The simulation shows that with the designed spacing, heaters are not affected by their neighbors, even for the room temperature (298 K) heater operated adjacent to the hottest (423 K) heater. When probing the insulating material between different pairs of heaters, the highest temperature increase at the midpoint was 10.3 K (between 423 K and 323 K heaters), and the lowest was 3.7 K (between 373 K and 298 K heaters). The temperature change of the insulating material right near the edge of the heater set to 298K was zero confirming adequate insulation of the heater from neighboring heaters

The model results were verified empirically on the heating platform through thermal imaging. The heaters on the heating platform were set to different temperatures, and the system was allowed to reach a steady-state. In this study, heaters 1 to 4 (i.e., counterclockwise, starting from the top right) were set to 373K, 323K, 413K, and 305K, respectively. The thermal IR plot can be seen in **Figure 5.10**. Positions probed between adjacent heaters on the insulating material show a maximum increase of 5.1 K compared to the temperature of the heater set to the lowest temperature (305 K), suggesting that the insulating material can adequately prevent thermal crosstalk.

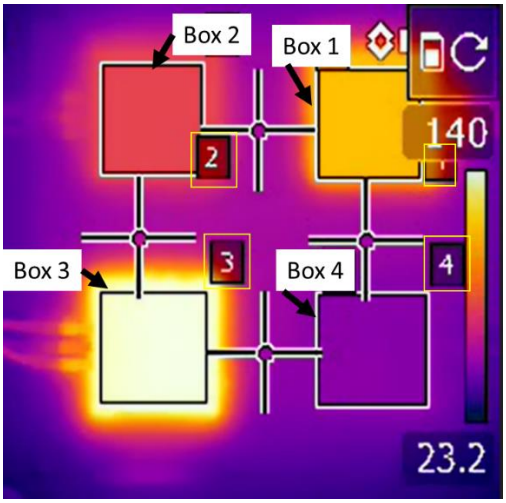

Figure 5. 10 Thermal image of the heater platform.

Box 1 through 4 corresponds to areas within heaters 1 through 4. Locations of spot probes between heaters are also shown.

Following the initial steady-state simulation, a transient simulation was performed to estimate the cooling time required for the system to reach room temperature. The model was set up similar to that of the static heating model mentioned above with some minor modifications. The transient model was performed over 600 s with a 1 s step size. Different simulations were performed using different starting temperatures (413 K, 373 K, 323 K) applied to all heaters. The bulk ambient temperature was set to 298 K. To mimic active cooling using fans, a convective coefficient of 200 W/m^2-K was applied to all surfaces in contact with the cooling airflow. The surfaces are highlighted in **Figure 5.11** by the green cones**.** All the other exposed surfaces were set with a convective coefficient for stagnant air modeled as 25 W/m^2-K. A solid mesh was applied consisting of 21594 nodes and 12641 elements.

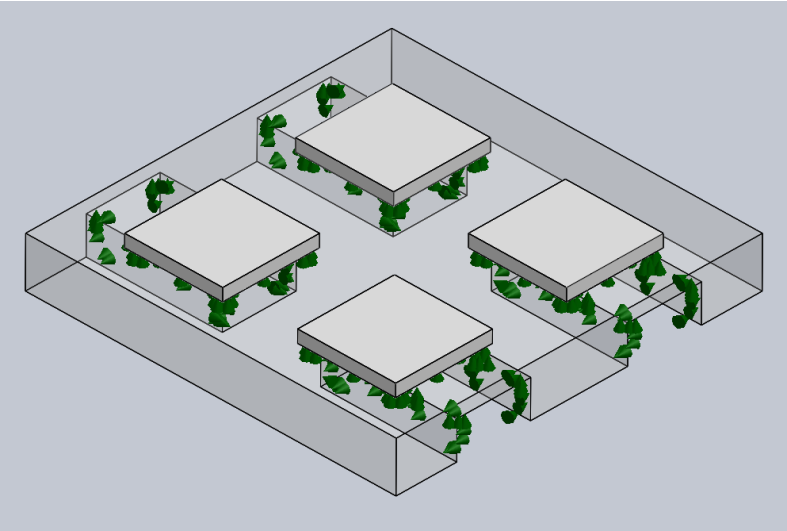

Figure 5. 11 CAD model of the insulating material with embedded heaters.
The green cones indicate the surfaces affected by active fan cooling.

For each simulation, temperature readings positioned at the center of each heater were measured as a function of cooling time. Due to symmetries in the geometry, all heaters behaved identically. Cooling temperature profiles for heater 1 as a function of different starting temperatures can be seen in **Figure 5.12**. The required cooling time (to 303K) decreases as we decrease the starting temperature. For starting temperatures of 413K, 373K, and 323K, the

cooling times were 108 s, 93 s, and 55 s, respectively. Empirical performance (presented in the main paper) was found to have a slower cooling time than the simulation.

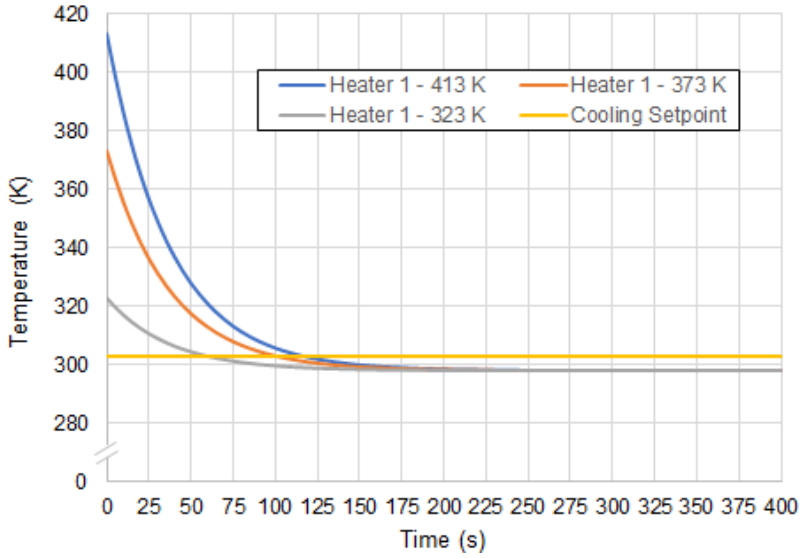

Figure 5. 12 Simulated cooling temperature profiles as a function of time for different starting temperatures.

The cooling setpoint temperature is plotted as a yellow line to visualize better when this setpoint temperature has been reached.

5.6.3 Heater calibration and characterization

We initially performed a 2-point linear calibration of thermocouple signal versus temperature by submerging each heater in 2 different water baths (ice water: 0°C; boiling water: 100°C) and measuring the output voltage from the corresponding thermocouple amplifier. Water baths were prepared in 500 mL glass beakers with stir bars, and the temperature was measured independently with a calibrated digital thermometer (53 II B, Fluke, Everett, WA, USA). The temperature stability of the heaters was assessed by setting each heater to a set temperature (50, 100, and 140 °C) and observing the integrated thermocouple measurement for 5 min (**Figure 5.13**). Temperature data were recorded every 0.5 s using the DAQami program (National Instruments) and plotted to examine the heating rate, cooling rate, and temperature stability at the setpoint.

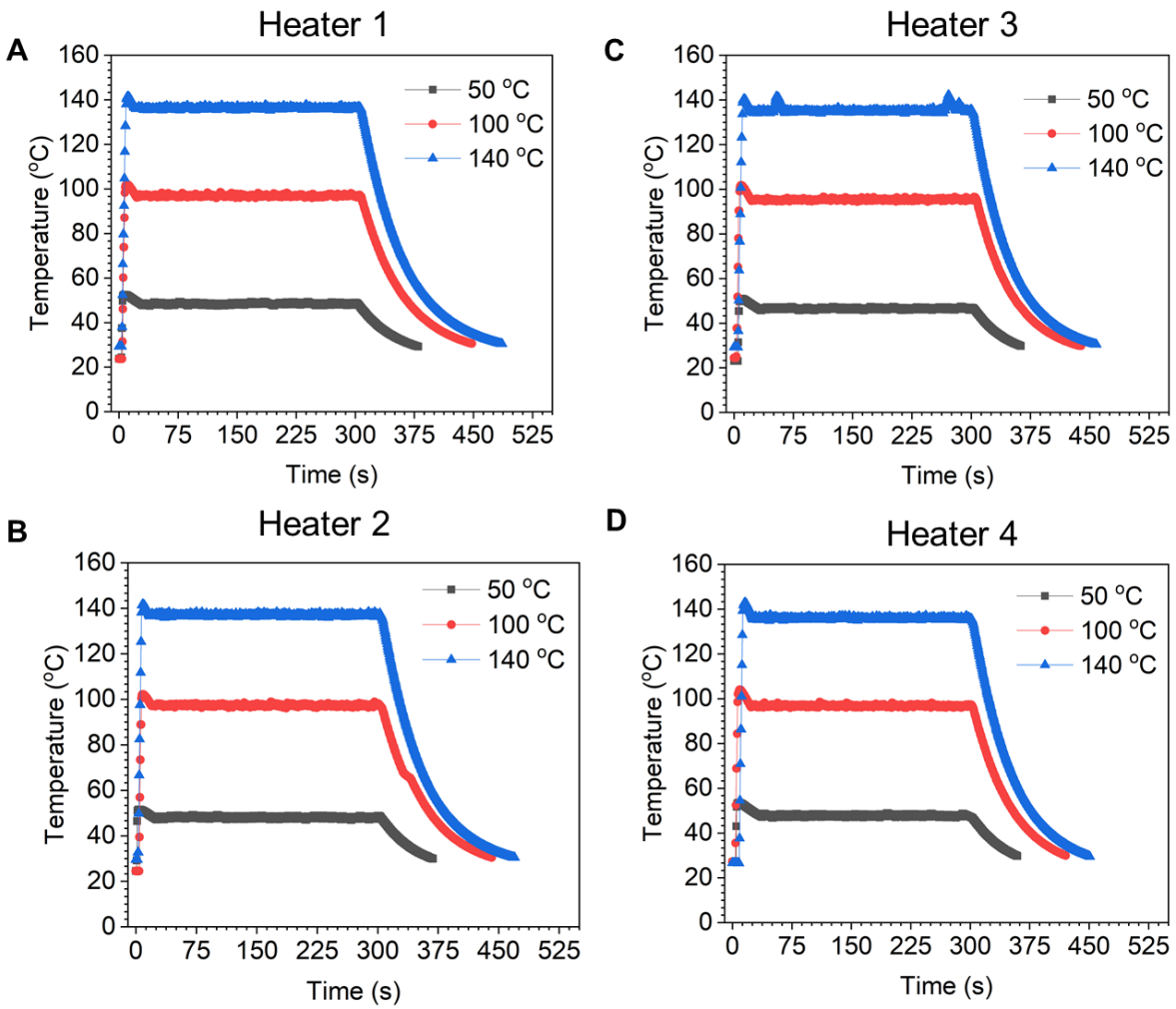

Figure 5. 13 Temperature stability of the four heaters at three different temperatures.

In each case, the heater was activated, and once it reached the setpoint, it was maintained at that temperature for 5 min, followed by forced-air cooling. (A) Heater 1; (B) Heater 2; (C) Heater 3; (D) Heater 4.

To improve accuracy, a 3-point linear calibration was later performed using a thermal camera (T440-25, FLIR, Wilsonville, OR, USA) to measure the average temperature on the heater surfaces (set at 50, 100, 140 °C, using the original calibration). For each thermal image, the temperature was allowed to stabilize for 5 min before recording the image. The spatial uniformity of temperature distribution was assessed via thermal imaging after this final calibration. **Table 5.2** shows the average thermocouple reading and standard deviation for the plots in **Figures 5.14** and **Figure 5.15**. Average and standard deviation were computed from the 5 min region where

the temperature had stabilized. All heater temperatures exhibited a standard deviation of <1 °C over time.

Table 5. 2 Average heater temperatures during 5 min heating.

	Average ± standard deviation (°C)				
Setpoint (°C)	**Heater 1**	**Heater 2**	**Heater 3**	**Heater 4**	**All Heaters**
50	48.5 ± 0.4	48.1 ± 0.5	46.6 ± 0.5	47.9 ± 0.6	47.8 ± 0.8
100	97.0 ± 0.5	97.4 ± 0.5	95.4 ± 0.4	96.9 ± 0.5	96.7 ± 0.9
140	136.3 ± 0.5	137.1 ± 0.5	135.5 ± 1.4	136.0 ± 0.5	136.2 ± 0.7

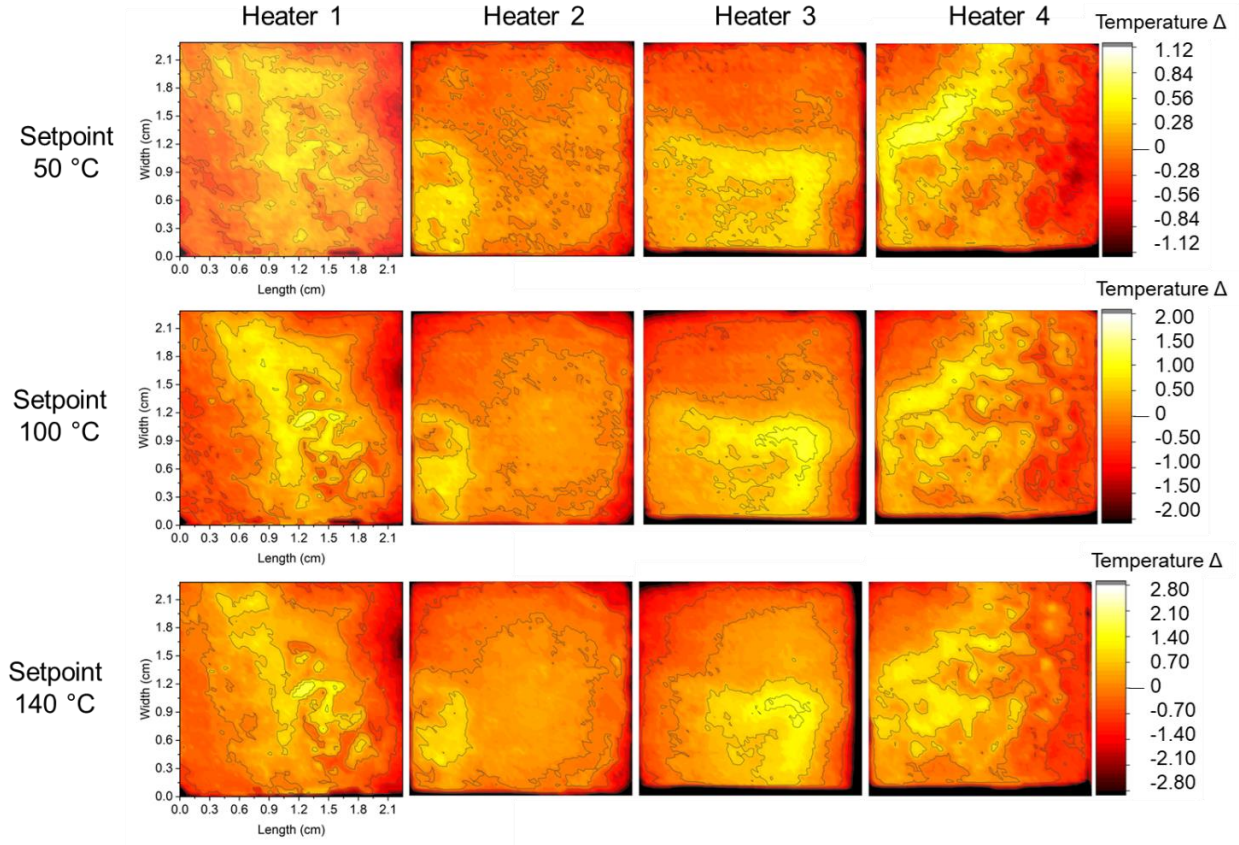

Figure 5. 14 Thermal images of all four ceramic heaters (columns) surface at three different temperature setpoints (rows).

The color represents the deviation of each pixel from the mean temperature. The dark areas show the pixels that deviate by >2% from the mean.

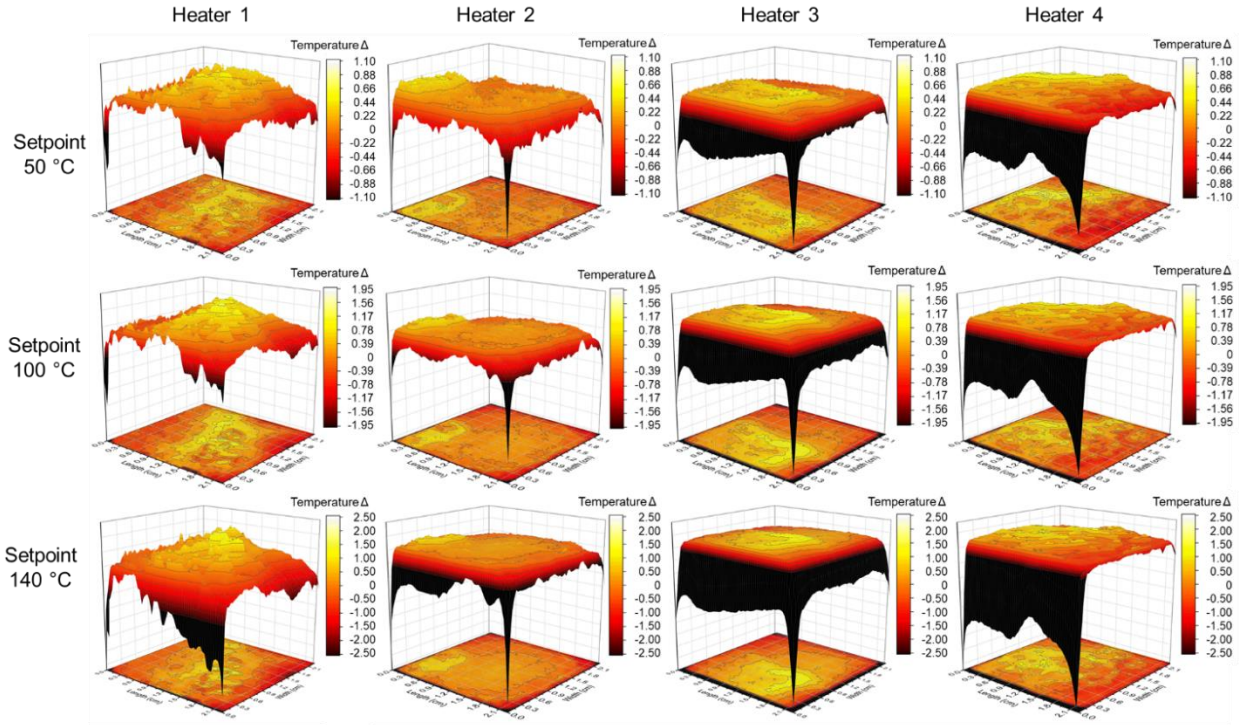

Figure 5. 15 The same data as Figure 5.14 was replotted in 3D to provide a different illustration of uniformity.

Regions of the heater with deviations >2% were considered to be unusable. **Table 5.3** summarizes the size of unusable regions of each heater at different set temperatures. The maximum width of the unusable region was 1.5 mm across all heaters and temperature setpoints. The maximum fraction of unusable heater surface was 8.3% (always at the edges).

Table 5. 3 Summary of unusable regions of heaters, defined as areas where temperature value deviated >2% above or below the mean temperature of each heater (computed from thermal images).

	Unusable fraction of heater area (%)				Max. width of unusable area (mm)			
Setpoint (°C)	**Heater 1**	**Heater 2**	**Heater 3**	**Heater 4**	**Heater 1**	**Heater 2**	**Heater 3**	**Heater 4**
50	0.27	0.43	3.88	4.01	0.38	0.38	0.76	1.15
100	0.33	0.98	6.85	3.90	0.38	0.38	1.15	1.14
140	1.01	2.81	8.27	4.89	0.38	0.76	1.52	1.52

Since the maximum width of the unusable region was 1.5 mm, we designed the multi-reaction chips such that the outermost 2.4 mm border was unused, and all reaction sites were entirely located within the usable portion of the heater surface. **Figure 5.16** shows the detailed chip design. Chips are installed onto the heater platform in the orientations shown in **Figure 5.17.**

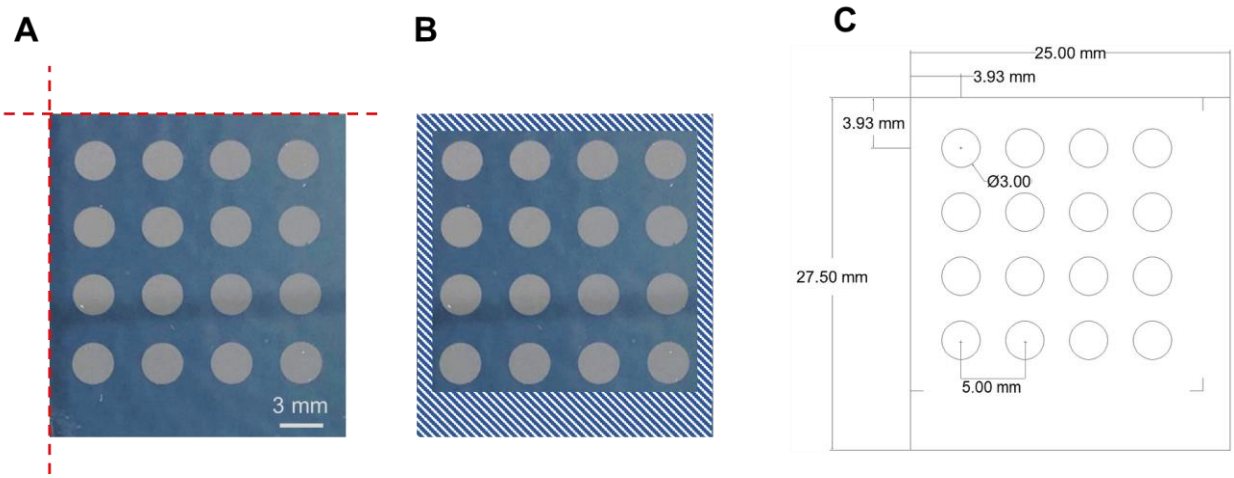

Figure 5. 16 Chip dimensions.

(A) Photograph of the chip with 16 reactions sites. The chip is made from silicon coated with Teflon AF, and then the Teflon AF layer is etched away in the circular regions. (B) The hatched region shows the unusable region of the chip (due to >2% temperature deviation from the mean temperature of the heater in these regions). (C) Detailed chip design.

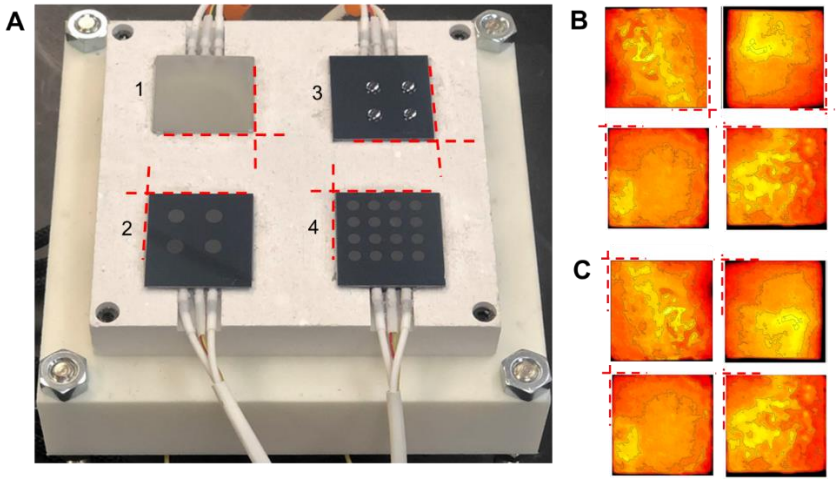

Figure 5. 17 Chip positioning on heaters.

(A) Orientation of heaters. Red dashed lines indicate the reference corner for the alignment of chips to heaters. (B) Example thermal images from heater surfaces, shown in the actual heater orientation. (C) Thermal images in this paper are all rotated such that reference corner is located at the top left of each image.

5.6.4 Radio-TLC Methods

In order to use high-throughput radio-TLC for analysis of [^{18}F]Flumazenil, we first investigated different types of TLC plates (normal and RP-18 versions of silica gel 60 F_{254}, Merck KGaA Darmstadt, Germany) and mobile phases from literature(*145,146,173,175*) (**Figure 5.18**). Crude samples were prepared in DMSO:water (2:1 v/v), and 1 μL samples were deposited on the TLC plates. Bands were identified by comparing their R_f values with the R_f values for samples of isolated (via HPLC purification) product. The best separation between [^{18}F]fluoride, [^{18}F]Flumazenil, and an unknown impurity was achieved using (normal) silica gel 60 F_{254} plates with 100% MeCN as the mobile phase. Due to the proximity of the impurity to the product under several conditions, it is possible that the bands might not be well resolved using some readout methods such as conventional radio-TLC scanners. When using DMSO as the reaction solvent, [^{18}F]Flumazenil samples exhibited up to 3 bands: [^{18}F]fluoride (R_f = 0), [^{18}F]Flumazenil (R_f = 0.7), and an unknown impurity (R_f = 0.9), but while using DMF, only 2 bands were observed: [^{18}F]fluoride (R_f = 0) and [^{18}F]Flumazenil (R_f = 0.8), with no impurity evident (also not observed using radio-HPLC).

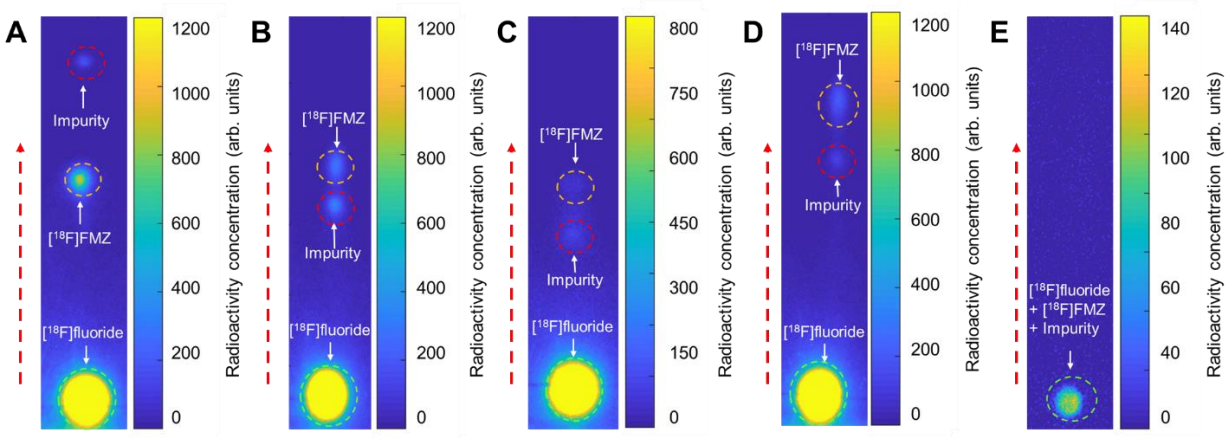

Figure 5. 18 Development of radio-TLC separation method for crude [18F]Flumazenil ([18F]FMZ).

(A) Silica gel 60 F_{254} plate with mobile phase of 100% MeCN. (B) Silica gel 60 F_{254} plate with mobile phase of ethyl acetate: ethanol (80:20 v/v) as reported in Ryzhikov *et al.*(*175*). (C) Silica gel 60 F_{254} plate with mobile phase ethyl acetate: ethanol: water (80:15:5 v/v) as reported in Vaulina *el al.*(*145*) and Nasirzadeh *et al.*(*146*). (D) RP-18 silica gel 60 F_{254} plate with mobile phase ethyl acetate: ethanol (95:5 v/v) as reported in Mandap *et al.*(*173*). (E) RP-18 silica gel 60 F_{254}

plate with mobile phase MeCN: water (90:10 v/v). Dashed circles represent the ROIs for analysis. The dashed arrow represents the direction of solvent flow during development.

[^{18}F]PBR06 samples were spotted on silica gel 60 F_{254} plates and separated using 13:10:24:54 (v/v) dichloromethane:chloroform:acetone:hexanes as the mobile phase. Chromatograms exhibited up to 2 bands: [^{18}F]fluoride (R_f = 0) and [^{18}F]PBR06 (R_f = 0.4). [^{18}F]FEPPA samples were spotted on silica gel 60 F_{254} plates and separated using 25.6:37.5:36.5:0.4 (v/v) nBuOH:THF:hexanes:TEA as the mobile phase. Chromatograms exhibited up to 2 bands: [^{18}F]fluoride (R_f = 0) and [^{18}F]FEPPA (R_f = 0.6). **Figure 5.19** shows example TLC images confirming the separation.

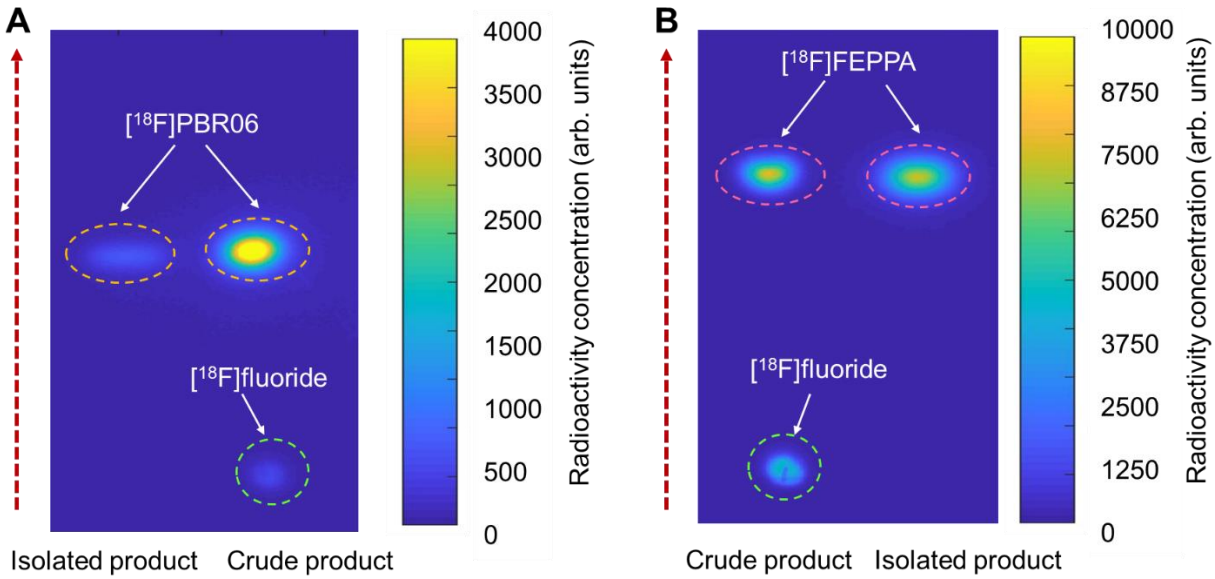

Figure 5. 19 Cerenkov images of TLC plates confirming separation for [18F]PBR06 and [18F]FEPPA.

(A) Isolated [^{18}F]PBR06 (left lane) and the crude product after the end of synthesis (right lane). (B) Crude [^{18}F]FEPPA (left lane) and isolated product (right lane). The dashed red arrows indicate the direction of solvent movement during development. (To show more details of bands, images are cropped and do not include the full extent of the TLC plate.)

[^{18}F]Fallypride samples were spotted on silica gel 60 F_{254} plates and separated using 60% MeCN in 25 mM HN_4HCO_2 with 1% TEA (v/v), as previously reported(*24*). [^{18}F]Fallypride

chromatograms exhibited up to 3 bands: [^{18}F]fluoride (R_f = 0), [^{18}F]Fallypride (R_f = 0.8), and an impurity was previously reported when using high base amounts for the reaction (R_f = 0.9)(*24*).

5.6.5 Optimization of [^{18}F]Flumazenil synthesis

5.6.5.1 Reaction temperature and solvent

Experiments were performed by drying of [^{18}F]fluoride/[^{18}O]H_2O under identical conditions (13-15 MBq [0.35-0.40 mCi], mixed with 480 nmol of $TBAHCO_3$), and then performing fluorination at different temperatures and in different solvents. The first batch of experiments was performed with heaters 1 – 4 set at 100, 120, 140, and 160 °C, respectively, and a second batch was performed with heaters 1 – 4 set at 180, 200, 220, and 240 °C, respectively (**Figure 5.3A**). Other parameters in the reaction were chosen to be similar to other syntheses we have adapted to droplet format, i.e., 8 µL reaction volume, 480 nmol of $TBAHCO_3$, and 280 nmol of precursor(*24,51,52*). The initial reaction time was chosen to be 2 min, matching the condition reported for a flow microreactor(*45*). The crude [^{18}F]Flumazenil product was then collected with 40 µL of 2:1 v/v solvent/water mixture (i.e., the same solvent as used in the reaction). The collection solution loading and collecting were 10 µL at a time and were repeated a total of 4 times to minimize the residue left behind at the reaction. Cerenkov images of chips showing residual activity after collection are shown in **Figure 5.3B** of the main paper and radio-TLC data are shown in **Figure 5.3C & D.** Detailed analyses for each individual reaction (collection efficiency, fluorination efficiency, crude RCY, and activity left on-chip) are tabulated in **Table 5.4.**

Table 5. 4 Summary of data acquired when exploring the effects of temperature and solvent in the radiosynthesis of [18F]Flumazenil.

Solvent	Temperature (°C)	Collection efficiency (%) n=4	Fluorination efficiency (%) n=4	Crude RCY (%) n=4	Activity left on chip (%) n=4
DMSO	100	93.4 ± 1.7	1.1 ± 0.5	1.0 ± 0.5	0.6 ± 0.1
	120	90.6 ± 3.5	4.0 ± 0.4	3.6 ± 0.5	1.1 ± 0.2
	140	78.8 ± 4.4	9.7 ± 0.9	7.7 ± 0.6	1.6 ± 0.1
	160	64.6 ± 2.5	13.3 ± 1.1	8.6 ± 0.7	1.8 ± 0.2
	180	33.4 ± 0.7	26.1 ± 2.0	8.7 ± 0.8	1.7 ± 0.2
	200	25.7 ± 2.5	41.7 ± 3.4	10.7 ± 1.6	2.2 ± 2.0
	220	12.8 ± 2.3	47.1 ± 1.6	5.9 ± 1.1	8.9 ± 2.6
	240	10.3 ± 2.7	50.0 ± 1.6	5.2 ± 1.5	8.9 ± 2.5
DMF	100	93.6 ± 2.4	2.1 ± 0.5	2.0 ± 0.5	1.0 ± 0.2
	120	90.0 ± 0.3	5.1 ± 0.6	4.6 ± 0.6	2.0 ± 0.4
	140	75.8 ± 4.2	14.2 ± 2.8	10.7 ± 1.7	2.3 ± 0.5
	160	65.7 ± 4.3	19.1 ± 1.8	12.5 ± 0.8	2.5 ± 0.2
	180	55.8 ± 3.2	21.7 ± 0.9	12.1 ± 0.8	2.9 ± 0.2
	200	49.0 ± 3.6	27.5 ± 0.9	13.5 ± 0.6	3.1 ± 0.5
	220	25.1 ± 3.3	30.5 ± 2.1	7.7 ± 1.4	5.4 ± 1.0
	240	17.9 ± 2.6*	39.1 ± 4.1*	7.0 ± 1.2*	5.7 ± 1.5 *

*One reaction was performed incorrectly, and so only n=3 repeats are summarized

5.6.5.2 Base amount and solvent

Experiments to explore the effect of base amount were conducted by mixing [^{18}F]fluoride/[^{18}O]H_2O (13-15 MBq [0.35-0.40 mCi]) with different amounts of the base $TBAHCO_3$ for the drying step as shown in **Figure 5.20A**. Chip 1 and 2 explored different base amounts using DMF as the solvent, and chips 3 and 4 explored different base amounts using DMSO as the solvent. All reactions were performed using 280 nmol of precursor in 8 μL of solvent and reacting for 2 min at 200°C. Cerenkov images of chips showing residual activity after collection are shown in **Figure 5.20B** and radio-TLC data from reactions is shown in **Figure 5.21**. Detailed analyses for each reaction are tabulated in **Table 5.5**.

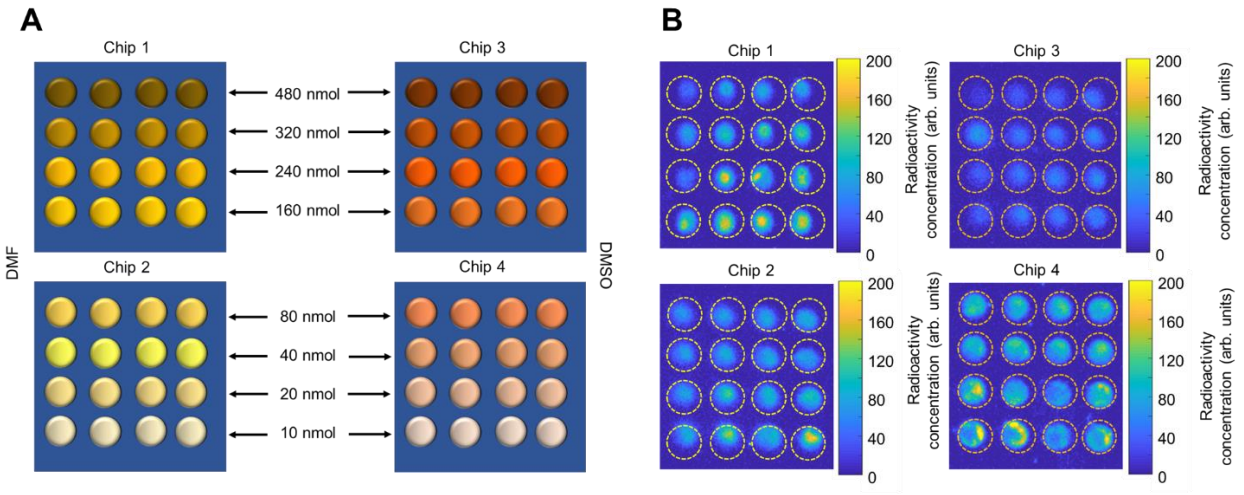

Figure 5. 20 Experimental setup for the exploration of base amount and solvent.

(A) Experimental setup for one batch of experiments that explored the influence of base amount (8 values) and solvent (2 types) on the synthesis of [^{18}F]Flumazenil. All 64 reactions were run simultaneously. (B) Cerenkov images showing the distribution of the residual activity on each chip after the collection of all the crude samples. Brightness is decay-corrected to a common timepoint for all images.

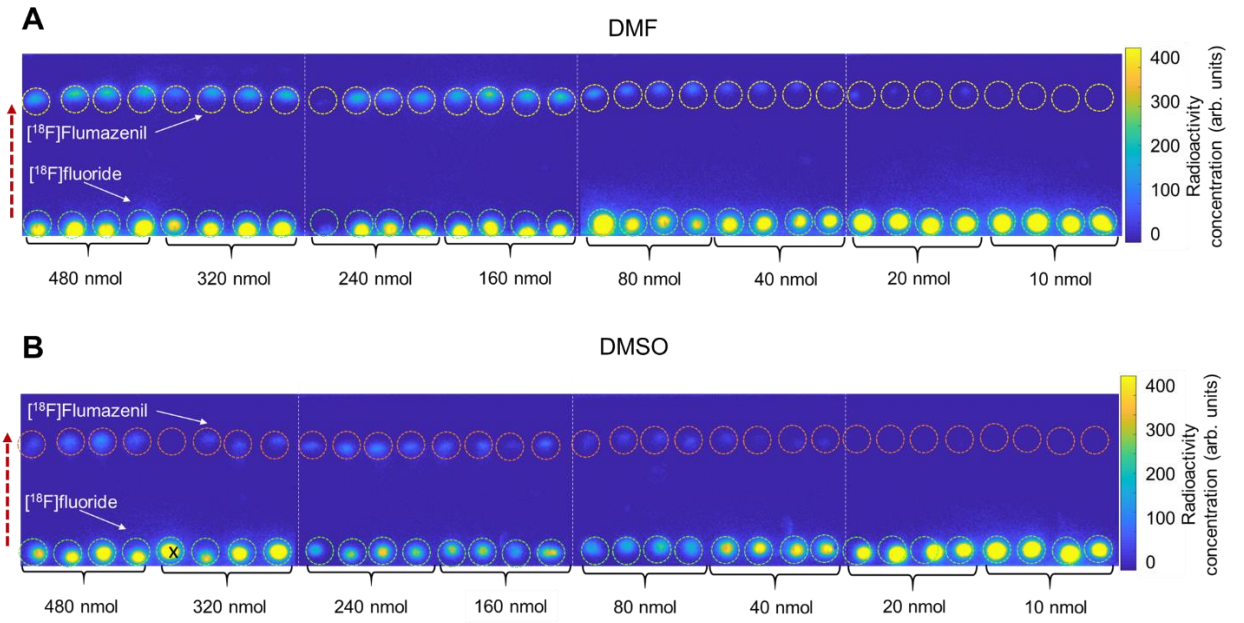

Figure 5. 21 Cerenkov images of TLC plates (each containing 8 samples) after developing.

In this case, each TLC plate contains samples from two different base amounts in one reaction solvent (n=4 replicates each). White dotted lines show the edges of each separate multi-sample TLC plate. (A) Spotted crude samples using DMF as the reaction solvent. (B) Spotted crude samples using DMSO as the reaction solvent. Dashed circles indicate the ROIs used for analysis.

The dashed red arrow indicates the direction of solvent movement during development. The “X” represents an experimental error and was excluded from further analysis.

Table 5. 5 Summary of data acquired when exploring the effect of the base amount in the radiosyntheses of [18F]Flumazenil in two different solvents.

Solvent	Base amount (nmol)	Collection efficiency (%) n=4	Fluorination efficiency (%) n=4	Crude RCY (%) n=4	Activity left on chip (%) n=4
DMF	480	47.0 ± 5.0	25.8 ± 3.6	12.1 ± 1.6	3.7 ± 1.9
	320	37.7 ± 8.0	30.5 ± 4.5	11.5 ± 0.5	5.4 ± 0.7
	240	38.7 ± 2.2	32.1 ± 2.8	12.4 ± 0.5	6.0 ± 2.0
	160	39.0 ± 3.9	32.7 ± 2.8	12.7 ± 0.9	7.9 ± 1.0
	80	27.7 ± 2.5	16.9 ± 3.1	4.6 ± 0.4	4.6 ± 0.2
	40	27.6 ± 2.5	7.0 ± 1.4	1.9 ± 0.5	4.9 ± 0.4
	20	37.6 ± 3.3	4.3 ± 0.7	1.6 ± 0.1	5.7 ± 0.7
	10	43.8 ± 3.0	1.1 ± 0.4	0.5 ± 0.1	6.8 ± 1.0
DMSO	480	43.0 ± 2.0	22.5 ± 2.5	9.7 ± 1.2	3.9 ± 1.0
	320	30.1 ± 0.5	32.5 ± 2.3	9.8 ± 0.3	5.2 ± 0.3
	240	27.9 ± 6.5	32.2 ± 1.8	9.0 ± 2.0	5.3 ± 0.8
	160	21.8 ± 2.7	22.9 ± 3.8	5.0 ± 1.2	5.2 ± 0.6
	80	25.6 ± 1.5	21.0 ± 2.0	5.4 ± 0.5	5.1 ± 0.3
	40	32.7 ± 2.2	8.2 ± 2.2	2.7 ± 0.6	5.3 ± 0.4
	20	45.6 ± 8.4	3.8 ± 1.5	1.6 ± 0.4	5.9 ± 1.3
	10	55.3 ± 4.8	1.9 ± 0.5	1.0 ± 0.2	6.9 ± 1.5

*One reaction was performed incorrectly, and so only n=3 repeats are summarized

5.6.5.3 Precursor amount and solvent

Effect of precursor amount experiments were conducted as depicted in **Figure 5.22A**. Drying of [^{18}F]fluoride/[^{18}O]H_2O was performed under identical conditions (13-15 MBq [0.35-0.4 mCi], mixed with 240 nmol of $TBAHCO_3$), and the subsequent fluorination reactions were performed with different amounts of precursor dissolved in the 8 μL droplet and reacted at 200°C for 2 min. Chips 1 and 2 used DMF as the solvent, while chips 3 and 4 used DMSO. Cerenkov images of chips showing residual activity after collection are shown in **Figure 5.22B** and radio-TLC data is shown in **Figure 5.23**. Detailed analyses for each individual reaction are tabulated in **Table 5.6**.

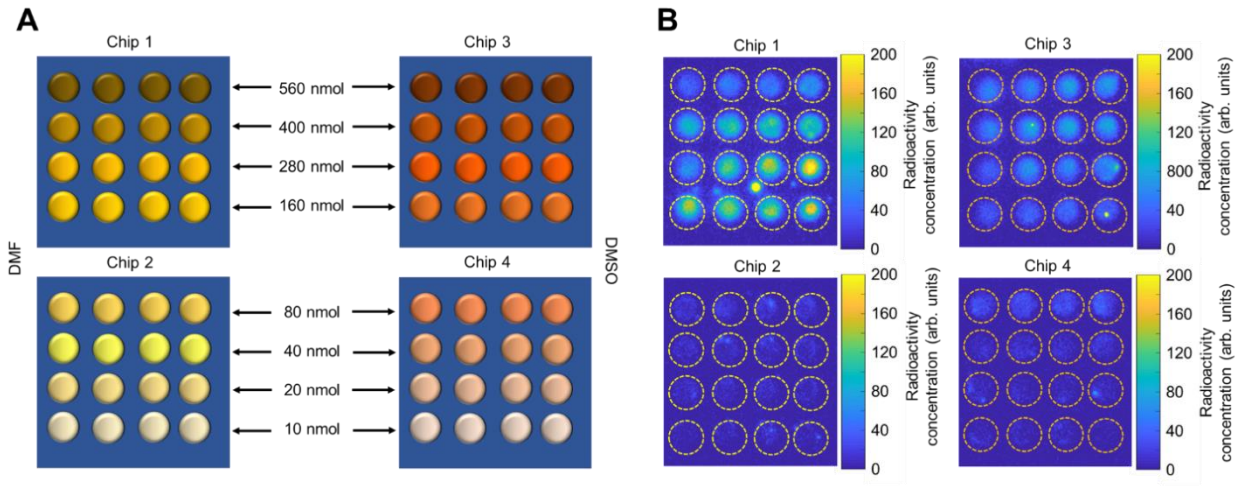

Figure 5. 22 Experimental setup for the exploration of precursor amount and solvent.

(A) Experimental setup for one batch of experiments that explored the influence of precursor amount (8 values) and solvent (2 types) on the synthesis of [^{18}F]Flumazenil. All 64 reactions were performed simultaneously. (B) Cerenkov images show the distribution of the residual activity on each chip after collecting all the crude samples. Brightness is decay-corrected to a common timepoint for all images.

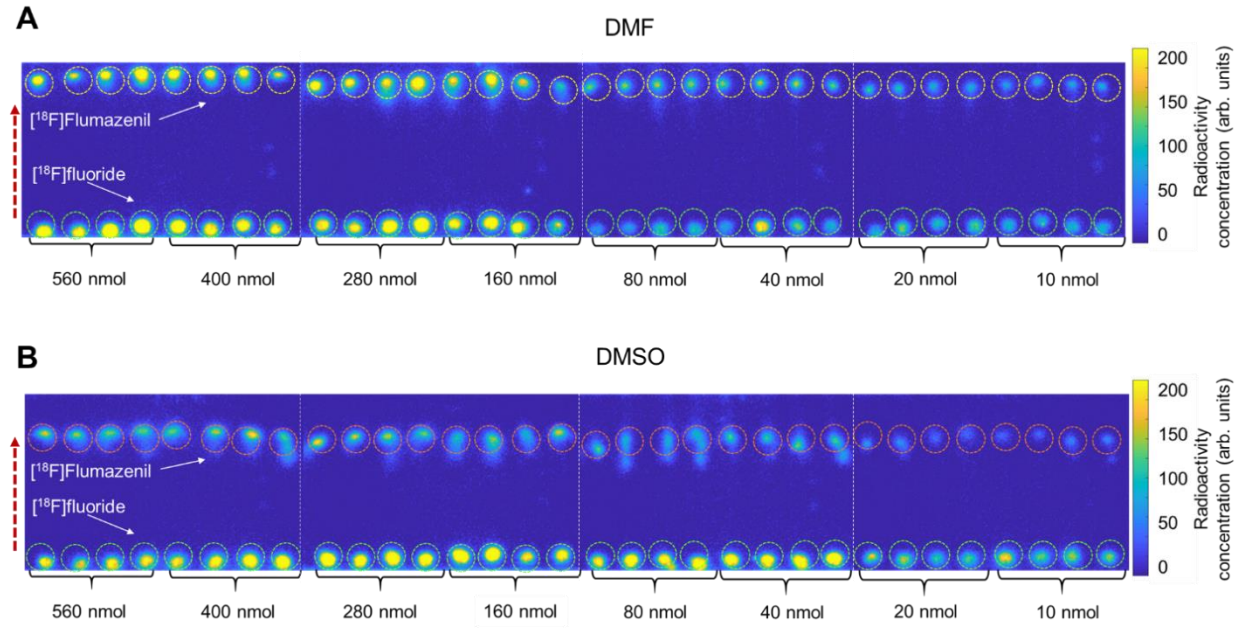

Figure 5. 23 Cerenkov images of TLC plates (each containing 8 samples) after developing in the mobile phase.

In this case, each TLC plate contains samples from two different precursor amount conditions in one reaction solvent (n=4 replicates each). White dotted lines show the edges of each separate multi-sample TLC plate. (A) Spotted crude samples using DMF as the reaction solvent. (B) Spotted crude samples using DMSO as the reaction solvent. Dashed circles indicate the ROIs

used for analysis. The dashed red arrow indicates the direction of solvent movement during development.

Table 5. 6 Summary of data acquired when exploring the effect of precursor amount in the radiosyntheses of [18F]Flumazenil.

Solvent	Precursor amount (nmol)	Collection efficiency (%) n=4	Fluorination efficiency (%) n=4	Crude RCY (%) n=4	Activity left on chip (%) n=4
DMF	560	23.3 ± 6.8	39.2 ± 4.9	9.2 ± 3.1	2.7 ± 0.5
	400	21.0 ± 4.2	44.6 ± 4.6	9.5 ± 2.7	5.3 ± 0.5
	280	24.0 ± 3.3	47.9 ± 1.6	11.5 ± 1.4	6.1 ± 1.9
	160	19.6 ± 3.5	48.3 ± 5.3	9.5 ± 2.3	6.6 ± 0.6
	80	20.4 ± 0.5	54.5 ± 2.3	11.1 ± 0.3	5.9 ± 0.3
	40	10.0 ± 1.8	48.0 ± 9.0	4.7 ± 0.3	4.9 ± 0.7
	20	8.7 ± 0.9	41.6 ± 3.7	3.4 ± 0.2	4.3 ± 0.3
	10	7.3 ± 0.7	41.9 ± 4.0	3.1 ± 0.3	3.7 ± 1.0
DMSO	560	22.3 ± 1.9	43.9 ± 4.0	9.7 ± 0.4	5.5 ± 0.6
	400	24.9 ± 1.7	39.8 ± 3.0	9.9 ± 0.2	6.3 ± 0.8
	280	23.9 ± 2.8	35.4 ± 3.6	8.5 ± 1.6	5.6 ± 1.6
	160	21.6 ± 3.3	38.3 ± 4.8	8.2 ± 1.3	3.9 ± 0.7
	80	20.7 ± 2.3	36.8 ± 2.3	7.6 ± 1.0	9.1 ± 0.6
	40	17.3 ± 1.2	32.9 ± 1.8	5.7 ± 0.5	4.2 ± 0.8
	20	14.2 ± 1.2	27.7 ± 3.2	3.9 ± 0.7	3.6 ± 1.0
	10	13.0 ± 0.8	19.7 ± 3.3	2.5 ± 0.3	2.7 ± 0.7

5.6.5.4 Effect of base to precursor ratio

Figure 5.24 summarizes the effect of base to precursor ratio on collection efficiency, fluorination efficiency, and crude RCY. This data has all been previously presented above, but here it is reorganized to show the dependence on base to precursor ratio. **Table 5.7** tabulates the values of base to precursor ratio used as the x-axis in **Figure 5.24.**

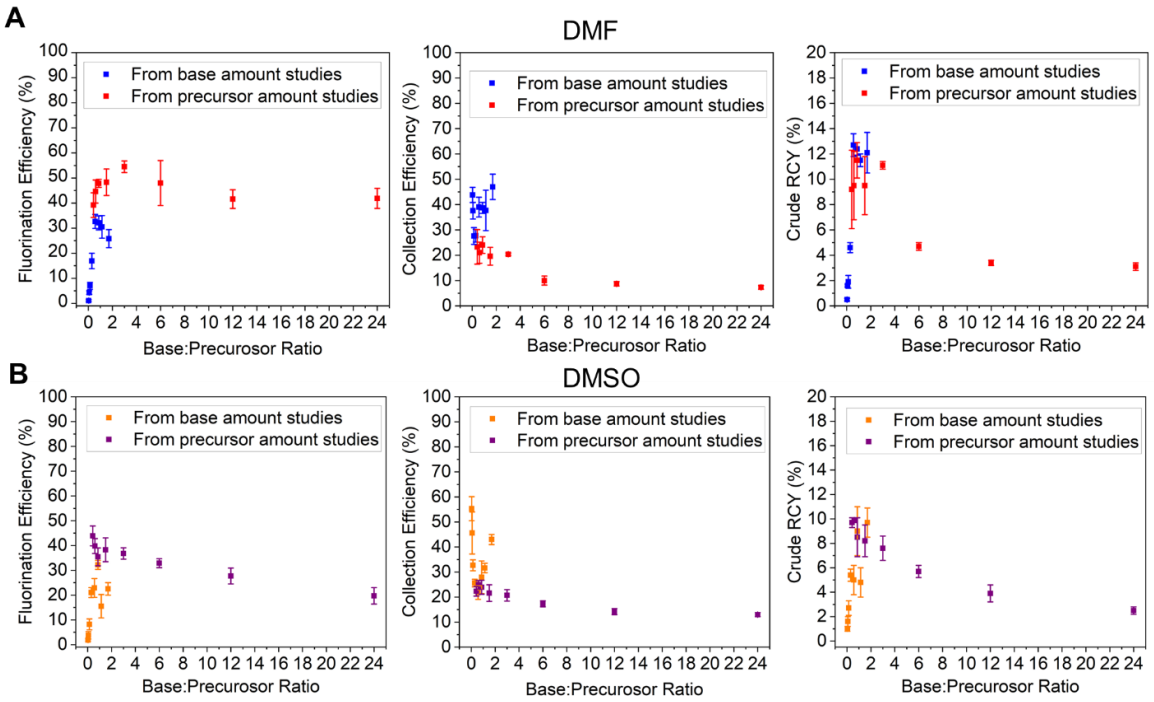

Figure 5. 24 Summary of the impact of the base to precursor molar ratio on the synthesis of [18F]Flumazenil.

Data points are derived from other experiments as indicated. Graphs in (A) used DMF as a reaction solvent. Graphs in (B) used DMSO as the reaction solvent.

Table 5. 7 Tabulated values of the base to precursor ratios used in both DMF and DMSO.

	Base:Precursor (nmol:nmol)	Base:Precursor ratio		Base:Precursor (nmol:nmol)	Base:Precursor Ratio
Data from base amount study	480:280	1.71	**Data from precursor amount study**	240:560	0.43
	320:280	1.14		240:400	0.60
	240:280	0.86		240:280	0.86
	160:280	0.57		240:160	1.50
	80:280	0.29		240:80	3.00
	40:280	0.14		240:40	6.00
	20:280	0.07		240:20	12.0
	10:280	0.04		240:10	24.0

5.6.5.5 Reaction time and solvent

The study of the effect of reaction time on the synthesis of [^{18}F]Flumazenil was conducted as shown in **Figure 5.25A**. First, [^{18}F]fluoride/[^{18}O]H_2O was dried under identical conditions (13-15 MBq [0.35-0.40 mCi], mixed with 240 nmol of $TBAHCO_3$), and then the fluorinations were carried out for different amounts of time and in different solvents. All fluorinations used 280 nmol of precursor in 8 μL of reaction solvent and were carried out at 200 °C. A first batch of experiments used reaction times of 30, 60, 120, and 180 s on heaters 1 – 4, respectively, followed by a second batch with reaction times of 240, 300, 360, and 420 s. Cerenkov images of chips showing residual activity after collection are shown in **Figure 5.25B** and radio-TLC data are shown in **Figure 5.26.** Detailed analyses for each individual reaction are tabulated in **Table 5.8**.

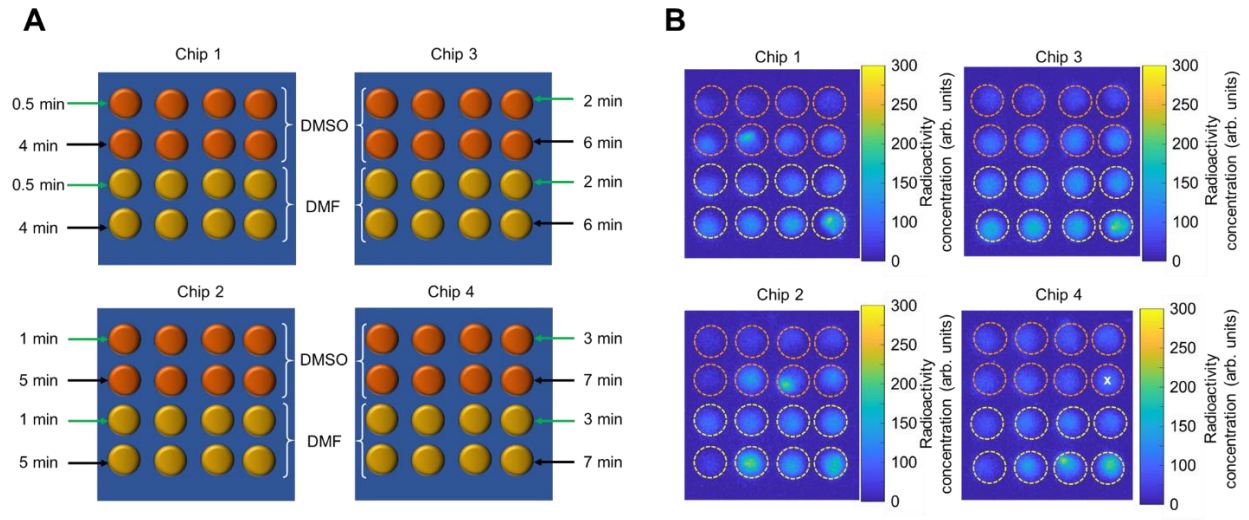

Figure 5. 25 Experimental setup for to study the effects of time and reaction solvent.

(A) Experimental setup for one batch of experiments that explored the influence of reaction time (8 values) and solvent (2 types) on the synthesis of [^{18}F]Flumazenil. (B) Cerenkov images showing the distribution of the residual activity on each chip after collection of all the crude samples. Brightness is decay-corrected to a common timepoint for all images. The reaction marked with an "X" was not analyzed as a mistake was made in the reaction.

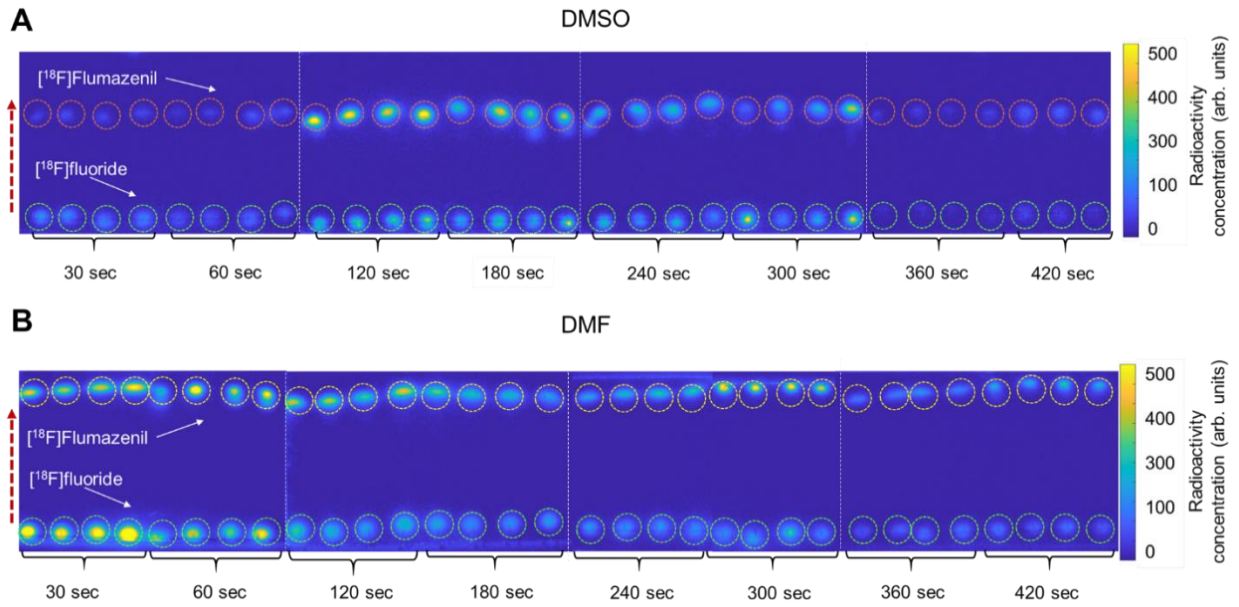

Figure 5. 26 Cerenkov images of TLC plates (each containing 8 samples) after developing in the mobile phase.

In this case, each TLC plate contains samples from two different time conditions in one reaction solvent (n=4 replicates each). White dotted lines represent the boundary of each multi-sample plate. (A) Spotted crude samples using DMSO as the reaction solvent. (B) Spotted crude samples using DMF as the reaction solvent. Dashed circles indicate the ROIs used for analysis. The dashed red arrow indicates the direction of solvent movement during development.

Table 5. 8 Summary of data acquired when exploring the effect of reaction time and solvent in the radiosyntheses of [18F]Flumazenil.

Solvent	Time (min)	Collection efficiency (%) n=4	Fluorination efficiency (%) n=4	Crude RCY (%) n=4	Activity left on chip (%) n=4
DMSO	0.5	27.1 ± 0.7	26.7 ± 2.7	7.2 ± 0.8	2.5 ± 0.1
	1.0	20.2 ± 0.6	36.4 ± 8.8	7.4 ± 1.8	2.8 ± 0.6
	2.0	14.2 ± 1.9	44.1 ± 4.3	6.2 ± 0.7	4.5 ± 0.4
	3.0	15.8 ± 1.0	65.0 ± 3.4	10.3 ± 0.7	4.5 ± 0.4
	4.0	14.9 ± 1.2	63.4 ± 3.9	9.4 ± 0.8	5.1 ± 0.9
	5.0	12.7 ± 4.4	60.1 ± 4.2	7.6 ± 2.2	7.7 ± 2.9
	6.0	12.5 ±0.8	60.8 ± 4.5	7.5 ± 1.0	5.2 ± 0.6
	7.0	16.8 ± 0.4*	66.7 ± 4.9*	11.2 ± 0.6*	7.2 ± 0.9*
DMF	0.5	35.7 ± 1.6	43.1 ± 2.0	15.4 ± 0.9	4.9 ± 0.2
	1.0	29.4 ± 4.4	47.5 ± 3.8	14.0 ± 2.4	5.1 ± 0.9
	2.0	26.8 ± 2.2	51.4 ± 1.6	13.7 ± 1.3	6.2 ± 0.5
	3.0	26 ± 2.1	54.4 ± 5.2	14.4 ± 1.5	6.7 ± 1.5
	4.0	18.3 ± 1.7	55.9 ± 4.0	10.6 ± 1.2	5.8 ± 0.2
	5.0	17.7 ± 0.3	59.8 ± 2.8	10.6 ± 0.4	6.0 ± 0.2
	6.0	18.8 ± 1.3	57.8 ± 2.1	11.0 ± 0.5	5.5 ± 0.3
	7.0	16.3 ± 0.8	61.2 ± 4.4	10.0 ±0.8	6.4 ± 0.4

*Reaction was performed incorrectly and so only n=3 repeats are summarized

5.6.5.6 Further studies of reaction solvent and temperature

We further explored the use of different aprotic solvents with a high boiling point for reactions at 200°C. In addition to DMF and DMSO, the solvents tested were N-methyl-2-pyrrolidone (NMP; BP: 202 °C), 1,3-dimethyl-3,4,5,6-tetrahydro-2(1H)-pyrimidinone (DMPU; BP: 247 °C), and ethylene glycol (BP: 197 °C). The experimental design is described in **Figure 5.27A.** Experiments were performed by drying of [^{18}F]fluoride/[^{18}O]H_2O under identical conditions (13-15 MBq [0.35-0.40 mCi], mixed with 240 nmol of $TBAHCO_3$), and then performing fluorination in different solvents (each replicated n=3 times). Cerenkov image of the chip showing residual activity after collection is shown in **Figure 5.27B**, and radio-TLC data is shown in **Figure 5.28.** Detailed analyses for each individual reaction are tabulated in **Table 5.9.**

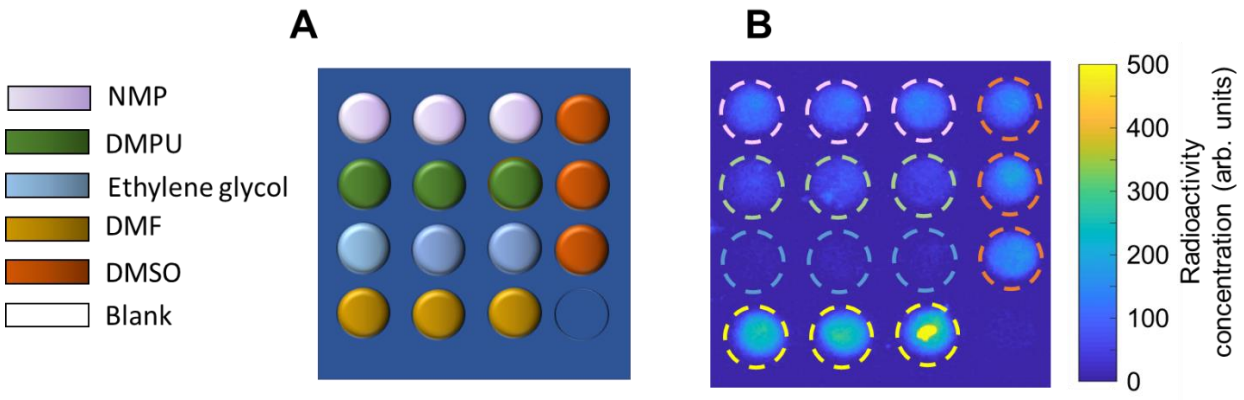

Figure 5. 27 Solvent effect experimental set up.

(A) Experimental setup for one batch of experiments that explored the influence of type of solvent (5 types) on the synthesis of [^{18}F]Flumazenil. (B) Cerenkov images showing the distribution of the residual activity on each chip after collection of all of the crude samples.

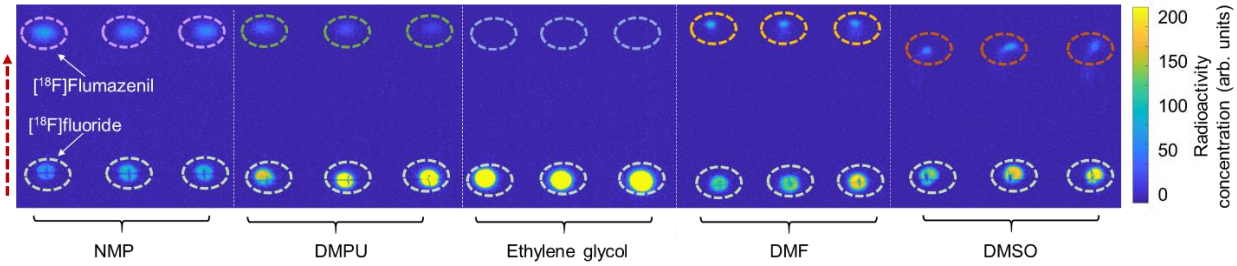

Figure 5. 28 Cerenkov images of TLC plates (each containing 3 samples) after developing in the mobile phase.

In this case, each TLC plate contains samples using one of the reaction solvents (n=3 replicates each). Dashed circles indicate the ROIs used for analysis. The dashed red arrow indicates the direction of solvent movement during development.

Table 5. 9 Summary of data acquired when exploring the effect of type of base and reaction solvent in the radiosyntheses of [18F]Flumazenil.

Solvent	Collection efficiency (%) n=3	Fluorination efficiency (%) n=3	Crude RCY (%) n=3	Activity left on chip (%) n=3
NMP	37.4 ± 1.1	48.8 ± 6.5	18.2 ± 2.0	5.0 ± 0.3
DMPU	49.5 ± 8.2	18.1 ± 3.5	8.8 ± 0.3	3.1 ± 0.8
Ethylene glycol	108.5 ± 5.0	2.3 ± 0.5	2.5 ± 0.4	0.6 ± 0.1
DMF	46.1 ± 1.8	32.8 ± 2.3	15.1 ± 0.5	10.5 ± 2.9
DMSO	35.1 ± 4.5	25.3 ± 0.2	8.9 ± 1.1	5.7 ± 0.6

We then explored the effect of temperature using NMP as reaction solvent for the radiosynthesis of [^{18}F]Flumazenil, as shown in **Figure 5.29A.** Experiments were performed by drying of [^{18}F]fluoride/[^{18}O]H_2O under identical conditions (13-15 MBq [0.35-0.40 mCi], mixed with 240 nmol of $TBAHCO_3$), and then performing fluorination at different temperatures. Though this experiment could be implemented using 4 chips on 4 heaters, since only 4 reaction sites were needed per temperature value, the experiment was instead performed using just 2 chips in multiple batches. The first batch of experiments was performed with heaters 1 and 2 set at 100 and 120 °C, respectively, a second batch with temperatures of 140, 160 °C, the third batch with temperatures of 180 and 200 °C, and a final batch with temperatures of 220 and 240 °C. All reactions were performed in 8 µL volume, with 240 nmol base, 280 nmol precursor, and 0.5 min reaction time. Cerenkov images of chips showing residual activity after collection are shown in **Figure 5.29B**, and radio-TLC data are shown in **Figure 5.30**. Detailed analyses for each individual reaction are tabulated in **Table 5.10**, and the results are plotted in **Figure 5.31**. The optimal temperature was 200 °C, giving a crude RCY of 19.1 ± 0.6% (n=4).

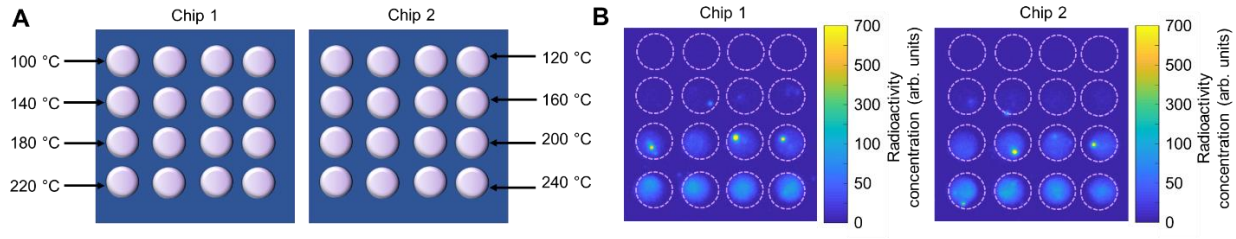

Figure 5. 29 NMP solvent and temperature study.

(A) Experimental setup for one batch of experiments that explored the influence of reaction temperature (8 values) in NMP as reaction solvent on the synthesis of [^{18}F]Flumazenil. (B) Cerenkov images showing the distribution of the residual activity on each chip after collection of all the crude samples. Brightness is decay-corrected to a common timepoint for all images.

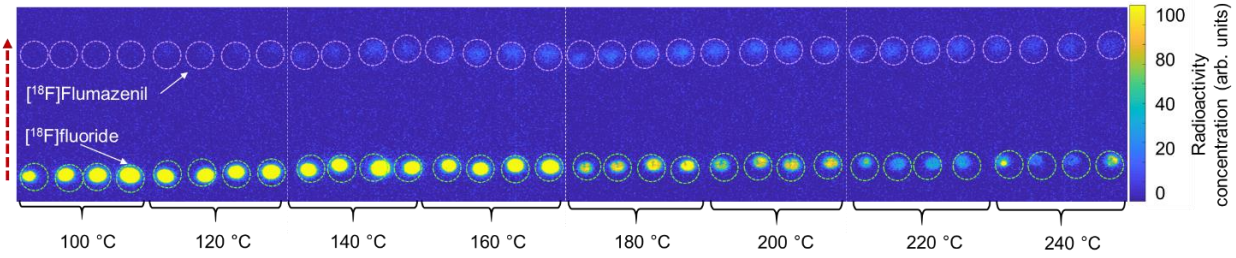

Figure 5. 30 Cerenkov images of TLC plates (each containing 8 samples) after developing in the mobile phase.

In this case, each TLC plate contains samples from two different temperatures (n=4 replicates each). White dotted lines show the edges of each separate multi-sample TLC plate. Dashed circles indicate the ROIs used for analysis. The dashed red arrow indicates the direction of solvent movement during development.

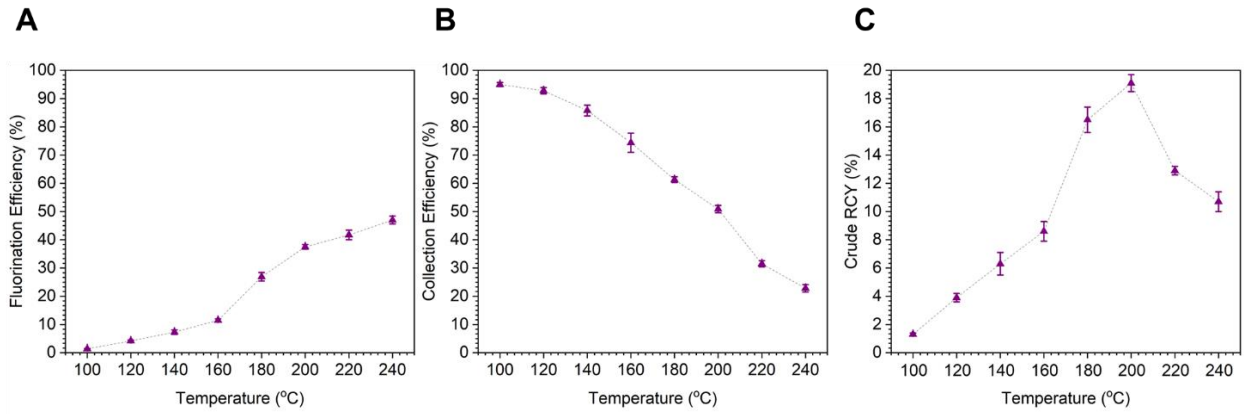

Figure 5. 31 Effect of temperature on the performance of [18F]Flumazenil synthesis with NMP as the reaction solvent.

(A) Effect on fluorination efficiency. (B) Effect on collection efficiency. (C) Effect on crude RCY.

Table 5. 10 Summary of data acquired when exploring the effect of temperature (with NMP as reaction solvent) on the radiosyntheses of [18F]Flumazenil.

Temperature (°C)	Collection efficiency (%) n=4	Fluorination efficiency (%) n=4	Crude RCY (%) n=4	Activity left on chip (%) n=4
100	95.0 ± 0.7	1.4 ± 0.1	1.3 ± 0.1	0.11 ± 0.01
120	92.8 ± 1.1	4.2 ± 0.3	3.9 ± 0.3	0.24 ± 0.03
140	85.8 ± 1.9	7.3 ± 0.8	6.3 ± 0.8	0.9 ± 0.2
160	74.4 ± 3.4	11.3 ± 0.5	8.6 ± 0.7	1.4 ± 0.4
180	61.3 ± 1.0	26.9 ± 1.5	16.5 ± 0.9	7.4 ± 0.9
200	50.9 ± 1.3	37.5 ± 0.8	19.1 ± 0.6	8.1 ± 1.7
220	31.5 ± 1.1	41.7 ± 1.7	12.9 ± 0.3	12.7 ± 0.1
240	22.8 ± 1.3	47.0 ± 1.9	10.7 ± 0.7	11.1 ± 2.1

5.6.5.7 Base type and solvent

Finally, we explored the use of different types of base/phase transfer catalyst, comparing Kryptofix (K_{222}) with K_2CO_3, K_{222} with Cs_2CO_3, and $TBAHCO_3$, as well as three different solvents (DMF, DMSO, and NMP). Only 2 chips were used for this study. For the drying step, 13-15 MBq [0.35-0.40 mCi] of [^{18}F]fluoride/[^{18}O]H_2O was loaded to each reaction site. The experiment was organized as shown in **Figure 5.32A**. After drying, the subsequent fluorinations were performed with 280 nmol of precursor in 8 µL of DMF, DMSO, or NMP and reacted at 200°C for 0.5 min. Cerenkov image of the chip showing residual activity after collection is shown in **Figure 5.32B**, and radio-TLC data is shown in **Figure 5.33**. Detailed analyses for each individual reaction are tabulated in **Table 5.11**.

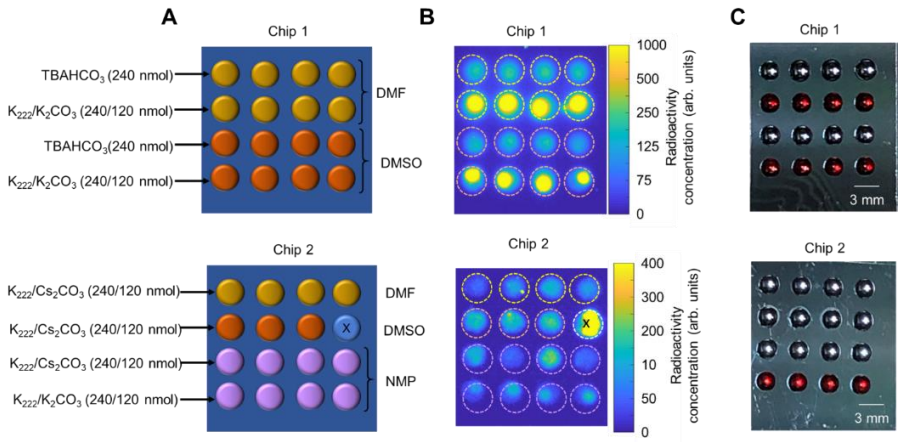

Figure 5. 32 Base type study.

(A) Experimental setup for one batch of experiments that explored the influence of type of base (3 types) and solvent (3 types) on the synthesis of [^{18}F]Flumazenil. (B) Cerenkov images showing the distribution of the residual activity on each chip after the collection of all of the crude samples.

(C) Photograph of chips showing the different droplet colors (during fluorination) depending on which base was initially dried on the chip. The reaction marked with an “X” was not analyzed as a mistake was made in the reaction.

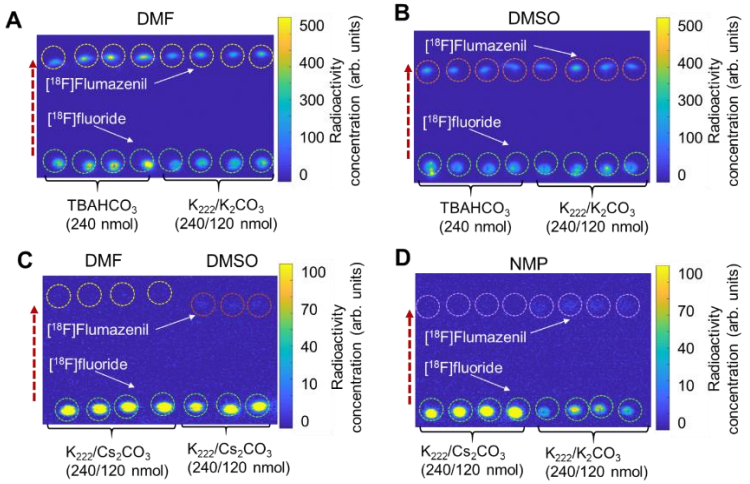

Figure 5. 33 Cerenkov images of TLC plates after developing. Each TLC plate contains data from 2 different combinations of solvent and base/phase transfer catalyst (n=4 replicates each).

Dashed circles indicate the ROIs used for analysis. The dashed red arrow indicates the direction of solvent movement during development. (A) Separated crude samples using DMF as the reaction solvent. (B) Separated crude samples using DMSO as the reaction solvent. (C) Separated crude samples using DMF or DMSO as the reaction solvent. (D) Separated crude samples using NMP as the reaction solvent.

Table 5. 11 Summary of data acquired when exploring the effect of type of base and reaction solvent in the radiosyntheses of [18F]Flumazenil.

Solvent	Base type and amount (nmol)	Collection efficiency (%) n=4	Fluorination efficiency (%) n=4	Crude RCY (%) n=4	Activity left on chip (%) n=4
DMF	$TBAHCO_3$ (240)	40.5 ± 3.0	38.6 ± 2.6	15.7 ± 1.5	3.3 ± 0.2
	K_{222}/K_2CO_3 (240/120)	28.4 ± 0.8	33.8 ± 5.1	9.6 ± 1.6	8.9 ± 0.9
	K_{222}/Cs_2CO_3 (240/120)	68.1 ± 2.9	2.5 ± 0.6	1.7 ± 0.3	3.7 ± 1.1
DMSO	$TBAHCO_3$ (240)	30.8 ± 3.8	33.4 ± 4.7	10.3 ± 2.0	2.8 ± 0.3
	K_{222}/K_2CO_3 (240/120)	30.8 ± 2.2	34.2 ± 2.5	10.4 ± 1.5	6.6 ± 1.4
	K_{222}/Cs_2CO_3 (240/120)	50.3 ± 4.1*	5.1 ± 2.4*	2.5 ± 1.0*	6.1 ± 0.4*
NMP	$TBAHCO_3$ (240)	50.9 ± 1.3#	37.5 ± 0.8#	19.1 ± 0.6#	8.1 ± 1.7#
	K_{222}/K_2CO_3 (240/120)	25.8 ± 2.8	21.9 ± 1.7	5.6 ± 0.2	3.1 ± 0.6
	K_{222}/Cs_2CO_3 (240/120)	76.2 ± 5.4	3.4 ± 1.3	2.6 ± 0.9	4.2 ± 1.9

*One reaction was performed incorrectly, and so only n=3 repeats are summarized

5.6.5.8 Comparison to literature methods

Table 5. 12 Comparison of optimized droplet conditions with literature reports for conventional and flow chemistry synthesis of [18F]flumazenil.

	This work	**Wong et al(*45*). (2012)**	**Vaulina et al(*145*). (2018)**	**Nasirzadeh et al(*146*). (2016)**	**Mandap et al(*173*). (2009)**	**Massaweh et al(*174*). (2009)**	**Ryzhikov et al(*175*). (2005)**
Synthesizer type	Microscale (droplet format)	Microscale (flow format)	Macroscale	Macroscale	Macroscale	Macroscale	Macroscale
Base type	$TBAHCO_3$	K_{222} / $KHCO_3$	K_{222} / K_2CO_3	K_{222} / K_2CO_3	K_{222} / K_2CO_3	K_{222} / K_2CO_3	K_{222} / K_2CO_3
Base amount (nmol)	240	2850 / 2590#	18900 / 10100	25000 / 12000	12100 / 1800	27700 / 1200	25000 / 12000
Precursor amount (nmol)	280	1500	4500	3000-6100‡	6100	18000-21000	25000
Reaction solvent	NMP	DMF	DMF	DMF	DMF	DMF	DMF
Reaction volume (mL)	0.008	0.10	1.5	0.7	0.5-2.0‡	0.6	0.5-1.0
Temperature (°C)	200	160	140	150	160	150-160	160
Reaction time (min)	0.5	2.5 (residence time)	20	15	5	30	30
Synthesis time (min)	35§	N. R.	53	50	55-60	80 Δ	75-80 Δ
Starting activity (MBq [mCi])	13.7 [0.37]	400 [10.8]	10000-2700 [270-730]‡	2000-3000 [54-81]‡	N.R.	50000-56000 [1350-1510]	1800 [49]
Fluorination efficiency (%)	42 ± 7 (n=7)	20 (n=1)	23 ± 5 (n=10)	30 ± 7 (n=9)	40 ± 5 (n=7)	27-35 (n=15)	80 (n=1)
Crude RCY (decay-corrected; %)	19.1 ± 0.6 (n=4)	–	–	–	–	–	–
RCY (decay-corrected; %)	11.6 (n=1)Δ	N.R.	9.0 ± 1.0 (n=6)*	8	26 ± 4	15-20Δ	30Δ

‡ The value corresponding to the optimized condition is not clearly specified, so the whole range reported in the paper is indicated

Not reported, but amount of $KHCO_3$ was computed based on the amount of precursor and an indicated 1.9:1 molar ratio of base to precursor. The amount of K_{222} was in turn computed based on the reported 1.1:1 molar ratio of K_{222} to $KHCO_3$.

N.R. = Not Reported

* Calculated from shorter and higher-yield SPE purification method instead of HPLC

Δ Isolated yield (i.e., not formulated)

§ 20 min for radiosynthesis and HPLC purification plus an estimated ~15 min additional time for formulation(*64*)

5.6.6 Optimization of [^{18}F]PBR06 synthesis

5.6.6.1 Precursor amount and solvent

Effect of precursor amount experiments were conducted as depicted in **Figure 5.34A**. Drying of [^{18}F]fluoride/[^{18}O]H_2O was performed under identical conditions (13-15 MBq [0.35-0.4 mCi], mixed with 240 nmol of $TBAHCO_3$). The subsequent fluorination reactions were performed with different amounts of precursor dissolved in the 8 μL droplet, and reacted at 100 °C for 5 min. Chips 1 and 2 used thexyl alcohol: MeCN (1:1, v/v) as the solvent while chips 3 and 4 used DMSO. Cerenkov images of chips showing residual activity after collection are shown in **Figure 5.34B**, and radio-TLC data is shown in **Figure 5.35**. Detailed analyses for each individual reaction are tabulated in **Table 5.13**

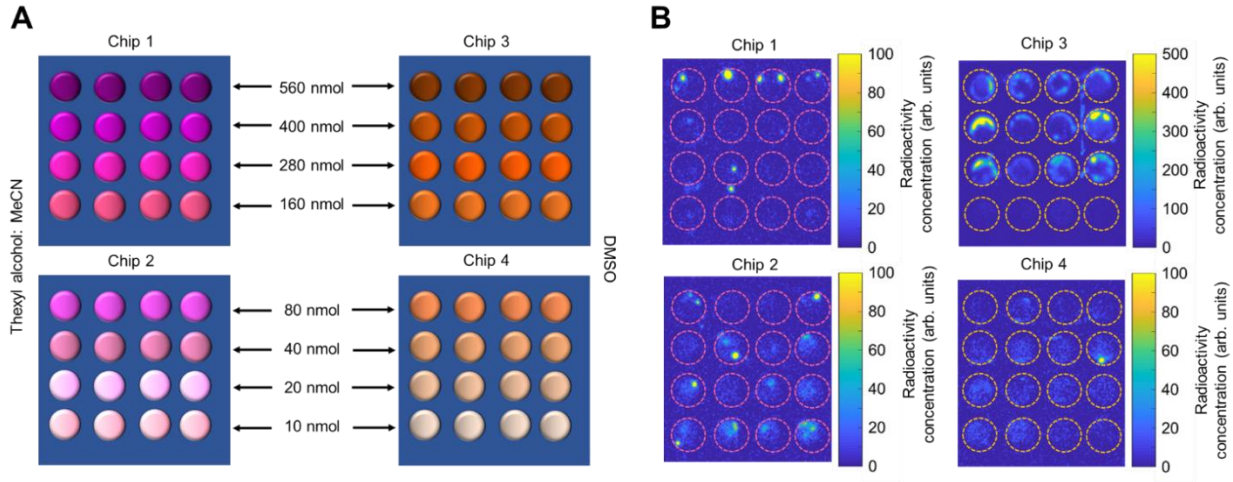

Figure 5. 34 Precursor amount and solvent study.

(A) Experimental setup for one batch of experiments that explored the influence of precursor amount (8 values) and solvent (2 types) on the synthesis of [^{18}F]PBR06. All 64 reactions were performed simultaneously. (B) Cerenkov images showing the distribution of the residual activity on each chip after collection of all of the crude samples. Brightness is decay-corrected to a common timepoint for all images.

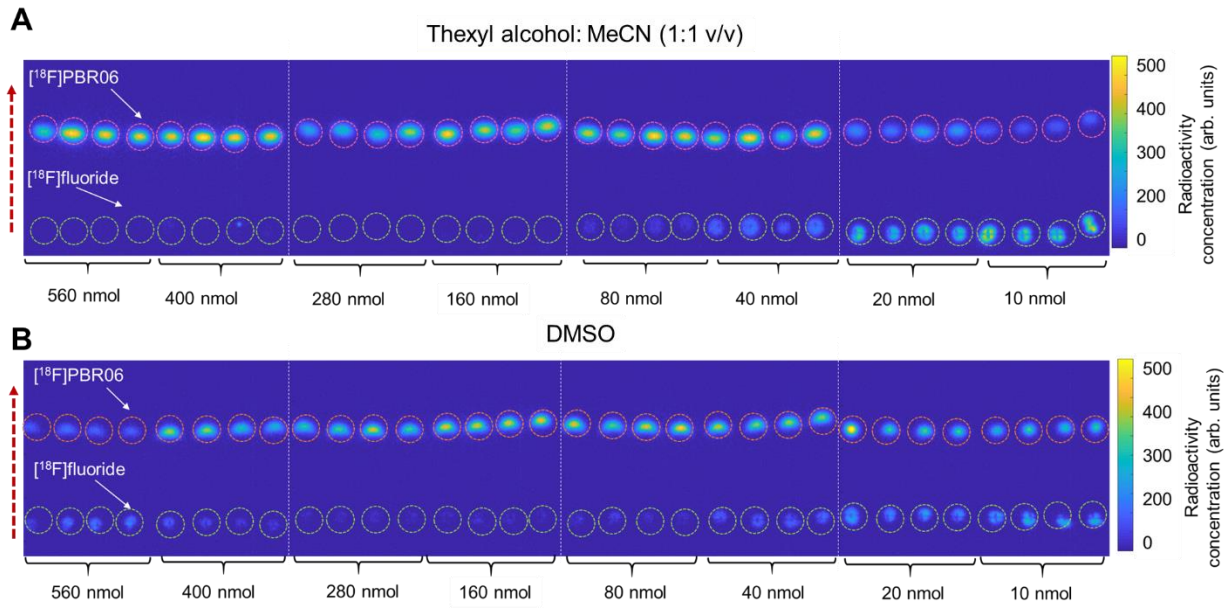

Figure 5. 35 Cerenkov images of TLC plates (each containing 8 samples) after developing in the mobile phase. In this case, each TLC plate contains samples from two different precursor amounts in one reaction solvent (n=4 replicates each).

White dotted lines show the edges of each separate multi-sample TLC plate. (A) Image of separated crude samples when using thexyl alcohol:MeCN (1:1 v/v) mixture as the reaction solvent. (B) Image of separated crude samples when using DMSO as the reaction solvent. Dashed circles indicate the ROIs used for analysis. The dashed red arrow indicates the direction of solvent movement during development.

Table 5. 13 Summary of data acquired when exploring the effect of precursor amount in the radiosyntheses of [18F]PBR06.

Solvent	Precursor amount (nmol)	Collection efficiency (%) n=4	Fluorination efficiency (%) n=4	Crude RCY (%) n=4	Activity left on chip (%) n=4
Thexyl alcohol: MeCN (1:1 v/v)	560	91.4 ± 1.5	98.0 ± 0.4	91.8 ± 5.2	4.6 ± 1.4
	400	94.9 ± 1.7	96.5 ± 1.5	91.8 ± 3.4	1.2 ± 0.8
	280	91.3 ± 1.6	97.8 ± 0.7	89.3 ± 1.7	2.3 ± 2.1
	160	93.2 ± 4.4	97.8 ± 0.1	91.1 ± 4.3	1.2 ± 0.2
	80	93.1 ± 0.9	92.7 ± 0.8	86.3 ± 1.5	2.4 ± 1.7
	40	94.3 ± 2.9	78.8 ± 1.9	74.4 ± 3.9	2.8 ± 1.2
	20	96.6 ± 2.7	45.4 ± 3.6	43.9 ± 4.7	3.5 ± 1.2
	10	94.6 ± 5.0	24.9 ± 1.6	23.6 ± 2.8	5.0 ± 2.0
DMSO	560	48.4 ± 4.2	59.7 ± 6.0	28.8 ± 2.7	4.6 ± 0.7
	400	72.9 ± 7.5	89.2 ± 2.0	65.1 ± 7.5	8.5 ± 6.3
	280	82.5 ± 5.9	93.9 ± 0.4	77.5 ± 5.8	6.7 ± 2.7
	160	90.8 ± 6.1	94.9 ± 0.3	86.3 ± 5.7	0.5 ± 0.2
	80	92.9 ± 0.7	92.8 ± 2.2	86.1 ± 2.2	1.9 ± 1.3
	40	93.5 ± 2.3	81.3 ± 2.1	76.0 ± 0.8	5.3 ± 2.9
	20	91.1 ± 6.4	66.6 ± 0.8	60.7 ± 4.2	4.2 ± 0.8
	10	91.3 ± 3.6	56.5 ± 1.3	51.6 ± 2.5	3.4 ± 1.2

5.6.6.2 Base amount and solvent

Investigation of the effect of base amount was conducted by mixing [^{18}F]fluoride/[^{18}O]H_2O (13-15 MBq [0.35-0.40 mCi]) with different amounts of the base $TBAHCO_3$ for the drying step as shown in **Figure 5.36A**. In the subsequent fluorination, chips 1 and 2 used thexyl alcohol:MeCN (1:1 v/v) mixture as a reaction solvent and chips 3 and 4 used DMSO. All reactions used 160 nmol of precursor and were performed at 100°C for 5 min. Cerenkov images of chips showing residual activity after collection are shown in **Figure 5.36B**, and radio-TLC data from reactions is shown in **Figure 5.37**. Detailed analyses for each individual reaction are tabulated in **Table 5.14**.

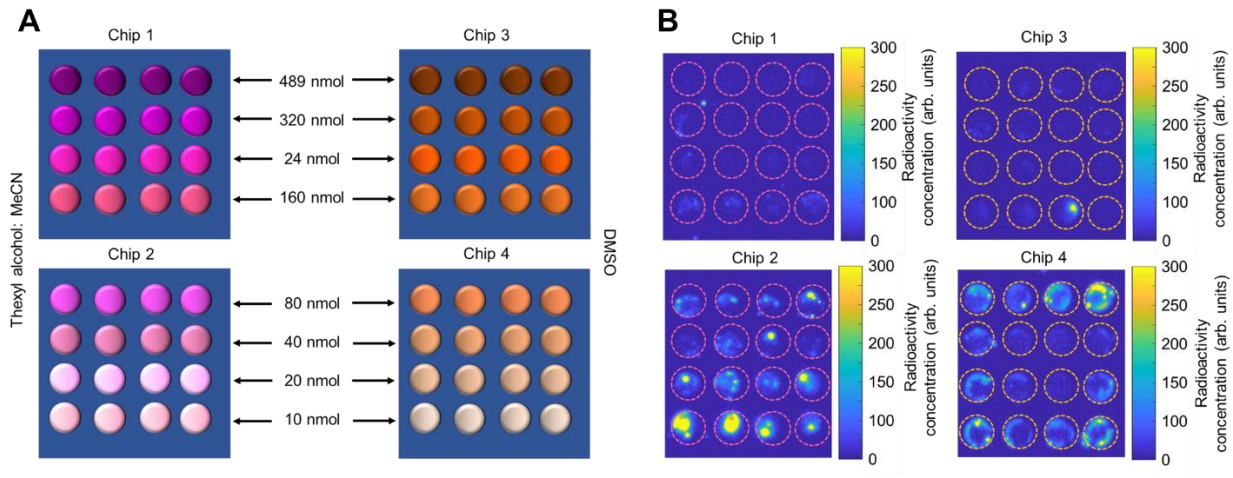

Figure 5. 36 Base amount and solvent study.

(A) Experimental setup for one set of experiments that explored the influence of base amount (8 values) and solvent (2 types) on the synthesis of [^{18}F]PBR06. All 64 reactions were run simultaneously. (B) Cerenkov images showing the distribution of the residual activity on each chip after collection of all the crude samples. Brightness is decay-corrected to a common timepoint for all images.

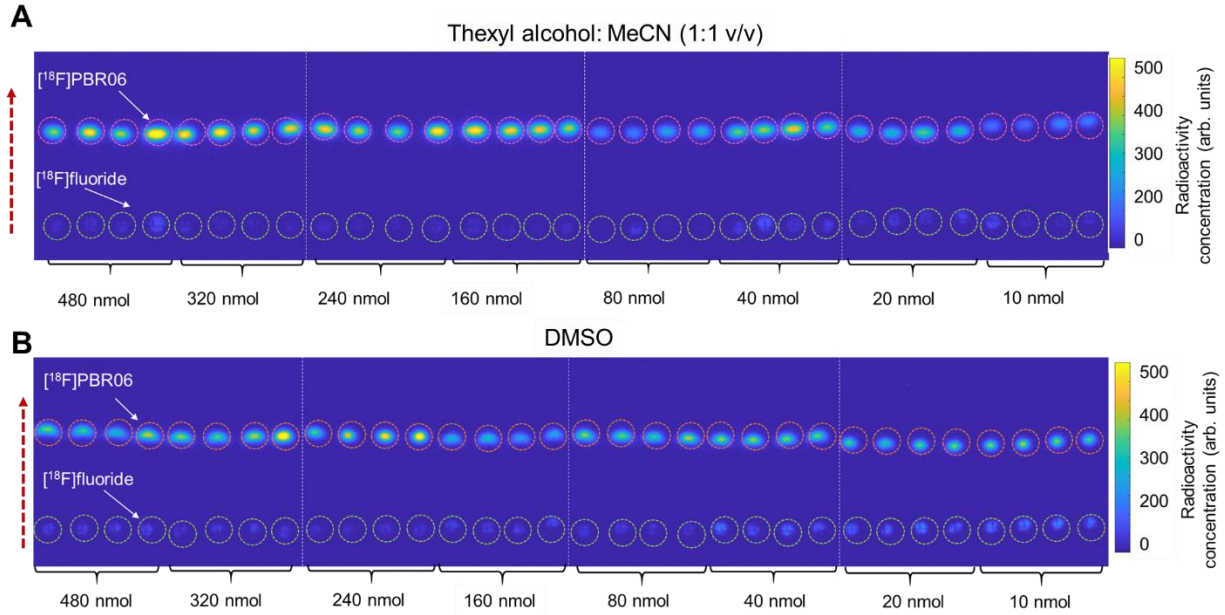

Figure 5. 37 Cerenkov images of TLC plates (each containing 8 samples) after developing in the mobile phase. In this case, each TLC plate contains samples from two different base amount conditions in one reaction solvent (n=4 replicates each).

White dotted lines show the edges of each separate multi-sample TLC plate. (A) Image of separated crude samples when using thexyl alcohol:MeCN (1:1 v/v) mixture as the reaction solvent. (B) Image of separated crude samples when using DMSO as the reaction solvent. Dashed circles indicate the ROIs used for analysis. The dashed red arrow indicates the direction of solvent movement during development.

Table 5. 14 Summary of data acquired when exploring the effect of the base amount in the radiosyntheses of [18F]PBR06 in two different solvents.

Solvent	Base amount (nmol)	Collection efficiency (%) n=4	Fluorination efficiency (%) n=4	Crude RCY (%) n=4	Activity left on chip (%) n=4
Thexyl alcohol:MeCN	480	94.8 ± 2.4	93.6 ± 2.0	88.7 ± 3.7	1.9 ± 0.7
	320	95.0 ± 1.4	96.8 ± 0.5	91.9 ± 1.4	2.4 ± 2.1
	240	95.5 ± 2.9	95.7 ± 0.6	91.5 ± 3.4	2.0 ± 0.8
	160	92.1 ± 3.9	96.0 ± 1.1	88.5 ± 4.7	5.9 ± 2.0
	80	96.9 ± 3.9	85.3 ± 2.6	98.3 ± 7.5	2.7 ± 1.3
	40	88.2 ± 1.9	89.6 ± 3.9	83.7 ± 4.5	2.1 ± 1.3
	20	88.0 ± 3.7	88.7 ± 3.1	79.4 ± 0.9	4.0 ± 1.6
	10	89.9 ± 6.8	85.2 ± 2.4	75.0 ± 8.5	9.0 ± 4.4
DMSO	480	94.4 ± 1.6	89.9 ± 1.5	84.8 ± 1.5	2.7 ± 0.6
	320	94.6 ± 2.4	91.9 ± 2.0	86.9 ± 2.6	2.4 ± 0.6
	240	94.8 ± 4.4	92.6 ± 0.7	87.8 ± 4.2	1.5 ± 0.2
	160	96.8 ± 2.9	85.0 ± 1.7	82.3 ± 4.0	5.0 ± 4.8
	80	86.1 ± 3.4	91.0 ± 0.6	78.4 ± 2.8	7.9 ± 4.5
	40	89.5 ± 1.3	83.2 ± 3.4	74.4 ± 4.1	1.6 ± 0.7
	20	80.7 ± 1.5	77.2 ± 3.8	62.3 ± 2.1	3.0 ± 1.9
	10	74.8 ± 4.0	74.6 ± 1.3	55.8 ± 3.2	5.9 ± 3.0

5.6.6.3 Reaction temperature and solvent

The experimental design for exploring temperature and solvent effect on the radiosynthesis of [^{18}F]PBR06 was described in **Figure 5.38A.** Experiments were performed by drying of [^{18}F]fluoride/[^{18}O]H_2O under identical conditions (13-15 MBq [0.35-0.40 mCi], mixed with 240 nmol of $TBAHCO_3$) , and then performing fluorination at different temperatures and in different solvents. A first batch of experiments was performed with heaters 1 – 4 set at 80, 90, 100, and 110 °C, respectively, and a second batch was performed with heaters 1 – 4 set at 120, 130, 140, and 150 °C, respectively. All fluorinations used 160 nmol of precursor in 8 µL of solvent and were reacted for 5 min. Cerenkov images of chips showing residual activity after collect are shown in **Figure 5.38B**, and radio-TLC data are shown in **Figure 5.39**. Detailed analyses for each individual reaction (collection efficiency, fluorination efficiency, crude RCY, and activity left on chip) are tabulated in **Table 5.15**.

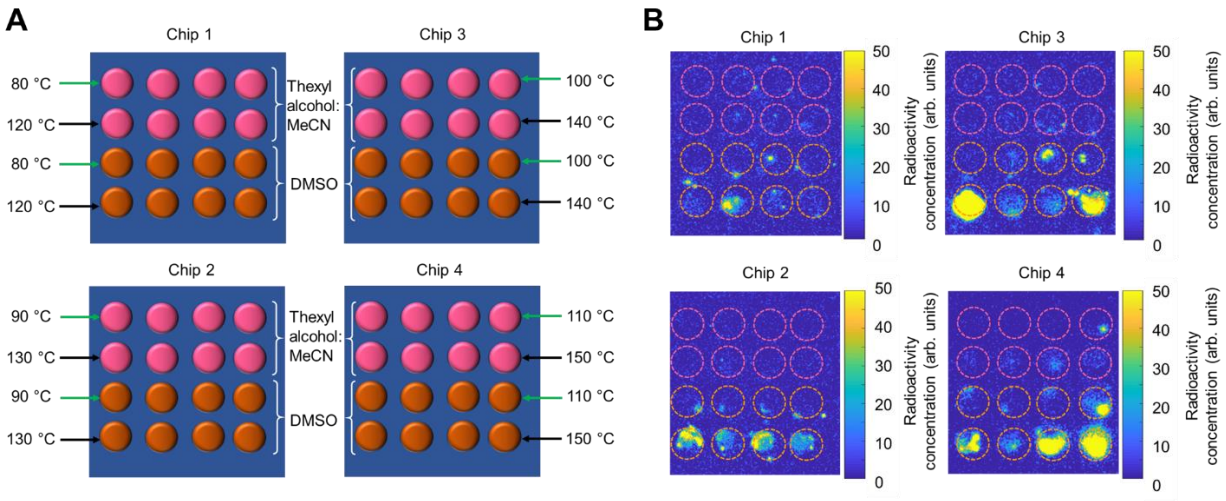

Figure 5. 38 Temperature and solvent test.

(A) Experimental setup for one batch of experiments that explored the influence of reaction temperature (8 values) and solvent (2 types) on the synthesis of [^{18}F]PBR06. Half of the reaction sites were used first to explore 4 different temperatures in a first set of 32 simultaneous reactions, and then the other half of the sites were used to explore 4 additional temperatures in a second set of 32 simultaneous reactions. (B) Cerenkov images showing the distribution of the residual activity on each chip after collection of all the crude samples. Brightness is decay-corrected to a common timepoint for all images.

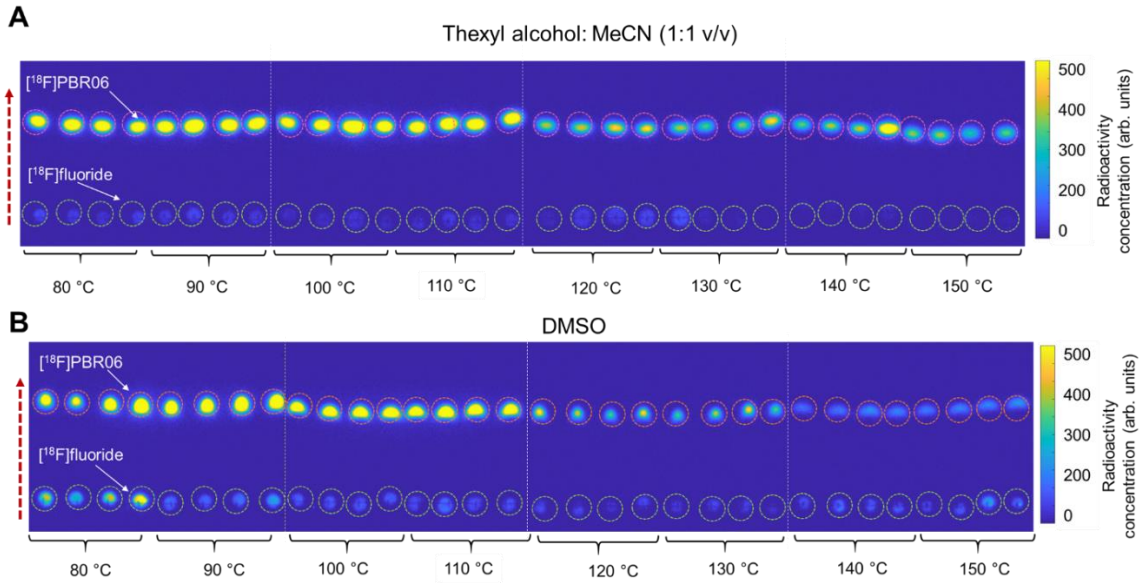

Figure 5. 39 Cerenkov images of TLC plates (each containing 8 samples) after developing in the mobile phase. In this case, each TLC plate contains samples from two different temperature conditions in one reaction solvent (n=4 replicates each).

White dotted lines represent the boundary of each multi-sample plate. (A) Image of separated crude samples when using thexyl alcohol:MeCN (1:1 v/v) as the reaction solvent. (B) Image of separated crude samples when using DMSO as the reaction solvent. Dashed circles indicate the ROIs used for analysis. The dashed red arrow indicates the direction of solvent movement during developing.

Table 5. 15 Summary of data acquired when exploring the effect of temperature and solvent in the radiosyntheses of [18F]PBR06.

Solvent	Temperature (°C)	Collection efficiency (%) n=4	Fluorination efficiency (%) n=4	Crude RCY (%) n=4	Activity left on chip (%) n=4
Thexyl alchohol: MeCN	80	93.0 ± 3.0	95.0 ± 1.2	88.4 ± 3.6	1.1 ± 0.4
	90	94.1 ± 1.4	95.7 ± 0.4	90.1 ± 1.6	0.6 ± 0.1
	100	94.2 ± 3.1	95.7 ± 0.6	91.1 ± 2.4	0.4 ± 0.2
	110	94.1 ± 1.2	96.3 ± 0.6	90.6 ± 1.1	0.4 ± 0.5
	120	93.6 ± 0.6	88.2 ± 3.7	82.6 ± 4.0	1.3 ± 0.4
	130	93.8 ± 1.4	90.8 ± 8.3	87.5 ± 10.9	0.5 ± 0.2
	140	91.3 ± 1.4	96.4 ± 0.7	91.7 ± 6.2	0.8 ± 0.3
	150	92.7 ± 0.9	94.7 ± 1.1	87.8 ± 1.2	0.9 ± 0.3
DMSO	80	94.3 ± 3.4	72.4 ± 4.4	68.2 ± 4.4	3.7 ± 1.1
	90	93.5 ± 4.8	91.4 ± 2.1	85.6 ± 5.5	2.0 ± 0.4
	100	93.0 ± 2.4	92.7 ± 0.5	86.2 ± 1.9	1.8 ± 1.1
	110	89.5 ± 2.5	91.9 ± 1.8	82.3 ± 1.9	2.5 ± 2.8
	120	89.1 ± 1.7	87.6 ± 1.0	78.7 ± 1.3	5.0 ± 4.1
	130	93.1 ± 3.3	87.6 ± 3.3	81.6 ± 3.5	9.6 ± 2.4
	140	90.6 ± 2.6	71.3 ± 5.9	64.9 ± 5.9	8.5 ± 6.4
	150	88.6 ± 2.4	75.3 ± 4.2	66.8 ± 4.9	8.4 ± 5.0

5.6.6.4 Reaction time and solvent

The study of the effect of reaction time on the synthesis of [^{18}F]PBR06 was conducted as shown in **Figure 5.40A**. First, [^{18}F]fluoride/[^{18}O]H_2O was dried under identical conditions (13-15 MBq [0.35-0.40 mCi], mixed with 240 nmol of $TBAHCO_3$), and then the fluorinations were carried out for different amounts of time and in different solvents. All fluorinations used 160 nmol of precursor in 8 μL of reaction solvent of thexyl alcohol:MeCN (1:1 v/v) mixture or DMSO and were carried out at 100 °C. A first batch of experiments used reaction times of 30, 60, 120, and 180 s on heaters 1 – 4, respectively, followed by a second batch of experiments with reaction times of 240, 300, 360, and 420 s on heaters 1 – 4, respectively. Cerenkov images of chips showing residual activity after collection are shown in **Figure 5.40B** and radio-TLC data are shown in **Figure 5.41.** Detailed analyses for each individual reaction are tabulated in **Table 5.16**.

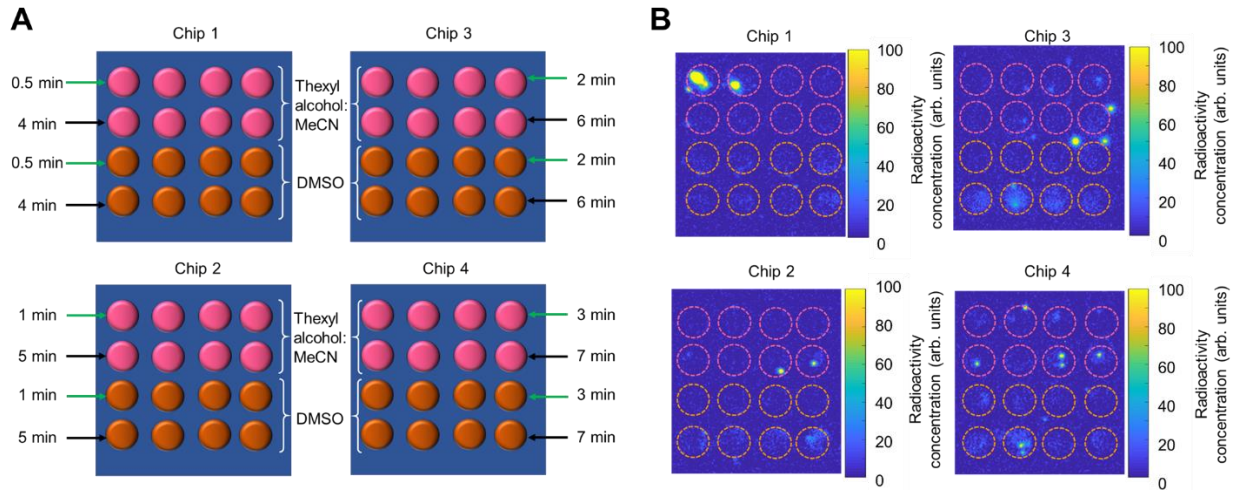

Figure 5. 40 Time and solvent test.

(A) Experimental setup for one batch of experiments that explored the influence of reaction time (8 values) and solvent (2 types) on the synthesis of [^{18}F]PBR06. Half of the reaction sites were used first to explore 4 different times in 32 simultaneous reactions, and then the other half of the sites were used to explore 4 additional times in 32 simultaneous reactions. (B) Cerenkov images showing the distribution of the residual activity on each chip after collection of all the crude samples. Brightness is decay-corrected to a common timepoint for all images.

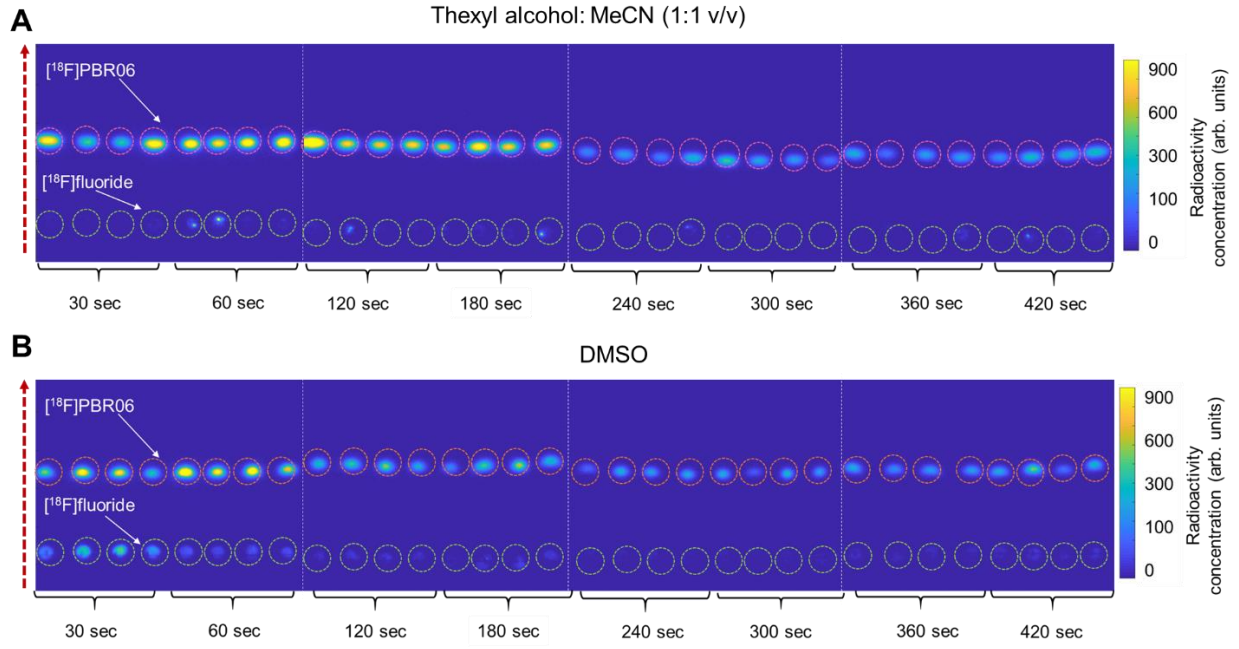

Figure 5. 41 Cerenkov images of TLC plates (each containing 8 samples) after developing in the mobile phase. In this case, each TLC plate contains samples from two different time conditions in one reaction solvent (n=4 replicates each).

White dotted lines represent the boundary of each multi-sample plate. (A) Image of separated crude samples when using thexyl alcohol:MeCN (1:1 v/v) mixture as the reaction solvent. (B) Image of separated crude samples using DMSO as the reaction solvent. Dashed circles indicate

the ROIs used for analysis. The dashed red arrow indicates the direction of solvent movement during developing. Red dashed circle represents an area of contamination that was inadvertently on the cover plate when imaging the TLC plates.

Table 5. 16 Summary of data acquired when exploring the effect of reaction time and solvent in the radiosyntheses of [18F]PBR06.

Solvent	Time (min)	Collection efficiency (%) n=4	Fluorination efficiency (%) n=4	Crude RCY (%) n=4	Activity left on chip (%) n=4
Thexyl alcohol: MeCN	0.5	92.9 ± 1.6	98.0 ± 0.1	91.0 ± 1.5	2.2 ± 2.0
	1.0	94.1 ± 1.4	94.1 ± 4.4	88.6 ± 4.6	0.5 ± 0.1
	2.0	91.5 ± 2.5	96.5 ± 2.7	88.3 ± 2.2	0.9 ± 0.2
	3.0	94.1 ± 0.9	96.1 ± 2.4	90.4 ± 2.1	0.8 ± 0.2
	4.0	88.7 ± 2.7	95.1 ± 2.7	84.3 ±1.7	0.5 ± 0.2
	5.0	93.3 ± 2.0	97.5 ± 1.0	91.0 ± 1.9	2.6 ± 2.1
	6.0	89.0 ± 5.4	92.6 ± 3.5	82.3 ± 9.1	0.8 ± 0.2
	7.0	94.1 ± 1.2	94.7 ± 2.8	89.1 ± 3.4	2.7 ± 1.7
DMSO	0.5	94.2 ± 3.0	66.5 ± 3.1	62.6 ± 3.1	0.6 ± 0.3
	1.0	94.5 ± 3.6	90.4 ± 0.6	85.3 ± 3.0	3.7 ± 2.6
	2.0	92.7 ± 2.0	91.9 ± 1.0	85.2 ± 2.5	0.9 ± 0.4
	3.0	93.8 ± 0.6	90.2 ± 0.9	84.6 ± 0.8	3.8 ± 2.0
	4.0	92.0 ± 2.4	92.8 ± 1.2	85.3 ± 2.6	1.7 ± 0.7
	5.0	91.0 ± 4.3	90.8 ± 1.5	82.7 ± 5.2	3.4 ± 1.8
	6.0	90.5 ± 8.9	90.3 ± 0.6	81.8 ± 8.6	1.5 ± 0.2
	7.0	94.2 ± 4.8	89.9 ± 1.1	84.7 ± 3.5	3.7± 3.3

5.6.6.5 Base type and solvent

Finally, we explored the use of different type of base / phase transfer catalyst, comparing Kryptofix (K_{222}) and K_2CO_3 versus $TBAHCO_3$ as shown in **Figure 5.42A**. Only one chip was used for this study. For the drying step, 13-15 MBq [0.35-0.40 mCi] of [^{18}F]fluoride/[^{18}O]H_2O was loaded to each reaction site. For half of the spots, the fluoride was mixed with 240 nmol of TBAHCO3. For the other half of the spots, the fluoride was mixed with 240 nmol of K_{222} and 120 nmol of K_2CO_3. After drying, the subsequent fluorinations were performed with 280 nmol of precursor in 8 µL of either thexyl alcohol:MeCN (1:1 v/v) mixture or DMSO, and reacted at 100°C for 0.5 min. Cerenkov image of the chip showing residual activity after collection are shown in **Figure 5.42B**, and radio-TLC data is shown in **Figure 5.43**. Detailed analyses for each individual reaction are tabulated in **Table 5.17**.

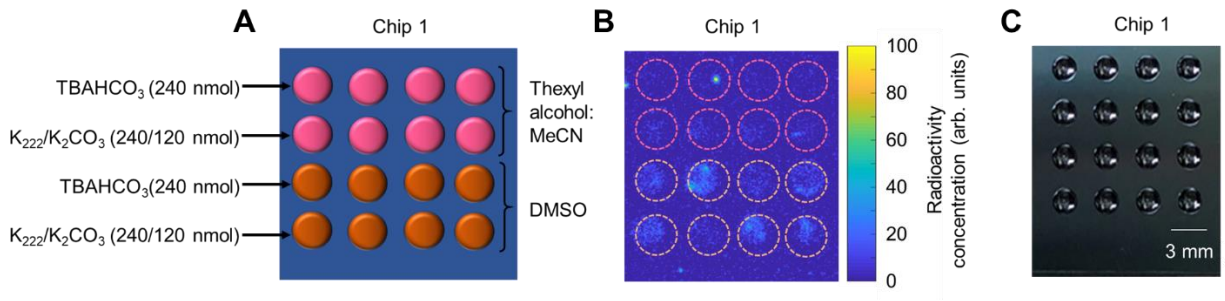

Figure 5. 42 Base type and solvent test.

(A) Experimental setup for one batch of experiments that explored the influence of type of base (2 values) and solvent (2 types) on the synthesis of [^{18}F]PBR06. (B) Cerenkov images showing the distribution of the residual activity on each chip after collection of all the crude samples. (C) Photograph of chip after precursor is loaded, showing absence of base-dependent color difference (seen for [^{18}F]Flumazenil).

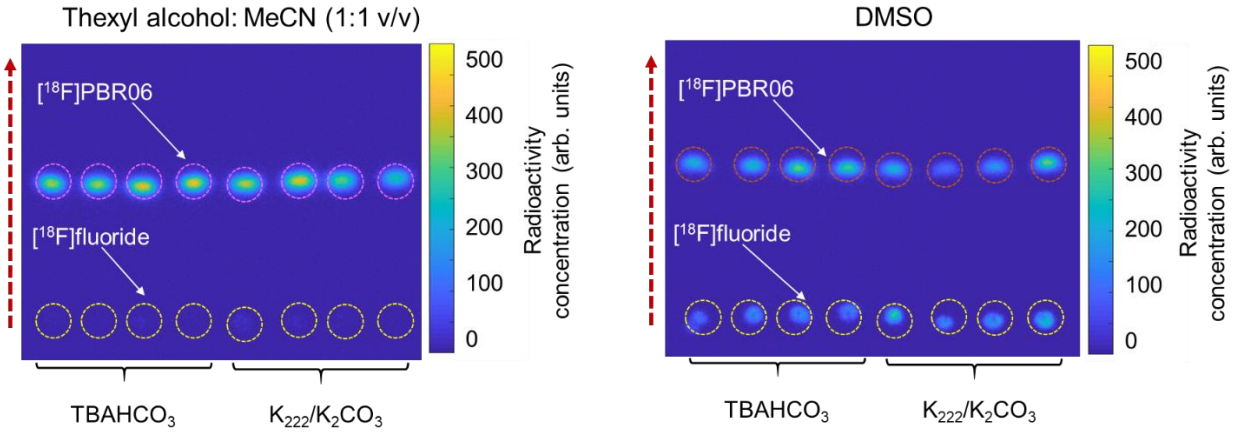

Figure 5. 43 Cerenkov images of TLC plates (each containing 8 samples) after developing in the mobile phase. In this case, each TLC plate contains samples from two different base type conditions in one reaction solvent (n=4 replicates each).

Dashed circles indicate the ROIs used for analysis. The dashed red arrow indicates the direction of solvent movement during developing. (A) Image of separated crude samples when using thexyl alcohol:MeCN (1:1 v/v) mixture as the reaction solvent. (B) Image of separated crude samples when using DMSO as the reaction solvent.

Table 5. 17 Summary of data acquired when exploring the effect of type of base and reaction solvent in the radiosyntheses of [18F]flumazenil.

Solvent	Base type and amount (nmol)	Collection efficiency (%) n=4	Fluorination efficiency (%) n=4	Crude RCY (%) n=4	Activity left on chip (%) n=4
Thexyl alcohol: MeCN	$TBAHCO_3$ (240)	96.4 ± 2.2	97.4 ± 0.2	93.9 ± 2.0	0.7 ± 0.1
	K_{222}/K_2CO_3 (240/120)	95.8 ± 3.5	96.5 ± 0.9	92.4 ± 3.0	1.63 ± 0.03
DMSO	$TBAHCO_3$ (240)	94.7 ± 4.1	70.7 ± 3.5	66.9 ± 2.9	4.4 ± 1.1
	K_{222}/K_2CO_3 (240/120)	93.5 ± 5.3	60.5 ± 3.2	56.5 ± 2.0	4.3± 1.9

5.6.6.6 Additional studies of reaction temperature

Using thexyl alcohol: MeCN (1:1 v/v) as a reaction solvent exhibited high crude RCY at 80 °C in a 5 min reaction, and high crude RCY at 100 °C in a 0.5 min reaction. We were interested whether short reactions (0.5 min) at lower temperatures would also give good performance. Experiments were performed by drying of [^{18}F]fluoride/[^{18}O]H_2O under identical conditions (13-15 MBq [0.35-0.40 mCi] with 240 nmol of $TBAHCO_3$), followed by fluorination with 160 nmol of precursor in 8 µL of solvent for 0.5 min at different temperatures. To conserve chips, temperatures were explored sequentially, using 4 fresh reaction sites each time. (Two chips were needed in total.) Radio-TLC data are shown in **Figure 5.44**. Detailed analyses for each individual reaction are tabulated in **Table 5.17** and the results are plotted in **Figure 5.45**. We observed that the temperature could be lowered to 90 °C without compromising performance. **Table 5.18** compares our approach with other literature macroscale reports.

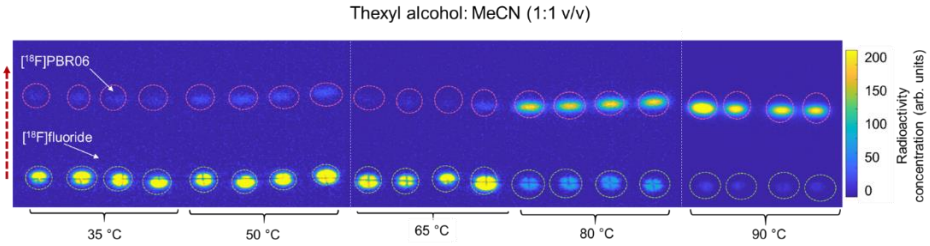

Figure 5. 44 Cerenkov images of TLC plates (two containing 8 samples and one containing 4 samples) after developing in the mobile phase.

In this case, each TLC plate contains samples from up to two different temperatures (n=4 replicates each). White dotted lines show the edges of each multi-lane TLC plate. Dashed circles indicate the ROIs used for analysis. The dashed red arrow indicates the direction of solvent movement during developing.

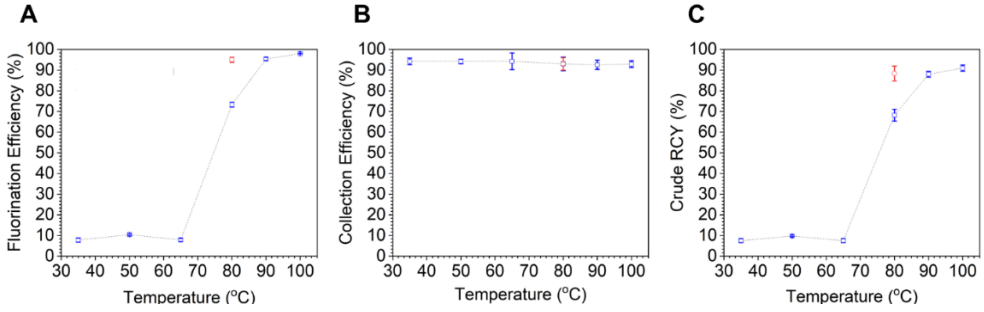

Figure 5. 45 Temperature studies of [18F]PBR06.

(A) Fluorination efficiency. (B) Collection efficiency. (C) Crude RCY. The blue markers represent 0.5 min reactions, and the red data points represent 5 min reactions.

Table 5. 18 Summary of data acquired when exploring the effect of temperature in the radiosyntheses of [18F]PBR06 (for 0.5 min reactions).

Solvent	Temperature (°C)	Collection efficiency (%) n=4	Fluorination efficiency (%) n=4	Crude RCY (%) n=4	Activity left on chip (%) n=4
Thexyl alchohol: MeCN	35	94.2 ± 1.6	7.8 ± 1.0	7.5 ± 1.0	2.2 ± 0.2
	50	94.2 ± 1.1	10.4 ± 0.4	9.8 ± 0.4	3.5 ± 1.0
	65	94.3 ± 4.0	7.9 ± 0.8	7.5 ± 1.0	1.5 ± 0.8
	80	93.0 ± 3.3	73.3 ± 1.2	68.2 ± 2.9	1.0 ± 0.6
	90	92.6 ± 2.2	95.4 ± 0.8	88.0 ± 1.4	2.5± 0.7

5.6.6.7 Comparison to literature methods

Table 5. 19 Comparison of optimized droplet conditions with literature reports for conventional synthesis of [18F]PBR06.

	This work (2021)	Wang et al.(*181*) (2011)	Zhang et al.(*182*) (2019)
Synthesizer type	Microscale (droplet format)	Macroscale	Macroscale
Base type	$TBAHCO_3$	K_{222} / K_2CO_3	K_{222} / K_2CO_3
Base amount (nmol)	240	27000/ 12000	40000/10000
Precursor amount (nmol)	160	1800	5500
Reaction solvent	Thexyl alcohol: MeCN (1:1 v/v)	DMSO	DMSO
Reaction volume (mL)	0.008	1	1
Temperature (°C)	100	140	140
Reaction time (min)	0.5	15	15
Synthesis time (min)	35 #	50-60	50
Starting activity (MBq [mCi])	13.8 [0.375]	N.R.	N.R.
Fluorination efficiency (%)	98.0 ± 0.1 (n=4)	N.R.	N.R.
Crude RCY (decay-corrected; %)	93.9 ± 2.0 (n=4)	N.R.	N.R.
RCY (decay-corrected; %)	75.8 (n=1)*	30-60	40-60

* Isolated yield (i.e., not formulated)

20 min for radiosynthesis and purification plus an estimated ~15 min additional time for formulation(*64*)

N.R. = Not reported

5.6.7 Optimization of [^{18}F]Fallypride synthesis

5.6.7.1 Precursor concentration and reaction temperature

A set of experiments to explore the effect of precursor concentration and temperatures were conducted as depicted in **Figure 5.46A**. Drying of [^{18}F]fluoride/[^{18}O]H_2O was performed under identical conditions (13-15 MBq [0.35-0.4 mCi], mixed with 240 nmol of $TBAHCO_3$), and the subsequent fluorination reactions were performed with different amounts of precursor dissolved in the 6 μL droplet, for 7 min. Chip 1 was run at 80 °C, chip 2 at 95 °C chip 3 at 110°C, and chip 4 at 125 °C. All reactions were conducted using thexyl alcohol:MeCN (1:1 v/v) mixture as solvent. Cerenkov images of chips showing residual activity after collected are shown in **Figure 5.46B**, and graphical representation is shown in **Figure 5.6A** in the main paper. Detailed analyses for each individual reaction are tabulated in **Table 5.20**.

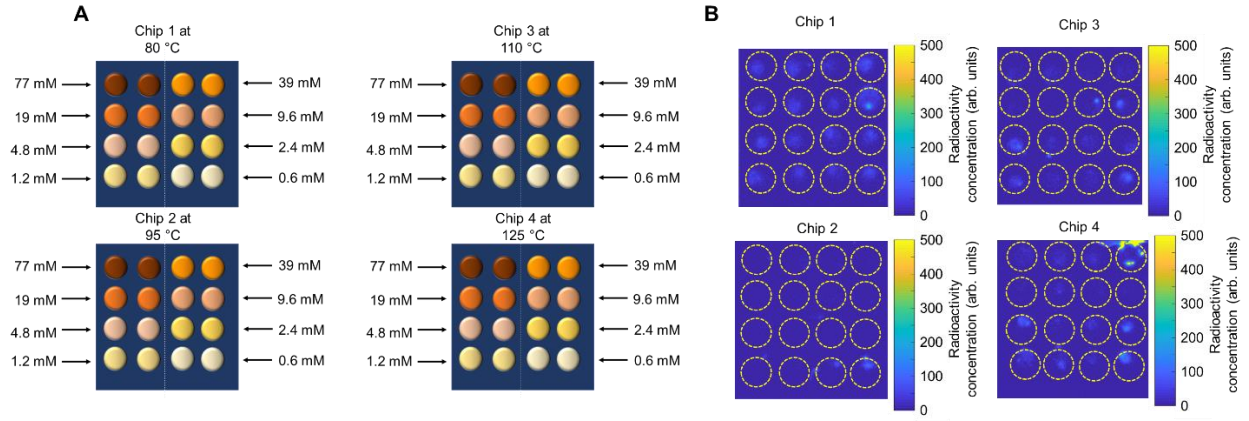

Figure 5. 46 Precursor concentration and temperature test.

(A) Experimental setup for one batch of experiments that explored the influence of precursor concentration (8 values) and temperature (4 types) on the synthesis of [^{18}F]Fallypride. Each chip explored 8 different precursor concentrations at one particular temperature. (B) Cerenkov images showing the distribution of the residual activity on each chip after collection of all the crude samples. Brightness is decay-corrected to a common timepoint for all images.

Table 5. 20 Summary of data acquired when exploring the effect of precursor concentration and temperature on the radiosyntheses of [18F]Fallypride.

Temperature (°C)	Precursor concentration (mM)	Collection efficiency (%) n=2	Fluorination efficiency (%) n=2	Crude RCY (%) n=2	Activity left on chip (%) n=2
80	77	93.64 ± 0.05	94.7 ± 1.3	88.6 ± 1.2	4.1 ± 0.4
	39	93.1 ± 1.6	91.9 ± 4.0	85.7 ± 5.2	4.2 ± 2.4
	19	93.2 ± 0.8	61.7 ± 3.6	57.5 ± 2.9	3.1 ± 1.2
	9.6	91.2 ± 8.3	33.4 ± 3.8	30.6 ± 6.2	5.8 ± 4.4
	4.8	94.9 ± 3.6	24.4 ± 1.7	23.1 ± 0.8	3.4 ± 1.2
	2.4	96.1 ± 2.0	13.0 ± 1.1	12.5 ± 0.7	4.3 ± 0.1
	1.2	93.9 ± 7.4	12.7 ± 0.8	12.0 ± 1.7	3.4 ± 0.7
	0.6	92.5 ± 5.7	6.7 ± 0.7	6.2 ± 0.3	3.8 ± 0.8
95	77	88.2 ± 3.0	95.5 ± 0.1	84.3 ± 3.0	4.6 ± 0.7
	39	89.8 ± 3.8	95.1 ± 1.0	85.3 ± 2.7	2.1 ± 1.0
	19	94.4 ± 3.1	85.0 ± 3.6	80.3 ± 6.0	1.4 ± 0.2
	9.6	93.6 ± 4.5	59.7 ± 0.5	55.9 ± 2.2	0.75 ± 0.02
	4.8	92.0 ± 1.2	34.9 ± 2.3	32.1 ± 2.5	1.3 ± 0.2
	2.4	90.3 ± 8.6	19.4 ± 0.4	17.2 ± 2.5	1.0 ± 0.3
	1.2	87.4 ± 9.1	15.9 ± 0.5	13.6 ± 1.4	1.0 ± 0.3
	0.6	89.3 ± 0.8	7.4 ± 0.8	6.6 ± 0.8	8.6 ± 5.5
110	77	91.7 ± 2.1	96.1 ± 0.5	88.1 ± 1.5	3.6 ± 0.2
	39	98.7 ± 1.7	96.0 ± 0.2	94.7 ± 1.8	2.1 ± 0.4
	19	94.0 ± 0.8	89.6 ± 0.4	84.2 ± 1.1	1.3 ± 0.4
	9.6	93.5 ± 2.8	61.0 ± 0.4	57.1 ± 2.1	4.6 ± 0.3
	4.8	86.0 ± 3.5	34.0 ± 2.4	29.2 ± 0.8	6.4 ± 3.1
	2.4	88.2 ± 7.4	18.6 ± 0.3	16.3 ± 1.1	3.4 ± 0.5
	1.2	88.6 ± 3.4	15.7 ± 1.1	13.9 ± 0.4	3.9 ± 1.6
	0.6	88.1 ± 6.1	7.1 ± 0.4	6.2 ± 0.1	5.0 ± 3.3
125	77	90.6 ± 0.5	95.3 ± 0.6	86.3 ± 1.0	1.34 ± 0.01
	39	90.0 ± 5.6	95.1 ± 0.3	85.5 ± 5.1	3.1 ± 2.8
	19	86.7 ± 3.8	90.2 ± 0.5	78.2 ± 3.0	0.6 ± 0.1
	9.6	85.6 ± 4.3	64.0 ± 3.8	54.7 ± 0.5	0.4 ± 0.1
	4.8	82.8 ± 6.2	37.5 ± 4.0	30.9 ± 0.9	1.7 ± 1.4
	2.4	78.6 ± 4.0	21.8 ± 0.2	17.1 ± 1.0	2.0 ± 1.3
	1.2	85.6 ± 0.7	21.3 ± 2.3	18.2 ± 2.1	2.6 ± 0.4
	0.6	82.6 ± 3.5	7.8 ± 1.5	6.4 ± 1.0	2.6 ± 2.3

5.6.7.2 Precursor concentration and reaction time

Another study of the impact of precursor concentration and reaction time was conducted as depicted in **Figure 5.47A**. Drying of [^{18}F]fluoride/[^{18}O]H_2O was performed under identical conditions (13-15 MBq [0.35-0.4 mCi], mixed with 240 nmol of $TBAHCO_3$), and the subsequent fluorination reactions were performed with different amounts of precursor dissolved in the 6 μL

droplet, at 110 °C. All reactions were conducted using thexyl alcohol:MeCN (1:1 v/v) mixture as solvent. Samples on each chip were reacted for different times. Cerenkov images of chips showing residual activity after collection are shown in **Figure 5.47B**. Detailed analyses for each individual reaction are tabulated in **Table 5.21**, and the results are plotted in **Figure 5.6B.**

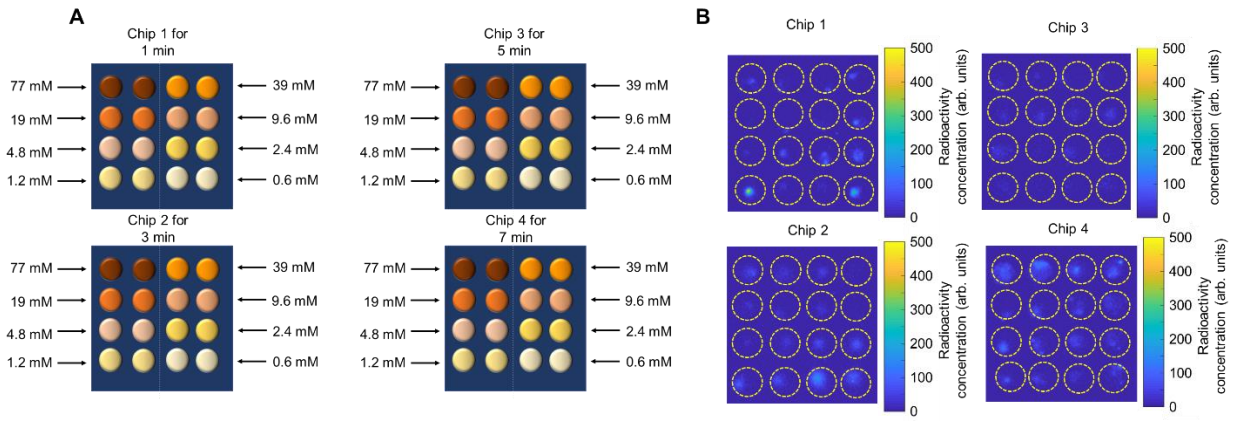

Figure 5. 47 Precursor concentration and reaction time test.

(A) Experimental setup for one set of experiments that explored the influence of reaction precursor amount (8 values) and reaction time (4 types) on the synthesis of [^{18}F]Fallypride. (B) Cerenkov images showing the distribution of the residual activity on each chip after collection of all the crude samples. Brightness is decay-corrected to a common timepoint for all images.

Table 5. 21 Summary of data acquired when exploring the effect of precursor amount and reaction time on the radiosyntheses of [18F]Fallypride.

Time (min)	Precursor concentration (mM)	Collection efficiency (%) n=2	Fluorination efficiency (%) n=2	Crude RCY (%) n=2	Activity left on chip (%) n=2
1.0	77	93.4 ± 0.7	80.5 ± 2.8	75.2± 2.1	4.1 ± 1.0
	39	99.2 ± 4.1	93.3 ± 1.1	92.7 ± 5.0	2.8 ± 0.5
	19	92. ± 6.9	93.4 ± 0.1	86.7 ± 6.4	1.7 ± 0.5
	9.6	90.1 ± 0.5	84.3 ± 2.8	75.9 ± 2.1	3.8 ± 1.0
	4.8	92.9 ± 2.3	72.2 ± 0.9	67.0 ± 2.5	3.6 ± 3.2
	2.4	95.9 ± 2.7	31.0 ± 0.6	29.7 ± 1.4	5.7 ± 2.6
	1.2	93.4 ± 4.7	18.4 ± 0.1	17.2 ± 1.3	5.8 ± 5.4
	0.6	95.9 ± 0.4	11.2 ± 1.3	10.7 ± 1.3	5.6 ± 4.9
3.0	77	93.8 ± 1.2	90.0 ± 0.1	84.4 ± 1.2	3.7 ± 0.5
	39	94.1 ± 1.5	93.9 ± 0.8	88.4 ± 2.2	1.7 ± 1.0
	19	92.9 ± 1.2	92.8 ± 2.5	86.2 ± 1.2	1.9 ± 0.2
	9.6	91.8 ± 2.7	61.3 ± 1.9	56.3 ± 3.4	1.4 ± 0.8
	4.8	93.4 ± 7.4	31.9 ± 3.3	29.9 ± 5.4	2.3 ± 1.3
	2.4	93.1 ± 4.8	15.4 ± 1.3	14.4 ± 2.0	3.6 ± 0.3
	1.2	92.3 ± 1.1	7.9 ± 1.3	7.3 ± 1.1	4.5 ± 0.3
	0.6	101.7 ± 2.1	5.5 ± 0.2	5.6 ± 0.1	8.7 ± 2.4
5.0	77	91.61 ± 0.01	87.0 ± 0.7	79.7 ± 0.7	2.4 ± 0.7
	39	91.0 ± 5.4	89.0 ± 0.2	81.0 ± 5.0	2.4 ± 0.7
	19	94.8 ± 0.4	89.2 ± 1.7	84.5 ± 1.9	3.4 ± 0.7
	9.6	91.6 ± 2.5	63.0 ± 1.5	57.7 ± 3.0	3.7 ± 1.3
	4.8	94.4 ± 7.8	59.2 ± 1.7	55.8 ± 3.0	3.5 ± 2.9
	2.4	93.5 ± 4.6	31.1 ± 5.0	29.2 ± 6.1	2.5 ± 1.2
	1.2	90.8 ± 6.7	16.7 ± 1.6	15.1 ± 0.3	2.1 ± 0.8
	0.6	90.2 ± 8.4	8.2 ± 1.0	7.4 ± 1.6	2.5 ± 1.1
7.0	77	89.7 ± 0.5	88.0 ± 1.1	78.9 ± 1.5	8.0 ± 1.0
	39	93.4 ± 2.1	90.7 ± 0.6	84.7 ± 1.3	5.2 ± 0.6
	19	93.5 ± 6.0	88.5 ± 1.2	82.8 ± 6.5	2.1 ± 0.8
	9.6	93.6 ± 3.7	64.8 ± 2.8	61.5 ± 0.2	2.85 ± 0.04
	4.8	93.8 ± 0.8	39.4 ± 1.1	35.9 ± 1.3	3.31 ± 0.03
	2.4	92.8 ± 8.4	17.5 ± 0.4	10.2 ± 1.9	2.9 ± 0.6
	1.2	93.3 ± 3.3	9.0 ± 0.7	8.4 ± 0.9	2.27 ± 0.05
	0.6	91.2 ± 9.9	5.2 ± 0.6	4.8 ± 1.0	2.7 ± 1.3

5.6.8 Optimization of [^{18}F]FEPPA synthesis

Experiments to explore the effect of reaction temperature were conducted as shown in **Figure 5.48A**. Drying of [^{18}F]fluoride/[^{18}O]H_2O was performed under identical conditions (13-15 MBq [0.35-0.4 mCi], mixed with 240 nmol of $TBAHCO_3$), and the subsequent fluorination reactions were performed at 8 different temperatures for 2 min using 240 nmol of precursor dissolved in the 8 μL droplet in thexyl alcohol: MeCN (1:1, v/v). Though this experiment could be implemented using 4 chips on 4 heaters, since only 4 reaction sites were needed per temperature value, the experiment was instead performed using just 2 chips as follows. A first batch of experiments was performed with heaters 1 and 2 set at 60 and 100 °C, respectively, a second batch with temperatures of 70, 110 °C, a third batch with temperatures of 80 and 120 °C, and a final batch with temperatures of 90 and 130 °C. Cerenkov images of chips showing residual activity after collection are shown in **Figure 5.48B**, and radio-TLC data is shown in **Figure 5.49**. Detailed analyses for each individual reaction are tabulated in **Table 5.22.**

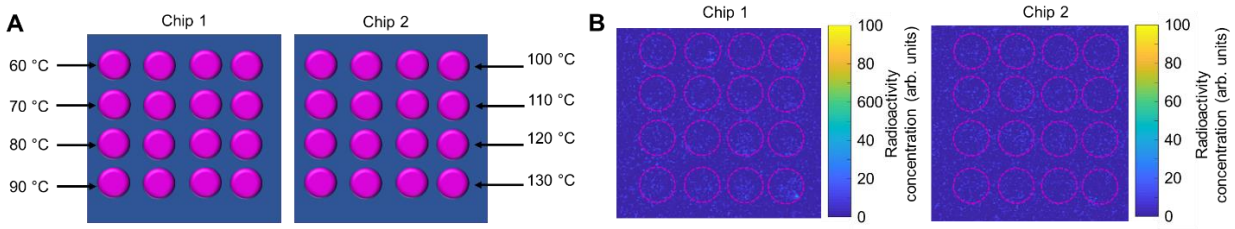

Figure 5. 48 Temperature studies.

(A) Experimental setup for one batch of experiments that explored the influence of reaction temperature (8 values) on the synthesis of [^{18}F]FEPPA. (B) Cerenkov images showing the distribution of the residual activity on each chip after collection of all the crude samples. Brightness is decay-corrected to a common timepoint for all images.

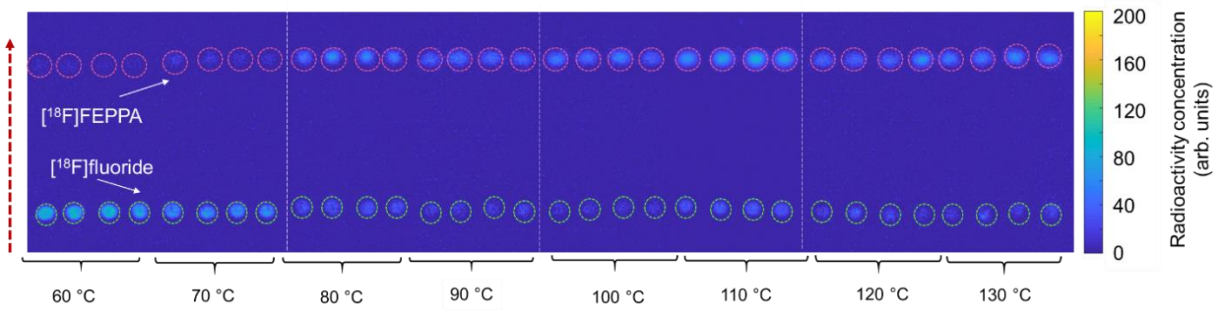

Figure 5. 49 Cerenkov images of TLC plates (each containing 8 samples) after developing in the mobile phase. In this case, each TLC plate contains samples from two different temperatures (n=4 replicates each).

White dotted lines show the edges of each separate multi-sample TLC plate. Dashed circles indicate the ROIs used for analysis. The dashed red arrow indicates the direction of solvent movement during developing.

Table 5. 22 Summary of data acquired when exploring the effect of temperature on the radiosyntheses of [18F]FEPPA.

Temperature (°C)	Collection efficiency (%) n=4	Fluorination efficiency (%) n=4	Crude RCY (%) n=4	Activity left on chip (%) n=4
60	94.1 ± 1.6	11.9 ± 1.8	11.2 ± 1.5	2.5 ± 0.4
70	91.6 ± 1.7	22.8 ± 2.0	20.9 ± 1.7	2.1 ± 0.3
80	91.6 ± 0.9	65.1 ± 1.1	59.6 ± 1.2	1.8 ± 0.2
90	92.7 ± 1.5	77.5 ± 1.6	71.8 ± 1.8	1.7 ± 0.2
100	93.8 ± 1.5	81.3 ± 1.5	76.3 ± 2.6	1.0 ± 0.2
110	92.9 ± 1.9	83.0 ± 1.4	77.1 ± 2.0	1.0 ± 0.3
120	91.4 ± 1.0	75.5 ± 1.8	69.0 ± 1.5	1.2 ± 0.2
130	90.6 ± 1.1	75.2 ± 2.7	68.1 ± 3.0	1.6 ± 0.1

5.6.8.1 Comparison to literature methods

Table 5. 23 Comparison of optimized droplet conditions to literature reports for conventional and flow-chemistry synthesis of [18F]FEPPA.

	This work (2021)	**Chang et al.**(*187*) **(2021)**	**Dahl et al.**(*192*) **(2019)**	**Vignal et al.** (*188*) **(2018)**	**Berroteran-Infante et al.**(*189*) **(2018)**
Synthesizer type	Microscale (droplet format)	Macroscale	Microscale (flow format)	Macroscale	Macroscale
Base type	$TBAHCO_3$	K_{222} / K_2CO_3	K_{222} / $KHCO_3$	K_{222} / K_2CO_3	K_{222} / K_2CO_3
Base amount (nmol)	240	28000/ 20000	2000/2000	40000/22000	58000/32000
Precursor amount (nmol)	240	9000	9000	9000	12000
Reaction solvent	thexyl alcohol: MeCN (1:1 v/v)	MeCN	MeCN	MeCN	MeCN
Reaction volume (mL)	0.008	0.6	0.2	1	0.5
Temperature (°C)	90	90	80	90	90
Reaction time (min)	2	10	10	10	10
Starting activity (MBq [mCi])	13.8 [0.375]	N.R.	3700 [100]	N.R.	N.R.
Fluorination efficiency (%)	88.5 ± 0.9 (n=4)	N.R.	N.R.	N.R.	N.R.
Crude RCY (decay-corrected; %)	80.7 ± 1.2 (n=4)	N.R.	N.R.	N.R.	N.R.
Activity yield (%)	53 (n=1)	30 ± 2 (n=8)	29*	34 ± 2 (n=17)	38 ± 3 (n=15)
RCY (decay-corrected; %)	67 (n=1)	50 ± 2 (n=8)	51 ± 6 (n=3)*	48 ± 2 (n=17)	46 ± 3 (n=15)
Synthesis time (min)	30	80	55*	55	30

* Isolated yield without formulation
N.R. = not reported.

5.6.9 Representation of chromatograms

5.6.9.1 [^{18}F]Flumazenil

Crude [^{18}F]Flumazenil was injected in HPLC to isolate the product (**Figure 5.50A**). A subsequent injection was performed to confirm purity (**Figure 5.50B**), and a co-injection with Flumazenil reference standard was performed to confirm product identity (**Figure 5.50C**). The crude product showed minimal UV impurities.

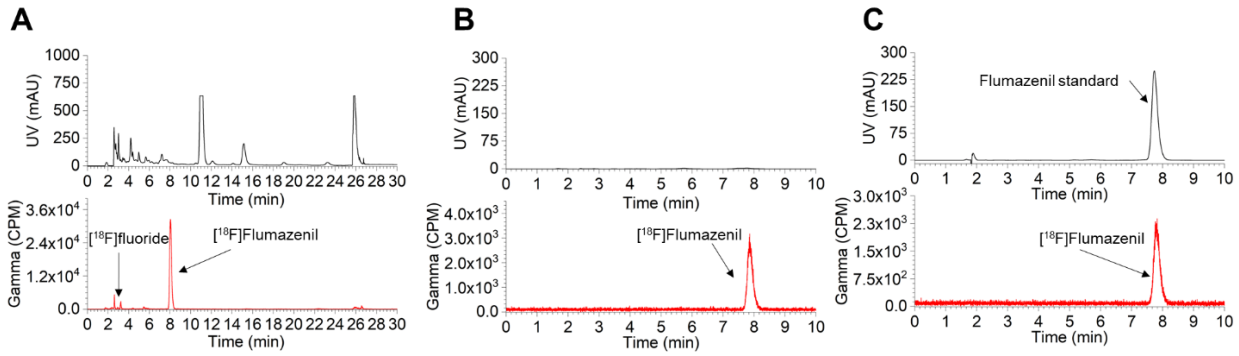

Figure 5. 50 HPLC chromatograms of [18F]Flumazenil.

(A) Crude product. (B) Isolated product. (C) Co-injection with reference standard.

5.6.9.2 [^{18}F]PBR06

Crude [^{18}F]PBR06 was injected in HPLC to isolate the product (**Figure 5.51A**). A subsequent injection was performed to confirm purity (**Figure 5.51B**), and a co-injection with PBR06 reference standard was performed to confirm product identity (**Figure 5.51C**). The crude product showed minimal UV impurities.

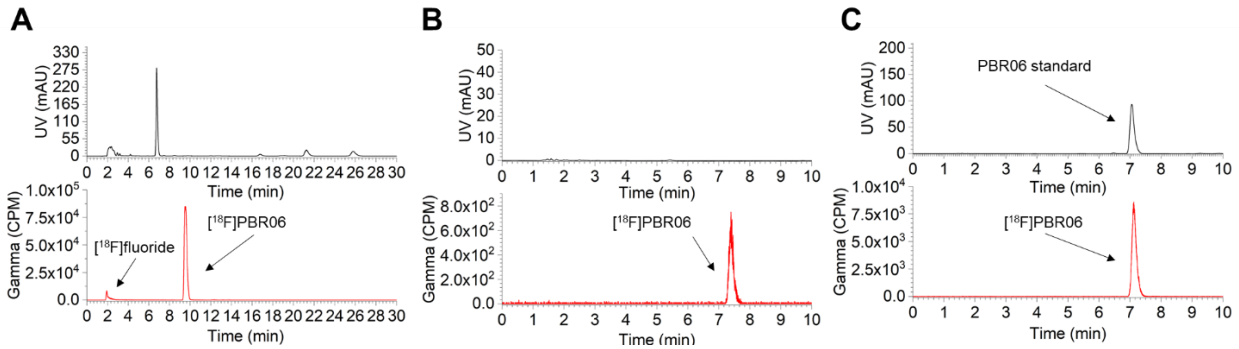

Figure 5. 51 HPLC chromatograms of [18F]PBR06.

(A) Crude product. (B) Isolated product. (C) Co-injection with reference standard.

5.6.9.3 [^{18}F]Fallypride

Crude [^{18}F]Fallypride was injected in HPLC to isolate the product (**Figure 5.52A**). A subsequent injection was performed to confirm purity (**Figure 5.52B**), and a co-injection with Fallypride reference standard was performed to confirm product identity (**Figure 5.52C**). The crude product showed minimal UV impurities.

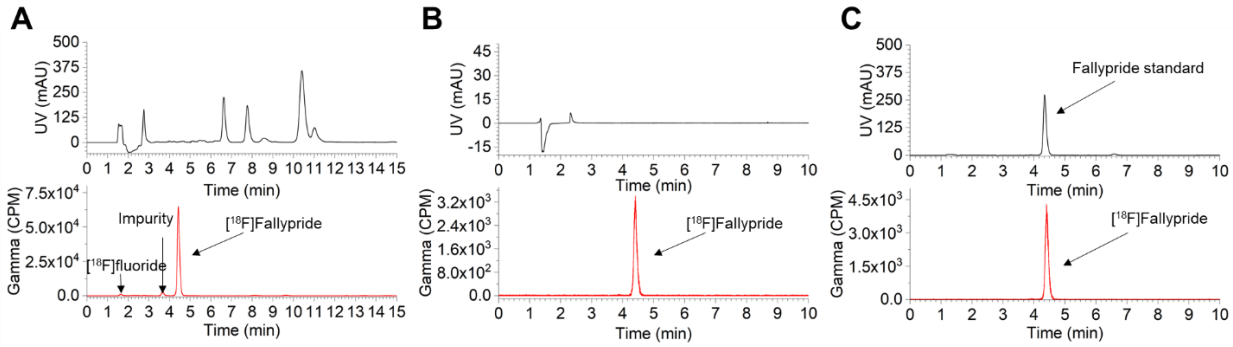

Figure 5. 52 HPLC chromatograms of [18F]Fallypride.

(A) Crude product. (B) Isolated product. (C) Co-injection with reference standard.

5.6.9.4 [^{18}F]FEPPA

Crude [^{18}F]FEPPA was injected in HPLC to isolate the product (**Figure 5.53A**). A subsequent injection was performed to confirm purity (**Figure 5.53B**), and a co-injection with FEPPA reference standard was performed to confirm product identity (**Figure 5.53C**). The crude product showed minimal UV impurities.

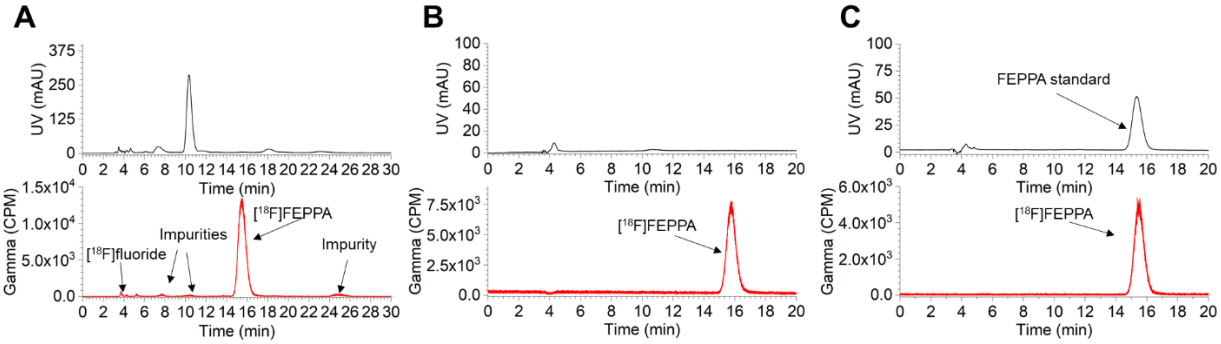

Figure 5. 53 HPLC chromatograms of [18F]FEPPA.

(A) Crude product. (B) Isolated formulated product. (C) Co-injection with reference standard.

5.6.10 Clinical-scale radiosynthesis

Summaries of high activity droplet syntheses of [^{18}F]PBR06 carried out with different starting activity are shown in **Table 5.24** and **Figure 5.54.**

Table 5. 24 Synthesis performance of [18F]PBR06 at increased activity levels.

Starting activity (MBq [mCi])	Number of replicates	Collection efficiency (%)	Fluorination efficiency (%)	Crude RCY (%)
14.1 [0.38]	n=4	95.8 ± 3.5	96.5 ± 0.9	92.4 ± 3.0
651 [17.6]	n=1	94.0	87.1	81.0
1120 [30.3]	n=1	90.3	80.9	73.0
2200 [59.7]	n=1	90.9	68.6	62.4
2390 [64.7]	n=1	89.5	88.7	71.5
2960 [80.8]	n=1	91.0	79.3	72.1
3170 [85.6]	n=1	90.3	65.6	59.2

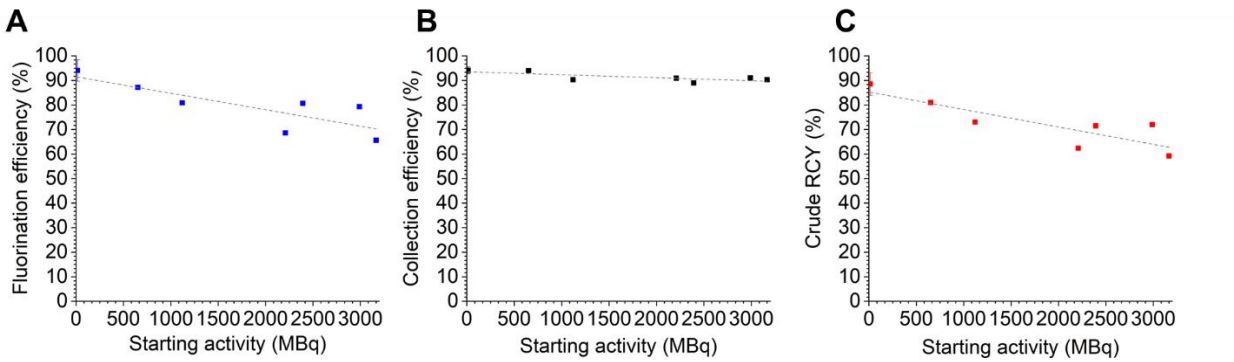

Figure 5. 54 Comparison of [18F]PBR06 synthesis performance for different starting activities.

(A) Fluorination efficiency. (B) Collection efficiency. (C) Crude RCY.

Chapter 6: A base free, universal [^{18}F]fluoride source cleaning and concentration for scale-up of microscale reactions to GBq levels.

6.1 Introduction

Positron emission tomography (PET) has become an indispensable method for patient diagnostics, monitoring response to drug treatment, and developing new therapeutics(*199*). PET uses biologically active molecules tagged with a short-lived positron-emitting radioisotopes that allow dynamic *in vivo* measurements of specific biochemical processes. The majority of such PET radiopharmaceuticals with regulatory approval and in clinical trials are labeled with F-18, due to its wide availability, high positron decay ratio (97%), moderate half-life (109.8 min), and good imaging resolution(*163*). Preparation of these compounds is expensive due to the high cost of the radiosynthesizer, radiation shielded facilities, reagents and radioisotope for each batch, and skilled personnel needed to operate the equipment.

For more than a decade, there has been an increase in the use of microreactors for the performance of radiochemical reactions due to the substantial cost reduction on production through the lower consumption of expensive reagents, small system footprint, and possible reduction of shielding(*29,49*). In addition, increase in yield can be increased due to rapid mixing of reagents, short evaporation times, and higher concentration of radionucleotide(*49*). While there have been several prototypes that leverage the advantages of microfluidics for PET radiopharmaceuticals, most focus on production for preclinical use(*32,79,200,201*). Recently, activity scale-up has been shown using a miniature trap and release process for the increase of activity on microdroplet reactions (e.g., up to 20 clinical doses of [^{18}F]Fallypride)(*30,47,62,71*). Another method that allowed the increase of activity on microdroplets was the dispensing and drying of relatively large amounts of activity by loading 30 µL droplets onto the chip, evaporating

them, and repeating until the desired activity is concentrated on the chip (e.g., up to 2 clinical doses of [^{18}F]FET and [^{18}F]Florobetaben(*63*)). Subsequent reactions were performed in 10 µL volumes, utilizing 4 mm reactor droplet trap reactors(*63*).

While both methods successfully enabled the production of clinical doses using a microfluidic chip, the results showed that with the increase of starting activity there was a decrease in the radiochemical yield of the reactions. The use of the microscale concentration method for the production of [^{18}F]Fallypride at high activities (ranging from 3.7 GBq to 41 GBq [0.10 Ci to 1.1 Ci]) showed a decrease in the crude RCY from 65% to 25% as the overall starting activity increased. The one factor that led to the decrease in the overall crude RCY was the drop in fluorination efficiency from 90% to 40%(*62*). Furthermore, utilizing microscale concentrations methods, increased activity scales led to lower [^{18}F]fluoride trapping on QMA resin (from ~94% to ~63%)(*62*). While mock experiments using KF showed 100% trapping efficiency with a mock sample of 37 MBq (1 Ci) (i.e., 50 µM KF) with the mass of 3 mg of QMA resin(*62*), the experiments with 37 GBq of activity showed that 3 mg of QMA only trapped ~63% of the activity.

The concentration of activity on chip via the dispensing and drying method allowed the desired amount of activity to be use without any losses during the concentration process. To increase the amount of starting activity on chip using the dispensing and drying method, more volume from the activity source needs to be dried on the reaction site. However, similar observations on the decrease of overall crude RCY for the production of [^{18}F]FET, [^{18}F]FBB, and [^{18}F]BPR06 were observed(*61*,*63*). In the case of [^{18}F]FET the overall crude RCY was reduced (from ~70% to ~40%) by the decrease in both the collection efficiency and fluorination efficiency as the starting activity increased from 0.2 to 4 GBq. Similarly, [^{18}F]FBB showed a decrease in the overall crude RCY from ~60% to ~40% as activity amount increases (from 0.02 to 4 GBq) due to the decrease in collection and fluorination efficiency(*63*). The dispensing and drying method to increase the amount of starting activity was also applied to the synthesis of [^{18}F]PBR06, while no decrease on the collection efficiency was observed as the amount of staring activity increased

like in the cases of [^{18}F]FET and [^{18}F]FBB (due to the lack of deprotection step), the fluorination efficiency of the reaction decreased from ~97% at 14.1 MBq (0.38 mCi) to ~65% at 3170 MBq (85.6 mCi), which led to the overall decrease of the crude RCY from ~90% at low activity to ~60% at high activities(*61*).

Many potential reasons for this decrease in observed yield could be due to: radiolytic degradation, stochiometric change in the precursor to contaminant [^{19}F]fluoride species, increased concentration of contaminant anionic impurities, increased concentration of any residual cationic impurities in the [^{18}F]fluoride solution introduced into the reactor. (i) Radiolysis is the process of chemical bond cleavage caused by radiation mediated by radicals, which can lead to the reduction in yield of the desired radiolabeled molecule and the formation of side products(*202–204*). The degree of radiolysis is related to the activity concentration in solution and the geometry of the activity volume(*205*). (ii) As activity is scaled up contaminant concentrations of [^{19}F]fluoride species can begin to outweigh the concentration of [^{18}F]fluoride, leading to a stochiometric precursor ratio that could have a significant [18F]fluoride labelled product yield impact(*46*). Since reaction conditions are optimized at lower activities (i.e., 15MBq [0.41 mCi])(*61*) and therefore lower source volumes, the conditions may no longer be optimal when the total amount of source is increased by orders of magnitude. (iii) Anionic impurities could be in abundances large enough to outcompete fluoride, labelling precursor and reducing the overall fluoride reactivity. (iv) It has been noted that metal contaminants are produced during bombardment of [^{18}O]water in a cyclotron for [^{18}F]fluoride production(*206*). For example, inorganic cationic impurities that come from parts of the target (body, foils) during the bombardment can dramatically decrease the synthesis yield by either reacting with the [^{18}F]fluoride to produce insoluble salts or to reduce its nucleophilicity(*207*).

In this chapter we explore approaches to look at these factors independently with the aim of determine the cause(s) of reduced yield so that it can be address for reaction scale-up. As part

of this study, we develop an improved method for [^{18}F]fluoride concertation that can enhance the removal of contaminants while remaining fast and able to concentrate arbitrary activity volumes into 100-80 µL that can rapidly be loaded and dried on the microdroplet chips. Compared to previous QMA methods, it involves additional cartridges and filtration steps to remove impurities, and also uses a volatile base for elution that enables “base free” elution of [^{18}F]fluoride to better decouple the fluoride concentration process from the downstream reaction, enabling base type and amount to be optimized independently for each tracer synthesis.

6.2 Materials and Methods

6.2.1 Materials

Anhydrous acetonitrile (MeCN, 99.8%), 2,3-dimethyl-2-butanol (thexyl alcohol, 98%), 4,7,13,16,21,24-hexaoxa-1,10-diazabicyclo[8.8.8]hexacosane (K_{222}, 98%), triethylamine (TEA, 99%), trifluoroacetic acid (TFA, >99%), tetrahydrofluran (THF, >99.9%, inhibitor-free), hexanes (95%), dichloromethane (DCM, >99.8%), acetone (99.5%), ammonium formate (NH_4HCO_2: 97%), ethylene glycol (99.8%) and potassium carbonate (K_2CO_3, 99.995%), and Chelex 100 (Sodium form, 50-100 mesh) resin were purchased from Sigma-Aldrich (St. Louis, MO, USA). Kimwipe (1-ply, cellulose) was purchased from Fisher Scientific (Pittsburgh, PA, USA). Strong cation exchange resin (SCX; 35-60 µm, 300 A) were purchased from Altech (USA). Sep-Pak Plus QMA Light cartridges (37-55 µm particle size) were purchased from Water Corporation (Milford, MA, USA). PTFE tubing (1/8” OD, 1/16” ID; 1530L. 1/16” OD, 0.04” ID; 1517L, 1/16” OD, 0.01” ID; 1529L) was purchased from IDEX Health and Science (Wallingford, CT, USA). n-butanol (n-BuOH, 99%) was purchased from Alfa Aesar (Ward Hill, MA, USA). Tetrabutylammonium bicarbonate ($TBAHCO_3$, 75mM in ethanol), 2-((2,5-dimethoxybenzyl)(2-phenoxyphenyl)amino)-2-oxoethyl 4-methylbenzenesulfonate ([^{18}F]PBR06 precursor, >95%), 2-fluoro-N-(2-methoxy-5-methoxybenzyl)-N-(2-phenoxyphenyl)acetamide (reference standard for [^{18}F]PBR06, >95%), tosyl fallypride (fallypride precursor, >90%), Fallypride (reference standard, >95%), acetamide,

N-[2-[2-[[(4-methylphenyl)sylfonyl]oxy]ethoxy]phenyl]methyl]-N-(4-phenoxy-3-pyridinyl) ([^{18}F]FEPPA precursor, >90%), and N-acetyl-N-(2-fluoroethoxybenzyl)-2-pehonoxy-5-pyridinamine (reference standard for [^{18}F]FEPPA, >95%) were purchased from ABX Advanced Biochemical Compounds (Radeberg, Germany). DI water was obtained from a Milli-Q water purification system (EMD Millipore Corporation, Berlin, Germany). No-carrier-added [^{18}F]fluoride was produced by the (p, n) reaction of [^{18}O]H_2O (98% isotopic purity, Huayi Isotopes Co., Changshu, Jiangsu, China) in an RDS-111 cyclotron (Siemens, Knoxville, TN, USA) at 11 MeV, using a 1.2 mL silver target with havar foil.

6.2.2 Methods

6.2.2.1 Ionic Exchange Theory

Previous reports have shown that various metal impurities arise during the production of [^{18}F]fluoride in medical cyclotrons(*208,209*). In addition to the ubiquitously used quaternary methylammonium (QMA) cartridge to trap and release fluoride in conventional systems, strong cation exchange (SCX) cartridges are also used in many cases such as aluminum fluoride (AlF) chemistry(*210*,*211*). Reagents prior to addition to the metal fluoride complex, need to be depleted of trace metals that can be introduced through their various production methods.

SCX cartridges have previously been used in conjunction with microscale [^{18}F]fluoride concentration to eliminate contaminants that could interfere with trapping on the QMA micro-cartridge(*62*). However, because SCX resin primarily interacts with positively charged basic compounds such as amines or cations (1+ charge), we sought to enhance this approach with additional resin to remove multivalent metal ions in greater specificity. Chelex consists of a stryrine-divinylbenzene copolymer functionalized with iminodiacetate ions that act as chelator groups for the binding of polyvalent metal ions, with high specificity to divalent cations. It is important to note that Chelex resin utilized in its sodium form cannot be used on its own or downstream of the SCX, since Na^+ would be displaced for each trapped metal ion. This Na^+ can interfere with the efficiency of the downstream radiofluorination reactions, due to the

nucleophilicity of Na^+ to fluoride. Thus, Chelex resin was placed upstream of the SCX cartridge. The SCX cartridge in its H^+ form, allows the efficient exchange of Na^+ which will not interfere with downstream radiofluorination.

[^{18}F]fluoride, and contaminant species are first directed through the Chelex resin, capturing polyvalent cations, and releasing Na+. [^{18}F]fluoride, anionic impurities, monovalent cations, and Na^+ ions are then directed through the SCX resin. This SCX resin captures monovalent cations, exchanging H^+. [^{18}F]fluoride, anionic impurities, and H^+ are then directed to the QMA. The QMA traps the [^{18}F]fluoride and anionic impurities. Sequential washing of the QMA, ensures that residual cationic contaminants are removed prior to the concentration of [^{18}F]fluoride. Cationic species (e.g., K^+ (from K_2CO_3), and TBA^+ (from $TBAHCO_3$)) are often then mixed with phase transfer catalysts (K_{222} or TBA^+) to release [^{18}F]fluoride in a nucleophilic form suitable for radiofluorination.

6.2.2.2 Remote [^{18}F]fluoride processing

A remote processing apparatus was developed to allow the processing of [^{18}F]fluoride (**Figure 6.1**). A series of vials can be pressurized with an external N_2 source, then flow paths can be effectively switched with the use of a selector valve for different processes. In the initial trapping process, the source vial is pressurized (~18 psi) and directed though the Chelex, SCX into an intermediate vial. Once the cartridges are blown dry, a secondary vial downstream of the eluent path is pressurized (~18 psi), to direct the activity through the QMA path. The activity in the trapping configuration, passes through the QMA, through line 1 of the selector valve, and into a vial marked for waste. To wash the path of this initial trapping, both pressure to the source and vial downstream of the eluent are reduced to 0. Preloaded water (1 mL), is pressurized ahead of the source vial, filling the source vial for rinsing the path length previously used. The source once full is pressurized (~18 psi), and the water is directed through the Chelex and SCX cartridges, into the intermediate hold vial. The vial downstream of the eluent is pressurized, directing water through the QMA and line 1 of the selector valve into waste. Nitrogen is directed through the line

to ensure complete drying of the QMA cartridge prior to elution of the concentrated activity. Pressure to the various vails is halted, and eluent is loaded remotely outside of the hot cell into the eluent vial (~100 µL). The eluent vial is sealed, then pressurized (~18 psi), delivering the eluent to the vial used previously for pressurization downstream, and into the intermediate vial. The line through the valve selector is switched to line 2, that is directly connected to an empty vial for capture of the concentrated activity. The eluent in the intermediate vial through pressurization is then directed through the QMA, through the selector valve and into the empty vial. To ensure complete recovery of the eluent solution through the path length, the vial downstream of the eluent vial is additionally pressurized (~18 psi), for an additional minute. The system is completely depressurized until recovery of the concentrated activity.

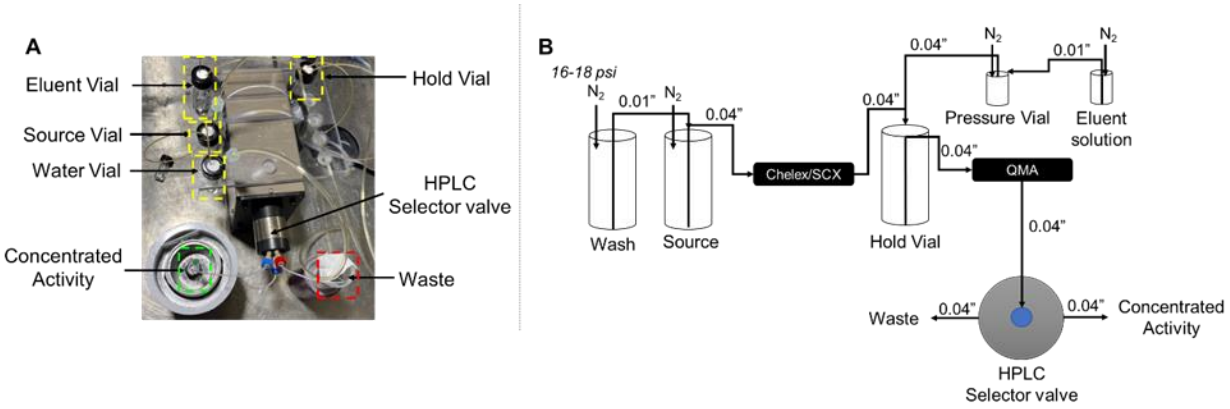

Figure 6. 1 Trap and release apparatus for the removal of metallic contaminants and concentration of [18F]fluoride.

(A) Photograph of the apparatus set up showing the placement of vials for the trap and release process of activity. (B) Schematic of the apparatus indicating the liquid direction throughout the system, the inner diameter of the connected PTFE tubing, and the vials where N_2 pressure was applied for the movement of the liquid.

6.2.2.3 Reagent preparation

Eluent solution (100 µL) was composed of 20 nmol/µL of TEA (aq.). [^{18}F]PBR06 precursor stock solution contained 20 mM precursor in a 1:1 v/v mixture of thexyl alcohol and MeCN. [^{18}F]Fallypride stock solution contained 39 mM of precursor in a 1:1 (v/v) mixture of theyxl alcohol and MeCN. [^{18}F]FEPPA stock solution contained 30 mM of precursor in a 1:1 (v/v) mixture of

theyxl alcohol and MeCN. The collection solution for [^{18}F]PBR06, [^{18}F]Fallypride, and [^{18}F]FEPPA was a 9:1 v/v mixture of MeOH and H_2O. 240 nmol of $TBAHCO_3$ base phase transfer catalyst was added to the concentrated activity volume after processing (i.e., the amount needed for the droplet-based synthesis of these 3 tracers(*61*)). TLC mobile phases for each tracer were similar to those reported in **Chapter 5.**

6.2.2.4 Micro-cartridge fabrication

Cationic impurities were removed with 10 mg of Chelex resin and 30 mg of SCX resin, which were packed into an 8” length of 1/8” OD 1/16” ID PTFE tubing. A small Kimwipe was torn and inserted into the tubing segment to act as a frit. Using a needle cleaning rod from a spinal needle (Quincke Spinal Needle, BD Biosciences, San Jose, CA, USA) it was positioned at about 7” away from the inlet and secured within the tubing by pinching the tube just downstream of the frit. A slurry of the SCX resin was prepared by adding 30 mg of the resin in 500 µL of ion chromatography (IC) grade water (Sigma-Aldrich, St. Louis, MO, USA). A syringe fitting was connected to the exit of the tubing, and a 1 mL syringe was connected to pull the slurry from the inlet side of the tubing. After complete, the resin container was filled with an additional 1 mL of IC water and the procedure repeated. A second frit was then inserted upstream of the SCX resin bed. A slurry of Chelex resin was prepared by dispersing 10 mg of the resin in 500 µL of IC water, repeating the packing procedure detailed above. A final frit was inserted upstream of the Chelex resin, secured by deforming the tubing upstream of this frit. (Resin masses for both Chelex and SCX ranged from 3 mg to 30 mg during the optimization phase.) The QMA cartridges were prepared in a similar fashion with 9 mg of resin packing into 1/16” OD, 0.04” ID tubing (3 to 9 mg were explored during optimization).

The purchased QMA resin consisted of quaternary methylammonium groups prepared with a bicarbonate counter ion. While complete conversion of the HCO_3^- form to the HO^- form is impossible, we treated the QMA resin (~1 g) with 1 N NaOH (10 mL) for 20 min. in a glass beaker with a stir bar. The treated resin was then transferred to an SPE tube fitted with a polyethylene

filter (20 µm), then rinsed with 3x 20 mL of IC water. At the end of this washing volume, the pH of the exiting water was tested to confirm a range of 6-7. The resin packed in the SPE tube was dried with N_2 (10 psi) for 60 min. Dried resin could be recovered from the SPE tube by gently tapping the tube into a capture falcon tube. QMA micro-cartridges were packed just prior to use to avoid the potential for microbial contamination. Conversion of the QMA was performed to avoid the deposition of bicarbonate salt residues, that could poison downstream radiofluorination. **Figure 6.2** shows that the residue of QMA resin in the HCO_3^- form, leaves increasing deposits as a function of base mass used during the elution process. When the QMA is in the HO^- form, this salt deposition is not observed.

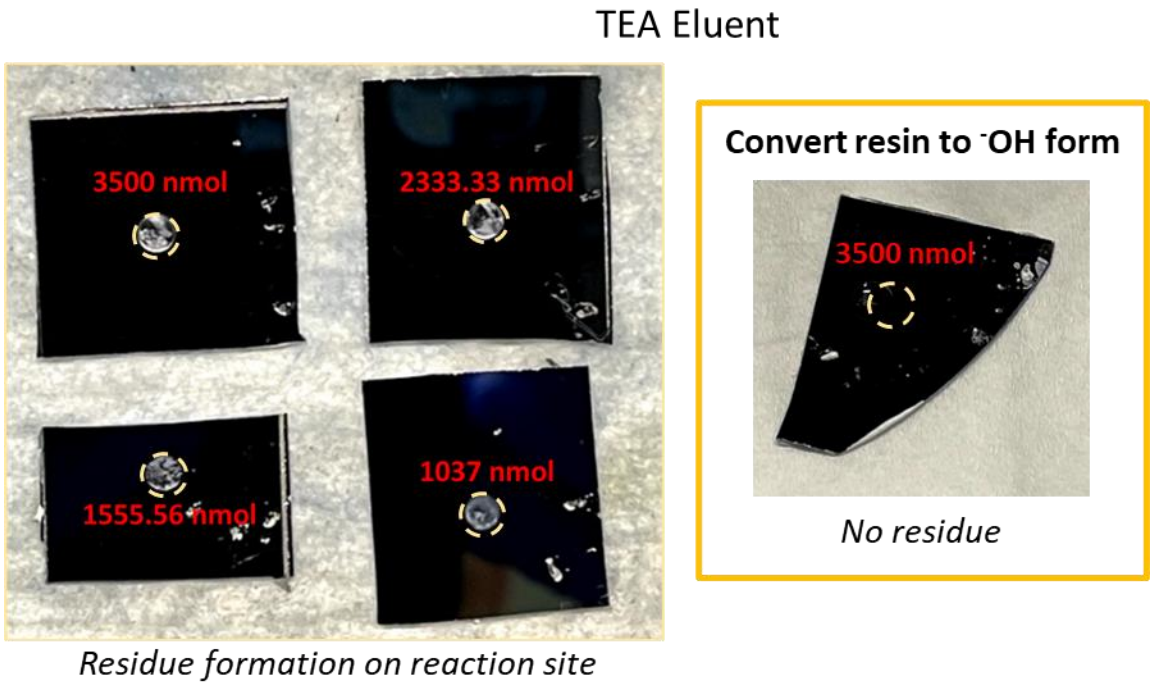

Figure 6. 2 Residue formation on reaction site after elution of activity through QMA micro-cartridge using different amounts of TEA.

Four chips on the left show the formation of white residue on the reaction site after drying activity volume eluted using 3500-1037 nmol of TEA, activity was eluted through QMA micro-cartridges that contained bicarbonate counter ions. Chip on the right shows the reaction site after drying the activity eluted through a QMA that was treated to contain hydroxyl counter ions, no residue was shown when using high amounts of TEA. Yellow circles show the reaction site on the chip.

6.2.2.5 Micro-cartridge trapping visualization

To optimize the resin amount of QMA needed for efficient [^{18}F]fluoride trapping, were Cerenkov luminescence imaging (CLI) was used. The QMA micro-cartridge was taped into the field of view (FOV) of the Cerenkov setup (**Figure 6.3**) to observe the distribution of radioactivity on cartridges in real-time during trapping, washing, and elution of the [^{18}F]fluoride. Additional measurements of waste activity, residual source vial activity, the eluted concentrated activity vial, and the residual cartridge activity were made at the end of the experiment to quantify trapping efficiency (and breakthrough), losses during washing, and elution efficiency.

Visualization of the cartridges was performed using a previously-described home-built CLI setup(*77*). The cartridge was enclosed in a light-tight apparatus, then connected to its respective source (**Figure 6.3**). The source was pressurized so that it allowed a drip rate of exit solution at a rate similar to the remote apparatus described above (~1 psi). Once the vial was pressurized, the light-tight enclosure was closed, then the QMA imaged for 1 s over 100 frames. Due to the readout of the camera, each frame represents a 3 s delay (e.g., frame 1 denotes 1 s, and frame 2 denotes 4 s). Following the collection of the CLI frames, pressure through the QMA was halted, and a brightfield image was taken for 7 ms. This brightfield image, allows user section of the QMA bed for activity breakthrough analysis in the MATLAB processing described below.

The CLI frames were imported into MATLAB and processed as previously described(*128*). After frame 1 is imported into MATLAB, a script was written that allows the selection of the brightfield image for overlay in the video file. The user after the CLI and brightfield image is overlaid, is asked to define the boundaries of the cartridge. The pixel intensity across this defined ROI is measured for each frame by the program. Overlays of the CLI and brightfield images, the pixel intensity distribution across the cartridge, and the gaussian smoothing of this profile are all written into separate video files for analysis by the user.

6.2.2.6 Micro-cartridge concentration efficiency determination

characterize trapping and elution efficiency, various radioactivity measurements were made with a calibrated dose calibrator (CRC-25 PET, Capintec, Inc., Ramsey, NJ). For the purposes of calculations, all radioactivity measurements were decay-corrected to a common timepoint. Measurements were made of the activity in the [^{18}F]fluoride source vial before trapping ($A_{0\ source}$), activity in the source vial after trapping (A_{source}), activity in the [^{18}O]H_2O recovery vial after trapping (A_{waste}), and the collected activity after elution ($A_{collect}$). The activity on the cartridge after trapping ($A_{cartridge}$) was determined indirectly (i.e., calculated as $A_{0\ source} - (A_{waste} + A_{source})$) to minimize radiation exposure. This method also proved to be significantly more accurate than directly measuring the cartridge in the dose calibrator, presumably due the differing geometry of the cartridge compared to the vials. Trapping efficiency (%) was computed as $A_{cartridge}/(A_{0\ source} - A_{source})$. Elution efficiency (%) was calculated as $A_{collect}/A_{cartridge}$. Recovery efficiency (%), defined as the amount of activity recovered following elution relative to starting activity, was calculated as trapping efficiency x elution efficiency. Starting activity was defined as $A_{0\ source} - A_{source}$ which can be approximated as $A_{0\ source}$ since we found $A_{source} < \sim 0.1\%$ of $A_{0\ source}$.

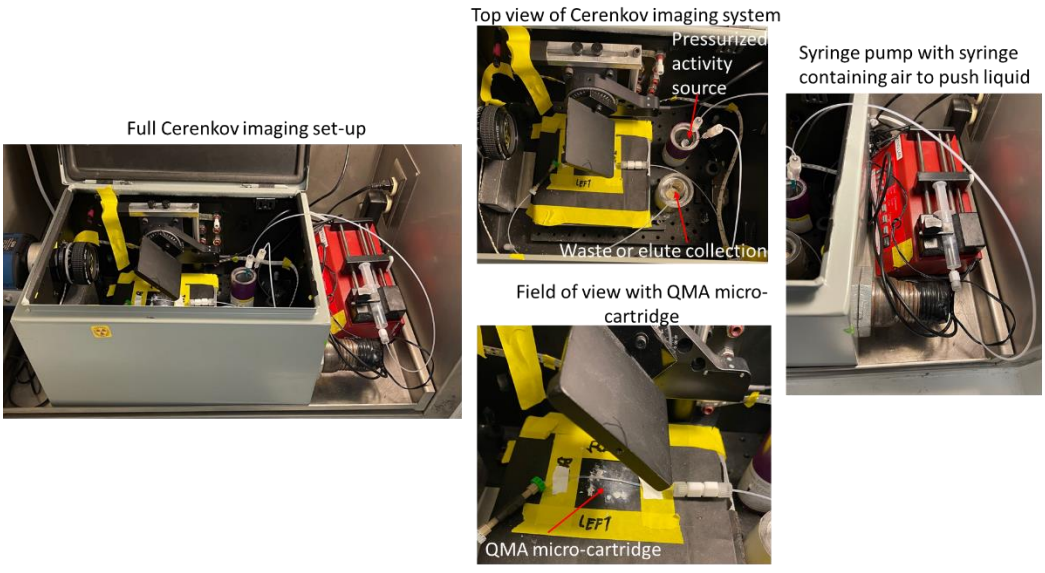

Figure 6. 3 Visualization apparatus utilized for QMA mass optimization studies.

6.3 Results

6.3.1 Scale-up via increased volume of radioisotope source

In addition to examining in previous work the impact of activity scale-up (via loading multiple increments of [^{18}F]fluoride/[^{18}O]water directly from the cyclotron) on the optimized synthesis of [^{18}F]PBR06(*61*), we explored scaling the activity in the syntheses of [^{18}F]Fallypride and [^{18}F]FEPPA. The volume of activity solution loaded and dried on the reaction site varied from 40 to 180 µL, corresponding to activity levels of 740 to 3000 MBq (20 to 80 mCi). Activity concentration varied from day to day due to the production of different amounts of activity. **Figure 6.4** and **Table 6.1** show the trends observed for the collection efficiency, fluorination efficiency, and crude RCY for [^{18}F]Fallypride, and **Figure 6.5** and **Table 6.2** show the results for [^{18}F]FEPPA. Both radiosynthesis exhibited a decrease in overall performance with increased starting activity.

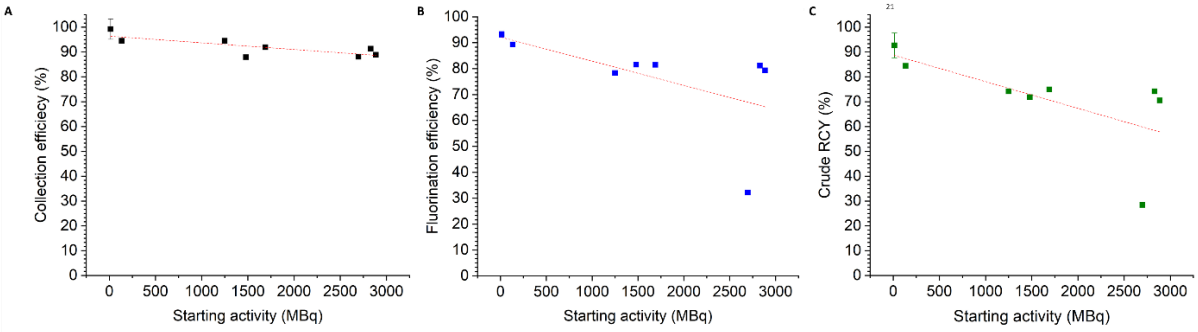

Figure 6. 4 Microscale reaction performance of [18F]Fallypride with variant activity scales.

(A) Collection efficiency, (B) Fluorination efficiency, and (C) Crude RCY performance. Activity scale was varied by using different volumes of the radioisotope source solution.

Table 6. 1 Synthesis performance of [18F]Fallypride at increased activity levels.

Starting activity (MBq [mCi])	Number of replicates	Collection efficiency (%)	Fluorination efficiency (%)	Crude RCY (%)
14.1 [0.38]	n=2	99.2 ± 4.1	93.3 ± 1.1	92.7 ± 5.0
135 [3.6]	n=1	94.5	89.3	84.4
1250 [34.0]	n=1	94.9	78.3	74.2
1480 [40.0]	n=1	87.9	81.6	71.8
1690 [46.0]	n=1	91.9	81.5	74.9
2700 [73.0]	n=1	88.1	32.2	28.4
2800 [76.0]	n=1	91.3	81.2	74.2
2900 [78.0]	n=1	88.9	79.3	70.5

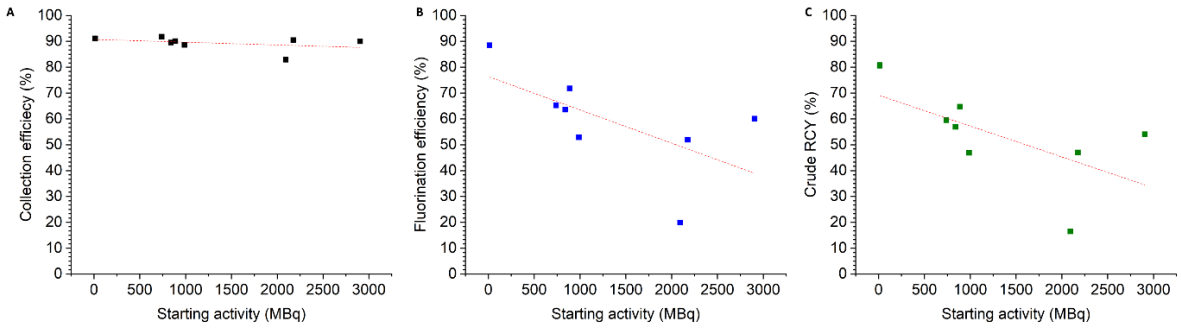

Figure 6. 5 Radiosynthesis performance of [18F]FEPPA with activity using microdroplets.

(A) Collection efficiency, (B) Fluorination efficiency, and (C) Crude RCY performance.

Table 6. 2 Synthesis performance of [18F]FEPPA at increased activity levels.

Starting activity (MBq [mCi])	Number of replicates	Collection efficiency (%)	Fluorination efficiency (%)	Crude RCY (%)
14.0 [0.38]	n=2	91.1 ± 0.4	88.5 ± 0.9	80.7 ± 1.2
740 [20.0]	n=1	91.8	65.2	59.5
800 [23.0]	n=1	89.5	63.6	56.9
900 [24.0]	n=1	90.1	71.8	64.7
1000 [27.0]	n=1	88.6	52.9	46.9
2100 [57.0]	n=1	82.9	19.9	16.5
2200 [59.0]	n=1	90.5	51.9	47.0
2900 [79.0]	n=1	90.0	60.1	54.1

6.3.2 Study of impact of source volume at constant activity scale

In the previous experiments, increasing the activity was achieved using a higher volume of source activity, with multiple potential causes of the reduced reaction performance. To eliminate the impact of radiolysis, we performed similar experiments using different volumes of decayed activity source (i.e., which would have the same amount of cyclotron impurities and total fluoride as the activity solution before decay) spiked with low volumes of source (2 µL) to ensure low activity (14.1 MBq [0.38 mCi]) and 240 mol of $TBAHCO_3$. 2x2 multi-reaction microdroplet chip was used to explore 4 different such volumes (0, 50, 130, and 230 µL). For the reaction site that did not contain any decayed source, 200 µL of IC water was used instead. To perform the study, activity was loaded to the reaction site in 30 µL increments. The syntheses of [^{18}F]PBR06, [^{18}F]Fallypride, and [^{18}F]FEPPA were each performed at the difference volume scales.

We noticed an increase of white residue on the reaction site with the increase of decayed source volume (**Figure 6.6**).

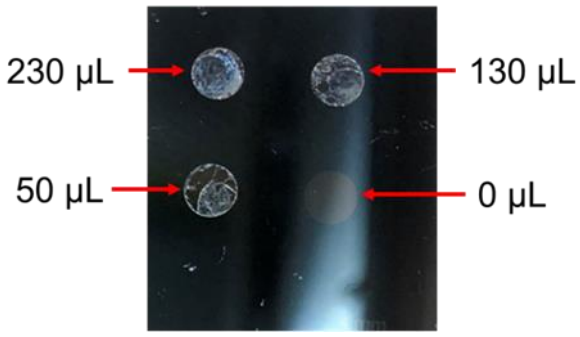

Figure 6. 6 Photograph of 2x2 microdroplet chip after drying decay source volume mixed with 14.1 MBq of activity and 240 nmol of base.

This observed a decrease in reaction performance for each radiopharmaceutical as the decay source volume increased, was similar to the effects seen with drying increasingly large volumes of source. The most noticeable change was in the fluorination efficiency of each reaction though we also noticed a decrease in the collection efficiency due to loss of activity on the chip.

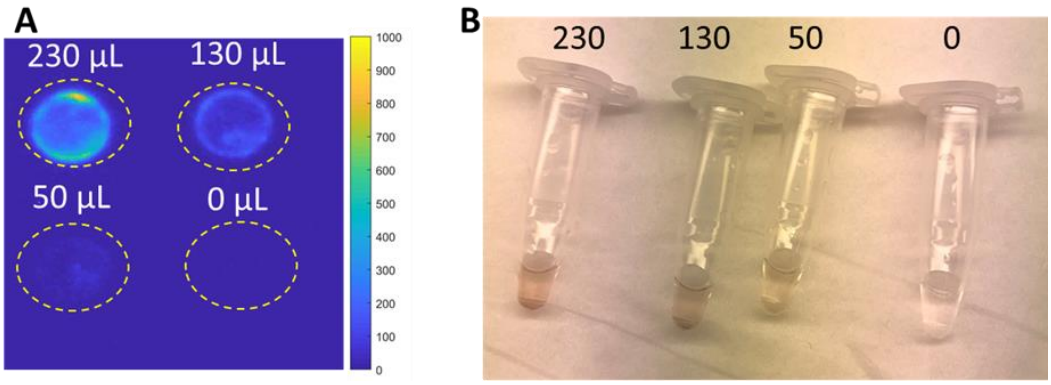

Figure 6. 7 Effects of decay source volume on activity retention on chip and color of collected crude product.

(A) Cerenkov image of a 2x2 chip after collection of products. The numbers indicate the amount of decay source that was added to that reaction site. (B) Photograph of crude products after collection from its corresponding reaction sites.

The radiosynthesis results are summarized in **Figure 6.8, Table 6.3, Table 6.4** and **Table 6.5.** In the case of [^{18}F]PBR06 we noticed a decrease on crude RCY from 90% to 49% as the volume of decayed source solution increased. For [^{18}F]Fallypride, the crude RCY decreased from 87% to 23%, and for [^{18}F]FEPPA it decreased from 80% to 2%. These results show the dramatic impact on reaction performance even when the possibility of radiolysis is eliminated by using low

activity levels, underscoring the need to remove impurities from [^{18}F]fluoride prior to performing scaled-up droplet reactions.

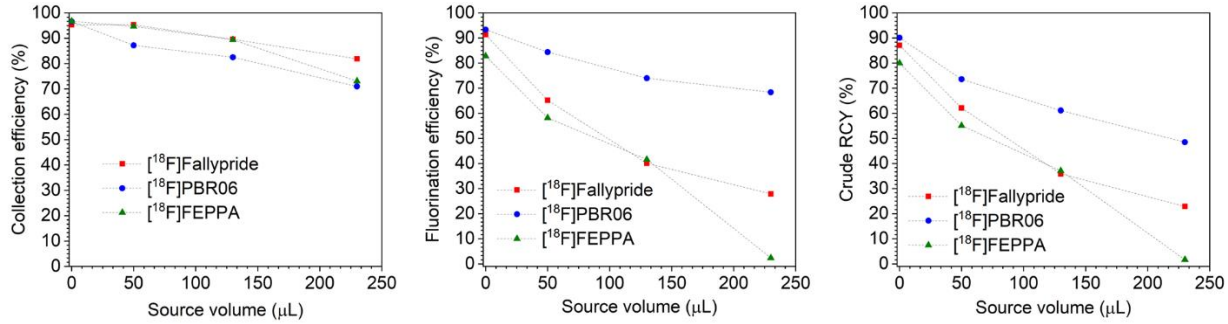

Figure 6. 8 Radiosynthesis performance of 3 radiopharmaceuticals as a function of activity source volume (all performed at 14 MBq level).

(A) Collection efficiency, (B) Fluorination efficiency, and (C) Crude RCY performance.

Table 6. 3 The effect of different source volumes on the reaction performance of [18F]PBR-06.

Volume dried (μL)	Collection efficiency (%)	Fluorination efficiency (%)	Crude RCY (%)	Activity lost to chip (%)
230	71.0	68.4	48.5	12.4
130	82.5	74.0	61.1	
50	87.2	84.4	73.6	
0	96.6	93.3	90.1	

Table 6. 4 The effect of different source volumes on the reaction performance of [18F]Fallypride.

Volume dried (μL)	Collection efficiency (%)	Fluorination efficiency (%)	Crude RCY (%)	Activity lost to chip (%)
230	81.9	27.9	22.9	6.0
130	98.6	40.1	35.9	
50	95.3	65.2	62.1	
0	95.3	91.3	87.1	

Table 6. 5 The effect of different source volumes on the reaction performance of [18F]FEPPA.

Volume dried (μL)	Collection efficiency (%)	Fluorination efficiency (%)	Crude RCY (%)	Activity lost to chip (%)
230	73.1	2.4	1.7	7.2
130	89.4	41.6	37.1	
50	94.7	58.2	55.1	
0	96.7	82.8	80.0	

6.3.3 Determination of resin masses for trap and release process

In previous work using 3 mg microscale QMA cartridges to scale-up [^{18}F]fallypride synthesis(*62*), there was not only a decrease in reaction performance at higher activity scales, but also in the efficiency of trapping [^{18}F]fluoride on the cartridge. Above ~20 GBq of activity, the efficiency dropped significantly, despite mock scale-up experiments (by adding KF) suggesting much higher capacity of the 3 mg cartridge. The reduction in performance when using the large volume of the radioisotope source may be indicative that other species / contaminants are either reducing the QMA cartridge capacity or interfering with binding of [^{18}F]fluoride ions.

To more realistically simulate higher activity scales, we spiked activity (0.37 – 1.1 GBq [10-30 mCi]) amounts into 1 mL of decayed [^{18}F]fluoride in [^{18}O]H_2O which realistically simulates the effects of the higher volume of solution and contains all the impurities and same total fluoride content as a ~37 GBq (~1.0 Ci) cyclotron bombardment. Under this low activity scale, radiolysis would not be expected to impact the efficiency of the trapping process (e.g., due to the direct damage of resin). Furthermore, activity level can be eliminated as a potential variable for determining the cause for trapping efficiency issues, by keeping the activity level low, and by utilizing the same source volume.

In a preliminary test, we performed trapping of 200 µL decayed source water spiked with 0.37 GBq of activity using a 3 mg QMA micro-cartridge and found only 89% of the initial activity was retained on the cartridge after trapping and 2 washes. We explored if more resin mass would be able to retain the activity. Using a 9 mg QMA micro-cartridge, the observed trapping and wash efficiency was only 78%. Noting this poor trapping behavior, the buildup of dark coloration at the entry port of the QMA micro-cartridge (**Figure 6.9A**) was observed, indicating the presence of significant amounts of contaminants that may interfere chemically or mechanically with trapping, perhaps leading to the surprisingly poor performance (and perhaps explaining the reduced trapping efficiency in the previous study(*62*)).

Next, a Chelex and SCX cartridge (30 mg Chelex, 30 mg SCX) upstream of the 9 mg QMA cartridge was tested to determine if contaminants could be removed prior to QMA trapping. This time, using 1000 µL of decayed source activity spiked with 0.37 GBq, there was no observed dark coloration in the QMA cartridge (**Figure 6.9B**), but faint traces of coloration could be observed across both the Chelex and SCX resin beds. Trapping efficiency was returned to near quantitative levels, but further optimization was performed to allow the best entrapment of [^{18}F]fluoride on the QMA cartridge (e.g., the lowest bed length utilized for trapping [^{18}F]fluoride).

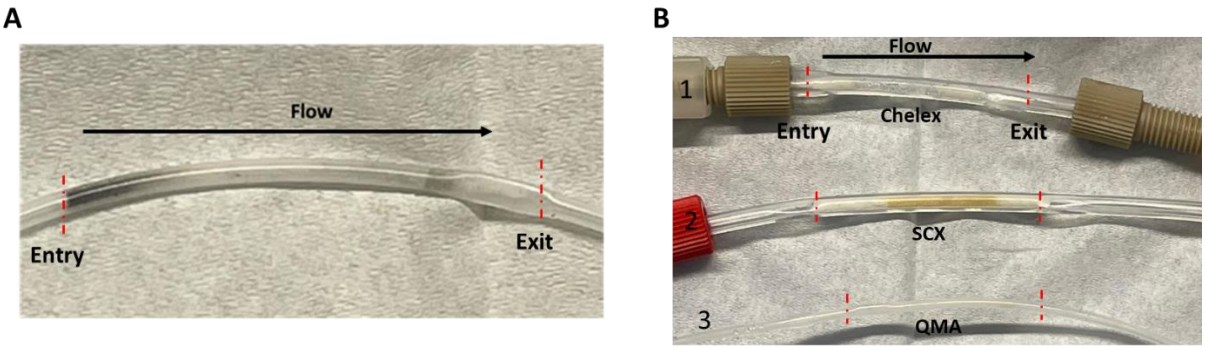

Figure 6. 9 Removal of contaminants from decayed source.

(A) Photograph of QMA micro-cartridge after the passing of 200 µL of decayed source. (B) Photograph of Chelex, SCX, and QMA micro-cartridges after passing 200 µL of decayed source. Numbers indicate the order of connection and liquid direction. Dashed red lines indicate the entry and exit port points of each cartridge.

To find the optimal mass of Chelex and SCX resin to be used for purification of the [^{18}F]fluoride, we performed a series of experiments with different combinations of masses (0 to 30 mg) of each of these resins upstream of a 9 mg QMA cartridge, in which activity (1 mL of decayed source spiked with 1 GBq [30 mCi] of activity) was trapped, washed, and eluted. The activity distribution in the QMA cartridge was imaged with Cerenkov imaging and plotted as a profile of activity along the length of the cartridge. Results are presented in **Figure 6.10**. The optimal distribution is one that is positioned as close as possible to the entrance of the cartridge (i.e., suggesting it may have additional capacity for trapping). We selected 10 mg of Chelex and

30 mg of SCX as the optimal values, which had activity distributed only along 150 pixels of the approximately 400 pixels long QMA cartridge.

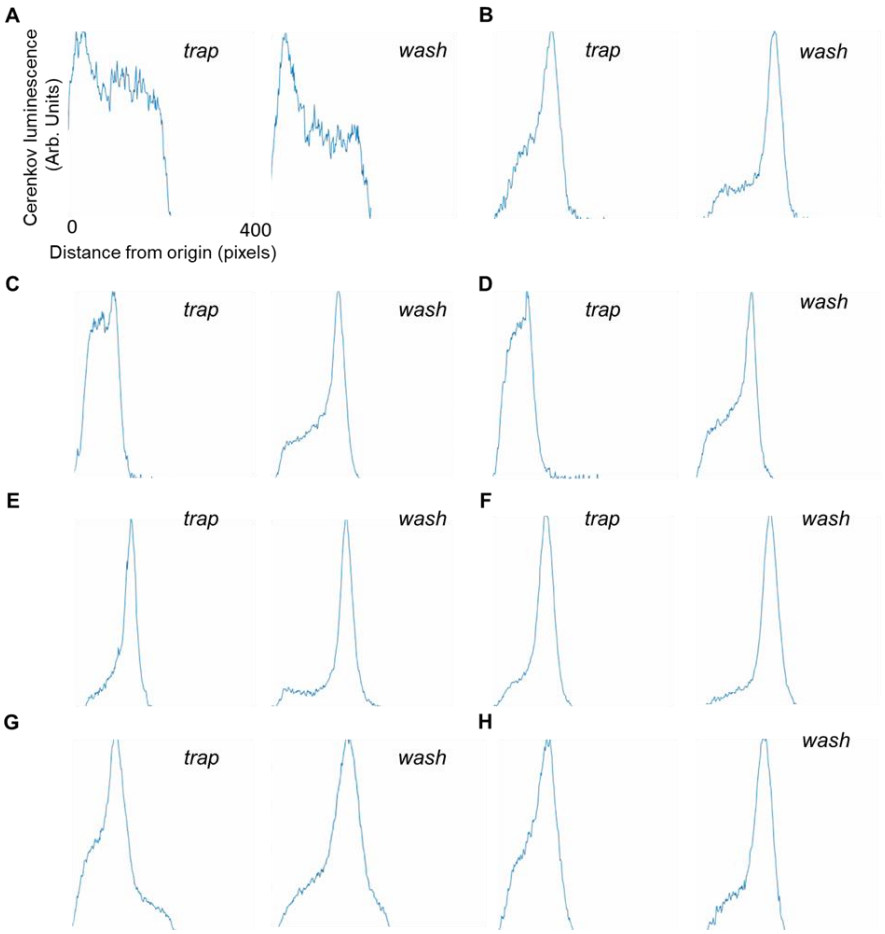

Figure 6. 10 Distribution of activity trapped in a 9 mg QMA cartridge with different sized Chelex and SCX cartridges upstream.

Images shown in the left of each pair is a snapshot at time 300 s for the trapping step. Images shown in the right of each pair is a snapshot in time at 300 s for the washing step. (A) 0 mg Chelex, and 0 mg SCX. (B) 0 mg Chelex, and 30 mg SCX. (C) 3 mg Chelex, and 30 mg SCX. (D) 10 mg Chelex, and 30 mg SCX. (E) 30 mg Chelex, and 30 mg SCX. (F) 10 mg Chelex, and 10 mg SCX. (G) 30 mg Chelex, and 3 mg SCX. (H) 30 mg Chelex, and 10 mg SCX.

6.3.4 Determination of eluent for activity release process

Previous work by Wang et al. (2020) showed that with the use of a 3 mg QMA micro-cartridge, 2 boluses of 6.2 µL (25 mM each) of $TBAHCO_3$ followed by 2 boluses of 6.2 µL water was sufficient to elute out the trapped activity form the cartridge and perform high activity

experiments of [^{18}F]Fallypride(*62*). However, the same amount of $TBAHCO_3$ was not sufficient to push out the activity trapped in a 9 mg QMA micro-cartridge (**Figure 6.11**).

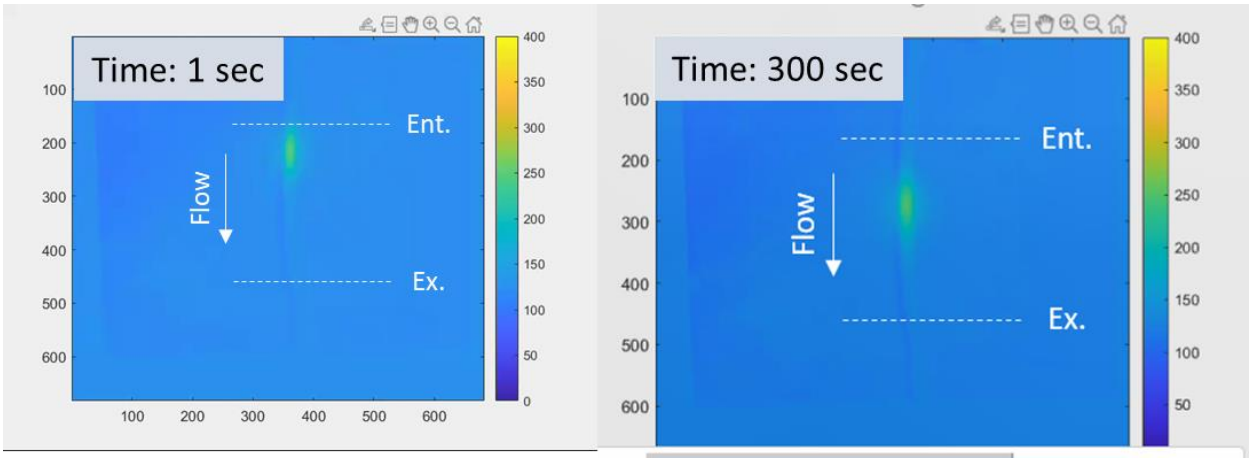

Figure 6. 11 Activity distribution in a 9 mg QMA micro-cartridge with 24 µL of 30 mM of TBAHCO3 for elution. Activity moved to the middle of QMA cartridge after 300 sec but did not elute from the micro-cartridge.

A solution would be to increase the amount of $TBAHCO_3$ for the elution process, but ambiguity on the final concentration of $TBAHCO_3$ in the reaction would be difficult to control precisely. Furthermore, the addition of base would contradict many of the optimal conditions found through previous optimization studies(*61*), hindering reactions. Therefore, there is a need for an efficient method to elute activity without affecting the optimized concentration of $TBAHCO_3$ for downstream reactions.

Triethylamine (TEA) is a commonly used base in organic chemistry and is commonly used in radiochemistry for HPLC mobile phase preparation. TEA is a weak base with a low boiling point of 88.6 °C and does not interact with free [^{18}F]fluoride (low nucleophilicity). Recently, its use has been reported for eluting [^{18}F]fluoride from a QMA cartridge(*130*). We hypothesized that TEA could provide a way to elute the activity from the cartridge and be removed by evaporation when loaded onto the reaction site prior to the downstream radiofluorination reaction – allowing a base "free" elution method. During the drying step, the optimized base concentration can be spiked to the reaction site, allowing optimized conditions to be followed for high activity reactions.

To test the effectiveness of TEA as an eluent of 0.37 GBq (10 mCi) of [^{18}F]fluoride trapped on a 9 mg QMA cartridge, a series of 10 µL boluses of 10 nmol of TEA (aq.) were passed through the cartridge and the collectivity measured (Error! Reference source not found.). Most activity was e luted after 40 µL of TEA, and nearly all was eluted within 80 µL. To ensure complete elution of activity, 150 nmol of TEA was utilized for further studies. To determine if the process could be simplified, we also tried a single 80 µL with 150 nmol of TEA to ensure full elution and we achieved 90.4 ± 0.8% (n = 4) elution efficiency.

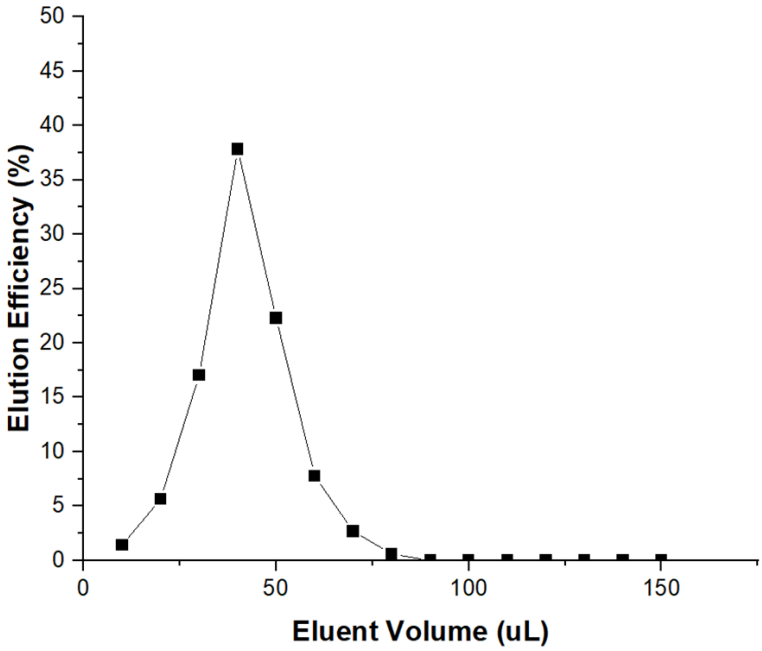

Figure 6. 12 Elution efficiency of activity using plugs 10 µL of 10 nmol TEA.

Initially, we tried to load the eluted [^{18}F]fluoride in 20 µL increments, directly to the chip and evaporate at 105 °C, but found a very high loss of activity due to volatility (e.g., >90%). Likely this problem occurs because as the TEA evaporates, the solution is no longer basic, allowing [^{18}F]HF to form and escape. To address this, we mixed the concentrated activity prior to loading with the optimized concentration of base (e.g., $TBAHCO_3$) needed for the optimal conditions of

the downstream radiosynthesis (For example, for the synthesis of [^{18}F]Fallypride, we added 240 nmol of $TBAHCO_3$).

Next, we optimized the amount of TEA. In theory, it should volatize during the fluoride drying step, leaving a minimal concentration that should not interfere with downstream fluorination. However, to determine the effect of residual TEA concentrations, on fluorination, a 4x4 multi-reaction microdroplet chip was used to vary the amounts of TEA (from 0 to 3500 nmol) used during the [^{18}F]fluoride drying step prior to the synthesis of [^{18}F]Fallypride. Briefly, experiments were conducted with 2 µL of activity (37 MBq [1 mCi]) loaded on each reaction site with 240 nmol of $TBAHCO_3$ and a varied amount of TEA. After drying at 105 °C for 1 min was completed, 39 mM (8 µL) of Fallypride precursor was added to each reaction and reacted for 1 min at 110 °C. Collected product was measured and analyzed via radio-TLC as previously described(*128*). We noticed no adverse impact on the reaction performance with the addition of TEA (**Figure 6.13**). Considering that the residual concentration of TEA has no effect on the downstream fluorination, 2000 nmol of TEA was utilized for the elution of activity trapped on the QMA.

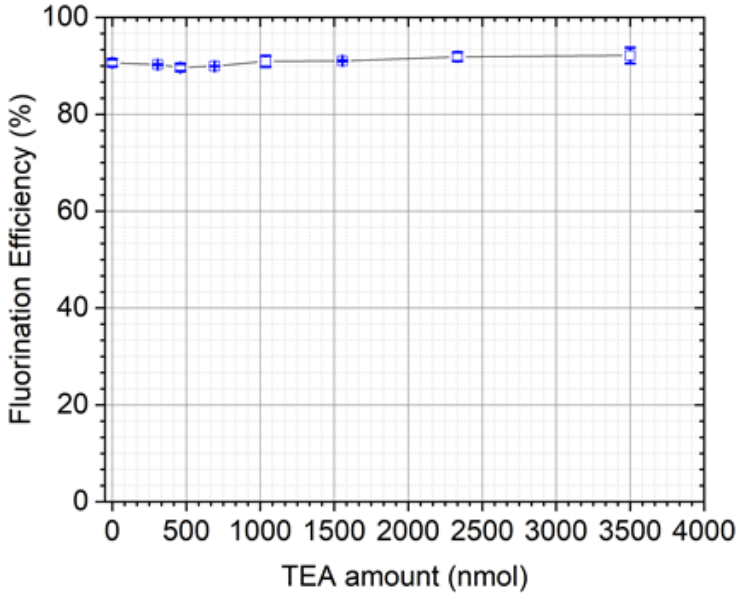

Figure 6. 13 Fluorination efficiency of [18F]Fallypride with different amounts of TEA (n = 2).

6.3.5 Evaluation of the full [^{18}F]fluoride purification process

Next, we combined the [^{18}F]fluoride processing with the downstream reaction. We performed an experiment with 1 mL of decayed source spiked with 185 MBq (5 mCi) in a system comprising 10 mg Chelex / 30 mg SCX and 9 mg QMA micro-cartridges. The efficiency of the concentration process in this format was >95%. Activity was then eluted using 2000 nmol of TEA (aq.) in a bolus of 100 µL. The elution efficiency of this format allowed 89%. Using a droplet chip that contained 240 nmol of $TBAHCO_3$ at the reaction site from addition with a micropipette, sequential 20 µL boluses of the eluted activity were loaded onto, and dried, on the reaction site. Next, 160 nmol of [^{18}F]PBR06 precursor in 8 µL of thexyl alcohol: MEOH (1:1 v/v) was added to the reaction site and reacted for 0.5 min at 100 °C. Product was collected with 60 µL of collection solution (9:1 MeOH: H_2O v/v) and spotted on TLC for analysis. A control reaction was performed separately with 4 µL of unprocessed [^{18}F]fluoride (18.5 MBq [0.5 mCi]). The results showed fluorination efficiency of treated decayed source to be 90.9% and the control reaction 91.7% (**Figure 6.14**), indicating that the processing method was effectively able to remove all impact of impurities from 1 mL of decayed source solution and achieve the same high yield as a small-scale reaction.

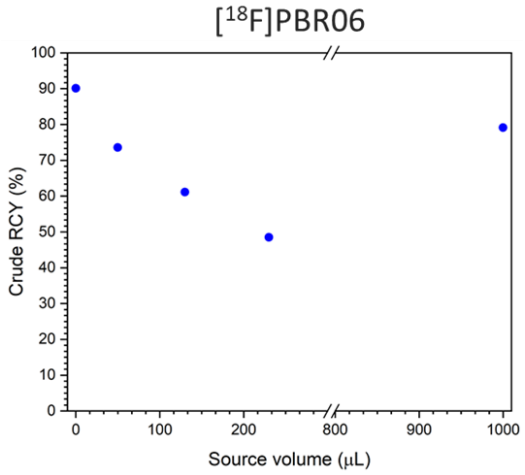

Figure 6. 14 Comparison of different decay source volume effects on the synthesis of [18F]PBR06 crude RCY without cartridge treatment and the effect on the crude RCY after treatment of 1 mL decay source with our serial cartridge method.

6.4 Conclusion

This chapter describes a new method for purifying and concentrating [^{18}F]fluoride suitable for use with microscale reactions. The use of 10 mg chelex and 30 mg SCX resins upstream of a 9 mg QMA resin (hydroxyl form) was able to completely remove coloration from the QMA and achieve high trapping and elution performance (trapping >95% and elution ~90%) in 80 µL of milli q water containing 150 nmol of TEA. This eluted solution can then be loaded in 20 µL increments to a droplet reaction chip (with the desired amount and type of base / phase transfer catalyst pre-loaded and dried). The yield of reactions ([^{18}F]PBR-06) exhibited identical performance whether using a tiny volume of unprocessed activity solution loaded directly to the reactor, or 1 mL of processed decayed source, processed with the novel method.

The next step is to apply this method to large volumes of non-decayed source activity, to enable loading of high activities to the droplet reactor and compare the reaction performance. With the cartridge able to remove the impact of impurities and potential stoichiometry effects (i.e. since the decayed source has the same amounts of these as non-decayed source), it will be possible to assess if and when radiolysis becomes an issue as activity scale is increased. If radiolysis is observed, radical scavengers can potentially be used to mitigate the effect.

Chapter 7: Development of new techniques for volatile reactions using microvolumes

7.1 Introduction

Droplet microfluidics involves the generation of many isolated compartments of small volumes to perform various chemical or biochemical reactions in a high throughput manner, in volumes ranging from microliters down to picoliters. The encapsulation of reactions in droplets ensures close proximity of precursor to nucleophile and accelerates the chemical reaction(*212*). Moreover, microdroplet usage in chemical synthesis offers a high degree of control over the chemical reactions by leveraging the high surface area-to volume ratio, which enables fast heat transfer and mixing and thus uniform conditions(*213*). Droplets can be generated in channels within a carrier media to perform reactions in rapid succession, or can be arrayed on surfaces to perform chemical syntheses in parallel(*214*).

The use of droplet-arrays for high-throughput optimization of radiotracers was described in **Chapters 2 and 5**. The use of open (uncovered) droplets (as shown in **Chapter 2**) to conduct synthesis of radiopharmaceuticals allows for reactions to be conducted faster than closed droplet platforms such as electrowetting-on-dielectric (EWOD) microfluidics(*30,215*), since drying of solvents can occur more efficiently. This is particularly important when removing [^{18}O]H_2O present in [^{18}F]fluoride obtained from a cyclotron. Droplets provide a dramatic improvement over conventional radiosynthesizer systems which require the use of QMA cartridges to separate [^{18}F]fluoride from [^{18}O]H_2O. [^{18}F]fluoride is trapped on the cartridge, and then a mixture of phase transfer catalyst in a mixture of MeCN and water is used to elute the [^{18}F]fluoride, and finally azeotropic drying to remove residual water(*216*). In contrast, in the open chip system, [^{18}O]H_2O is removed directly via evaporation after mixing the [^{18}F]fluoride with the phase transfer catalyst.

The open droplet system also allows for fast heat transfer in other steps such as the fluorination reaction. However, when reactions are conducted using volatile solvents and/or high reaction temperatures, or the product is volatile, the open structure can lead to high activity loss and reduced radiochemical yields.

In fact, for a number of tracers previously studied have exhibited substantial losses of volatile radioactivity(*61,65,136*). During high-throughput optimization studies, such losses can make it challenging to analyze results of reactions performed under different conditions. Previous attempts to explore different reaction conditions to radiolabel peptides with 4-[^{18}F]Fluorobenzaldehyde ([^{18}F]FBA) and production of [^{18}F]FBA using the open chip format made it difficult to achieve decent yields. Due to the high volatility of [^{18}F]FBA and its low vapor pressure (19 hPa at 70 °C), radiolabeling of peptides or [^{18}F]FBA product formation led to high loss of activity throughout the process, thus meaningful measurements were difficult to obtain and resulted not repeatable results within the same conditions. In some cases, the performance of the reaction is comparable to macroscale systems despite the losses. However, in other cases, the losses strongly affect performance. In the study of the production of [^{18}F]AMBF$_3$-TATE (via isotopic exchange), it was necessary to cover the reaction droplet with a glass plate to reduce activity loss(*65*). To ensure a consistent distance from the chip to the cover plate, strips of tape were used as spacers as shown in **Figure 7.1**(*65*).

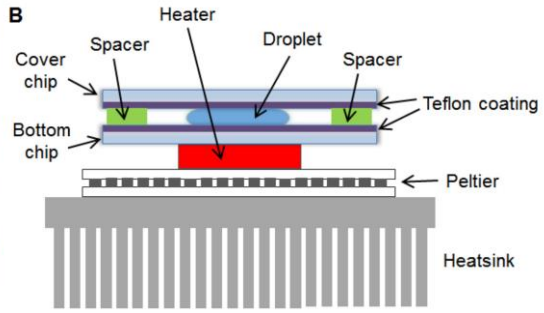

Figure 7. 1 Schematic of the setup used for the droplet-based radiosynthesis of [18F]AMBF3-TATE.

A cover plate is added during the fluorination step to reduce activity losses. Adapted with permission from Lisova *et al*. ©2018 Nuclear Medicine and Biology(*65*).

Another radiopharmaceutical that has been studied using an open chip format is 3,4-dihydroxy-6-[^{18}F]fluoro-L-phenylalanine ([^{18}F]FDOPA), which can be used to image neuroendocrine tumors(*217*) or Parkinson's disease(*218*). The results previously reported by Wang et al. showed that the volatility during the fluorination and the deprotection steps in [^{18}F]FDOPA radiosythesis resulted in a crude RCY of 11% (n = 1)(*136*), using the optimal deprotection conditions (6 M H_2SO_4 at 120 °C for 5 min). However, by adding a Teflon coated glass cover plate over the droplet during deprotection (**Figure 7.2**) the crude RCY could be further increased to 14.3 ± 0.5% (n = 2) (**Table 7.1**). Looking in detail at the data revealed a reduction in volatile activity from 84% (of starting activity, decay-corrected) with no cover to 53.7 ± 0.4 (n=2) with a cover, but some of the gains were negated by additional new losses due to residual activity on the cover plate (26 ± 2% (n=2) of starting activity, decay-corrected). However, the net result was an improvement in reaction performance.

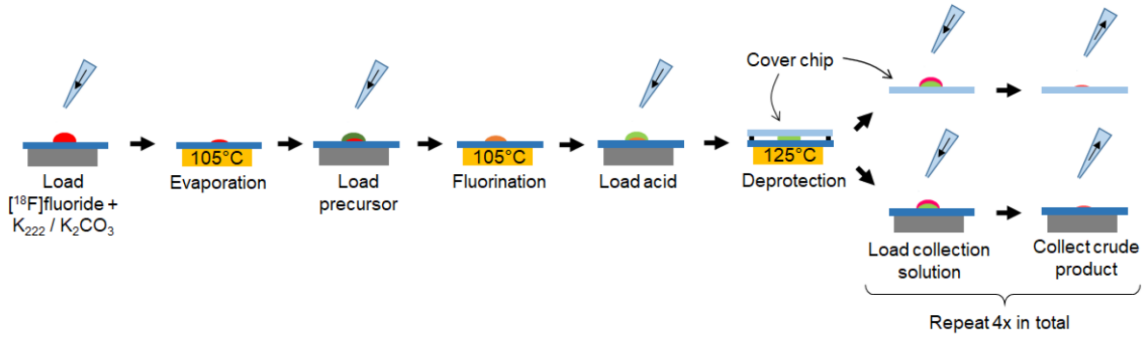

Figure 7. 2 Schematic of droplet synthesis of [18F]FDOPA using a cover chip during the deprotection step.

Figure adapted from Adapted with permission from Wang *et al*. ©2019 Royal Society of Chemistry(*136*).

Table 7. 1 Effect of cover plate on the synthesis performance.

Radioactivity loss indicates the combined activity losses (due to formation of volatile species) during evaporation, fluorination and deprotection steps. Percentages are corrected for decay(*136*). Adapted with permission from Wang *et al*. ©2019 Royal Society of Chemistry.

	No cover chip (n=1)	With cover chip (n=2)
Radioactivity loss (%)	84	53.7 ± 0.4
Residual activity on cover plate (%)	N/A	26 ± 2
Residual activity on bottom chip (%)	3	1.5 ± 0.2
Radiochemical recovery (%)	12	17 ± 2
[^{18}F]FDOPA conversion (%)	91	84 ± 5
Crude RCY (%)	11.0	14.3 ± 0.5
Isolated RCY (%)	7.2	10.0 ± 0.7

Finally, the studies described in **Chapter 5** showed the high volatile losses during the droplet synthesis of [^{18}F]Flumazenil. Even with extensive optimization, a maximum yield of 19.1 ± 0.6% (n=4) was observed, despite very high fluorination efficiencies observed(50.0 ± 1.6, n=4)(*61*). This observation suggests that there may be a competition between volatility of [^{18}F]fluoride and speed of the fluorination reaction; covering the reaction may reduce the rate of [^{18}F]fluoride loss, giving more time for reaction with the precursor. In this chapter, we will focus on the different approaches aimed to reduce the volatility losses during the production of [^{18}F]Flumazenil by increasing the collection efficiency of crude product and potentially a further increase the fluorination efficiency.

While the cover provides advantages during the reaction step, as mentioned previously, it is a significant advantage to have an open droplet configuration during the initial [^{18}F]fluoride drying step. Thus we a strong interest in develop a removable cover that is compatible with an automated droplet radiosynthesis system(*32*).

We first consider the use of close reactor systems that can seal small-volume reactions. Recently, an automated microfluidic closed reactor system (PHENYX) based on molded plastic (PEEK) reactor vessel was reported for performing multi-step radiosynthesis in 5-50 µL volumes(*219*). The PHENYX system contained special attachments for pipetting reagents, performing radioisotope concentration, pressurizing of reservoirs for transfer, and sealing of the reaction vessel with a heated lid. Heating of the lid was critical to inhibit liquid condensation on

the lid, where it is effectively removed from the reaction potentially leading to complete elimination of the reaction solvent(*219*). Lu et al. reported the collection efficiency of crude product using the PHENYX system to be 92 ± 1% (n = 3), no activity left on the lid-heater, and only 1 ± 1% (n=3) loss in the reactor. The results show no volatility loss of the reaction and the use of the lid-heater prevented condensation of solvents. The remaining activity loss was found to be residual activity in the cassette after measurement in dose calibrator (5 ± 2%, n=3)(*219*). Another approach for sealed microvolume reactions is the use of small vials as a reaction vessel. Laube et al. (2021) performed parallel reactions in sealed vials (50 µL of reactant) to compare the impact of various conditions, such as solvent, time, temperature, and precursor amount by placing multiple vials into heating blocks(*59*). The use of sealed HPLC vials showed efficient ^{18}F-fluoride incorporation with the use of minimal amounts of precursor and demonstrated 20-30% product formation of [^{18}F]celecoxib and low volatility(*59*). We explored both the PHENYX system and the use of HPLC vials to determine if these approaches could improve the performance of the synthesis of [^{18}F]Flumazenil by limiting volatility.

We also explored the concept of using a cover with rubberized seal to allow for gas-tight but reversible attachment to the bottom chip at selected times during the synthesis process. The elastomer polydimethylsiloxane (PDMS) is a commonly used in the fabrication of microfluidic devices due to the material's transparency in the UV-visible regions, low electrical conductivity, and elasticity(*220*). Moreover, the cost of fabrication in PDMS is low compared to other materials such as silicone or glass, yet can incorporate detailed features commonly used in microdevices, making it suitable for rapid prototyping. The elasticity of PDMS allows it to form reversible seals against flat surfaces without the need for chemical bonding. The use of PDMS in microdevices for bioanalysis is greatly due to the material's biocompatibility, lack of swelling in water, and gas permeability that allows gas exchange for cell-based assays, but in recent years there has been a growing interest in using microfluidic systems for functions other than bioanalysis in water, such

as organic synthesis with organic solvents(*221*). However, PDMS exhibits significant swelling when in contact with nonpolar solvents (e.g., hydrocarbons, toluene, and dichloromethane)(*222*) or absorption of certain species(*223*). Fortunately, for commonly used solvents in radiochemistry (e.g. DMSO, DMF, MeCN, MeOH, or aqueous buffers) and NMP (used in the droplet synthesis of [^{18}F]Flumazenil) the swelling is relatively low. Moreover, PDMS exhibits reasonably good thermal stability(*224*), suitable for high reaction temperatures used in droplet radiochemistry. While PDMS is known for its gas permeability, it was a good material to explore initially, since previous studies have shown a reduction on absorption on PDMS by coating it with Teflon to make PDMS surface more hydrophilic.

Another strategy we tried was to increase the local concentration of [^{18}F]fluoride to drive the fluorination reaction faster, and thus hopefully increase yield by changing the balance of volatile activity loss versus reaction with the precursor. The increase on the uniform interaction of precursor with [^{18}F]fluoride may lead to better product formation before activity can leave the reaction as volatile [^{18}F]HF. Tucker et al. (2020) developed a chip with a hydrophobic/hydrophilic pattern as a preconcentration procedure that could be used for the analysis of small tracer amounts of analytes in microvolumes without the need of centrifuge, chromatography, or solid-phase extraction(*225*). The chip was fabricated by using laser micromachining on a Teflon coated glass slide, where milled rings with patches were constructed. The rings with patches geometry had outer ring diameter of 3000-700 µm and inner patch diameters of 120-200 µm (20 µm pitch)(*225*). The technique of preconcentration can allow us to achieve a higher spatial localization of [^{18}F]fluoride after the drying step, enabling a higher local concentration of [^{18}F]fluoride at the start of the subsequent fluorination step once the precursor droplet is added (**Figure 7.3**).

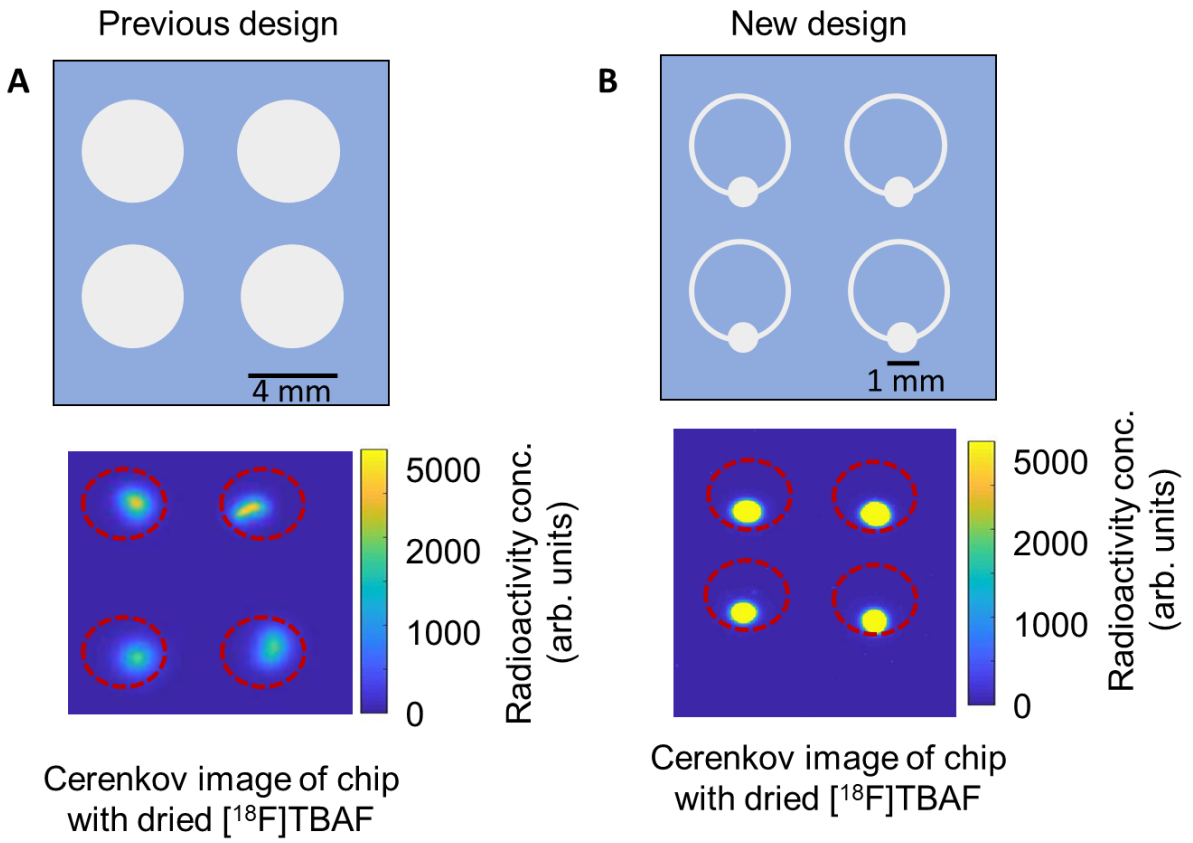

Figure 7. 3 Comparison on the radioactivity distribution.

(A) Previous chip design 2x2 reaction sites with 4 mm diameter. Cerenkov image shows the radioactivity distribution on the reaction site. (B) New concentration zone chip design and Cerenkov image showing activity concentration at the small reaction site (1 mm diameter).

In this chapter, we focus on the exploration of three different approaches to mitigate the loss of activity via volatility: (i) using the closed reactor of PHENXY and HPLC vials, (ii) using a cover plate based on PDMS, (iii) or by increasing the concentration gradient to accelerate the reaction.

7.2 Materials and Methods

7.2.1 Materials

N-methyl-2-pyrrolidone (NMP, 99.5% anhydrous) was purchased from Sigma-Aldrich (St. Louis, MO, USA). Tetrabutylammonium bicarbonate ($TBAHCO_3$, 75mM in ethanol), ethyl-5-methyl-8-nitro-6-oxo-5,6-dihydro-4*H*-benzo[f]imidazo[1,5-*a*][1,4]diazepine-3-carboxylate (nitromazenil; precursor for [^{18}F]Flumazenil, > 97%) were purchased from ABX Advanced

Biochemical Compounds (Radeberg, Germany). DI water was obtained from a Milli-Q water purification system (EMD Millipore Corporation, Berlin, Germany). No-carrier-added [^{18}F]fluoride in [^{18}O]H_2O was obtained from the UCLA Crump Cyclotron Facility. Glass microscope slides (76.2 mm x 50.8 mm, 1 mm thick) were obtained from C&A Scientific (Manassas, VA, USA). PDMS was fabrication consisted of two-part mixture of polymers RTV-615 purchased from Momentive. Quaternary methylammonium (QMA) resin (Waters Corporation, Milford, USA); ethylene tetrafluoroethylene (ETFE) tube (1/16″ OD × 0.040″ ID, 1517L; IDEX Health and Sciences, Wallingford, USA). Fabrication of microdroplet chips required 1% Teflon AF 2400 solution was purchased from Chemours. Positive photoresist (MEGAPOSIT SPR 220-7.0) and developer (MEGAPOSIT MF-26A) were purchased from MicroChem (Westborough, USA). Additional solvents and chemicals used for microfluidic chip fabrication, including methanol (MeOH, Cleanroom LP grade), acetone (Cleanroom LP grade), isopropanol (IPA, Cleanroom LP grade), sulfuric acid (96%, Cleanroom MB grade) and hydrogen peroxide (30%, Cleanroom LP grade), were purchased from KMG Chemicals (Fort Worth, USA).

7.2.2 Methods

7.2.2.1 Close reactor approaches

The PHENYX system previously described by Lu et at. (2022) consists of a fixed instrument and interchangeable cassettes(*219*). In summary a 127 mm x 80 mm x 22 mm cassette was fabricated using polyether ether ketone (PEEK), since the material has excellent chemical resistance and good thermal stability (see **Figure 7.4**). To avoid plastic deformation of the cassettes, the maximum operating temperature is 160 °C. The cassette's features contained a radio-isotope concentrator and a reactor reservoir with a heated lid. The concentration of activity and radiochemistry were performed as previously reported by Lu et al. (2022)(*219*). First, a desired amount of radioisotope was added into the QMA inlet reservoir, which was then pushed through

a QMA mini cartridge (3 mg) to trap the [18F]fluoride while the [^{18}O]H_2O was sent to a waste reservoir by applying 20 psi for 90 s via the Pressure-lid. The trapped [^{18}F]fluoride was eluted by pipetting 30 µL of eluent solution (240 nmol of $TBAHCO_3$ in 9:1 MeCN:H_2O (v/v)) into the QMA inlet reservoir and [^{18}F]fluoride was pushed through QMA cartridge and content was transfer to the reactor reservoir where the Pressure-lid was moved to the reaction to provide nitrogen flow at 5 psi to accelerate evaporation. The evaporation was performed at 100 °C for 5 min and then ramped to 105 °C for 5 min with the heat supplied by the bottom heater. After drying, the reactor was cooled down to 25 °C by turning both the top and bottom cooling fans. The fluorination step for [^{18}F]Flumazenil was performed by adding 8 µL of precursor (280 nmol in NMP solvent) into the reactor. After closing the reactor using the Lid heater, the mixture was heated for 7 min with 140 °C heating applied to both the bottom cassette heater and the lid heater. After the reaction was completed, the reactor was cooled down to 25 °C for 2 min, then opened, then 100 µL of collection solution (9:1 MeOH:H_2O (v/v)) was added to the reactor and crude product was aspirated with a pipette and dispensed into an Eppendorf tube for TLC analysis.

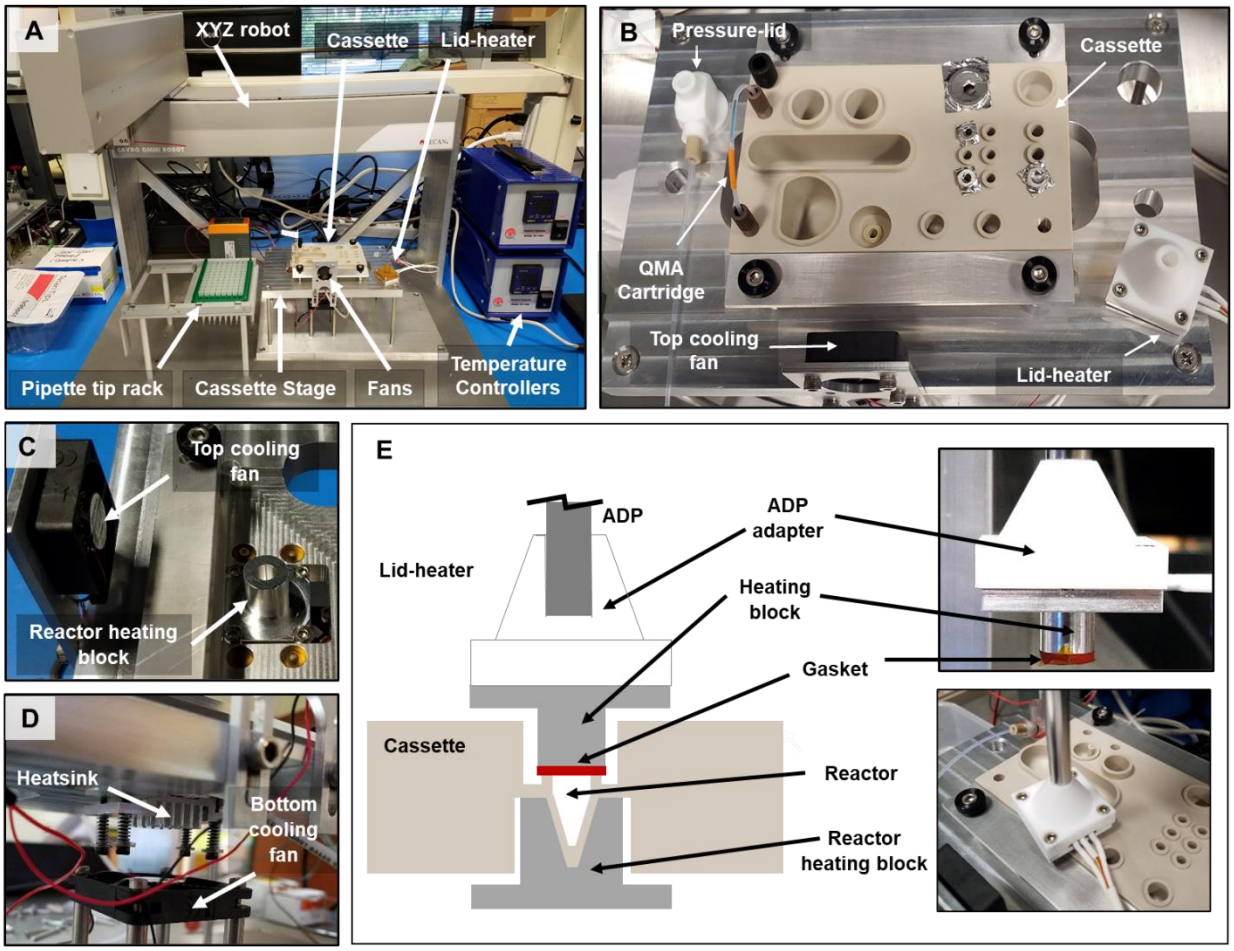

Figure 7. 4 PHENYX prototype system.

(A) Photograph of full PHENYX prototype system containing the Cassette stage, control electronics, and disposable pipette tips. (B) Photograph of PEEK cassette placed atop of reactor heater and showing the individual parts of the cassette such the QMA cartridge for trap and release of activity, Lid-heater and Pressure-lid. (C) Photograph of the top side of the Reactor heater with heat block with conical cavity where Reactor reservoir on the cassette would be place. (D) Photograph showing the bottom side of the Reactor heater that includes heatsink and bottom cooling fan. (E) Schematic and photograph of sealed Reactor that consist of the Lid-heater made of Teflon attached to a heat block with a silicone elastomer layer on the top, sealing the Reactor reservoir. Figure adapted from Lu *et al.* © 2022 Chemical Engineering Journal(*219*).

The use of sealed HPLC vials for performing radiochemistry was recently demonstrated by Laube et al. (2021)(*59*). We tested whether the sealed vials could reduce volatile losses during the fluorination step of [^{18}F]Flumazenil. First, 7 µL of [^{18}F]fluoride (26 MBq [0.7 mCi]) with 3.2 µL of $TBAHCO_3$ (240 nmol) was added to an uncapped 2 mL HPLC vial, which was placed on top of a heater coated with a thin layer of thermal paste. The heater was set to 100 °C for 1 min and

then temperature was elevated to 105 °C for 1 min to ensure removal of residual [^{18}O]H_2O, however due to the cooler temperature at the top of the vial, some condensation remained. Then, heater was cooled to 25 °C for 2 min and the activity of the vial was measured in dose calibrator to ensure no loss of activity occurred during the drying step. The reaction proceeded by adding 8 µL of nitromazenil precursor (280 nmol in NMP) directly to the dried activity residue inside the HPLC vial and then the vial was capped, followed by placement of the vial into one of the cavities (filled with silicon oil) of a metal heating block, pre-heated to 200 °C on a hot plate. Due to the different heating characteristics of the bottom of the glass vial versus the Teflon-coated silicon chip, different reaction times were explored (0.5, 2, 5, and 7 min). Finally the HPLC vial was removed from the heating block and activity was measured (uncap vial) with dose calibrator to calculate the loss of activity during the fluorination step. 50 µL of collection solution (9:1 MeOH:H_2O (v/v)) was added to HPLC vials to dissolve crude and analyze using radio-TLC. TLC were spotted with 1 µL of crude product and develop using 100 % MeCN. **Figure 7.5** shows the experimental set up using HPLC vials as closed reactor vials.

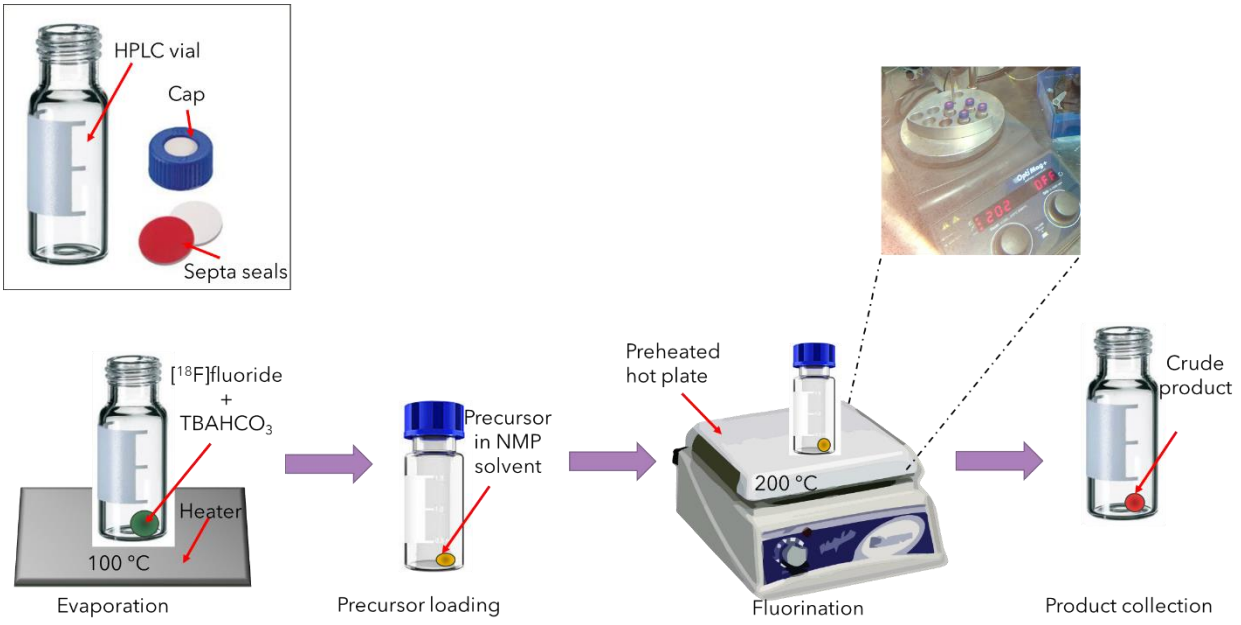

Figure 7. 5 Schematic of experimental setup using HPLC vials to enclose the reaction droplet.

7.2.2.2 Cover plate design and fabrication

Though the use of a cover plate separated by tape spacers reduces volatility(*65,136*), under extremely high temperatures as used for [^{18}F]Flumazenil, the activity still escaped out the gaps in the plate. Thus, we designed a cover that could fully enclose the reaction site. Typical reaction volumes used in our multi-reaction chip are in between 4-10 µL (~0.5-1.0 mm height). An initial cover comprised a thin PDMS gasket with a cylindrical hole (to fit around the droplet) with a transparent glass slide to seal the top. To fabricate the PDMS gasket, 40 g of 10:1 mass ratio of RSV615 A:B (Momentive, New Smyrna Beach, FL, USA) was mixed in a plastic cup for 1 min until the mixture became a white foam, followed by degassing in a vacuum desiccator for 1 h. The mixture was then removed from the desiccator and poured into a Pyrex Petri dish to a depth of ~2 mm (140 mm DI, Corning Inc. Corning, NY, USA). Bubbles were removed by placing the Petri dish into the vacuum desiccator for 20 min, and then dish was covered and placed in an over at 80 °C for 24 h. The cured PDMS was cut into 25 x 27 mm2 rectangles (the same size as the Teflon-coated silicon droplet synthesis chips) with a razor blade. Adhesive tape (810 Scotch Tape, 3M, Saint Paul, MN, USA) was used to keep the surface of the PDMS clean before alignment. A 5 mm hole was punched in the center with a 5 mm biopsy punch (504646, World Precision Instruments). To make the glass portion, pieces of size 25 x 27 mm^2 were cut from microscope slides and treated with Piranha (3:1 mixture of sulfuric acid (H_2SO_4) with hydrogen peroxide (H_2O_2)) for deep cleaning and removal of dust and oils. Once glass slides were rinsed with DI water and dried, the PDMS and clean glass slides were assembled using a corona discharge bonder (LM4816-11MS-MSA, Enercon Industries). The dimensions of the fully assembled cover plate for the encapsulation of microdroplets was 25 x 27 x 3 mm^3 with a 2 mm deep x 5 mm diameter cavity in the middle (**Figure 7.6**).

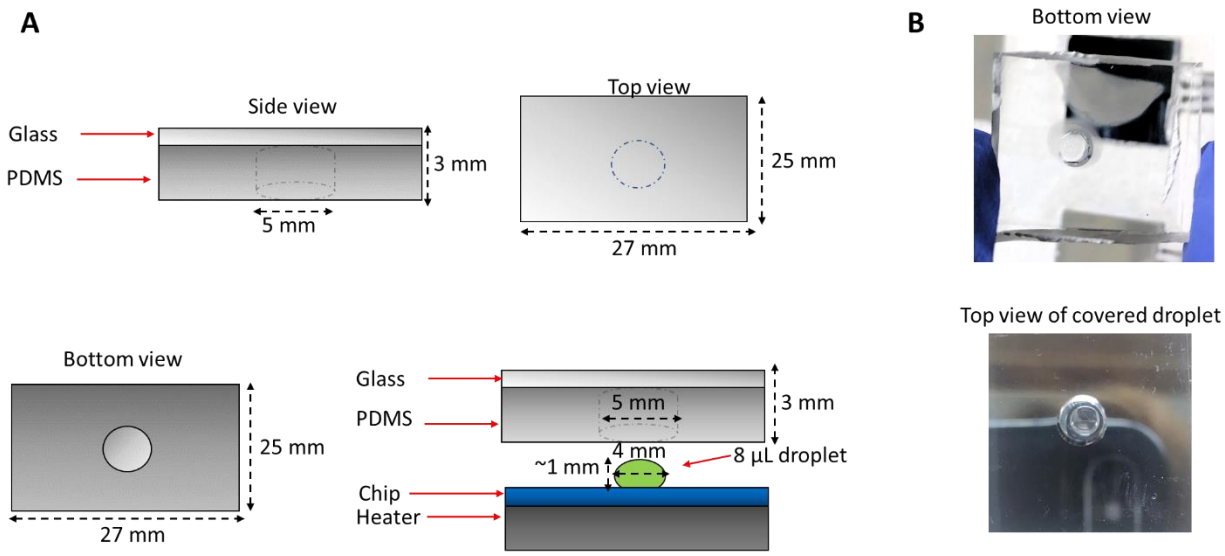

Figure 7. 6 PDMS-glass cover design and assembly for covering droplet reactions.

(A) Schematic of PDMS-glass cover plate design, dimensions, and placement on top of droplet. (B) Photograph of bottom side of PDMS-glass cover plate showing the 5 mm punched hole (Top) and photograph of top view of PDMS-glass cover plate placed on top of the droplet (Bottom).

Efficiency of the cover plate was tested by looking at the shrinking of a solvent droplet for 1 min at different temperatures and measurement of volume recovery thereafter. Evaporation tests were conducted with two different approaches. The first approach was placing an 8 µL droplet of DI water and green food dye (5 mM) on top of a single reaction site chip (4 mm diameter), then the PDMS-glass cover was placed on top of droplet and heater was set to 100°C for 1 min. In a similar test, a hot metal plate was placed on top of the cover plate glass to reduce condensation. The metal plate was pre-heated to 120 °C for 3 min (to equilibrate) and placed onto the cover just prior to heating the droplet. Evaporation tests were also conducted using droplets of NMP. Heating of the droplet was performed at 160, 180, and 200°C for 0.5 min (i.e. relevant times and temperatures for the synthesis [^{18}F]Flumazenil). In a series of experiments with a pre-heated cover, the heater was set to 140 °C (to compare with the maximum operating temperature of the PHENYX system) and the heated cover (using pre-heated metal plate) was tested at 110, 120,

130, 140, and 150 °C. **Figure 7.7** shows the two different approaches to test evaporation of the droplet.

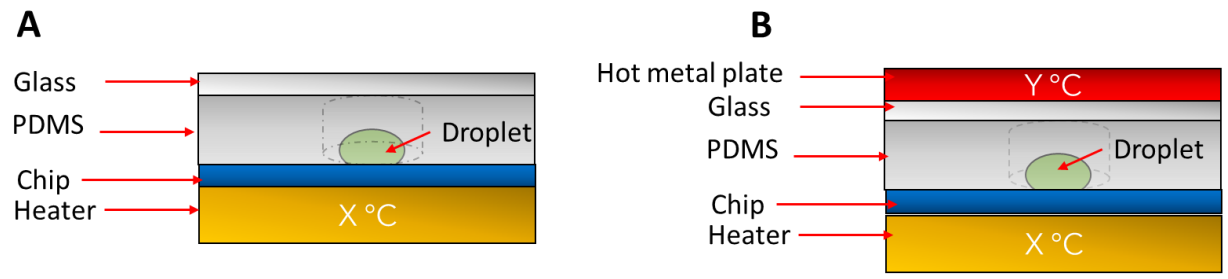

Figure 7. 7 Schematics for testing liquid retention with cover plate using an 8 µL water or NMP droplet.

(A) In the unheated cover experiments, the PDMS-glass cover plate is initially at room temperature and placed on top of the droplet just prior to heating of the bottom chip to X°C. The cover is removed after the heater is cooled for 1 min. B) Experiments with the heated cover are similar except that a pre-heated metal block (at a higher temperature, Y°C) is placed on top of the cover just prior to heating the bottom chip.

Measurements of loss of volatile activity during the fluorination step for [^{18}F]Flumazenil were conducted using the previously optimized conditions(*61*) with only a change in reaction temperature to match the highest possible temperature of the PHENXY system, i.e. 140 °C. First, an 8 µL droplet of [18F]fluoride (~3.7 MBq) mixed with TBAHCO3 (240 nmol) was added to the open chip and then dried at 105 °C for 1 min. Next, an 8 µL droplet of NMP containing 280 nmol precursor and 240 nmol base <<WHICH BASE>> was added and the PDMS-glass cover attached. The heater was then set at 140 °C for 0.5 min. Then, an 8 µL droplet of 240 nmol of precursor solvated in NMP was added to the dried residue the PDMS-glass cover plate was placed on top droplet. The heater was set at 140 °C for 0.5 min and after cooling the cover plate was removed and both the cover plate and bottom chip products were collected with 40 µL of 9: 1 MeOH: H2O (v/v) solution. Then, residual activity on chip and the cover plate was measured using a calibrated dose calibrator and imaged using Cerenkov imaging to visualize the residual activity distribution. **Figure 7.8** shows the overall procedure of the radiochemical reaction for [^{18}F]Flumazenil using the PDMS-glass cover plate.

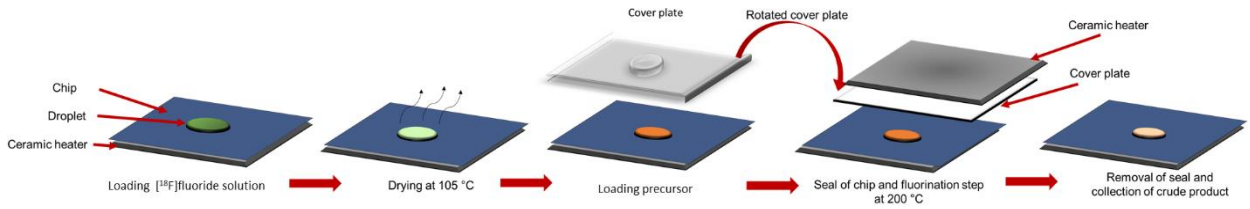

Figure 7. 8 Schematic of the radiosynthesis of [18F]Flumazenil using the designed PMDS cover plate.

Activity on chip is loaded and dried at 105 °C without the cover plate. After cooling, an 8 µL droplet of precursor is be loaded to the dried [^{18}F]fluoride. Then, PMDS cover plate is placed on top of droplet the heater is set to 140 °C. Finally, heater is cooled, and the collection of crude products is performed with a 9: 1 MeOH: H_2O (v/v) mixture for both reaction chip and top cover plate (40 µL on each).

7.2.2.3 Radioisotope concentration chip design

Work by Tucker et al. (2020) demonstrated a chip with hydrophobic coating with a larger, thin hydrophilic ring connected to a small hydrophilic disc(*225*). The design allows the deposition of large droplets, which then are shrunk by evaporation and the design of the chip ensures the concentrated droplet ends up in the small disc region(*225*). The authors utilized glass microscope slides coated with a hydrophobic coating and shapes were edged via laser micromachining. Inspired by this work, we designed microdroplet chips out of Teflon-coated silicon with similar concentration zones to help increase the concentration gradient (and reaction rate) between [^{18}F]fluoride and the precursor.

The multi-reaction microdroplet chips with concentration patterns were fabricated utilizing 4" silicon wafers (P type, boron doped, thickness 525 ± 25 µm; Silicon Valley Microelectronics Inc., Santa Clara, CA, USA) as substrates, which were then coated with Teflon AF and the hydrophilic patterns created via standard lithographic processes reported previously(*31*). The photomask design contained 4 reaction sites positioned in 2 x 2 array with 9 mm pitch and final chips were cut to a size of 25.0 x 27.5 mm^2. In our design, the outer hydrophilic ring had a diameter of 4 mm and line thickness of 10 µm. The circular hydrophilic disk was prepared with different designs: A) Hydrophobic circle was placed in the middle of the ring and 10 µm thick lines connected the circle with the inner edge of the ring. Diameter of the hydrophobic cycle varied to 2.0 mm, 1.5 mm, 1.0

mm, and 0.5 mm. B) Hydrophobic circle was placed at the bottom of the ring connecting with ring's inner diameter; the diameter of the hydrophobic cycle varied to 2.0 mm, 1.5 mm, 1.0 mm, and 0.5 mm. C) Hydrophobic circle was placed at of the bottom of the ring and across it; the diameter of the hydrophobic cycle varied to 2.0 mm, 1.5 mm, 1.0mm, and 0.5 mm. **Figure 7.9** shows the different concentrations patters designed for testing the efficacy of the [^{18}F]Flumazenil radiosynthesis with localized activity.

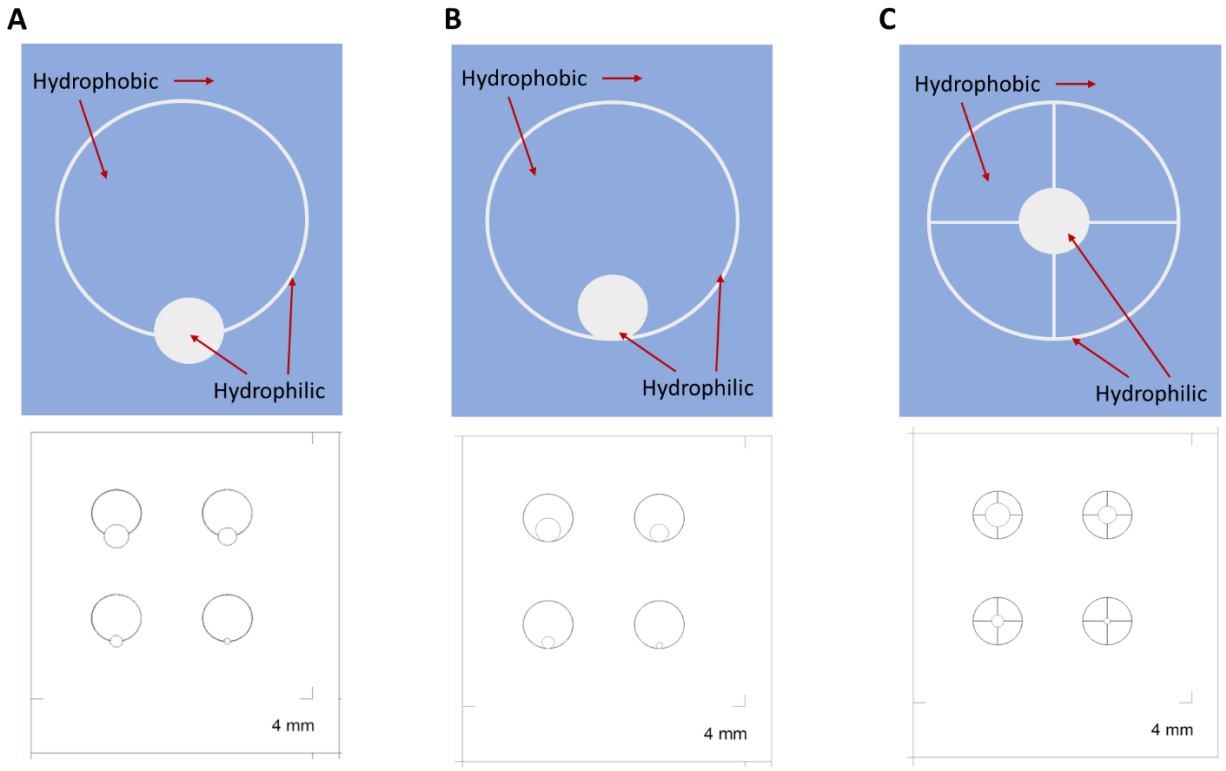

Figure 7. 9 Schematic of photomasks for the reaction sites capable of [18F]fluoride pre-concentration.

For the top image in each case, the blue area represents hydrophobic Teflon coating, and the white area represents where the Teflon will be etched away to reveal the hydrophilic surface beneath. The bottom image in each case shows the arrangement of 4 reaction sites on each chip, where each design has slightly different sized hydrophilic disk.

We have observed in previous experiments that when an 8 µL droplet of [^{18}F]fluoride mixed with $TBAHCO_3$ is dried on a 4 mm diameter reaction site, the dried activity is inconsistently distributed, sometimes spread uniformly over the reaction site and sometimes localized to different points within the

reaction site (see **Figure 7.10A**). The unpredictable distribution sets a lower bound on the volume of precursor solution that needs to be added (i.e. it has to fully cover the reaction site to ensure that the dried activity can dissolve into the precursor solution). This minimum volume is typically 6-10 µL, depending on solvent. The new concentration chip designs allow for the activity to be localized to a smaller area and at a very specific location, i.e. within the small hydrophilic disk region within the reaction site. Additionally, this approach leaves the potential to reduce the volume of the precursor solution (and thus mass of precursor) added. **Figure 7.10B** shows the guided localization of activity for a more uniform interaction with the precursor.

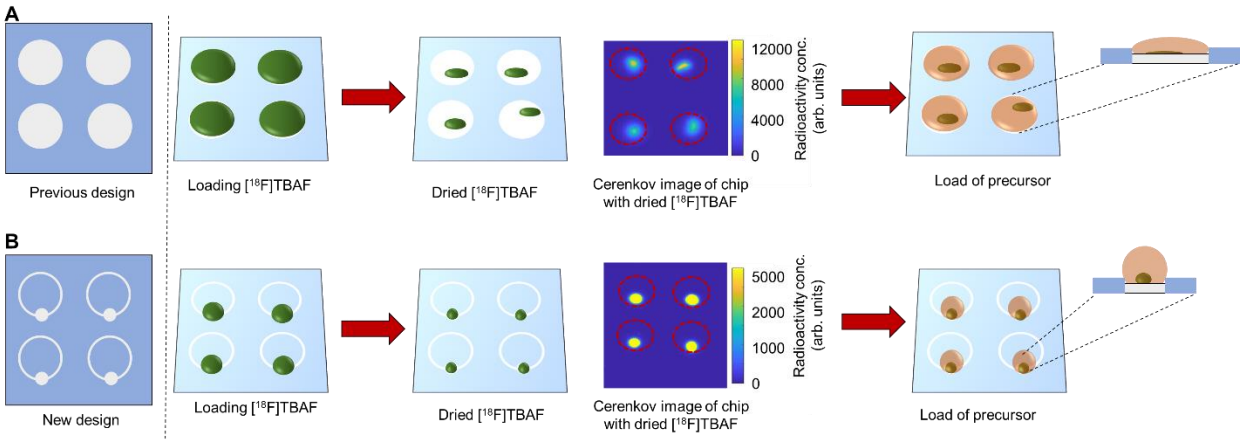

Figure 7. 10 Activity localization after [18F]fluoride drying on different reaction site design.

(A) Chip design showing the 4 mm diameter hydrophilic reaction site (left). Blue represents hydrophobic surface while white represents hydrophilic surface. An 8 µL droplet of activity solution evaporates to an inconsistent spatial distribution of dried activity (middle). The 6-8 µL precursor solution droplet has a large size (right). (B) Chip design showing patterned reaction sites for pre-concentration of activity. The pattern causes an 8 µL droplet of activity solution to evaporate to a consistent small-diameter region of activity residue with predictable position. The concentrated activity transiently increases the concentration of [18F]fluoride when the precursor solution is first added, and the 6-8 µL droplet of precursor solution has a smaller size, potentially reaching a uniform concentration in a shorter time.

On these chips, radiosynthesis of [^{18}F]Flumazenil was performed by adding an 8 µL droplet of [^{18}F]fluoride mixed with 240 nmol of $TBAHCO_3$. Drying was performed for 1 min at 105 °C. Next, 8 µL of precursor solution (280 nmol in NMP) was added to the dried residue and reacted at 200 °C for 0.5. After the reaction was complete, crude product was collected by dispensing 10 µL of

collection solution (9:1 MeCN:H_2O v/v) to the reaction site and aspirating the volume and repeating these steps 4x for a total of 40 µL of collected crude product. For all configurations, the reaction performance was determined by measuring both the conversion of [^{18}F]fluoride to product via radio-TLC, as well as the recovered activity from each reaction (compared to starting activity, i.e. collection efficiency), and multiplying these values to determine an overall crude radiochemical yield (RCY).

7.2.3 Results

7.2.3.1 Closed reactors

Previous results reported by Lu et al. (2022) showed the efficacy of the PHENYX system on the feasibility to perform the radiosynthesis of the radiopharmaceutical [^{18}F]Fallypride using an automated enclosed microfluidic system(*219*). The synthesis of [^{18}F]Fallypride does not suffer from volatility and has successfully been synthesis in open format [[REF Jia ultra-compact platform paper]]. However, for a synthesis such as [18F]Flumazenil, with a high degree of volatile loss, we hypothesized that the platform could be used to explore the benefits of the closed reaction.

Unfortunately, due to the use of plastic materials (PEEK) in the reaction vessel, the operating temperature is limited to 140 °C instead of the desired 200 °C, and thus we performed the reaction at 140 °C. Another change we made was the increase the reaction time to 7 min instead of 0.5 min, since the PHENYX system requires a longer period to achieve the desired temperature inside the reaction volume. All other conditions were the same as the droplet chip reaction. With this system, the collection efficiency was 69.5 ± 0.7% (n=2), fluorination efficiency was 13.5 ± 1.4% (n=2), and the overall crude RCY was 9.5 ± 0.7% (n=2). It was encouraging to see an improved result compared to the open chip, but the performance was still well below the previously optimized open chip reaction at 180 °C. Meaningful evaluation of the potential for the covered reactor to improve performance through volatility reduction would require making modifications to the system that allow a higher temperature range to be explored.

Another approach using close reactors as a test on the improvement on the reaction is the use of sealed HPLC vials(*59*). An advantage of using the HPLC vials as reactors instead of the PDMS-glass cover plate or the PHENYX system was the compatibility with elevated temperatures. Vials were heated by placing them in a metal vial holder containing silicon oil and pre-heated on top of a hot plate to 200 °C. Since the glass walls of the vial are not as good a conductor as the silicon droplet reaction chips, we explored a variety of reaction times to account for slower heating, including 0.5, 2, 5, and 7 min at 200 °C. Other conditions of the reaction were identical to the droplet chip reactions. Results are summarized in **Table 7.2**.

Table 7. 2 Synthesis of [18F]Flumazenil via droplet reactions at 200 °C inside sealed HPLC vials.

Reaction time (min)	Collection efficiency (%), n=3	Fluorination efficiency (%), n=3	Crude RCY (%), n=3
0.5	99.5 ± 0.5	8.6 ± 0.8	8.7 ± 0.8
2	99.7 ± 1.7	9.1 ± 1.1	9.1 ± 1.3
5	99.0 ± 0.4	11.1 ± 0.5	11.0 ± 0.5
7	100.4 ± 1.1	12.8 ± 0.9	12.9 ± 1.1

The results show a complete retention of activity (i.e. no volatile losses; collection efficiency ~100%) in all cases An increase in crude RCY was observed for an increase in reaction time. Unfortunately, the crude RCY is still lower than that for an open droplet reaction (19.1 ± 0.6; [n=4] for 0.5 min reaction time). Some issues with the use of HPLC vials as reactors were their poor heat transfer and poor removal of water during the drying step due to condensation on the vial walls.

7.2.3.2 PDMS-glass cover

Heating of an 8µL droplet of water with food dye for 1.0 min at 100 °C showed accumulation of a significant amount of water on the cover plate via condensation of the liquid, likely due to the cooler surface of the cover plate in comparison the bottom chip that was placed on the heater. However, using a micropipette, 4 µL of liquid could be recovered from both the chip and cover, suggesting that PDMS is effective in preventing loss of vapor from the heated droplet. To reduce

the condensation on the cover, a preheated hot metal plate was placed on top of the cover. **Figure 7.11** shows the no condensation on the unheated versus heated cover.

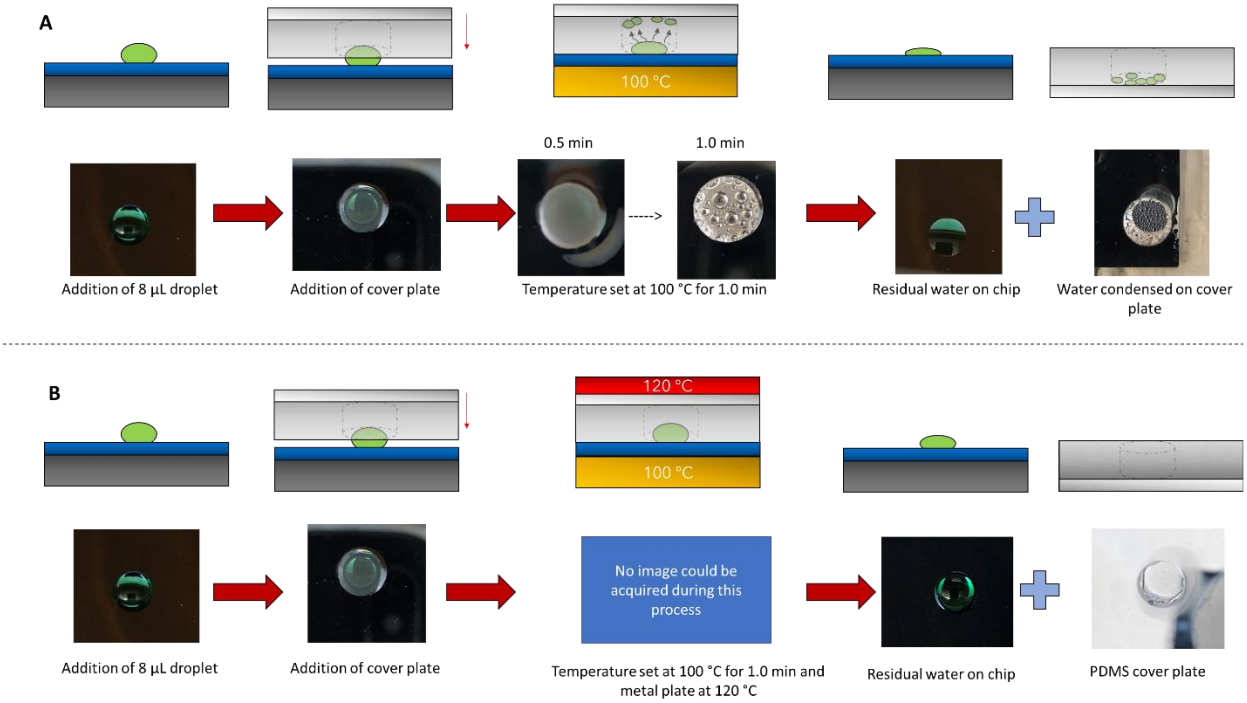

Figure 7. 11 Experiments to evaluate retain of liquid in a heated droplet (on a chip with 4 mm hydrophilic disk reaction site) using the PDMS-glass cover.

(A) First, an 8 µL water droplet with green food dye is dispensed onto the chip. An unheated PDMS-glass cover is then placed on top of the droplet, and then the chip is heated from below at 100 °C for 1 min. Condensation of liquid builds up on the cover, and after cooling and 'opening' the chip, liquid is observed on both the reaction site and the cover. (B) In this part, a heated cover (120 °C) is used in an analogous experiment. The heated cover inhibits condensation and most of the volume ends on the bottom chip.

Next, a similar test was performed using an 8 µL droplet of NMP (the reaction solvent for [18F]Flumazenil; boiling point 202 °C). Initially, an unheated cover was used, and covered droplets were heated to 140, 160, 180, and 200 °C for 0.5 min to mimic several reaction temperature conditions. The results using an unheated cover are shown in **Figure 7.12**. When heating the droplet to 160 °C, very little condensation was observed on the cover plate. However, at 180 and 200 °C we noticed high condensation on the cover plate where most of the liquid stayed; surprisingly even though these temperatures are below the boiling point, significant evaporation and condensation was observed at these temperatures.

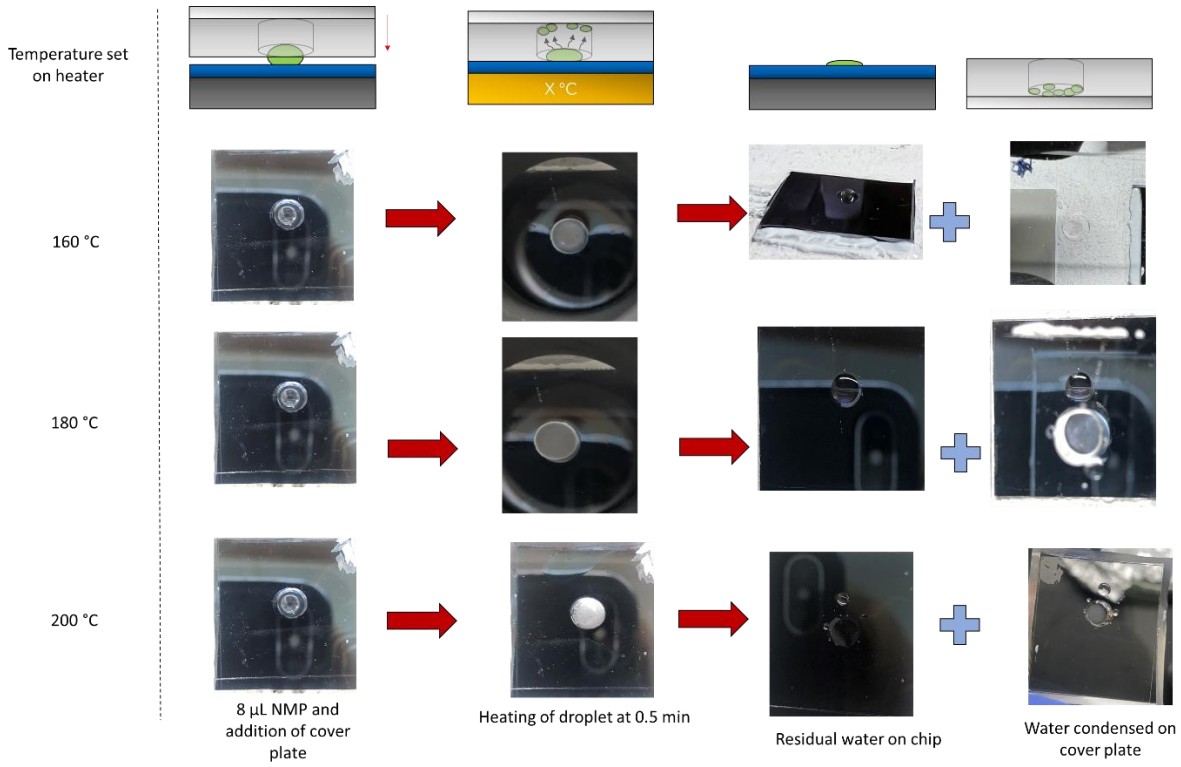

Figure 7. 12 Evaluation of heating of NMP droplets to different temperatures when covered with an unheated PDMS-glass cover.

For the heated cover, we found temperatures at 150 °C or above to lead to shattering of the glass portion of the cover, presumably due to thermal stress, and thus experiments could only be performed up to 140 °C. **Table 7.3** shows the volume recovered at the bottom chip and the cover plate when using a hot metal plate on the top.

Table 7. 3 Measurements of volume at the reaction site and condensed on the cover plate after heating an initial 8µL droplet of NMP when using a heated PDMS-glass cover.

Temperature set on bottom heater (°C)	Temperature set on metal plate (°C)	Volume recovered on the reaction site (µL)	Volume lost on the top cover plate (µL)
140	110	2.7	5.3
140	120	3.5	4.5
140	130	5.9	2.1
140	140	6.3	1.4
140	150	7.5	0.5

Given the temperature limitation, we attempted to perform the [18F]Flumazenil fluorination step at 140 °C, using the cover heated to 150°C. For comparison, open chip reactions were also

performed at 140 °C (to compare effect of cover) and at 180 °C. In the reaction with the cover plate, the collection efficiency was improved (92%, n=1, compared to 74%, n=1, for the open droplet reaction), while the fluorination efficiency was similar (7.3%, n=1 versus 7.0%, n=1, for the open reaction), leading to an improved crude RCY (i.e. 6.1%, n=1 versus 5.2% for the open reaction). This result suggests the cover is improving the synthesis by reducing volatility, but unfortunately with this cover method we had to significantly reduce the reaction temperature, leading to an overall low performance. For contrast, when the open reaction was performed at 180 °C, the collection efficiency was 61% (n=1) and fluorination efficiency was 29% (n=1), corresponding to a crude RCY of 17.6% (n=1). Thus, to meaningful pursue this strategy of volatility reduction will require development of a cover method that is compatible with at least a 200 °C cover heating.

Figure 7.13 shows the summary of reaction performance using different closed reactor methods (PDMS-glass cover, PHENYX system, and HPLC vials) compared to open chip reactions. In general, the closed platforms effectively improve the collection efficiency, but the fluorination efficiency suffers.

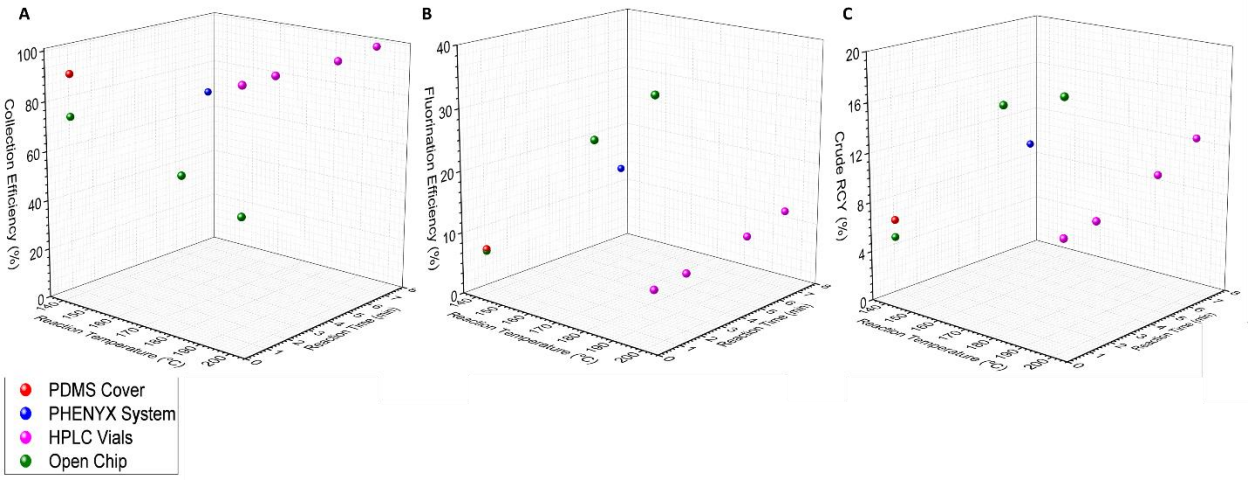

Figure 7. 13 Summary of the overall performance using different closed reactor approaches vs open chip reactions.

(A) Collection efficiency. (B) Fluorination efficiency. (C) Crude radiochemical yield (RCY).

7.2.3.3 Preconcentration reaction sites

To test the compatibility of the new reaction site design with pre-concentration features, we observed the behavior when a 30 µL droplet of water with food dye is dried at 100 °C for 2 min. The results (**Figure 7.14A**) showed that the food dye became concentrated at the small hydrophilic disk as expected(*225*). Among the design variations shown in **Figure 7.9**, we noticed that the best configuration was the originally reported geometry, i.e. where the small hydrophilic disk is centered on the larger ring as originally reported by Tucker *et al.*(*225*). The configuration the hydrophilic disk tangent to the inside of the larger ring showed liquid to be retained on the hydrophilic ring at its 0.5 mm diameter. The configuration with the hydrophilic disk centered and connected via straight lines to the larger outer ring showed a splitting of the droplet with some liquid left on portions of the ring in addition to the hydrophilic disk. To assess if these configurations would be compatible with the use of [^{18}F]fluoride with $TBAHCO_3$ ([^{18}F]TBAF), 30 µL of activity mixed with the base phase transfer catalysis was added to each of the different configurations and dried at 100 °C for 2 min, and Cerenkov luminescence was used to visualize the localization of activity (**Figure 7.14B**). All configurations showed a concentration of activity at the desired hydrophilic disk region, perhaps differing from the behavior of the aqueous food dye solution due to differences in surface tension.

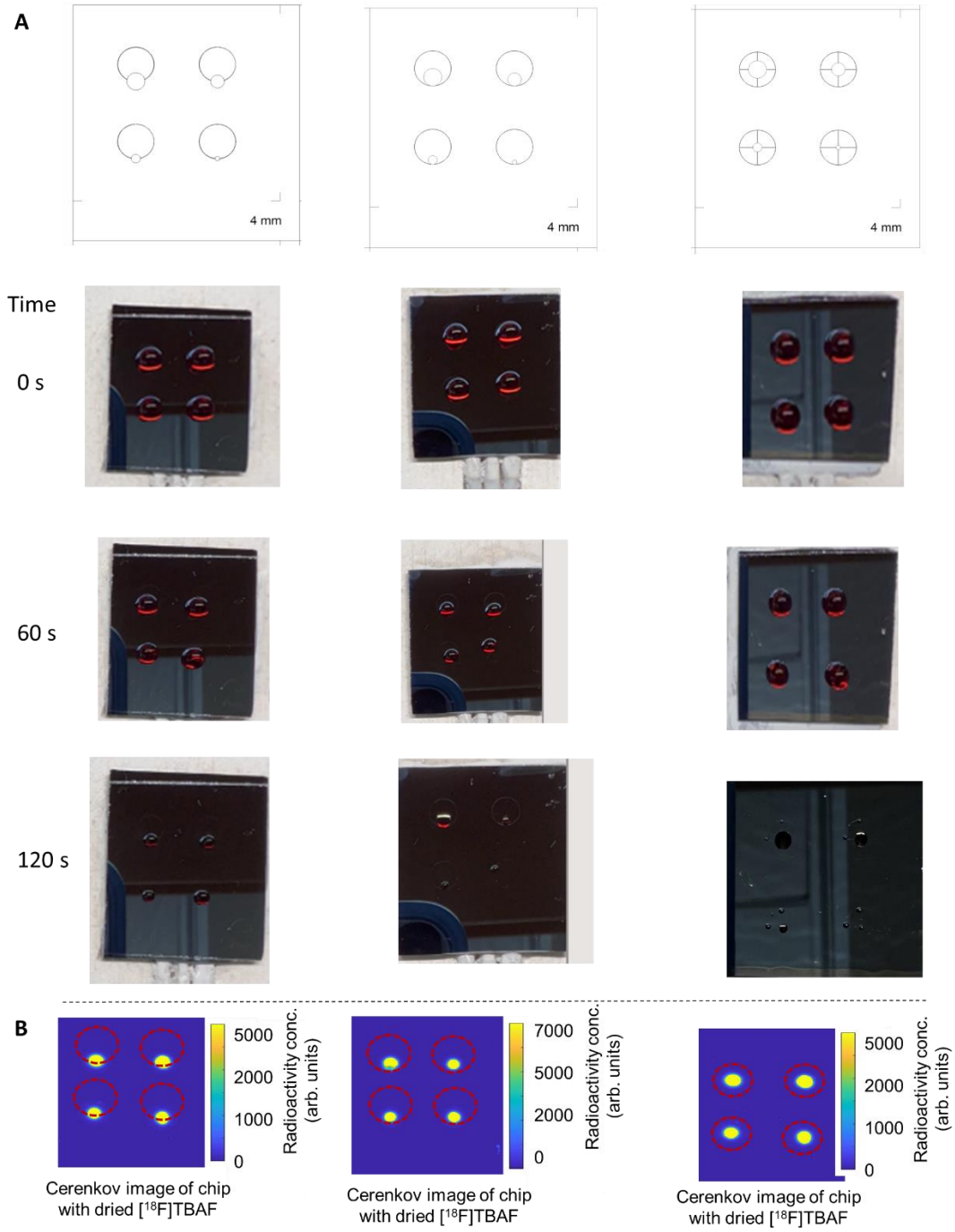

Figure 7. 14 Behavior of droplets on the pre-concentration chips.

(A) Images of the mask design (showing the set of different sized hydrophilic disks for each design) are shown at the top. The photographs below show the behavior of the red food dye solution droplet at different timepoints during heating. (B) Cerenkov images of the distribution of [18F]TBAF residue after heating for 2 min. A red dash circle is drawn on each image to show the location of the larger diameter ring.

To assess the compatibility of the reaction chips with a radiochemical reaction, the three configurations shown above in **Figure 7.14** were used to perform the product formation of [^{18}F]Fallypride, which is a non-volatile reaction. A reaction was also performed with a typical 4 mm disk reaction site on the same day as a control. The results on the performance of [^{18}F]Fallypride showed no difference with respect to circle position or diameter (**Table 7.4**) and were comparable to what was previously reported in other work(*24,31*). Configuration A and B at the 1 mm diameter were outlier results since some activity was spilled during collection.

Table 7. 4 Performance on the production of [18F]Fallypride using different chip configurations.

Chip configuration	Reaction diameter size (mm)	Collection efficiency (%)	Fluorination efficiency (%)	Crude RCY (%)
A	2	95	93	88
	1.5	90	90	81
	~~1~~	~~61~~	~~88~~	~~53~~
	0.5	95	88	84
B	2	95	92	87
	1.5	93	81	76
	~~1~~	~~70~~	~~93~~	~~65~~
	2	95	92	87
C	2	94	91	86
	1.5	93	91	84
	1	93	92	86
	0.5	94	90	85
Single reaction	4	84	91	76

Though all configurations had similar performance, we opted to assess the synthesis of [18F]Flumazenil using configuration A based on the earlier evaporation results. In addition to the use of configuration A to test the reaction, the use of lime pattern and checkers were used to test the performance as well since activity concentration at the reaction site may be split into smaller areas due to the alternation on hydrophobic and hydrophilic by the patterns. The reactions were performed using the optimized conditions previously reported(*61*), i.e. using an 8 µL droplet of [18F]fluoride containing 240 nmol of $TBAHCO_3$ for the drying step and then adding an 8 µL droplet of precursor (280 nmol) in NMP and reacting at 200 °C for 0.5 min. All results showed reasonably

good fluorination efficiency, but collection efficiency improved as the hydrophilic disk size decreased, leading to higher crude RCY with smaller size of the hydrophilic disk (**Figure 7.15, Table 7.5**).

Encouragingly, the maximum crude RCY observed was 27% (n=1), which was a 40% improvement (i.e. 8 point improvement) from the previously reported 19.1 ± 0.6 % (n=4) in open droplet chips(*61*). For those previous droplet reactions, the collection efficiency was 50.9± 1.3 % (n=4) for 3 mm diameter disk-shaped reaction sites, and thus the new chip design exhibited a modest improvement. A larger improvement was seen for the fluorination efficiency, which increased from 37.5 ± 0.8 % (n=4) for the simple 3mm disk design (*61*) up to 51% for the new design.

We hypothesize that the higher local concentration of [18F]fluoride at the beginning of the speeds the reaction with the precursor, enabling greater formation of the product before the activity is volatilized. In the future, it would be interesting to design new chips and experiments to test this hypothesis.

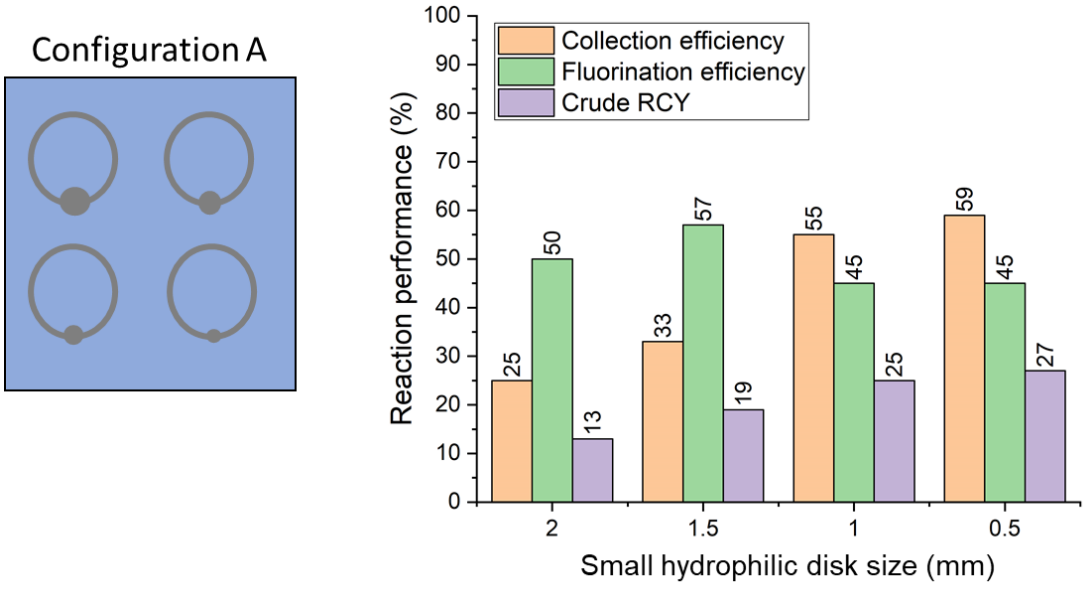

Figure 7. 15 Schematic of the different configurations of the pre-concentration reaction sites and the performance of [18F]Flumazenil synthesis.

The graph shows collection efficiency, fluorination efficiency, and crude RCY.

Table 7. 5 Summary of performance of [18F]Flumazenil synthesis on different configurations of the pre-concentration reaction sites.

Chip pattern	Reaction diameter (mm)	Collection efficiency (%)	Fluorination efficiency (%)	Crude RCY (%)
A	2	25	50	13
	1.5	33	57	19
	1	55	45	25
	0.5	59	45	27

7.3 Conclusion

In this chapter we explored the use of different approaches to reduce the loss of activity via volatility during the fluorination step for [^{18}F]Flumazenil. Closed reactors that were explored include a microvolume radiochemistry system with a closed reactor (PHENYX), capped HPLC vials, and a PDMS-glass cover. All three methods showed high retention of all the activity during the reaction, i.e. collection efficiency close to ~100%. For some cases a portion of the reaction solvent had moved to another part of the reactor (e.g. condensation under the PDMS-glass cover), but this could be mitigated by heating the cover to a sufficiently high temperature. Temperature limitations of the PDMS-glass cover and PHENYX system prevented testing of the synthesis at the usual 200 °C temperature and the fluorination efficiency suffered significantly. For the PDMS-glass cover, it was still apparent that the cover improved the reaction performance compared to the open droplet case, but due to the temperature effect, it is not possible to know if it would improve the yield at a 200 °C reaction temperature. A removable cover that could withstand these temperatures is ideally desired to further pursue this direction. HPLC vials were compatible with the higher temperature but required a longer reaction time and achieved a lower crude RCY performance than the open droplet chip, and furthermore, it would be difficult to automate the process. It is possible that smaller vials would help to better contain the activity in small area during the drying step and potentially improve performance, or that better

characterization of heating could help to determine the optimal setting of the heating system to achieve an actual in-droplet temperature similar to the open droplet chips.

The other approach explored for the improvement on efficiency of the volatile reaction was to use a new reaction site design that could pre-concentration the [18F]fluoride solution into a smaller area prior to adding the precursor solution. The chips achieved significantly improved fluorination efficiency and moderate improvement in collection efficiency (for sufficient degree of concentration), leading to an improved crude RCY beyond what was possible with the open droplet chip, suggesting further exploration and optimization of this approach is warranted to better understand and leverage the mechanism of the performance improvement for the synthesis of [18F]Flumazenil and other tracers exhibiting high volatile losses when performed in an open droplet format.

Chapter 8: Electrochemical fluorination and radiofluorination of methy(phenylthiol)acetate

8.1 Introduction

Incorporation of fluorine into a lead molecule can have a positive impact on metabolic stability, pKa, intrinsic potency, membrane permeability and pharmacokinetic of bioactive molecules.(*226–231*) Organofluorine molecules can rarely be found in nature and hence the introduction of a fluorine atom into a naturally occurring organic molecule requires the development of appropriate synthetic methods developed in the lab. Fluorine gas and fluorinating agents derived from it have widely been used as the source of fluorine atom for fluorination of organic compounds.(*232–235*) However, fluorination of organic substances using fluorine gas is difficult because fluorine gas is highly toxic and reactive. Furthermore, the ^{18}F isotope of fluorine, which has been established as the most promising isotope for Positron Emission Tomography (PET), is most accessible and practical for PET tracer development in 18F-fluoride form produced via a $^{18}O\text{-}H_2O(p,n)^{18}F$ nuclear reaction in a cyclotron.(*236*) PET has extensive clinical applications in early disease diagnosis, treatment progression monitoring as well as in drug discovery and development.(*237*) Despite the synthesis of a wide variety of ^{18}F labeled PET probes, their clinical translation is often hindered due to a lack of viable late-stage synthesis methods with ^{18}F-fluoride and the 110-minute half-life of the isotope.(*238*) The biggest roadblock in making a wider scope of fluorinated molecules easily accessible, is that precursors with no positive charge at the site of fluorine labeling are not readily amenable to nucleophilic substitution reactions with fluoride.(*239*) Development of PET tracers and availability of fluorinated bioactive molecules synthesized by nucleophilic fluoride would benefit from a convenient late stage fluorination method.(*240*) Electrochemical nucleophilic fluorination of organic molecules has been reported as a powerful method for introduction of the fluorine atom into organic compounds.(*241–243*) Electrochemical

fluorination has commonly been performed in solutions containing an excess of poly HF salts such as $Et_3N.3HF$ and $Et_3N.4HF$ as a fluoride source.(*244–247*) However, HF salts are expensive, toxic and corrosive. Tetrabutylammonium fluoride (TBAF) is a source of fluoride which is less toxic, easier to handle and also inexpensive compared to HF salts, making it a suitable alternative for electrochemical fluorination. A further advantage of using TBAF, instead of HF salts as a source of fluoride, is the traditional use of ^{18}F-TBAF in radiofluorination.(*248*) Previous attempts at electrochemical radiofluorination with ^{18}F-poly-HF salts, which severely limits specific activity and places a theoretical limit on radiochemical yield, have been reported.(*249*,*250*) However, previous reports on the use TBAF for electrochemical fluorination of phenyl(2,2,2-trifluoroethyl)sulfane, have not been successful.(*241*) [^{18}F]fluoride in form of ^{18}F-TBAF in this report was obtained by first trapping [^{18}F]fluoride anion on an anion exchange resin in order to remove the water, and subsequent elution of [^{18}F]fluoride from the cartridge using tetrabutylammonium fluoride.

Electrochemical fluorination using TBAF was only made possible with the addition of trifluoromethanesulfonic (triflic) acid during electrolysis. Triflic acid is a known super acid whose conjugate base is a very weak nucleophile.(*251*) The addition of triflic acid may form HF molecules that can participate in electrochemical fluorination, while the very weak conjugate base of triflic acid will not react with the intermediate carbocations formed during electrochemical oxidation.

The successful electrochemical fluorination of methyl(phenylthio)acetate using TBAF as a source of fluorine will be shown. Furthermore, ^{18}F-methyl 2- fluoro-2-(phenylthio)acetate was radiosynthesized using ^{18}F-TBAF as a source of fluorine. The products were detected and analyzed using HPLC, GC-MS and NMR. Effect of several parameters such as electrolysis potential, time, temperature, triflic acid concentration and TBAF concentration were investigated and optimized.

8.2 Experimental methods and materials

High-resolution mass spectra and chromatograms were obtained with an Agilent 5975C TAD inert MSD mass spectrometer coupled with an Agilent 7890A gas chromatograph. Cyclic voltammeteric (CV) and electrosynthesis experiments were performed using the Metrohm PGSTAT128N electrochemical workstation. All CVs were performed at room temperature using a 200 mV/s scan rate.

Radiofluorination conversion was measured using Radio-thin-layer-chromatography (radio-TLC). Radio-TLC was performed on silica plates (TLC Silica gel 60 W F_{254}s, Merck). After dropping a sample volume (~1–5 µL) using a glass capillary, the plate was developed in the mobile phase (ACN). Chromatograms were obtained using a radio-TLC scanner (miniGita Star, Raytest).

Analytical High Performance Liquid Chromatography (HPLC), equipped with a UV and gamma detector was used to determine radiochemical purity (RCP) of the radio-fluorinated product. HPLC was performed using a 1200 Series HPLC system (Agilent Technologies) equipped with a GabiStar flow-through gamma detector (Raytest). Data acquisition and processing was performed using GINA Star Software version 5.9 Service Pack 17 (Raytest). Typically, 20 µL of radioactive sample was diluted with 180 µL of ACN and 5–20 µL of this solution was injected for HPLC analysis. Column: Phenomenex Luna 5u C18 (2) 100 A, 250 × 4.6 mm, 5 micron. Gradient: A = ACN; B = water; flow rate = 1.8 mL/min; 0–12 min 90% B to 5% B, 12–13 min 5% B, 13–14 min 5% B to 90% B.

Radio-TLC chromatograms were used to measure radiochemical conversions (RCC). RCP and RCC were measured by dividing the area under the curve (AUC) for the desired product by the sum of AUC for all peaks. The TLC purity accounts for unreacted ^{18}F-fluoride while the HPLC purity corrects for radiochemical side-products. The radiochemical fluorination efficiency (RCFE) was determined by the equation: RCFE = TLC RCC × HPLC RCP.

The GC-MS, TLC and HPLC analysis were performed on crude samples, and the reported yields in optimization studies are based on the quantification of GCMS results. The reaction products were HPLC purified and isolated for purposes of proton and fluorine NMR analysis for further identification.

The electrochemical fluorination and CVs were carried out using a conventional undivided 3-electrode cell with two platinum wires (length = 200 mm, diameter = 0.33 mm) as working and counter electrode and Ag/Ag^+ reference electrode in a 13.2 mL solution containing dry ACN (11 mL), 2 mL of 1 M TBAF solution in tetrahydrofuran (THF) (154 mM TBAF final concentration), 120 µl of triflic acid (104.6 mM final concentration) and 50.8 µl of methyl(phenylthio)acetate (25 mM final concentration). The reference electrode solution was 10 mM $AgNO_3$ plus 100 mM tetrabutylammonium perchlorate in dry ACN. The reference electrode solution was separated from the reaction mixture by porous glass frit.

The counter electrode and working electrode were cleaned before each experiment using potential cycling in 1 M sulfuric acid solution in water. The electrodes were cycled between −2 V and 2 V (2 electrode configuration) 10 times before each experiment.

Trifluoromethanesulfonic acid (triflic acid, CF_3SO_3H, 99%) and methyl(phenylthio)acetate ($C_9H_{10}O_2S$, 99%) were purchased from Oakwood Chemical. Acetonitrile (ACN, anhydrous, 98%), tetrabutylammonium fluoride solution 1.0 M in THF (TBAF solution, ~5 wt% water) and platinum wire (99.9%) were purchased from Sigma-Aldrich.

Electrolysis was performed using a constant potential technique while the solution was stirred at 300 rpm. In order to prevent formation of polymerized products on the working electrode, the polarity of the electrode was alternated every 60 s between the chosen fluorination potential and −0.6 V; electrode was kept at −0.6 V for 5 s.

No-carrier-added ^{18}F-fluoride was produced by the (p,n) reaction of $^{18}O–H_2O$ (84% isotopic purity, Medical Isotopes) in a RDS-112 cyclotron (Siemens) at 11 MeV using a 1 mL tantalum

target with havar foil.(*252*) The radioactive isotope was trapped on an anion exchange resin by passing through the 1mL of bombarded $^{18}O–H_2O$. Most of the water on the resin was removed by washing with 10 mL of anhydrous ACN and drying with ultra-pure N_2 for 10 min. [^{18}F]fluoride was subsequently eluted out from the cartridge with a 2 mL solution containing 0.5 mmol TBAF in THF + ACN solution (1:1). In a typical experiment, approximately 5 mCi was eluted from the anion exchange cartridge in ^{18}F-TBAF form in dry ACN.

8.3 Results and discussion

Figure 8.1 shows CVs of different combination of chemicals used in the electrochemical fluorination experiments. It can be seen that the CV of ACN + precursor shows a very small cathodic or anodic current between −1 V to 2 V. While CVs of ACN + triflic acid and ACN + triflic acid + THF also shows very small anodic current at potentials higher than 0 V vs Ag/Ag^+, a high cathodic current can be observed at potentials below 0 V vs Ag/Ag^+, which can be attributed to the hydrogen evolution on the working electrode. Although ACN + precursor and ACN + triflic acid don't show any anodic current at positive potentials, a combination of these (ACN + triflic acid + precursor) displays an anodic current at potentials higher than 1 V vs Ag/Ag^+.

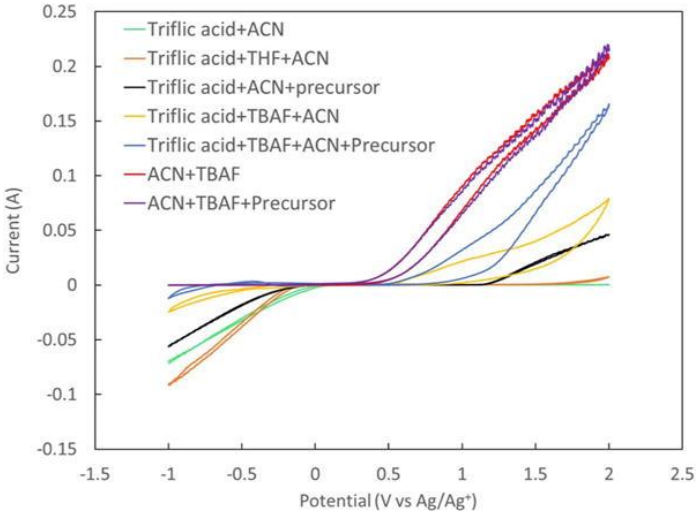

Figure 8. 1 CVs of different combination of materials were used in the electrochemical fluorination of methyl(phenylthio)acetate.

The CVs were run using 200 $mv.s^{-1}$ at room temperature (21°C).

This can be due to the oxidation of the precursor, promoted by the addition of triflic acid. Furthermore, CVs of ACN + TBAF and ACN + TBAF + precursor are very similar, in the way that they don't show any cathodic current, while at potentials higher than 0.5 V vs Ag/Ag^{+} an increase in anodic current can be observed. Similarity in anodic current is due to the high oxidation current from the TBAF solution which has a lower onset potential and occurs at much higher rate compared to the oxidation of the precursor and masks any additional negligible current contribution from the oxidation of the precursor. The addition of triflic acid to these solutions causes a sharp decrease in the anodic current, which is in line with the proposed reaction of triflic acid with TBAF, with hydrogen fluoride as a possible product of this reaction.

The anodic fluorination of methyl(phenylthio)acetate was carried out at constant potential in an undivided cell. The products were analyzed using GC-MS. **Figure 8.2** shows a representative GC-MS chromatogram of the solution before and after electrolysis at 1.4 V for 30 min at room temperature. The chromatogram of the solution before electrolysis shows only one peak for the precursor with the m/z equal to 182. **Figure 8.2** shows that after electrolysis the precursor peak area has decreased and the product peak is observed at 11 min with the m/z of 200.

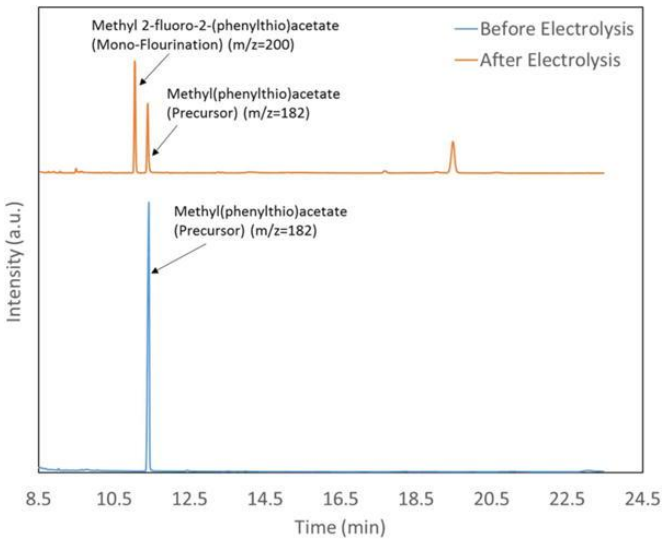

Figure 8. 2 GC-MS chromatogram of the solution before and after electrochemical fluorination. The solution contains 25 mM of 1, 154 mM TBAF and 104.6 mM of triflic acid in acetonitrile.

The 11 min product is attributed to methyl 2-fluoro-2- (phenylthio)acetate (**2**) (monofluorination). The schematic for the electrochemical fluorination of methyl(phenylthio)acetate (**1**) has been shown in the **Figure 8.3**.

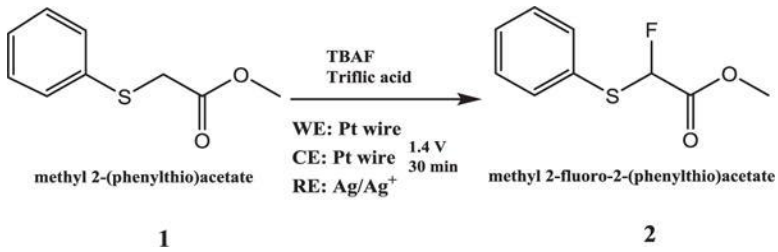

Figure 8. 3 Schematic of the electrochemical fluorination of methyl-2(phenylthio)acetate 1 using TBAF.

Product yields and precursor conversion of the electrofluorinated samples are presented in **Figure 8.4** with different oxidation potentials and in **Figure 8.5** with different electrolysis times.

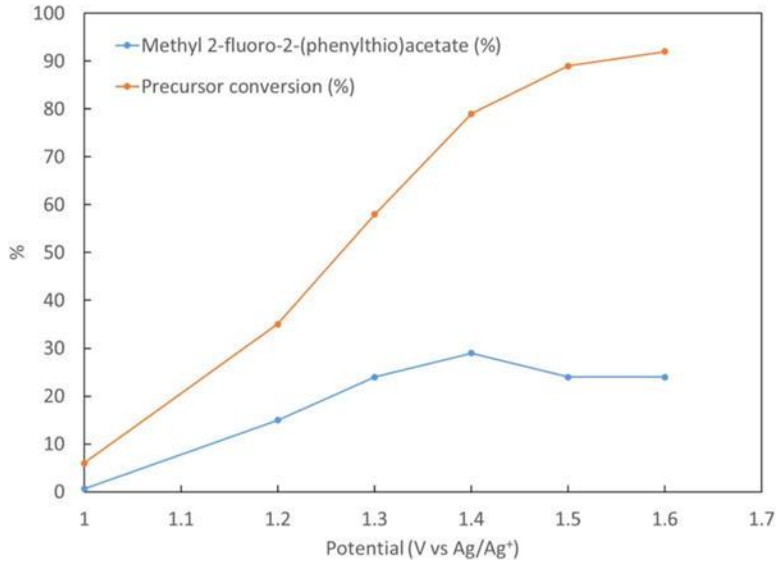

Figure 8. 4 Effect of electrolysis potential on the yield of product and precursor conversion.

Synthesis has been performed at the constant time of 30 min, using ACN solution containing 154 mM of TBAF, 25 mM of precursor 1 and 104.6 of triflic acid.

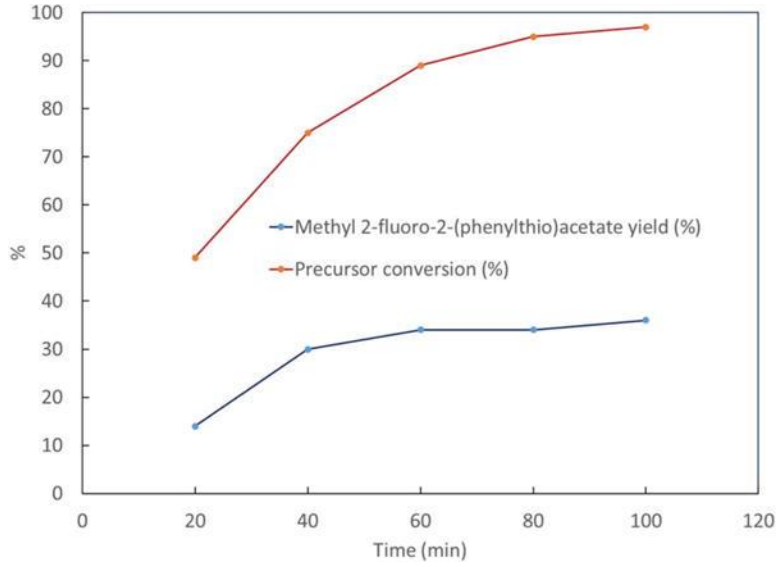

Figure 8. 5 Effect of time on the yield of product and precursor conversion.

Synthesis has been performed at constant potential of 1.4 V vs Ag/Ag+, using ACN solution containing 154 mM of TBAF, 25.1 mM of 1 and 104.56 of triflic acid.

Experiments were performed in triplicates. It can be seen that by increasing the potential from 1 V to 1.4 V vs Ag/Ag^+ both the yields and precursor conversion increase. However, further increase in the potential reduces yields. This may be due to enhanced product oxidation and decomposition at potentials higher than 1.4 V vs Ag/Ag^+. It can also be seen from **Table 8.1** that by increasing electrolysis time, the yield increases with time until a saturation is reached at 36% yield for **2** at 100 min when most of the precursor has been consumed.

Table 8. 1 Effect of acid type on the product yield and precursor conversion.

Synthesis was performed at constant time and potential of 30 min and 1.4 V vs Ag/Ag^+, using ACN solution containing 154 mM of TBAF, 25 mM of 1 and 104.6 mM acid.

Type of Acid	**Methyl 2-fluoro-2-(phenylthio) acetate yield (%)**	**Precursor conversion (%)**
Trifluoromethanesulfonic Acid	29 ± 2	74 ± 14
Sulfuric Acid	3.0 ± 0.2	11 ± 2
Acetic Acid	0.3 ± 0.1	42 ± 8

A shorter electrolysis time of 30 min with a comparable yield of 29% was selected for further optimization. This was selected in preparation for radiochemical fluorination with ^{18}F-fluoride, which has a 110 min half-life, and benefits from increased non-decay-corrected radiochemical yield with shorter synthesis times.

The effect of triflic acid concentration was also examined. The results are shown in Figure A6. When acid concentration increases from 0 to 104.6 mM yield of **2** increases from 0.7% to 29%. Further increase in acid concentration beyond 104.6 mM results in a decrease in yield of **2** until a yield of 0.03% is reached using 208 mM triflic acid.

Electrofluorination was performed using triflic acid, acetic acid and sulfuric acid to study the effect of acid type on product yield. The results are shown in the **Table 8.2**, with triflic acid providing the highest precursor conversion and yield for **2**.

Table 8. 2 Results of the electrofluorination experiments performed at three different temperatures.

It was observed that elevating the temperature has a positive effect on the electrofluorination yield.

Temperature (°C)	Methyl 2-fluoro-2-(phenylthio)acetate (%)	Precursor conversion (%)
0	7.6 ± 0.5	65 ± 12
21	29 ± 2	74 ± 14
60	44 ± 3	63 ± 12

For instance, the yield of the **2** could be increased from 8% to 44% by increasing temperature from 0 °C to 60°C. Elevating the temperature can enhance the diffusion of the molecules in the solution leading to increased yields. The solution was also sonicated in order to confirm if promoting convection in the solution could enhance the yield. Sonication at room temperature increased the yield of **2** from 29% to 42%, a similar gain in yield as was observed with the increase in temperature.

It was also observed that triflic acid to TBAF concentration ratio has a crucial effect on the electrofluorination yield. As the TBAF concentration was decreased and triflic acid concentration was maintained constant, much lower yield of **2** was observed as compared to when TBAF and triflic acid concentrations were proportionally decreased together to maintain a constant ratio. The triflic acid to TBAF ratio, with 154 mM of TBAF, was optimized at 0.68 from the data in **Figure 8.6**.

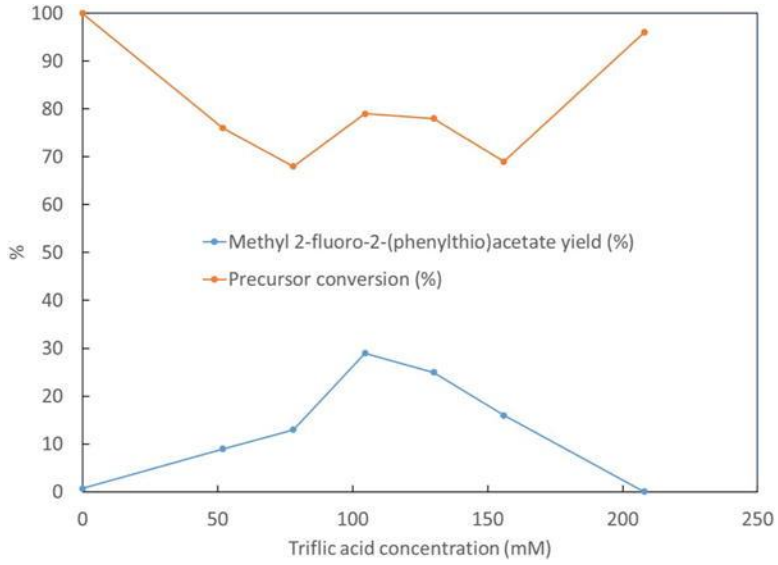

Figure 8. 6 Effect of triflic acid concentration on the product yield and precursor conversion.

Synthesis has been performed at constant time and potential of 30 min and 1.4 V vs Ag/Ag+, using ACN solution containing triflic acid, 154 mM of TBAF and 25 mM of 1.

To study the effect of acid to TBAF concentration ratio, two sets of experiments were performed. In the first set the concentration of TBAF was changed and the triflic acid concentration was kept constant, in the second set the TBAF concentration was changed and the triflic acid concentration also was changed in order to keep the triflic acid to TBAF concentration ratio constant at 0.68. The results are compared and presented in the **Table 8.3** for TBAF concentration ranging from 154 mM to 10 mM.

Table 8. 3 Effect of triflic acid to TBAF concentration ratio on the product yield and precursor conversion.

Synthesis was performed at constant time and potential of 30 min and 1.4 V vs Ag/Ag+, using ACN solution containing triflic acid, TBAF, and 25 mM of 1.

TBAF Concentration (mM)	**Acid Concentration (mM)/TBAF concentration (mM)**	**Methyl 2-fluoro-2-(phenylthio)acetate yield (%)**	**Precursor conversion (%)**
154	0.68	29 ± 2	74 ± 14
	1.36	0.03 ± 0.01	95 ± 3
100	0.68	21 ± 2	68 ± 12
	1.04	5.0 ± 0.3	69 ± 13
25	0.68	6.0 ± 0.4	37 ± 7
	4.16	0	94 ± 3
10	0.68	3.0 ± 0.2	24 ± 4
	10.40	0	74 ± 13

One of the advantages of using TBAF as a fluoride source in electrochemical fluorination is its compatibility and traditional use in radiofluorination with ^{18}F-fluoride. Compared with poly-HF salts, TBAF introduces fewer carrier ^{19}F-fluoride molecules, increasing specific activity and radiochemical yield, which is measured with respect to ^{18}F-fluoride incorporation into the desired product. Since the concentration of ^{18}F-fluoride used in radiochemistry is negligibly small, we studied the effect of decreasing TBAF concentration on electrofluorination yield. The results are shown in **Table 8.4**, indicating that lowering the fluoride concentration from 308 mM to 154 mM does not significantly change the yield of **2**, however a further decrease in fluoride concentration below 154 mM decreases yield of **2**.

Table 8. 4 Effect of TBAF concentration on the product yield and precursor conversion.

Synthesis was performed at constant time and potential of 30 min and 1.4 V vs Ag/Ag+, using ACN solution containing 154 mM of TBAF, 25 mM of 1 and the ratio of triflic acid to TBAF concentration was kept constant at 0.68.

TBAF Concentration (mM)	Methyl 2-fluoro-2-(phenylthio)acetate yield (%)	Precursor conversion (%)	Methyl 2-fluoro-2-(phenylthio)acetate yield (%)[a]
308	29 ± 2	76 ± 14	2.5 ± 0.2
154	29 ± 2	74 ± 14	5.0 ± 0.3
100	21 ± 2	68 ± 12	5.0 ±0.3
25	6.0 ± 0.4	37 ± 7	5.5 ± 0.4
10	3.0 ±0.2	24 ± 4	7.5 ± 0.5
5	0.15 ± 0.01	10 ± 2	0.75 ± 0.05

While lowering fluorine concentration below the concentration of precursor would limit the theoretical chemical yield, the decrease in yield at higher concentrations may be attributed to the limited lifetime of carbocations formed at the surface of the working electrode. At lower concentrations of TBAF, cationic intermediates created on the anode with no fluoride in close vicinity, will have a diminishing chance to react with the fluoride nucleophile before they undergo side reactions. **Table 8.4** also shows the yield of **2** based on the fluoride concentration. It can be seen that by lowering the fluoride concentration from 308 mM to 10 mM the yield of **2** increases, while a further decrease in concentration of fluoride below 10 mM causes a drastic decrease in the yield of **2**.

Electrochemical radiofluorination of the **1** was successfully achieved using the optimized parameters obtained from the cold electrofluorination experiments. (1.4 V, 30 min, 60°C, 154 mM of TBAF, 25 mM of **1** and 104.6 mM of triflic acid). Radiochemical fluorination efficiency obtained by TLC and gamma HPLC was 7 ± 1% (n = 3). The chemical yield (based on the initial precursor

concentration) obtained from the decayed samples analyzed by GC-MS showed a yield of 43% ± 3% (n = 3), which would predict a fluorination yield (based on the initial fluorine concentration) of 7 ± 1% (n = 3) for the mono-fluorinated product, in line with the radiochemical yields obtained.

8.4 Conclusion

For the first time, electrochemical fluorination of methyl(phenylthio)acetate has been achieved using TBAF as a source of fluorine under controlled potentiostatic conditions. It was observed that the use of triflic acid along with TBAF is crucial for successful fluorination and that the TBAF to triflic acid concentration ratio plays a key role in the process. Electrochemical cell parameters such as potential, electrolysis time, and temperature as well concentrations of fluoride source and triflic acid were optimized. CVs guided the selection of oxidation potentials and our understanding of the electrochemical oxidation/reduction response of the system. The optimum oxidation potential of **1** was found to be 1.4 V vs Ag/Ag^+. Potentials higher than 1.4 V vs Ag/Ag^+ resulted in lower yields, likely due to the breakdown of the product. Fluorination at potentials between 1.3 V vs Ag/Ag^+ and 1.1 V vs Ag/Ag^+ required a long time to achieve acceptable yields, which isn't desirable for radioelectrochemical fluorination with ^{18}F-fluoride, which has a 110 min half- life. It was also observed that elevating temperature and sonication could enhance the yield. The highest yield for the mono fluorinated product at 44% was obtained after 30 min of electrolysis at 1.4 V vs ag/Ag^+ using an ACN solution containing 154 mM of TBAF, 25 mM of precursor **1** and 104.6 mM of triflic acid at 60°C.

Electrochemical radiofluorination of methyl 2- [^{18}F]fluoro-2-(phenothio) acetate was confirmed by GC-MS, radio-TLC and HPLC analysis. A radiochemical fluorination efficiency of 7 ± 1% was achieved under the same conditions as the optimized cold reaction for the mono fluorinated product.

Chapter 9: Electrochemical flash fluorination and radiofluorination

9.1 Introduction

Fluorinated organic compounds have distinguishing physical, biological and chemical properties with a wide range of applications in fields such as agrochemicals, pharmaceuticals and materials science.(*253–255*) Recently, there has been growing interest in the chemistry and properties of fluorinated organic compounds.(*255*,*228*,*256*) Fluorine gas and anhydrous HF have been broadly used for fluorination of organic compounds.(*232*,*257*,*229*) However, these chemicals are costly, highly reactive, corrosive, hazardous, and difficult to handle. There is a consensus in the community that given the wide-ranging applications of fluorine in design of bioactive molecules and molecular imaging through positron emission tomography (PET), there is still a strong demand for further development of new synthetic methodologies to expand the chemist's toolbox for easier access to a broader scope of fluorinated and radiochemical compounds.(*258*) There have been significant recent developments in the area of nucleophilic fluorination, a more accessible form of fluorination, and their application to radiochemistry with [18F]fluoride, such as syn-thesis of aryl fluorides directly from the corresponding phenols,(*234*) hypervalent iodine reagents used as fluorine sources in fluorocyclization reactions,(*259*,*260*) radiofluorination of diaryl-iodonium salts and Cu-catalyzed mesityl-aryl-iodonium precursors,(*261*) metal-catalyzed aryl fluoride bond formation,(*262*) and recent reviews on these advances and their limitations.(*263*) Despite the development of modern fluorination techniques, many challenges still exist in terms of limited substrate scope, lack of functional group tolerance, difficulty in synthesizing the precursors and their stability, and the need for strict control of synthesis conditions. No one technique can address all the challenges for site specific fluorination. The electro-chemical approach to fluorination of stabilized cations presents a unique method for direct and very rapid fluorination in one step under mild conditions. The method described here

can target moieties such as thioethers not amenable to late-stage fluorination with existing methodologies, allowing their radio-fluorination for PET tracer development. Electrochemistry is gaining renewed prominence as a versatile tool in organic synthesis.(*264*,*265*) Electrochemical fluorination of organic compounds can be a powerful alternative technique for direct fluorination. Electrochemical oxidation can create an electron-poor carbon, potentially without the need for chemical modification, preparing the organic molecules for nucleophilic fluorination.(*243*,*266*) Fluorine atoms can be added to organic compounds in one step under mild conditions using electrochemistry, even for electron rich moieties such as aromatic and heteroaromatic rings, without the need to have leaving groups.(*267*,*249*) Traditionally, the oxidative formation of a carbocation intermediate in electroorganic synthesis has been performed in the presence of an excess of nucleophile due to the instability of the carbocations. The presence of reactive and low oxidation potential nucleophiles and products in the anodic chamber during electrolysis can limit reaction yields and scope. To overcome this problem Yoshida and co-workers developed the cation pool method, with which they could stabilize the carbocations formed during the electrochemical oxidation of carbamates by performing the electrochemical oxidation at low temperatures (-72˚C) followed by addition of nucleophiles such as allylsilanes post electrolysis.(*268*) Subsequently, the same group reported thiofluorination of alkenes and alkynes using low-temperature anodic oxidation of ArSSAr in Bu4NBF4/CH_2Cl_2.(*269*) In their process, the counter anion of the supporting electrolyte (BF_4^-), which was present during the electrolysis was also the source of fluoride. Here, for the first time, the electrochemical fluorination and radiofluorination of organic molecules using the cation pool technique is reported, where the fluoride is added post electrolysis. This approach enables the use of the cation pool method for the widely useful application of rapid and late-stage fluorination and radiochemistry. The cation pool method has tremendous potential especially for radiofluorination experiments. The excess concentration of reactive cations can provide an efficient reaction mechanism for late-stage fluorination under low fluoride concentrations encountered during radio-fluorination.(*270*)

Furthermore, radiochemical yield, which is reduced by decay of the radioisotope, can benefit from a rapid late-stage fluorination reaction. The cation pool can be prepared prior to cyclotron production of [18F]fluoride isotope, thereby, providing a truly late-stage fluorination reaction, maximizing radiochemical yield by minimizing decay through a flash reaction of the previously prepared cations with[18F]fluoride.

9.2 Materials and methods

9.2.1 Materials

2,2,2-trifluoroethanol (TFE, 99.9%, C2H3F3O), trifluoromethanesulfonic acid (triflic acid, CF3SO3H, 99%), methyl (ethylthio)acetate (99%, C5H10O2S) and methyl(phenylthio)acetate (C9H10O2S, 99%) were purchased from Oakwood Chemical. Acetonitrile (ACN, anhydrous, 98%), tetrabutylammonium fluoride solution 1.0 M in THF (TBAF solution, ~5 wt% water), cesium fluoride (99%, CsF), Potassium fluoride (≥99.9%, KF), triethylamine trihydrofluoride (98%, (C2H5)3N·3HF) and platinum wire (99.9%) were purchased from Sigma-Aldrich. Tetrabutylammonium perchlorate (TBAP, >98.0%, C16H36ClNO4) methyl (methylthio)acetate (>99.0%, C4H8O2S), tetrabutylammonium tetrafluoroborate (>98.0%, C16H36BF4N) and ptoluenesulfonic acid (>98.0%, C7H8O3S·H2O) were purchased from TCI America. 2,6-Di-Tertbutyl-4-methylpyridine (98%, C14H23N) was purchased from Ark Pharm, Inc. Nafion® membrane N117, 7 mils (178 µm thickness) was purchased from Fuel Cell Earth. Analytical grade (AG) MP1M anion exchange resin was purchased from Bio-Rad.

9.2.2 Methods

In this study, a divided electrochemical cell was used for electrolysis. The anodic and cathodic chambers were separated by a Nafion membrane. Methyl (phenylthio) acetate (12 mM) was used as substrate and 2,2,2-trifluoroethanol (TFE) as solvent with different supporting electrolytes in the anodic chamber. TFE, tetrabutylammonium perchlorate (TBAP) and triflic acid were used in the cathodic chamber. 1,1,1,3,3,3-Hexafluoroiso-propanol (HFIP) has also recently been reported as a solvent for electroorganic synthesis with a stabilizing effect on carbocation

intermediates.(*271–274*) However, yields were negligible due to instability of fluorinated products reported here in HFIP. Previous reports on electrochemical fluorination of Methyl(phenylthio) acetate guided our choice for the substrate.(*271*,*275*) Traditional fluorination of sulfoxides have been based on fluoro-Pummerer rearrangement with DAST, electrophilic fluorination of thioethers and the combinations of chemical oxidants with nucleophilic fluorinating reagents.(*276*) Previous electro-chemical fluorination of thioethers were performed with excess amounts of HF salts or TBAF present in the cell during electrolysis, resulting in low fluoride conversion yield and preventing no-carrier-added fluorination.(*267*,*277*,*278*).

9.2.3 Results and discussion

Here, electrochemical oxidation was performed for 60 min at a constant potential of 1.6 V vs Ag wire quasi-reference electrode followed by addition of a fluoride nucleophile to the anodic chamber at the end of electrochemical oxidation. The mixture was stirred and allowed to react for 30 min while the temperature was rising to room temperature. With 168 mM of CsF, KF, Et3Nx3HF and tetrabutylammonium fluoride (TBAF) used as fluoride (nucleophile) sources, respective yields of 4.5%,1.4%, 4% and 4.5% of methyl 2-fluoro-2-(phenylthio) acetate were obtained. The yields were quantified using gas chromatography mass spectrometry (GC-MS). **Figure 9.1** shows the schematic of the reaction and representative GC-MS chromatograms can be found in the supporting information.

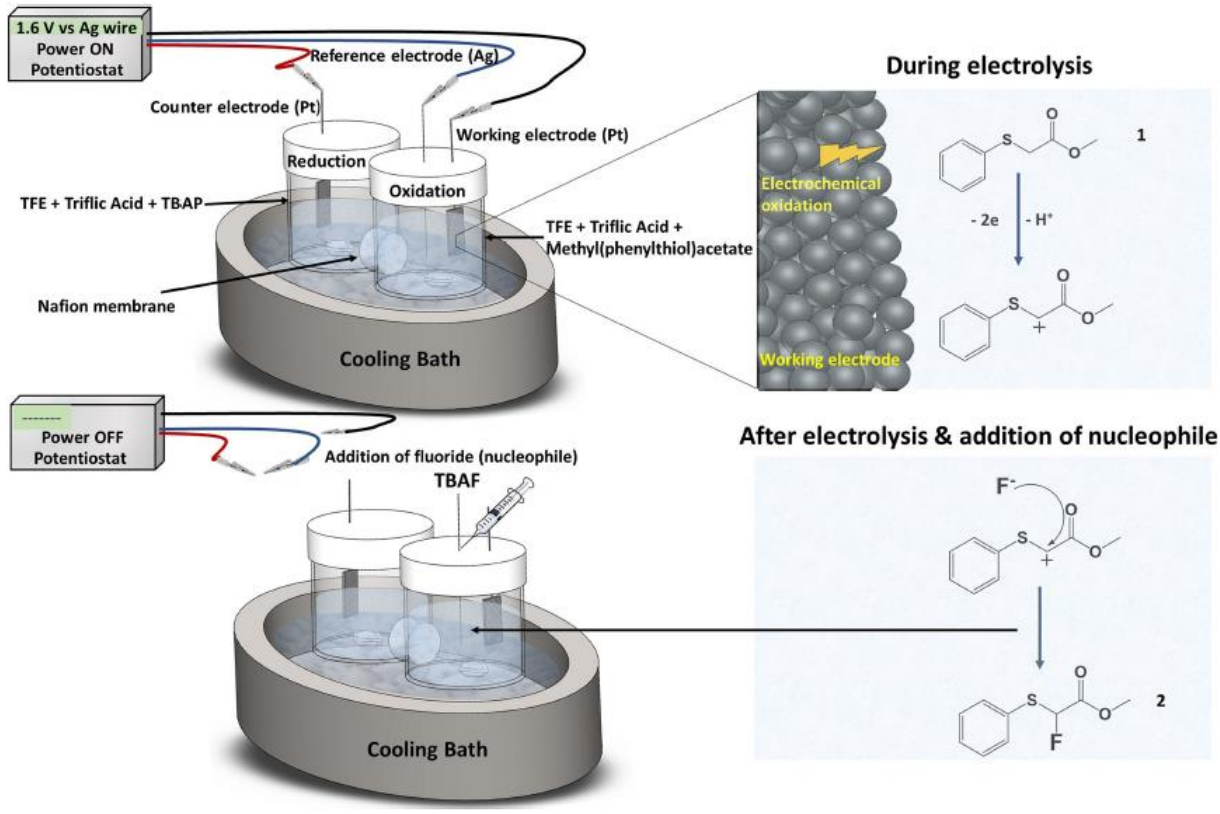

Figure 9. 1 Schematic of the cation pool method for fluorination of methyl-2-(phenylthiol) acetate

Electrolysis was repeated with TBAF at different temperatures of 21˚C, 0˚C, -20˚C and-40˚C and chemical yields of 2.2%, 4%, 6% and 3% were obtained respectively. The drop in the yield from -20˚C to -40˚C is due to the low oxidation current resulting in the slowing of precursor oxidation. 68% of the precursor was consumed when oxidation was performed at -20˚C, while only 12% of the precursor was consumed at -40˚C. -20˚C was chosen as the optimum temperature for further optimization. The effect of changes in supporting electrolyte on the chemical yield is shown in **Table 9.1.**

Table 9. 1 Effect of supporting electrolyte on the chemical yield of 2.

Electrolysis was carried out using 12 mM of **1** in TFE for 60 min at 1.6 V vs Ag wire at -20 °C followed by addition of 168 mM of TBAF post electrolysis.

Supporting electrolyte	Yield (%)
50 mM Tetrabutylammonium perchlorate (TBAP)	0
300 mM Tetrabutylammonium perchlorate (TBAP)	0
300 mM Tetrabutylammonium perchlorate + 14.2 mM triflic acid	6.0
300 mM Tetrabutylammonium tetrafluoroborate + 14.2 mM triflic acid	1.3
300 mM p-Toluenesulfonic acid + 14.2 mM triflic acid	2.0
142 mM triflic acid	12.5

It can be seen from Table 1 that TBAP alone results in negligible product formation, while addition of 14.2 mM of triflic acid increases the yield to 6%. The highest yield of 12.5% was obtained where only 142 mM of triflic acid was used without addition of salts as supporting electrolyte.

Further optimization was performed using only triflic acid as supporting electrolyte and the effect of triflic acid concentration on the yield was examined. Yields of 3.6%, 12.5% and 0% was obtained when 71 mM, 142 mM and 284 mM of triflic acid were used, respectively. The effect of precursor concentration on the product yield is presented in **Table 9.2**.

Table 9. 2 Effect of precursor 1 concentration on the chemical yield of product 2.

Electrolysis was carried out using precursor **1,** and 142 mM of triflic acid in TFE for 60 min at 1.6 V vs Ag wire at -20 °C. 168 mM TBAF was added at the of electrochemical oxidation.

Precursor concentration (mM)	Yield (%) (n=3)
0.5	8.5±0.9
1	9.6±1.0
2	11.5±1.2
4	10.6±1.1
6	12.7±1.4
12	11.2±1.3
24	9.2±1.0

Precursor concentration changes from 0.5 mM to 24 mM resulted in only a moderate change in the yield. Due to the diminishing [18F]TBAF concentration during no-carrier-added radiochemistry experiments, the effect of lowering of TBAF concentration and ratio of TBAF to triflic acid concentration were also investigated and the results are shown in **Table 9.3**.

Table 9.3. Effect of TBAF concentration and TBAF concentration/tiflic acid concentration ratio on the chemical yield of product *2*.

Electrolysis was carried out using 12 mM of **1** and triflic acid in TFE for 60 min at 1.6 V vs Ag wire at -20 °C. The values marked with an asterisk in the second column reflect experiments where triflic acid concentration was kept constant at 142 mM.

TBAF concentration [mM]	TBAF concentration/trific acid concentration	Yield [%]
21	1.18	1.6
	0.15*	0
42	1.18	3.8
	0.30*	0
84	1.18	4.0
	0.60*	0
168	1.18*	12.5
	0.60	0
	2.36	3.6

It was observed that by lowering the TBAF concentration the product yield decreased to 1.5% when 21 mM of TBAF was used. It was further observed that the ratio of TBAF to triflic acid concentration plays a crucial role with optimum product yield obtained when this ratio is maintained at 1.18. This may be due to the instability of product at low pH where TBAF addition can act as a base to increase the pH of the solution.

Using the optimized parameters, radiofluorination of 1 was performed with the cation pool method with 142 mM of triflic acid and 24 mM of 1in TFE in the anodic chamber. Radio-chemical fluorination efficiencies (RCFEs) were calculated based on conversion of [^{18}F]fluoride to product 2. Initially [^{18}F]fluoride in the form of [^{18}F]TBAF was added to the anodic chamber after60 min of

electrolysis, however no radio-fluorinated product was observed. Due to the diminishing TBAF concentrations in the radiochemistry experiment, addition of a non-nucleophilic base was necessary to increase the pH to 3, at which point the product was observed to be stable. To address this challenge,5 mCi of [^{18}F]fluoride was mixed with 300 mM of 2,6-di-tert-butyl-4-methylpyridine and the mixture was added to the anodic chamber after electrolysis resulting in RCFE of 5.7±1.0% (n=3) and molar activity of 1.13±0.2 Ci/mM (n=3).Similar to cold experiments with [^{19}F]-TBAF, samples for characterization were taken 30 min after [^{18}F]fluoride addition. Notably, RCFE of 4.8±0.6% (n=3) was obtained after just 5 min post [^{18}F]fluoride addition. Successful radiofluorination of methyl 2-(methylthio) acetate and methyl 2-(ethylthio) acetate were performed using cation pool technique with same condition as above, the RCFE of 20.6±2.0% and 18.2±1.5% were obtained, respectively **Figure 9.2**.

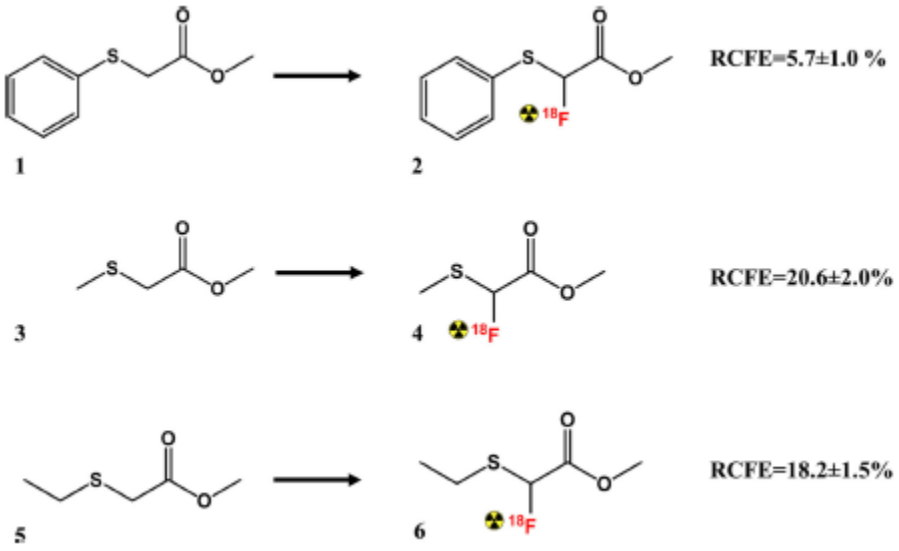

Figure 9. 2 Schematic of the radiofluorination reactions

9.3 Conclusion

In Summary, this report demonstrates a new tool for rapid late-stage fluorination and radiofluorination using the cation pool method. This is made possible through generation and pooling of stable cations under low temperature using TFE as solvent, and the subsequent

fluorination reaction of carbocations with fluoride under non-oxidative conditions. Cation pool fluorination prevents further oxidation of the fluorinated product during the electrolysis and rapid late-stage radio-fluorination can minimize the losses of [^{18}F]fluoride due to radioactive decay. More in-depth studies of scope and the use of microfluidic platforms are currently in progress to increase yields and introduce automation. Flash fluorination and radio-fluorination based on the cation pool method can be used to produce PET radiotracers and fluorinated pharmaceuticals, potentially expanding the library of fluorinated bioactive molecules available for medicinal chemistry and molecular imaging.

9.4 Appendix

9.4.1 Electrochemical synthesis

The electrochemical oxidation (the cation pool formation) and cyclic voltammetry (CV) were performed using an H shape divided 3-electrode cell with two platinum wires (length = 200 mm, diameter = 0.33 mm) as working and counter electrodes and Ag wire as quasi-reference electrode. The cathodic chamber and anodic chamber were separated by a nafion membrane. The anodic chamber contained 10 ml of TFE as solvent, methyl(phenylthio)acetate (precursor) and different supporting electrolytes such as triflic acid, tetrabutylammonium perchlorate, tetrabutylammonium tetrafluoroborate and p-toluenesulfonic acid. The cathodic chamber contained 10 ml of TFE as solvent, 300 mM tetrabutylammonium perchlorate and 757 mM of triflic acid. The reference electrode (Ag wire) was immersed in the anodic reaction mixture. The counter electrode and working electrode were cleaned before each experiment using potential cycling in 1 M sulfuric acid solution in water. The electrodes were cycled between −2 V and 2 V (2 electrode configuration) 10 times before each experiment. The electrochemical oxidation of methyl(phenylthio)acetate (carbocations formation) was performed at constant potential of 1.6 V vs Ag wire for 60 min. At the end of electrolysis, the nucleophile (TBAF) was added to the anodic chamber and allowed to react for 30 min while the reaction mixture was stirred using a magnetic stirring bar at 500 RPM and temperature was rising to the room temperature. The CVs and

electrochemical oxidation experiments were performed using the Metrohm PGSTAT128N electrochemical workstation. The CVs were performed using a 200 mV/s scan rate and no stirring. **Figure 9.3** shows the CV of background (TFE + supporting electrolyte in the anodic chamber) and CV of the cation pool reaction mixture (methyl(phenylthio)acetate + TFE + supporting electrolyte in the anodic chamber).

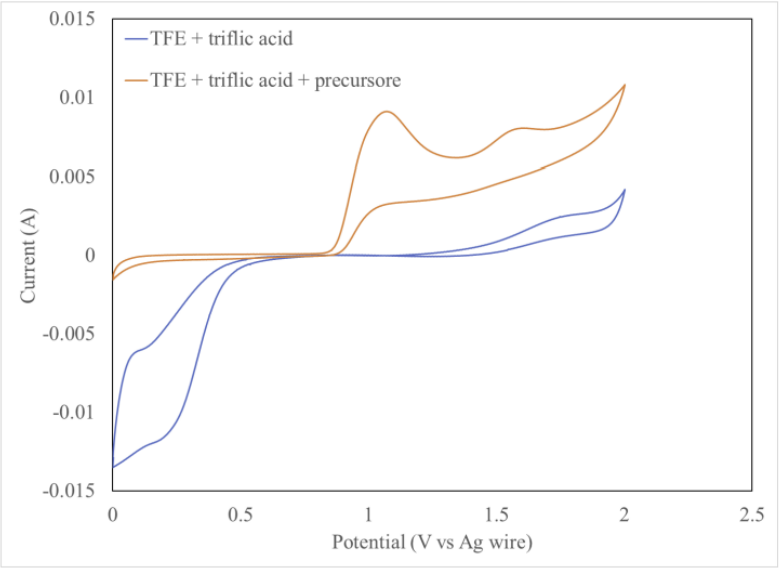

Figure 9. 3 CVs of TFE and triflic acid with and without precursor (background).

The CVs were run with 200 mv.s−1 scan rate at room temperature (21 °C) using a divided cell and no stirring.

It can be seen from figure A3.5.1 that the oxidation of precursor starts at 0.9 V vs Ag wire and reaches a peak at 1.08 V vs Ag wire due to the diffusion limit. The CV of the background shows very small anodic currents up to 1.5 V vs Ag wire; by increasing the potential further the background anodic current starts to increase to higher values. It also can be seen that adding the precursor to the solution can suppress the cathodic currents at potentials lower than 0.5 V vs Ag wire.

9.4.2 Gas chromatography-mass spectrometry (GC-MS) spectra

The product identification and quantification was performed using GC-MS. Mass spectra and chromatograms were carried out using an Agilent 5975C Triple-Axis Detector (TAD) inert MSD

mass spectrometer coupled with an Agilent 7890A gas chromatograph. The mass spectrum was set to electron ionization mode with a voltage of 1.9 kV. The mass range was 50-250 (amu). The details of gas chromatograph's column and the method are outlined below: Inlet was set at 120 °C and had 1:10 split ratio. Oven was set to 120 °C and held for 1 min, then increased to 138 °C at a rate of 1 °C/min and held for 15 mins. Column was Agilent 122-5532, maximum operating temperature 325 °C; 30 m length, 250 µm internal diameter and 0.25 µm film thickness. A constant flow of 1 mL/min was delivered to the transfer column. The transfer column Agilent G3185-60062, 450 °C; 0.17 m length, 100 µm internal diameter and 0 µm film thickness delivered a constant flow of 1.5 mL/min to the source. The GC-MS method had a 10 min solvent delay in order to enhance the MS filament lifetime. **Figure 9.4** is the GC-MS calibration plot used in the quantification of product 2 yield.

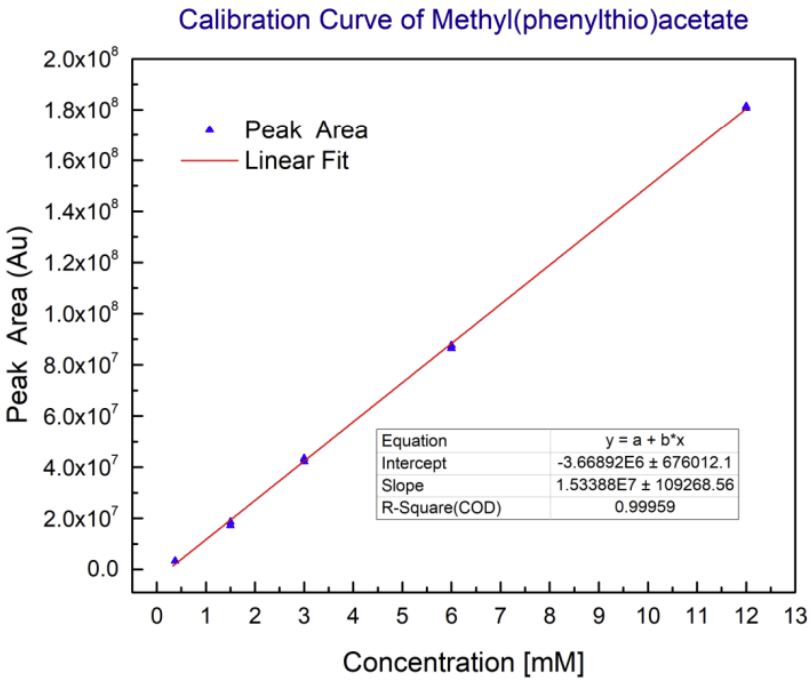

Figure 9. 4 The GC calibration plot used in the quantification of formation of product 2.

Figures 9.5, 9.6 and **9.7** show the GC-MS mass spectra of the products 2, 4 and 6, respectively. **Figure 9.8** shows a representative GC-MS chromatogram of the crude product.

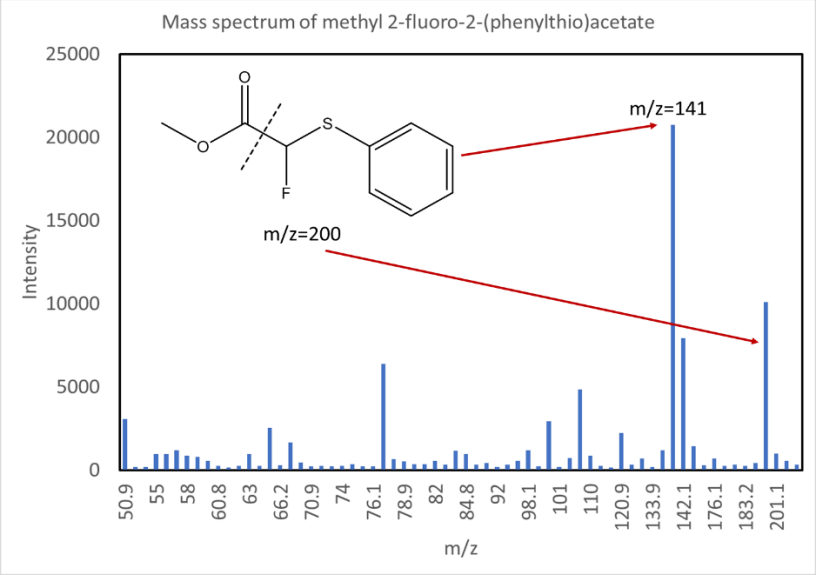

Figure 9. 5 Mass spectrum of the product 2.

It can be seen from **Figure 9.8** that after electrolysis, 70% of the precursor has been consumed and no product peak can be observed at 21.7 min. The product is only observed after the injection of TBAF post electrolysis, pointing to the reaction of fluoride anions with stabilized carbocations formed during electrolysis.

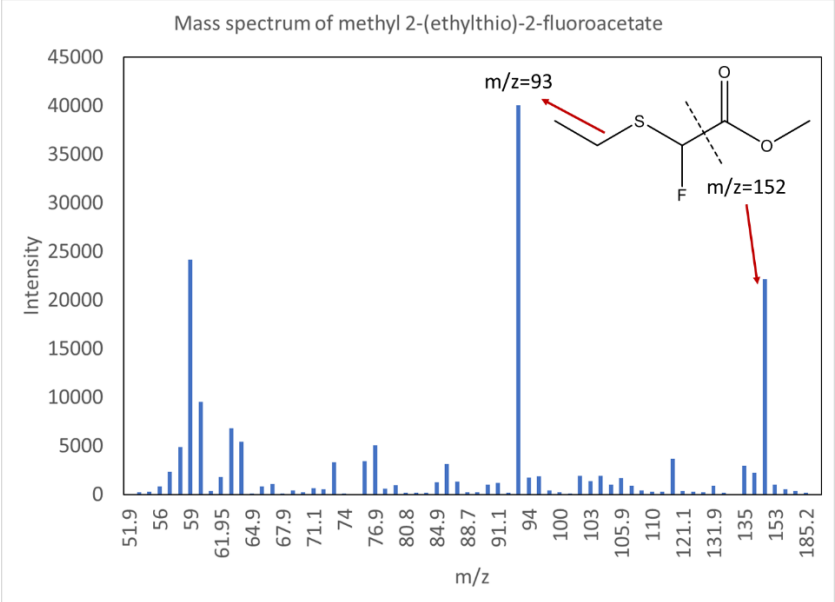

Figure 9. 6 The mass spectrum of the product 4.

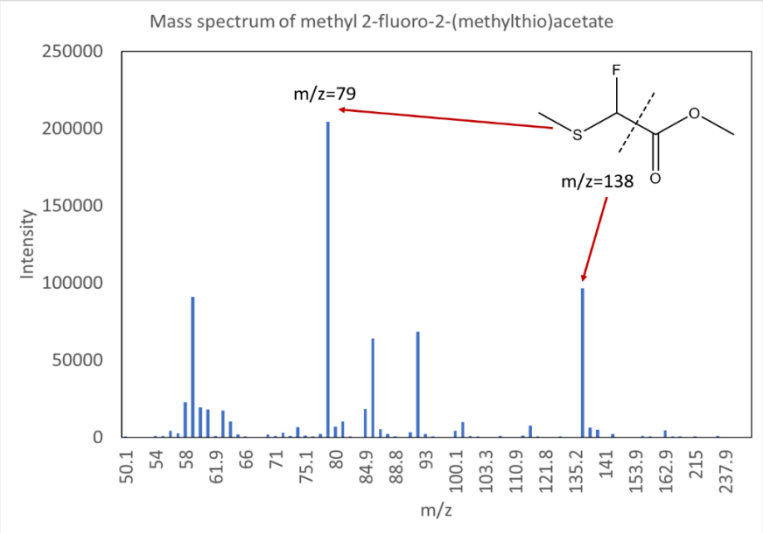

Figure 9. 8 The mass spectrum of the product 6.

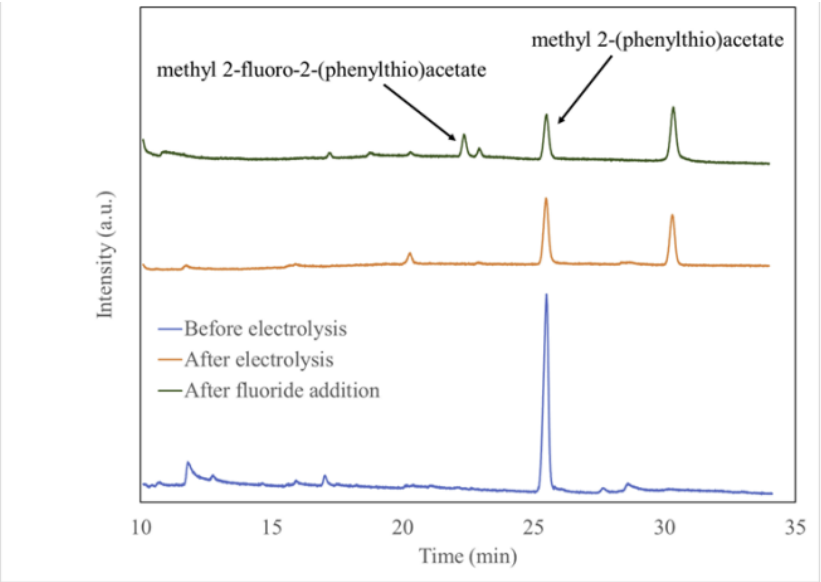

Figure 9. 7 GC-MS chromatograms of the crude reaction mixture before and after electrochemical oxidation and after fluoride addition.

Electrolysis was carried out using 12 mM of 1 and 142 mM of triflic acid in TFE for 60 min at 1.6 V vs Ag wire at -20 °C. 168 mM TBAF was added at the end of electrochemical oxidation and allowed to react for 30 min while the reaction mixture was stirring and temperature was rising to the room temperature.

9.4.3 Nuclear magnetic resonance (NMR) spectra

^{19}F-Nuclear-Magnetic-Resonance (^{19}F-NMR) was performed on the ^{19}F-fluorinated thioether reference standards. ^{19}F-NMR spectroscopic data were in agreement with previous reports [1-8]. Nuclear magnetic resonance spectroscopy (NMR) The identity of the product 2 was also further

characterized by ^{19}F-NMR. The 19F-NMR spectrum was obtained on a Bruker AV400 (400 MHz). 19F chemical shift is reported in parts per million (ppm) using the trifluoro acetic acid (CF3COOH) as a reference. **Figures 9.9, 9.10** and **9.11** show the 19FNMR spectra of the products 2, 4 and 6, respectively. 19F-NMR spectroscopic data for products 2 and 6 were in agreement with previous reports.

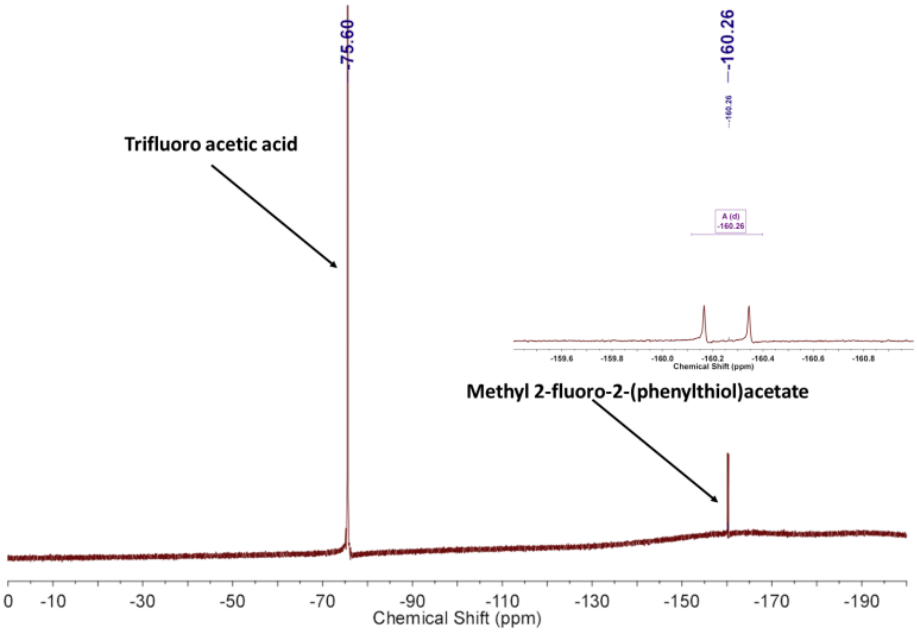

Figure 9. 9 The 19F NMR of the HPLC purified product 2 plus trifluoro acetic acid as standard for further identification of the fluorinated product obtained by cation pool method.

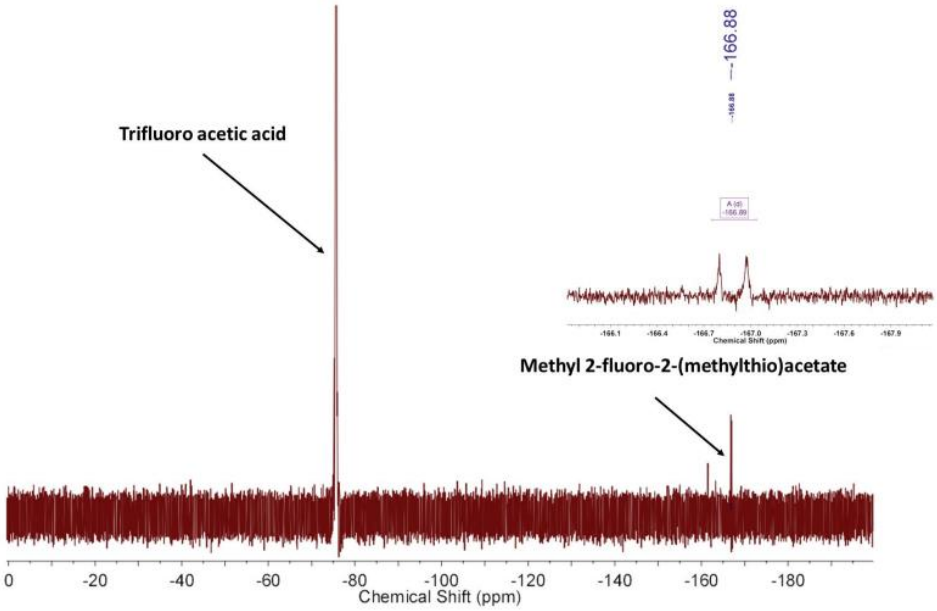

Figure 9. 10 The 19F NMR of the HPLC purified product 4 plus trifluoro acetic acid as standard for further identification of the fluorinated product obtained by cation pool method.

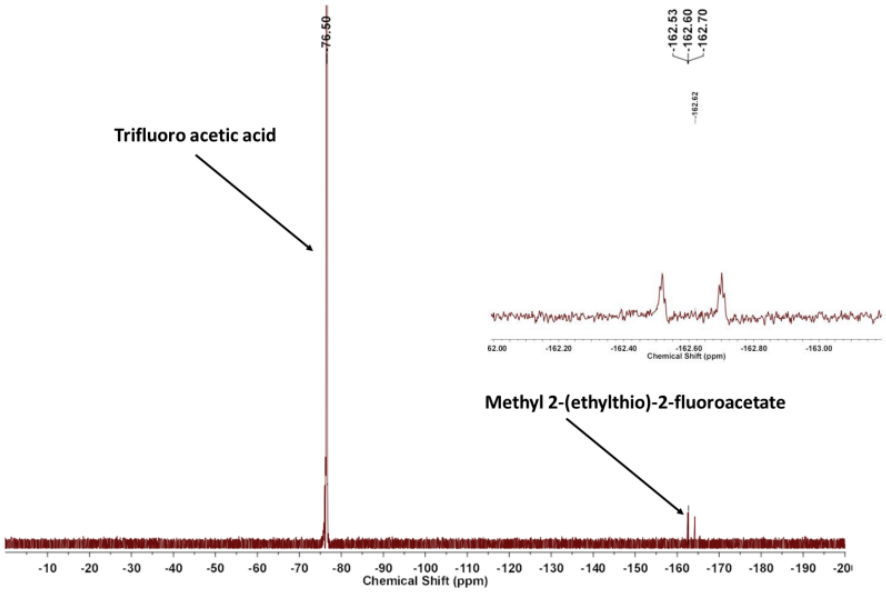

Figure 9. 11 Figure 9.11. The 19F NMR of the HPLC purified product 6 plus trifluoro acetic acid as standard for further identification of the fluorinated product obtained by cation pool method.

9.4.4 Radiochemical characterization

No-carrier-added [^{18}F]-fluoride was produced by the (p,n) reaction of $^{18}O–H_2O$ (84% isotopic purity, Medical Isotopes) in a RDS-112 cyclotron (Siemens) at 11 MeV using a 1 mL tantalum target with havar foil. The radioactive isotope was trapped on analytical grade (AG) MP-1M anion exchange resin by passing through the 1 ml of bombarded $^{18}O–H_2O$. Most of the water on the resin was removed by washing with 10 mL of anhydrous ACN and drying with ultra-pure N2 for 10 min. [^{18}F]fluoride was subsequently eluted out from the cartridge with a 2 ml TFE containing 25 mM TBAP salt. In a typical experiment, approximately 5 mCi was eluted from the anion exchange cartridge in [^{18}F]-TBAF form in TFE. Radiofluorination conversion was measured using Radio-thinlayer-chromatography (radio-TLC). Radio-TLC was performed on silica plates (TLC Silica gel 60 W F254s, Merck). After dropping a sample volume (~1–5 µL) using a glass capillary, the plate was developed in the mobile phase (ACN). Chromatograms were obtained using a radio-TLC scanner (miniGita Star, Raytest). Analytical High Performance Liquid Chromatography (HPLC), equipped with a UV and gamma detector was used to determine radiochemical purity (RCP) of the radio-fluorinated product. HPLC was performed using a 1200 Series HPLC system (Agilent Technologies) equipped with a GabiStar flow-through gamma detector (Raytest). Data acquisition and processing was performed using GINA Star Software version 5.9 Service Pack 17 (Raytest). Typically, 20 µL of radioactive sample was diluted with 180 µL of ACN and 5–20 µL of this solution was injected for HPLC analysis. Column: Synergy 4u Polar RP 80 A, 250 × 4.6 mm, 4 micron. Gradient: A = ACN; B = water; flow rate = 1.8 mL/min; 0–28 min 95% B to 45% B, 28–29 min 45% B to 5% B, 29–32 min 5% B, 32–34 min 5% B to 95% B. Radio-TLC chromatograms were used to measure radiochemical conversions (RCC). RCP and RCC were measured by dividing the area under the curve (AUC) for the desired product by the sum of AUC for all peaks. The TLC purity accounts for unreacted [^{18}F]-fluoride while the HPLC purity corrects

for radiochemical side-products. The radiochemical fluorination efficiency (RCFE) was determined by the equation: RCFE = TLC RCC × HPLC RCP.

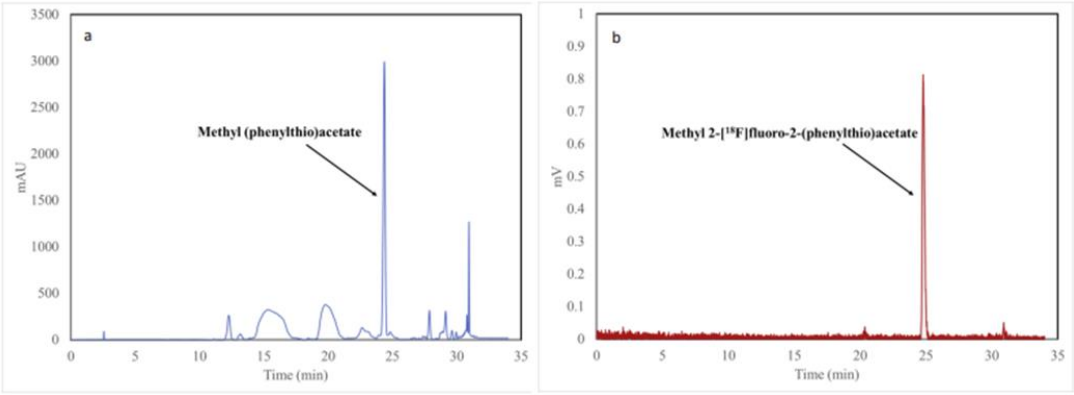

Figure 9. 12 Analytical (A) UV HPLC and (B) gamma HPLC profiles of the crude sample after electrolysis.

Electrolysis was performed for 60 min at 1.6 V vs Ag wire at -20 ºC using TFE solution containing 24 mM of product 1, 142 mM of triflic acid. 2 ml of TFE solution containing 25 mM TBAP and 5 mCi [^{18}F]-fluoride was added after electrolysis was finished and the sample was taken for analysis 30 min after [^{18}F]-fluoride addition.

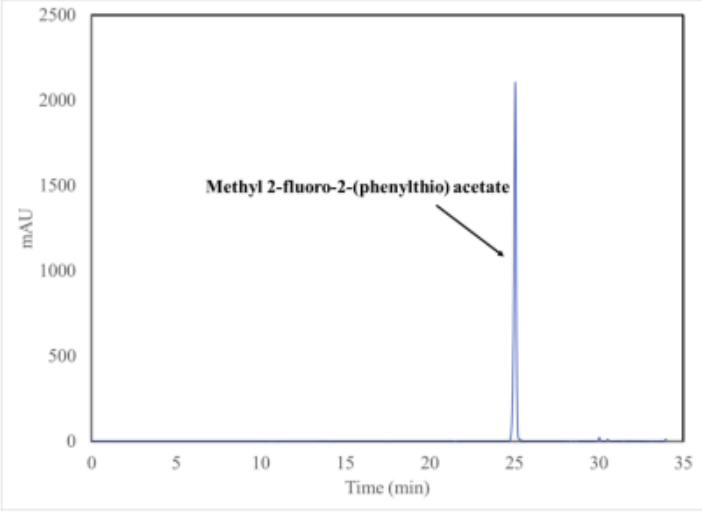

Figure 9. 13 UV HPLC profile of purified product.

Electrolysis was performed for 60 min at 1.6 V vs Ag wire at -20 ºC using TFE solution containing 24 mM of product 1, 142 mM of triflic acid. 2 ml of TBAF solution was added after electrolysis was finished and the sample was HPLC purified 30 min after TBAF addition.

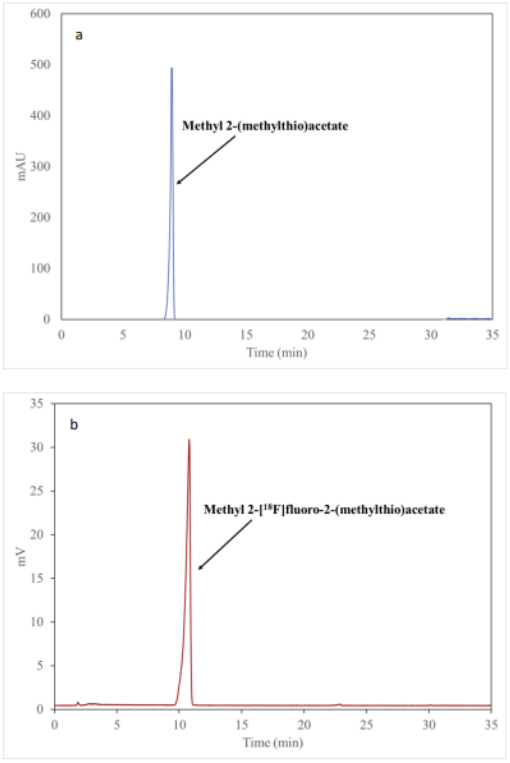

Figure 9. 14 Analytical (A) UV HPLC and (B) gamma HPLC profiles of the crude sample after electrolysis.

Electrolysis was performed for 60 min at 1.6 V vs Ag wire at -20 ºC using TFE solution containing 24 mM of product 3, 142 mM of triflic acid. 2 ml of TFE solution containing 25 mM TBAP and 5 mCi 18F-fluoride was added after electrolysis was finished and the sample was taken for analysis 30 min after 18F-fluoride addition.

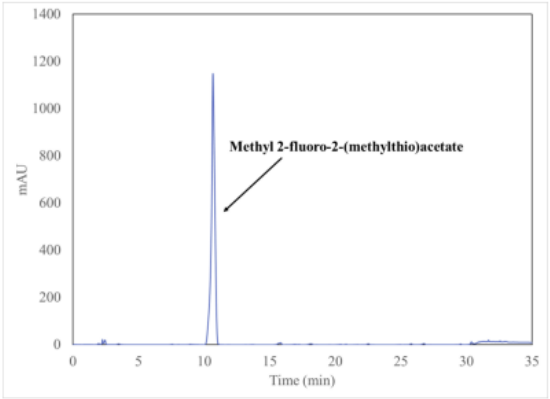

Figure 9. 15 UV HPLC profile of purified product.

Electrolysis was performed for 60 min at 1.6 V vs Ag wire at -20 ºC using TFE solution containing 24 mM of product 3, 142 mM of triflic acid. 2 ml of TBAF solution was added after electrolysis was finished and the sample was HPLC purified 30 min after TBAF addition.

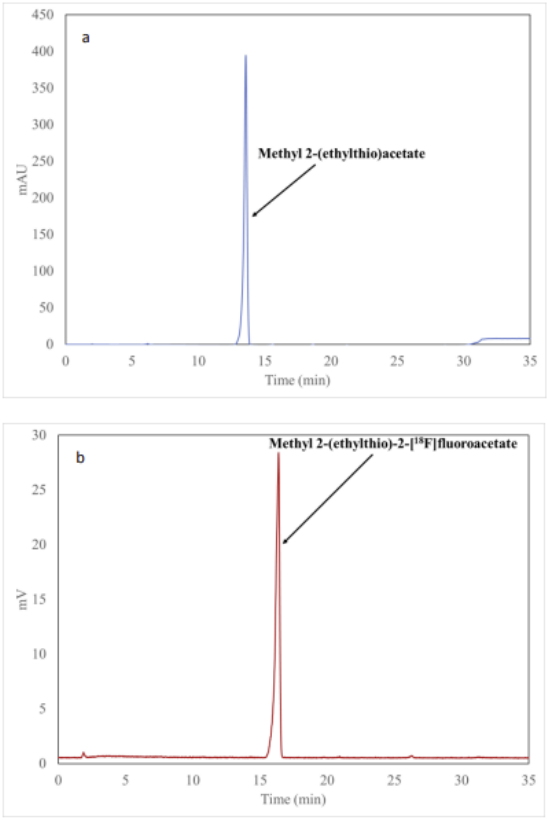

Figure 9. 16 Analytical (A) UV HPLC and (B) gamma HPLC profiles of the crude sample after electrolysis.

Electrolysis was performed for 60 min at 1.6 V vs Ag wire at -20 ºC using TFE solution containing 24 mM of product 5, 142 mM of triflic acid. 2 ml of TFE solution containing 25 mM TBAP and 5 mCi [^{18}F]-fluoride was added after electrolysis was finished and the sample was taken for analysis 30 min after [^{18}F]-fluoride addition.

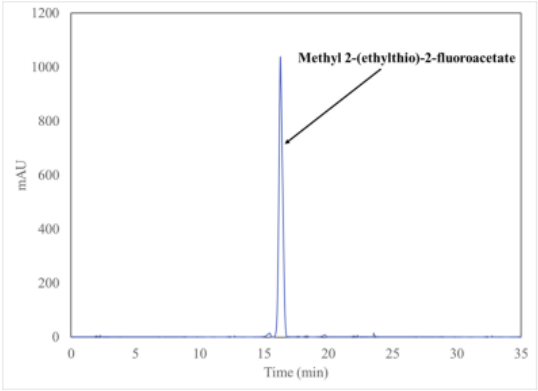

Figure 9. 17 UV HPLC profile of purified product.

Electrolysis was performed for 60 min at 1.6 V vs Ag wire at -20 ºC using TFE solution containing 24 mM of product 5, 142 mM of triflic acid. 2 ml of TBAF solution was added after electrolysis was finished and the sample was HPLC purified 30 min after TBAF addition.

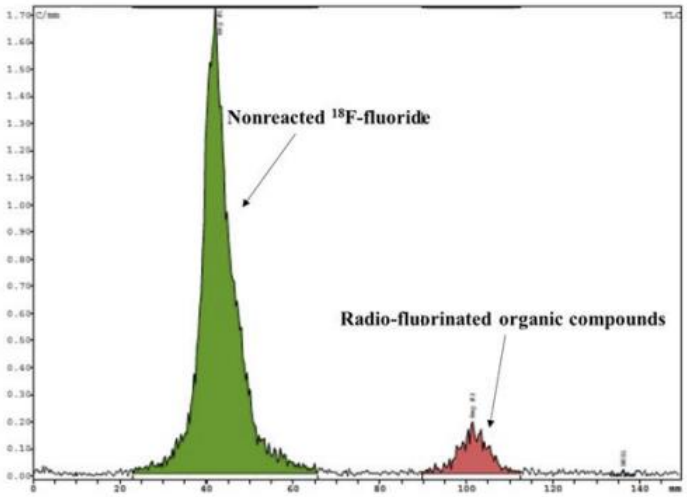

Figure 9. 18 Gamma TLC of the crude sample post radio-electrochemical synthesis.

Electrolysis was performed for 60 min at 1.6 V vs Ag wire at -20 ºC using TFE solution containing 24 mM of product 1, 142 mM of triflic acid. 2 ml of TFE solution containing 25 mM TBAP and 5 mCi [^{18}F]-fluoride was added after electrolysis was finished and the sample was taken for analysis 30 min after [^{18}F]fluoride addition.

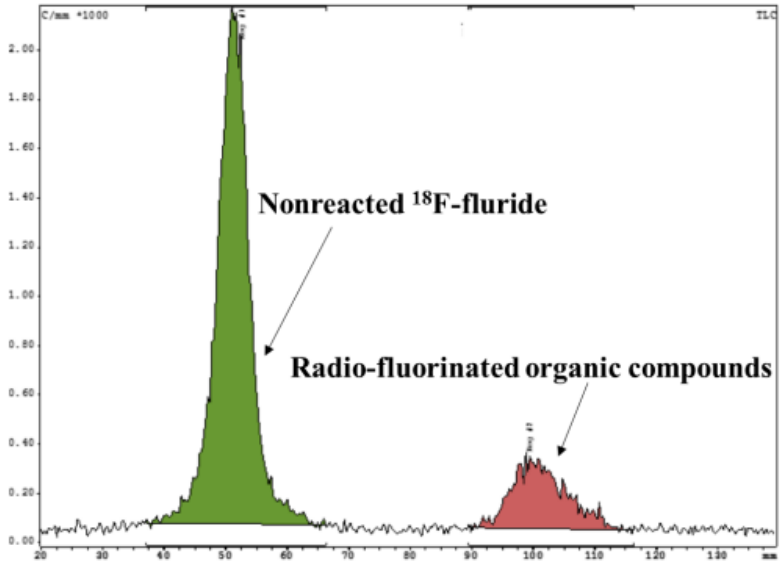

Figure 9. 19 Gamma TLC of the crude sample post radio-electrochemical synthesis.

Electrolysis was performed for 60 min at 1.6 V vs Ag wire at -20 ºC using TFE solution containing 24 mM of product 3, 142 mM of triflic acid. 2 mL of TFE solution containing 25 mM TBAP and 5 mCi [^{18}F]-fluoride was added after electrolysis was finished and the sample was taken for analysis 30 min after [^{18}F]-fluoride addition.

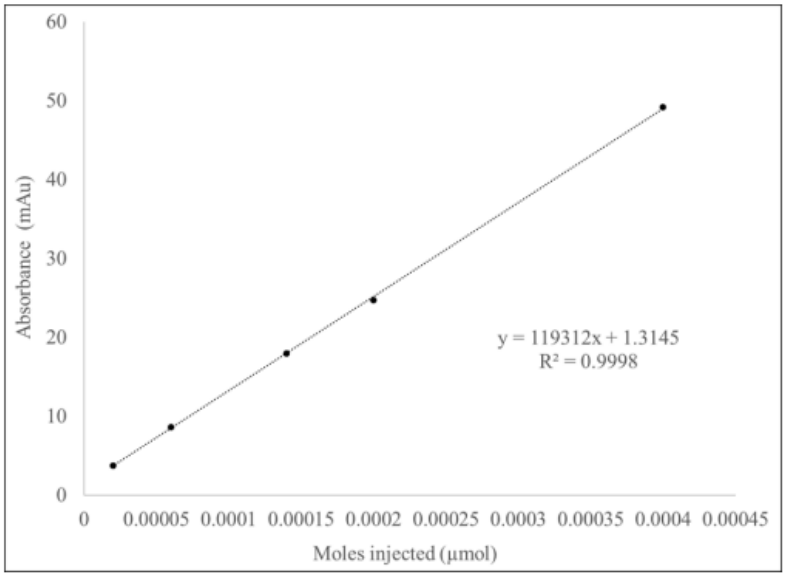

Figure 9. 20 Calibration curve of UV absorbance vs. molar mass.

Chapter 10: Electrochemical radiofluorination of thioethers

10.1 Introduction

Positron Emission Tomography (PET) is an established molecular imaging technology widely used for the visualization of biological processes in clinical and research settings(*237*). This technology relies on radioactively labeled molecules, called tracers. Fluorine-18 is the most frequently used radionuclide in PET due to its wide availability, physical half-life (t1/2 = 109.8 min), which closely matches biological half-life of many small molecules, and its favorable decay characteristics for imaging. Importantly, [^{18}F]fluoride is routinely produced in a no-carrier-added (NCA) form, that is, without added stable ^{19}F-species. Tracer formulations prepared from NCA [^{18}F]fluoride(*279*) contain only nanomolar quantities of the physiologically active molecule. This low amount allows for imaging without perturbing the biochemical process under investigation. If ^{19}F-carrier is added for production purposes, product molar activity (Am – amount of radioactivity per mole of product) is decreased and total amount of physiologically active tracer in the final formulation is increased. Low Am formulations can lead to saturation of the biological target under investigation and is suitable for only a handful of applications. Thioethers are attractive scaffolds for PET tracer development, yet approaches for their radiolabeling are limited. Examples of biologically relevant thioethers include radiolabeled methionine and cysteine, which are important in elucidating amino acid metabolism in multiple diseases(*280–282*). The strongly nucleophilic sulfur atom hinders the use of weakly nucleophilic [^{18}F]fluoride in labeling reactions. Due to this interference, methionine radiolabeling mostly relies on electrophilic agents based on [^{11}C]carbon, a suboptimal choice due to 20 min half-life of this isotope. Despite these limitations, [^{11}C]-methionine has demonstrated significant clinical utility(*283*), urging further development in this area(*284*). Several pharmaceuticals in clinical use contain thioether scaffolds and can be potentially radiolabeled by electrochemical radiofluorination if appropriately protected precursors are synthesized(*283*,*285*). Among them are nucleotide receptor antagonist Ticagrelor(*286*),

antiretroviral Nelfinavir(*287*), and a urate transporter inhibitor Lesinurad(*288*). Using [^{18}F] fluoride for radiolabeling of thioethers remains an important but elusive target.

10.2 Materials and methods

10.2.1 Materials

Chemicals were purchase from commercial sources and used without further purification. Tetrabutylammonium perchlorate (TBAP, >99%, for electrochemical analysis) was purchased from Fluka. Tetraethylammonium fluoride tetrahydrofluoride (>97%) and Pyridinium pToluenesulphonate (>98%) were purchased from TCI. Methyl 2-(phenylthio)acetate (99%) was purchased from Alfa Aesar. Acetonitrile (ACN, anhydrous, >99.8%) and pToluenesulphonic Acid (99%) were purchased from Agros Organics. Methyl 2-(methylthio)acetate (>98%), 2-(Phenylthiol)acetonitrile (98%), diethyl ((phenylthio)methyl)phosphonate (96%), Dimethoxyethane (DME) (>99%) and Trifluoroethanol (TFE) (>99%) were purchased from Fisher. Trifluoromethanesulfonic acid (Triflic Acid) (99.5%) and Methyl 2-(ethylsulfanyl)acetate (99%) were purchased from Oakwood Chemical. Ethanol (200 proof, anhydrous) was purchased from Decon. 2-(Phenylthiol)acetamide (97%) was purchased from Synthonix. Hexafluoroisopropanol (HFIP) (99%) was purchased from VWR International. All water used was purified to 18MΩ and passed through a 0.1 mm filter. No-carrier-added [18F]fluoride was produced using [18O]H2O (84% isotopic purity, Medical Isotopes) in a RDS-112 cyclotron (Siemens) from a 11 MeV bombardment with a 1 mL tantalum target with havar foil.

10.2.2 Experimental methods

10.2.2.1 Carrier added electrochemical fluorination procedure

The carrier added experiments were performed to produce the ^{19}F-labelled thioether reference standards. Electrolysis was performed at an oxidation potential of 1.9V. The electrochemical solution contained 50 mM thioether precursor, 50 mM TBAP and 100 mM tetraethylammonium fluoride tetrahydrofluoride. A 30 mL single chamber electrochemical cell was used with 20 mL of solution using ACN as the solvent. An oil bath was used to set the temperature to 70°C.

Electrolysis was performed for 60 mins with stirring at 600 rpm using a three-electrode system under a constant potential mode controlled by an Autolab128 potentiostat-galvanostat (Metrohm USA). Alternating pulses were applied to reduce passivation of the electrodes. The oxidation pulse was held for 60 seconds and a reduction pulse of -0.6V for 6 seconds. Platinum wire was used for the working and counter electrodes. Silver wire was used as a pseudo reference electrode.

The crude electrochemical solution after electrolysis was concentrated using a C18 SPE cartridge (Waters). The crude was added to 500 mL of water, stirred and then trapped on the C18 cartridge. 100 mL of water was then passed through the cartridge and dried with N_2 for 10 mins. The organics with the ^{19}F-labelled product were then eluted with 1 mL of ethanol, which was mixed with 1 mL of water. The resulting mixture was transferred into the loading loop of the HPLC followed by water (0.5 mL) and injected onto the HPLC column for purification. This was performed with our previously reported radio-electrochemical fluorination platform HPLC separation subunit. Column: (Phenomenex, Gemini 5u C18 110A, 250 × 10 mm); gradient A = ACN (0.1% TFA); B = water (0.1% TFA); flow rate = 5 mL/min; 0 min 95% B, 0–30 min 95%-40% B. The product containing fraction was collected in ~4–5 mL. The collected fraction was then concentrated using a C18 CPE cartridge by adding 20x volume of water, mixing and then trapping the product on the cartridge. 100 mL of water was then passed through the cartridge and it was dried for 10 mins with N_2. The product standards were then eluted with 1 mL of ethanol. The thioether product standards were identified using GC-MS and NMR as described below. The HPLC retention times of the ^{19}F labelled thioether product standards was used to verify the NCA-ECF ^{18}F labelled products.

10.2.2.2 No-carrier added electrochemical [^{18}F]fluorination procedure

No-carrier-added ^{18}F-fluoride was produced by the (p,n) reaction of ^{18}O–H_2O (84% isotopic purity, Medical Isotopes) in a RDS-112 cyclotron (Siemens) at 11 MeV using a 1 mL tantalum target with havar foil. The radioactive isotope was trapped on analytical grade (AG) MP-1M anion

exchange resin by passing through the 1 ml of bombarded $^{18}O–H_2O$. The cartridge was built using PEEK tubing with SPE frits (Agilent) on both ends containing 5 mg of the anion exchange resin. The cartridge was dried with a stream of ultra-pure N_2 for 5 mins followed by 3 mL of anhydrous ACN. The cartridge was further dried with a stream of N_2 for 5 mins. ^{18}F-fluoride was subsequently eluted off the cartridge with 1 mL of TFE containing 50 mM Bu_4NClO_4 and used in the electrochemical fluorinations. In a typical experiment, approximately 5 mCi of no-carrier-added ^{18}F-fluoride was eluted from the anion exchange cartridge in ^{18}F-TBAF form in TFE.

The electrochemical reaction cell volume was 1.5 mL. Electrolysis was performed for 30 mins. The solvent used was trifluoroethanol (TFE). No $Et_4NF{\cdot}4HF$ was added. Electrolysis was performed at an oxidation potential of 1.9V with 1.5 mL 50 mM thioether precursor, 50 mM TBAP and in TFE at 70°C for 30 mins and stirring at 600 rpm under a constant – potential mode controlled by an Autolab128 potentiostat-galvanostat (Metrohm USA). The cell used alternating pulses to reduce passivation of the electrodes. The oxidation pulse was held for 60 seconds and cleaning pulse of -0.6V for 6 seconds. Pt was used for the working and counter electrodes. Ag wire was used as a pseudo reference electrode.

10.3 Results and discussion

In this paper we report no-carrier-added electrochemical fluorination (NCA-ECF) of a range of thioethers (**Figure 10.1)**

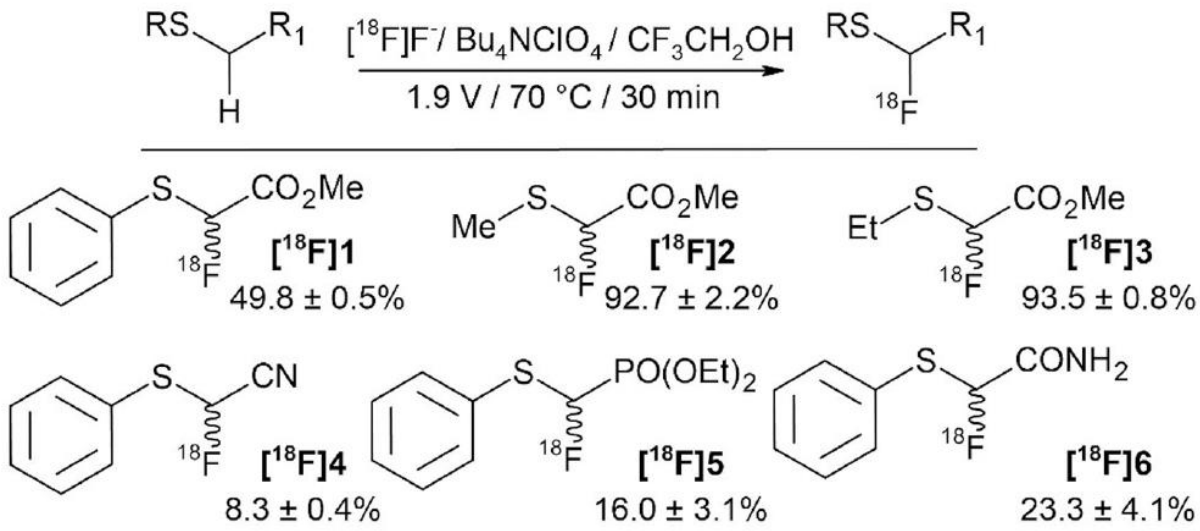

Figure 10. 1 Scope of the NCA-ECF. Radiofluorination was performed on platinum electrodes under potentiostatic conditions.

Radiochemical yield is reported as an average of three experiments.

This success is enabled by electrochemical methodology, which to the best of our knowledge, is the first report of electrochemical production of NCA radiotracers in quantities typically used in clinical settings. Outside of radiochemistry, electrochemical methods offer a unique approach to the fluorination of thioethers(*243*,*289–292*). Unfortunately, it relies on excess of (HF)n salts and thus cannot yield NCA products. Fuchigami et al. first proposed a mechanism for the electrochemical fluorination (ECF) of thioethers(*247*,*293*) (**Figure 10.2**).

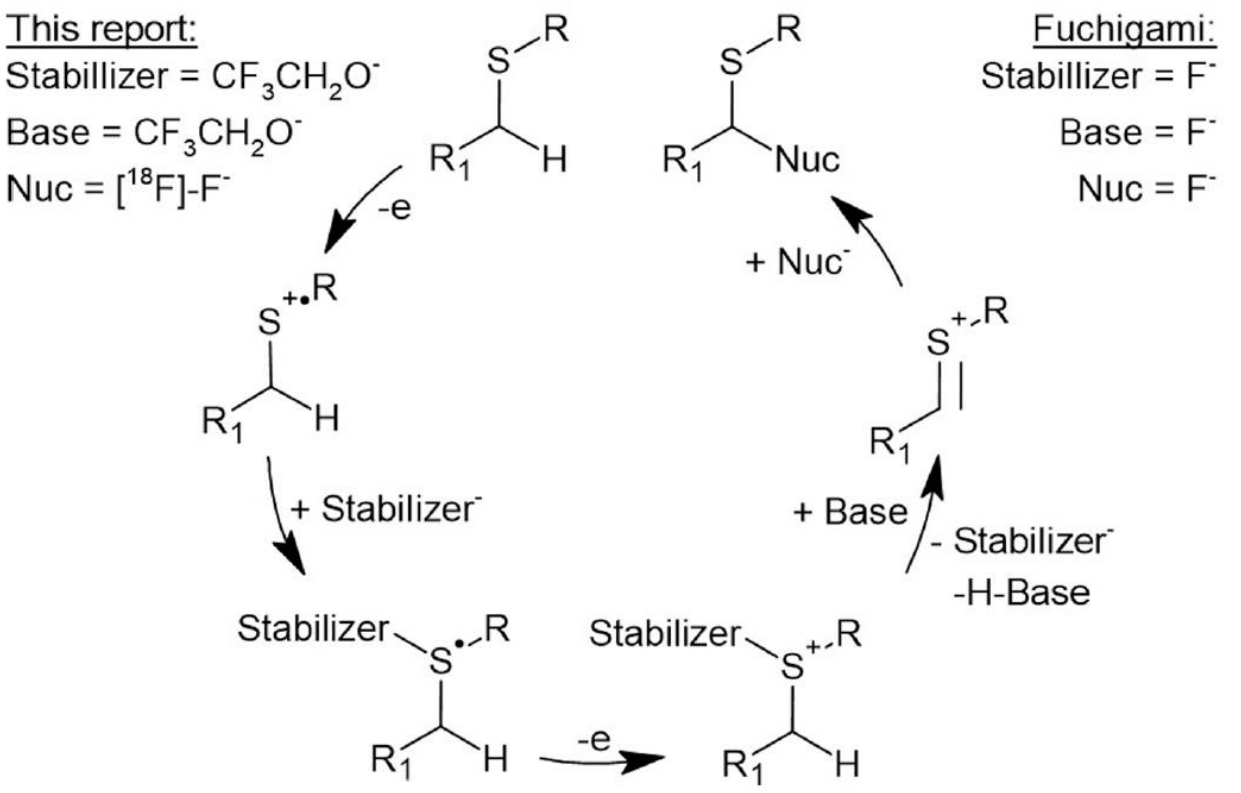

Figure 10. 2 Proposed mechanism for the NCA-ECF compared to Fuchigami mechanism.

In this mechanism, fluoride plays a 3-fold role: it stabilizes the radical cation intermediate after first oxidative step, acts as a base in the elimination step and as a nucleophile to produce the α-fluorinated sulfide(*294*). There is a clear need for an excess of fluoride for this reaction to proceed in good yields(*295*). The use of fluorinating agents that are not HF-based is still very rare(*296*). In previous reports, we applied the Fuchigami methodology for the electrochemical 18F-fluorination of a model compound, methyl-2-(phenylthio)acetate(*272*,*274*). Predictably, only low Am product was produced and lowering HF concentration reduced Radiochemical Yield (RCY) without significant gain in Am. We hypothesized that an auxiliary reagent could be used to replace fluoride in two roles that it plays in the Fuchigami mechanism: to stabilize the radical intermediate and to act as Lewis base. This study reports the successful search for a Brønsted acid that plays a role of this auxiliary reagent and facilitates no-carrier-added electrochemical radiofluorination (NCA-ECF). **Table 10.1**. summarizes RCY, [^{18}F]fluoride conversion (Radiochemical Conversion, RCC;

assessed with radio-TLC) and radiochemical purity (RCP; assessed with radio-HPLC) in a series of experiments exploring radiolabelling conditions of methyl(phenylthiol) acetate.

Table 10. 1 NCA-ECF of Precursor 1 Using Potential Auxillary Groups (average of 3 experiments).

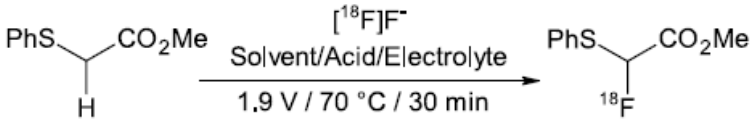

#	Solvent	Acid (mM)	Electrolyte (50 mM)	RCC,%	RCP, %	RCY, %
1	MeCN	–	TBAP	18.9 ± 0.8	2.2 ± 0.1	0.5 ± 0.1
2	DME	–	TBAP	0	0	0
3	TFE	–	TBAP	59.3 ± 1.0	84.1 ± 2.1	49.8 ± 0.5
4	HFIP	–	TBAP	58.1 ± 4.4	27.2 ± 0.4	15.8 ± 1.4
5	TFE	–	PPTS	70.5 ± 1.9	21.9 ± 0.6	15.4 ± 1.8
6	MeCN	–	PPTS	62.6 ± 7.7	6.1 ± 1.2	3.9 ± 1.2
7	TFE	–	TBA-OTf	30.9 ± 1.8	79.9 ± 1.3	24.7 ± 1.8
8	MeCN	–	TBA-OTf	0	0	0
9	TFE	2 mM TfOH	TBAP	27.5 ± 1.5	84.2 ± 4.1	23.2 ± 2.1
10	TFE	10 mM TfOH	TBAP	2.4 ± 0.1	13.5 ± 0.8	0.3 ± 0.1
11	MeCN	2 mM TfOH	TBAP	0	0	0
12	MeCN	10 mM TfOH	TBAP	0	0	0
13	TFE	2 mM TsOH	TBAP	35.8 ± 0.4	71.1 ± 1.7	25.5 ± 0.3
14	TFE	10 mM TsOH	TBAP	15.9 ± 0.5	85.8 ± 2.6	13.7 ± 0.8
15	MeCN	2 mM TsOH	TBAP	0	0	0
16	MeCN	10 mM TsOH	TBAP	0	0	0

PPTS= Pyridinium p-Toluenesulfonate; TBA-OTf= Bu_4N^+ $CF_3SO_3^-$; TfOH= CF_3SO_3H; TBAP= Bu_4NClO_4.

To establish a baseline yield, NCA-ECF of [^{18}F]**1** in acetonitrile (MeCN) with tetrabutylammonium perchlorate (TBAP) as the electrolyte was investigated. The non-isolated, decay-corrected RCY of the reaction was 0.5 ± 0.2% (*n* = 3; **Table 10.1**, entry 1). Using

dimethoxyethane (DME) as a solvent failed to produce any radioactive products (Table A4.1, entry 2) despite its reported ability to solvate quaternary ammonium cations, thereby increasing the availability of fluoride for ECF(*297*,*298*). We explored the use of relatively weak nucleophilic triflate (OTf) and tosylate (OTs) additives in an attempt to provide stability for the cation-radical without competing with [^{18}F]fluoride nucleophile(*299*). TBAP was replaced with either pyridinium tosylate or Bu4N-OTf in the NCA synthesis of [^{18}F]**1**. While the use of OTf yielded no product (**Table 10.1** entry 8), a more nucleophilic(*300*) OTs additive led to an observed RCY of 3.9 ± 1.2% (*n* = 3): an order of magnitude increase from that observed with TBAP. This led us to hypothesize that using triflic or toluenesulfonic acids instead of their salts might have a beneficial effect. In this way, respective conjugate bases would form after cathodic reduction of acidic protons in situ. However, low pH was previously reported to diminish product yields in ECF(*272*), leading us to examine two concentrations of TfOH and pTSA (2 mM, 10 mM). Unfortunately, these studies did not lead to product formation. In search of additives that would be more nucleophilic than OTs, yet only modestly competitive with [^{18}F]fluoride species, we discovered that Eberson suggested use of trifluoroethanol (TFE) and hexafluoroisopropanol (HFIP) for stabilization of radical cations(*301*). These solvents are known to have high dielectric constants, low polarizabilities and propensities to solvate competing anions thereby increasing the cationic intermediate lifetime(*276*,*277*,*301–303*). Recently, fluorination of thioethers has been successfully demonstrated in these solvents(*304*). This data encouraged us to try TFE and HFIP in NCA-ECF. This strategy proved to be fruitful and good conversion of [^{18}F] fluoride in the NCA synthesis of [^{18}F]**2** was observed with TFE and HFIP as the solvent and TBAP as the electrolyte. Whereas in the case of HFIP, considerable amounts of unknown byproducts were formed, with TFE, the vast majority of [^{18}F]fluoride incorporation resulted in the formation of the desired product [^{18}F]**2**. It is likely that the byproducts are formed through formation of perfluorinated ethers previously described(*305*). The observed RCY of 49.8 ± 1.0% with TFE as the solvent marked a breakthrough in the NCA-ECF of thioethers. In a series of follow-up experiments, the previously

investigated triflate and tosylate compounds (pTS, TBATF, TfOH and pTSA) were retested as additives to the solvent TFE, resulting in reduced formation of [^{18}F]**2** as compared to the use of neat TFE. The promising results with TFE as the solvent can be explained by the proposed fluoro-Pummerer-type mechanism. **Figure 10.2** presents a combined illustration of commonly accepted fluoro-Pummerer mechanism (**Figure 10.2**, right) and its modification that we suggest to explain the no-carrier added reaction reported here (**Figure 10.2**, left). Trifluoroethanolate enhanced by reduction of TFE on the cathode in the single chamber cell, acts as a promoting agent in the fluoro-Pummerer-type rearrangement. TFE and HFIP alcoholates stabilize the sulfur carbocation after the first anodic oxidation. Following the second anodic oxidation reaction, fluorinated alcoholate abstracts proton in the α-position to sulfur forming a sulfonium ion. The latter can react with either [^{18}F]fluoride or competing nucleophiles to yield the desired product or an auxiliary-ether, respectively. Indeed, a substantial amount of the auxiliary-ether was observed using GC–MS(*272*). HFIP alcoholate seems to have weaker stabilizing effect on the sulfur carbocation as suggested by the increased formation of undesired side products. TFE is likely to extend the cation intermediate lifetime, thereby increasing the probability of the nucleophilic attack at diminishing NCA concentrations of fluoride. In a limited study of the scope of this approach, NCA-ECF of several thioethers in TFE was performed (**Figure 10.1**). Excellent RCYs were observed in the formation of [^{18}F]**2** and [^{18}F]**3**. Notably, both respective substrates lack the phenyl group adjacent to sulfur as compared to substrate 1. Poor RCY was observed in the formation of [^{18}F]**4**. The nitrile group potentially exerts a destabilizing effect on the sulfonium/carbenium cation resulting in the formation of unidentified radiochemical side products. A similar trend was seen in case of [^{18}F]**5** with the second lowest RCY within the scope, likely caused by electron withdrawing properties of the phosphonate group. The NCA-ECF of 2-(phenylthio) acetamide to yield [^{18}F]**6** is notable since the primary amide has an oxidation potential similar to that of sulfur. The fact that this transformation proceeds without the protection of the primary amide illustrates the versatility of this methodology, in that a wider range of thioethers can potentially be fluorinated without prior

modification. A complete radiosynthesis of [^{18}F]**2** that includes the HPLC isolation of the final product was performed. Up to 700 MBq of [^{18}F]**2** were synthesized within 90 min from the end of bombardment in 88 ± 3% isolated RCY and RCP of >95%. Am ranged from 4.7 to 5.3 GBq/μmol, representing >100x increase compared to previous reports on electrochemical radiofluorination, and approaching values observed in other NCA techniques(*306*).

10.4 Conclusion

This is the first example of no-carrier added radiofluorination of thioethers. The methodology tolerates a range of functional groups, including unprotected amides. This methodology offers the possibility to produce high Am ^{18}F-fluorinated thioethers as tracers for PET imaging. Further research is underway to increase the yield of NCA-ECF and extending the scope beyond thioethers and to biologically relevant molecules.

10.5 Appendix

10.5.1 Synthesis parameter optimization

The NCA procedure described in section 4 was used for all experiments with the changes annotated in tables S1 and S2. The experimental results of the NCA-ECF using the precursor Methyl (phenylthio) Acetate **1** are tabulated in **Table 10.2** and **Table 10.3**. **Table 10.2** contains the experiments to optimize the electrochemical reaction for time and temperature. The optimal temperature was 70°C and time was 30 mins. **Table 10.3** summarizes results for alternative auxiliary groups in the fluoro-Pummerer mechanism to facilitate NCA-ECF with ACN and TFE were used as solvents in these experiments. The only successful fluorination in ACN was performed using Pyridinium pToluenesulfonate (PPTS) with an RCY of 3.9$\pm$1.2% (n=3). Triflic Acid (TfOH) and pToluenesulphonic Acid (TsOH) both reduced RCY in TFE. PPTS and Tetrabutylammonium Trifluoromethanesulfonate (TBA-OTf) also resulted in reduced RCY in TFE compared to using TBAP.

Table 10. 2 NCA-ECF optimization of 1 in TFE (n=3)

Time (mins)	Temp (°C)	RCC	RCP	RCY
10	70	34.5±5.2%	90.5±3.5%	31.4±5.9%
30	70	59.3±1.0%	84.1±2.1%	49.8±0.5%
60	70	57.5±1.4%	34.7±4.9%	19.9±2.3%
30	25	21.2±2.6%	91.9±0.7%	19.4±2.2%

Trifluoroethanol (TFE).

Table 10. 3 NCA-ECF of 1 Testing of Possible Auxiliary Groups (n=3)

Solvent	Acid (mM)	Electrolyte (50 mM)	RCC	RCP	RCY
TFE	-	PPTS	70.5±1.9%	21.9±0.6%	15.4±1.8%
ACN	-	PPTS	62.6±7.7%	6.1±1.2%	3.9±1.2%
TFE	-	TBA-OTf	30.9±1.8%	79.9±1.3%	24.7±1.8%
ACN	-	TBA-OTf	0%	0%	0%
TFE	2mM TfOH	TBAP	27.5±1.5%	84.2±4.1%	23.2±2.1%
TFE	10mM TfOH	TBAP	2.4±0.1%	13.5±0.8%	0.3±0.1%
ACN	2 mM TfOH	TBAP	0%	0%	0%
ACN	10 mM TfOH	TBAP	0%	0%	0%
TFE	2 mM TsOH	TBAP	35.8+0.4%	71.1+1.7%	25.5±0.3%
TFE	10 mM TsOH	TBAP	15.9±0.5%	85.8+2.6%	13.7±0.8%
ACN	2mM TsOH	TBAP	0%	0%	0%
ACN	10 mM TsOH	TBAP	0%	0%	0%

Acetonitrile (ACN). Pyridinium pToluenesulfonate (PPTS). Tetrabutylammonium trifluoromethanesulfonate (TBA-OTf). Triflic Acid (TfOH). pToluenesulphonic Acid (TsOH). Tetrabutylammonium Perchlorate (TBAP).

10.5.2 Molar activity calculations

NCA-ECF was performed to synthesize the radiofluorinated product methyl 2-[^{18}F]fluoro-2-(methylthio)acetate ([^{18}F]3) as described above. TLC and HPLC Analysis were performed on product. Due to the similarity of the absorbance of the fluorinated and non-fluorinated molecules and the slow decomposition of the synthesized non-radioactive reference, a more precise known concentration of the precursor was used to measure UV absorbance vs. molar mass. A calibration curve of the UV absorbance at 205 nm was used to determine the concentration of the radiofluorinated product after NCA-ECF. Curves were obtained using a linear-least square fit of absorbance versus molar mass spanning the expected mass range. Molar activity was calculated by dividing the radioactivity of the injected sample by the molar mass (as determined from the AUC for the UV peak and the calibration curve). The radioactivity was determined by a well counter (Capintec Inc.) and corrected for RCC determined by TLC and RCP determined by HPLC. All results were corrected for radioactive decay. A molar activity (Am) example calculation is shown below.

$$\frac{\mathbf{570}\ \mu\boldsymbol{Ci}}{\mathbf{4.2}\ \mu\dfrac{\boldsymbol{mol}}{\boldsymbol{Lit}} \times \mathbf{100}\ \mu\boldsymbol{l}} = \mathbf{1.36}\ \boldsymbol{Ci}/\mu\boldsymbol{mol}$$

10.5.3 HPLC analysis

HPLC chromatograms of the carrier added electrochemical syntheses for the fluorinated standards are shown in the graph below.

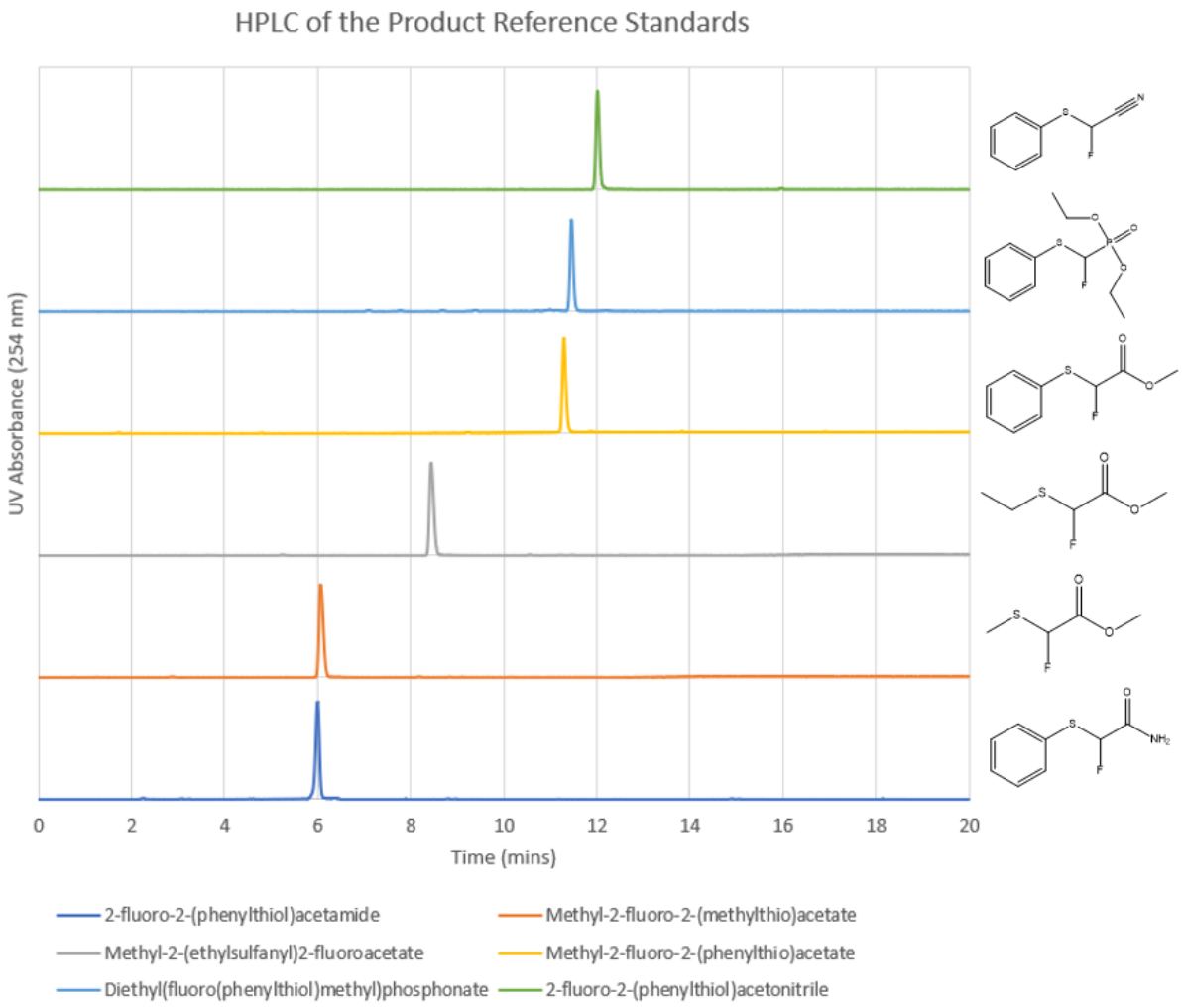

Figure 10. 3 HPLC chromatograms of different thioether molecules.

The crude HPLC of the NCA-ECF UV and gamma chromatograms using each of the 6 thioether precursors are shown below. The procedure for the NCA-ECF is described above. The top chromatogram of each graph is the gamma signal from ^{18}F-labelled molecules with the gamma peak of the product highlighted with an arrow. The bottom chromatogram of each graph is the UV (205 nm) of the molecules produced during electrolysis. The remaining precursor is highlighted with an arrow.

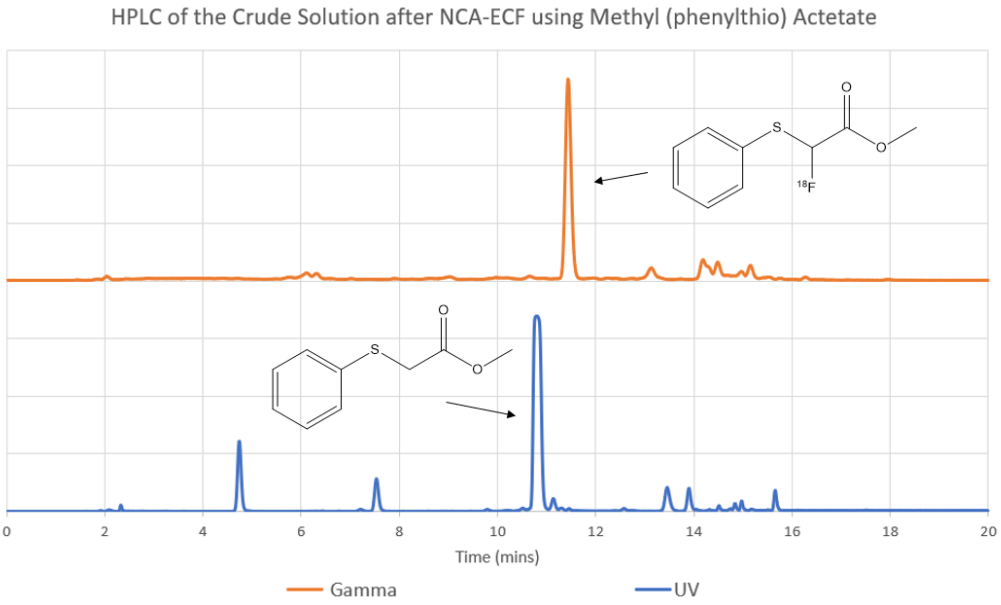

Figure 10. 4 HPLC chromatogram of crude methyl(phenylthiol)acetate

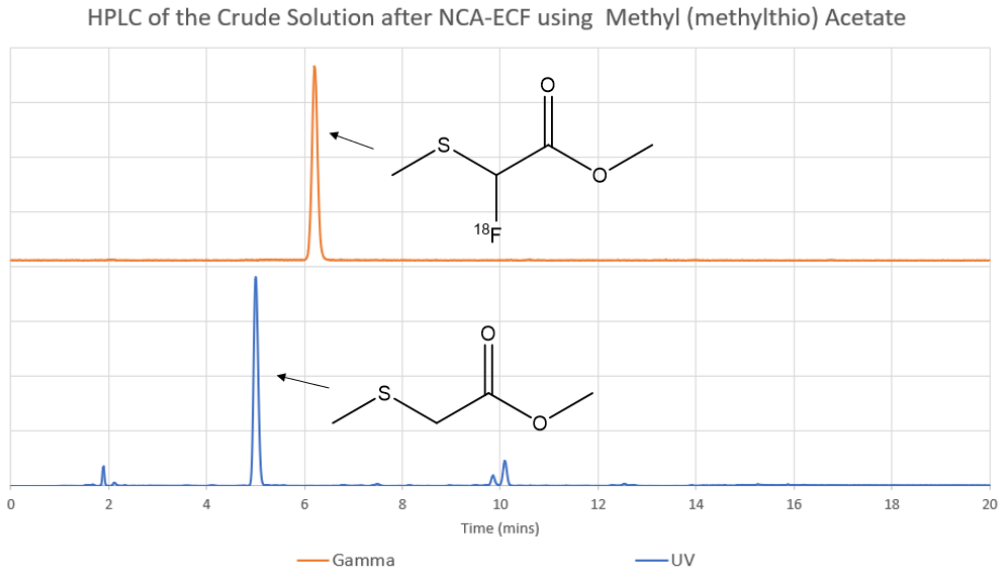

Figure 10. 5 HPLC chromatogram of crude methyl(methylthiol)acetate

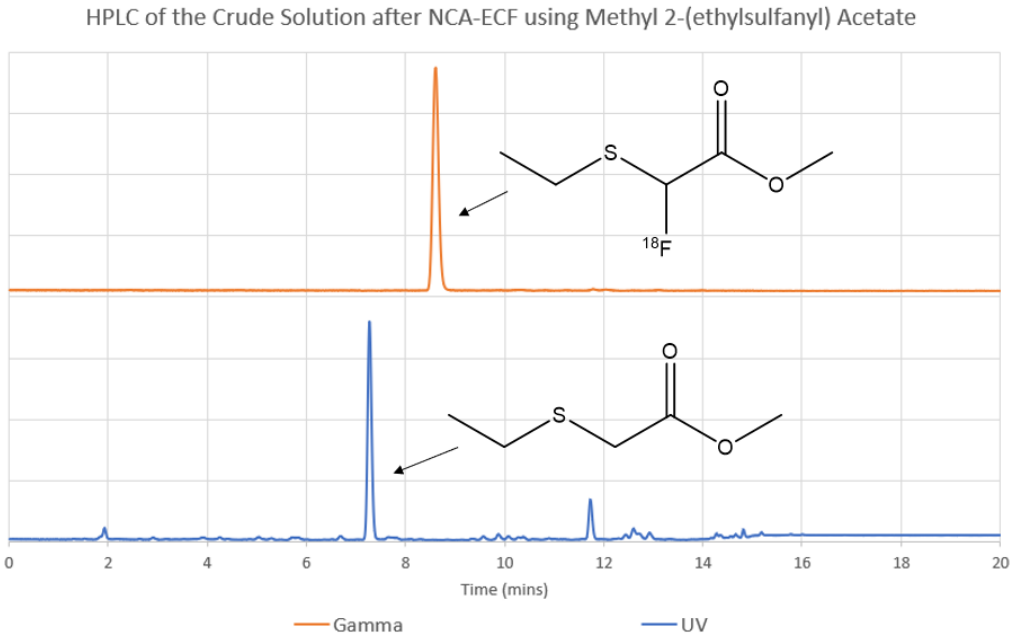

Figure 10. 7 HPLC chromatogram of crude methyl 2-(ethylsulfanyl)acetate

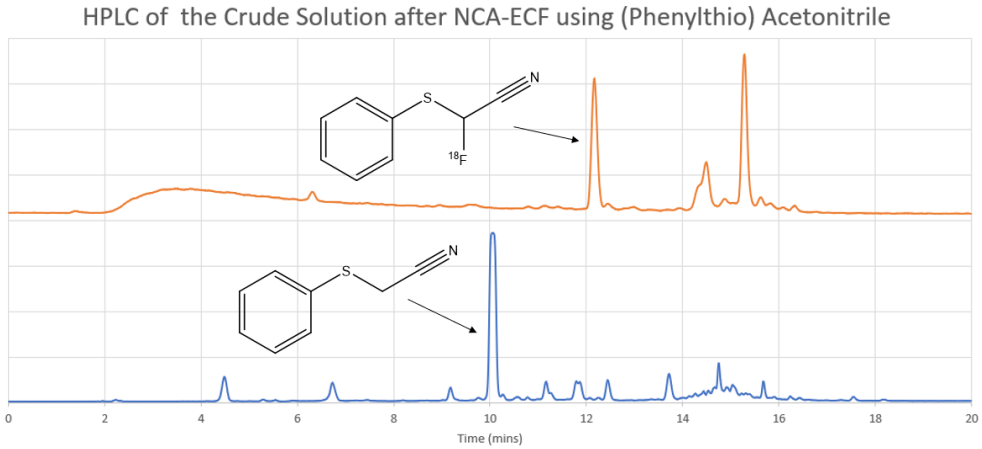

Figure 10. 6 HPLC chromatogram of crude methyl 2-(ethylsulfanyl)acetate

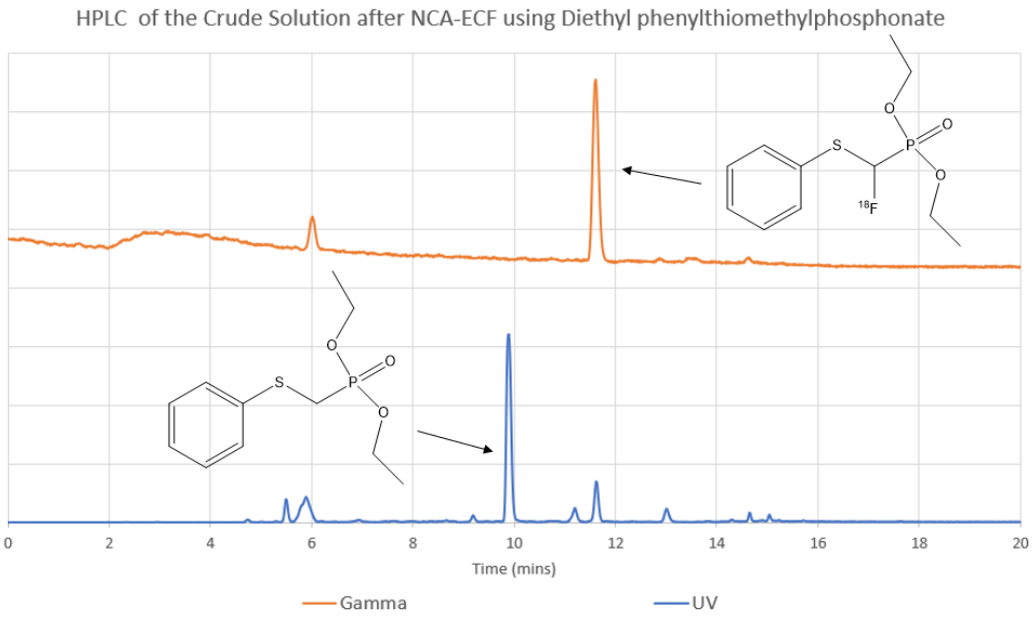

Figure 10. 8 HPLC chromatogram of crude diethyl phenylthiomethylphosphonate

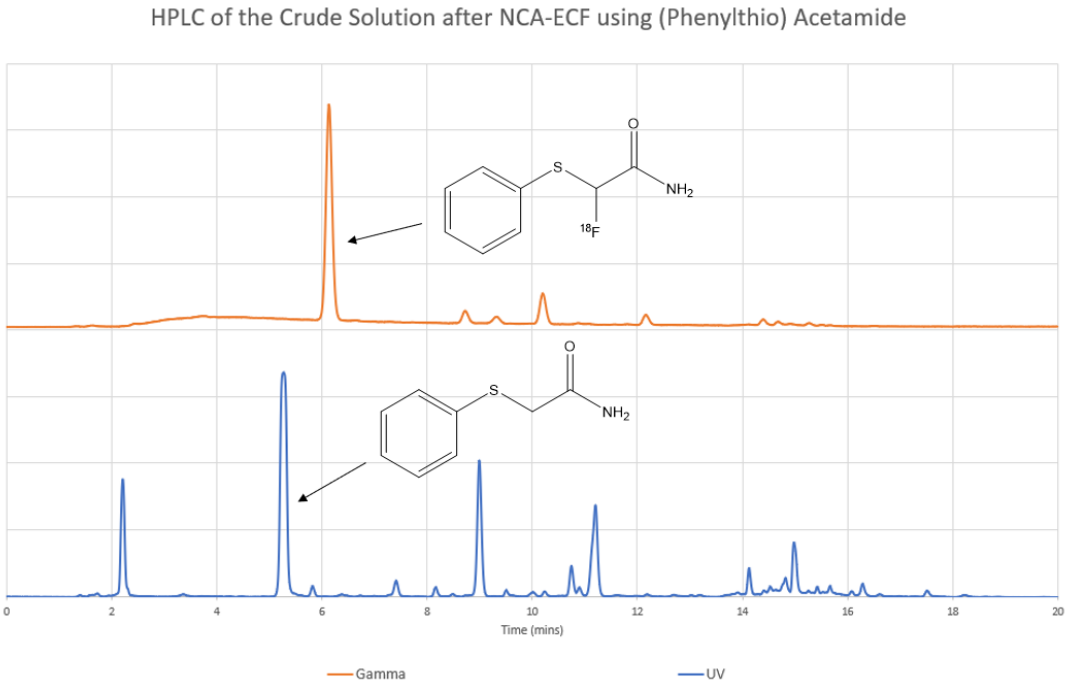

Figure 10. 9 HPLC chromatogram of crude (phenylthiol)acetamide

Chapter 11: High-throughput optimization of electrochemical radiofluorination via arrays of microscale electrochemical cells

11.1 Introduction

As discussed in **Chapters 7-9,** electrochemical radiofluorination provides a novel route for synthesizing [^{18}F]fluorinated thioethers. Previous work demonstrated the successful production of [^{18}F]methyl 2-fluoro-2-(phenylthio)acetate(*307*) and radiofluorination of thioethers via cation pool technique(*308*), as well as a no-carrier added approach(*309*). As electrochemical approaches are further developed and applied to additional precursors, it will be necessary to optimize the parameters of the labeling process, such as concentration, voltage, temperature, etc. Similar to the arguments made in **Chapter 10** for conventional radiosynthesizers, current electrochemical apparatus is not well suited for optimization studies. They require a large amount of precursor material (for the 7 mL -1.5 mL reaction volumes used) and require thorough cleaning of the electrochemical cell between experiments. To enable more efficient study of electrochemical reactions, it would be beneficial to have the ability to perform electrochemical reactions using less reagents and to perform them in parallel.

High throughput electrochemical 96-well plates have been previously used for detection of enzyme function, biomarker analysis, and small molecule synthesis(*310–313*). Recently, arrays of electrochemical cells became available in microplate format, a seemingly ideal optimization platform. In this chapter, we explore the use of these plates for efficient and high-throughput screening of reaction parameters for the electrochemical radiofluorinations of two thioethers: methyl 2-(methylthio)acetate (MMA) and methyl-2-(ethylthio)acetate (MEA). As previously reported, thioethers are attractive scaffolds for PET tracer development, due to their biological presence in methionine and cystine, which are relevant in various metabolic functions(*314*). Rapid optimization using less reagents and testing various parameters such as voltage, time, precursor

concentration, electrode material, and base concentration can aid on the radiofluorination of other biological related small molecules.

11.2 Materials and methods

11.2.1 Materials

All chemicals were purchased from commercial sources and used without further purification. Tetrabutylammonium perchlorate (TBAP, >99%, for electrochemical analysis) was purchased from Fluka. Tetraethylammonium fluoride tetrahydrofluoride (>97%) was purchased from Innovative chemical technologies (TCI). Methyl-2-(phenylthio)acetate (99%) was purchased from Alfa Aesar. Acetonitrile (MeCN, anhydrous, >99.8%) and p-toluenesulphonic acid (99%) were purchased from Agros Organics. Methyl 2-(methylthio)acetate (>98%), and trifluoroethanol (TFE) (>99%), silica plates (TLC Silica gel 60 W F254s, Merck) were purchased from Fisher. Ethanol (200 proof, anhydrous) was purchased from Decon. All water used was deionized (18MΩ) and passed through a 0.1 mm filter. No-carrier-added [^{18}F]fluoride was produced using [^{18}O]H_2O (84% isotopic purity, Medical Isotopes) in a RDS-112 cyclotron (Siemens) from a 11 MeV bombardment with a 1 mL tantalum target with havar foil.

11.2.2 Reagent preparation

[^{18}F]fluoride in [^{18}O]H_2O (20 mCi) was trapped on a custom-made cartridge containing analytical grade MP-1 anion exchange resin (5 mg)(*308*). The cartridge was dried with a stream of N_2 for 5 mins, washed with 3 mL of anhydrous MeCN, and further dried with a stream of N_2 for 5 mins. [^{18}F]fluoride was subsequently eluted off the cartridge with 1 ml of TFE containing a desired concentration of base/electrolyte, e.g. 1 mL of TFE containing 50 mM TBAP. A 20 µL aliquots (containing ~0.4 mCi of the resulting [^{18}F]TBAF complex) was loaded into each well, followed by an additional 30 µL of TFE containing the precursor, for a total of 50 µL volume with 20 mM TBAP).

11.2.3 Electrochemical radiofluorination

Electrochemical reactions were performed in 96-well electrochemical well plates (Metrohm Dropsens, Asturias, Spain), connected to a multi-potentiostat/galvanostat (µStat 8000, Metrohm Dropsens) via a connector (DRP-96-Well Plate Connector, Metrohm DropSens). With the setup it is possible to perform 8 electrochemical reactions at a time. Electrochemical plates had screen-printed electrodes, including a reference electrode made of silver, and either platinum or carbon working electrode (3 mm diameter) and counter electrode.

In each well, electrolysis was performed at a desired voltage under a constant-potential mode at room temperature for a desired amount of time. The plates were set to fast oscillation, slow oscillation, or no oscillation via shaker. To reduce passivation of the electrodes, the oxidation pulse (voltage set) was held for 60 s, followed by a cleaning pulse of 0 V for 1 s. The activity of crude electrochemical mixture after electrolysis was collected with 20 µL of TFE. To analyze each collected crude products, samples (~1 µL) were spotted on a TLC plate, as previously described in **Chapter 3**. TLC plates were developed in 100% MeCN, then read out via Cerenkov luminescence imaging. TLC plates exhibited 2 bands: [^{18}F]fluoride, R_f:0 and product band R_f: 0.7. Radiochemical conversion was calculated by using a custom made MATLab program described in **Chapter 3**. Collection efficiency was computed as the activity of the collected crude reaction divided by the starting activity for the same well, corrected for decay. The crude RCY was determined by multiplying the radiochemical conversion by the collection efficiency. The overall procedure is summarized in **Figure 11.1**.

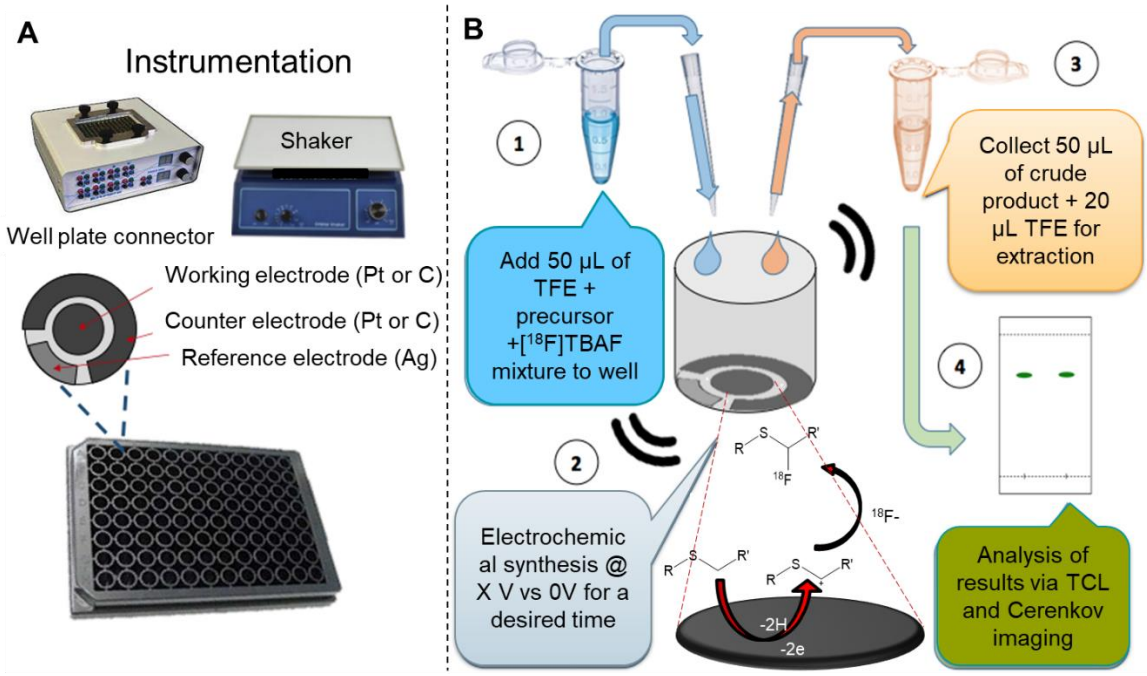

Figure 11. 1 Schematic of high-throughput electrochemical radiofluorination.

(A) Instrumentation. An electrochemical plate is installed in the well plate connector which was in turn connected to the multi-potentiostat. To provide some agitation, the well plate connector was installed on top of a shaker. (B) For each electrochemical cell (well), a mixture of precursor and [^{18}F]TBAF in TFE was added to the well, then the desired voltage was applied for the desired time with or without shaking. Next, the crude product was collected, and collection solution was added to extract excess product. Finally, collected crude products are spotted on TLC and analyzed via Cerenkov luminescence imaging.

11.3 Results

11.3.1 Radiolabeling of methyl 2-(methylthio)acetate (MMA)

In our previous study of electrochemical radiofluorination of MMA in a 1.5 mL cell (HPLC vial), we explored multiple reaction conditions, achieving an optimal crude RCY by using: TFE as solvent, 50 mM precursor, voltage of 1.9V vs -0.6V, 60 min duration, temperature of 70 °C, platinum working and counter electrodes, silver reference electrode, and 50 mM of base/electrolyte (TBAP)(*309*).

As a starting point to test the feasibility of performing electrochemical fluorinations in the 50 µL in the electrochemical well plate instead of the 1.5 mL of the conventional method, we adopted the following conditions. Also, to understand if less precursor could be used at microvolumes,

precursor concentration was changed to 25 mM, time of reaction was reduced from 30 min to 8 min, voltage was changed to 1.6 V vs 0V, and carbon electrodes were used for these experiments. In an initial study, we explored the impact of changing the amount of the base (TBAP), exploring the range 2.5 mM to 75 mM (**Figure 11.2** and **Table 11.1**).

Each condition was performed once (n=1), but TLC analysis was performed twice (n=2). Collection efficiency from each well was above 70% with the exception of the test at 30 mM TBAP, but this may be due to inefficient collection of crude product for that particular well. It was observed that the radiofluorination of the MMA precursor increased with the increase of base concentration up to 30 mM of TBAP (i.e. fluorination efficiency of 17 ± 0%, crude RCY of 7 ± 0%,), however it had a steady decrease after 30 mM of TBAP. It was also noticed that side product formed at high base amounts, i.e. 2% at 50 mM and 6% side product at 75 mM. We chose 30 mM TBAP as the optimum value. Based on the results obtained from the base concentration studies, the optimal concentration was found to be 30 mM of TBAP.

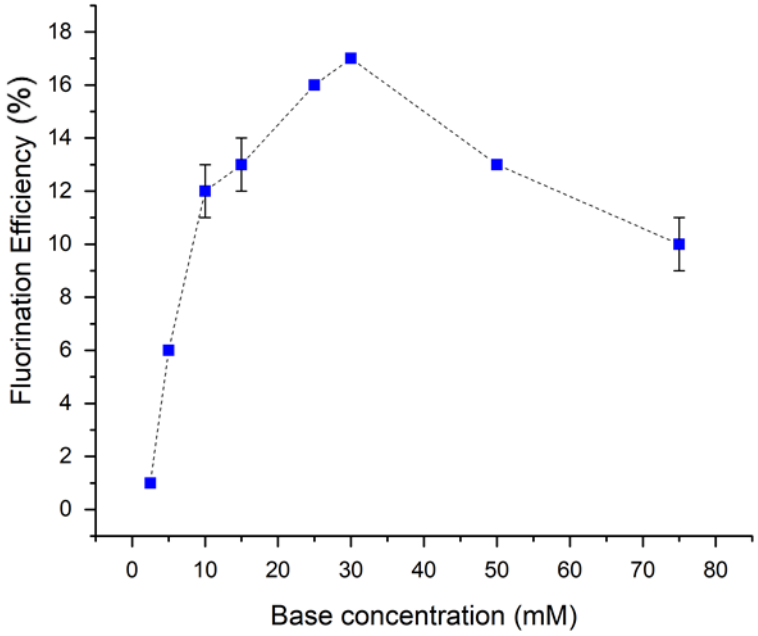

Figure 11. 2 Effect of TBAP concentration on the fluorination efficiency of MMA precursor (n=1; spotting analysis was performed 2X).

Table 11. 1 Raw data showing collection efficiency (%), fluorination efficiency (%) and crude RCY (%) with changes in TBAP concentration during the radiolabeling of MMA precursor (n=1; spotting analysis was performed 2X).

TBAP (mM)	Collection efficiency (%)	Fluorination efficiency (%)	Crude RCY (%)
2.5	71	1 ± 0	0
5	67	6 ± 0	5 ± 0
10	82	12 ± 1	10 ± 1
15	87	13 ± 1	11 ± 1
25	87	16 ± 0	14 ± 0
30	40	17 ± 0	7 ± 0
50	73	13 ± 0	9 ± 0
75	89	10 ± 0	9 ± 0

The next parameter studied was the precursor concentration, in the range 2.5 to 100 mM (**Figure 11.3**, **Table 11.2**). Other parameters were kept constant: 8 min reaction, 1.6 V vs 0 V, and carbon electrodes with silver reference electrode. We noticed an increase in radiofluorination efficiency with an increase of MMP precursor concentration, plateauing above 25 mM. Collection efficiency was overall above 80%. Also, it was observed that side product formation was found at the low precursor amounts, i.e. 2% and 6% impurities for the 2.5 mM and 5 mM precursor concentrations, respectively. As an optimal value, we chose a point early in the plateau region (30 mM precursor) which gave a crude RCY of 20%.

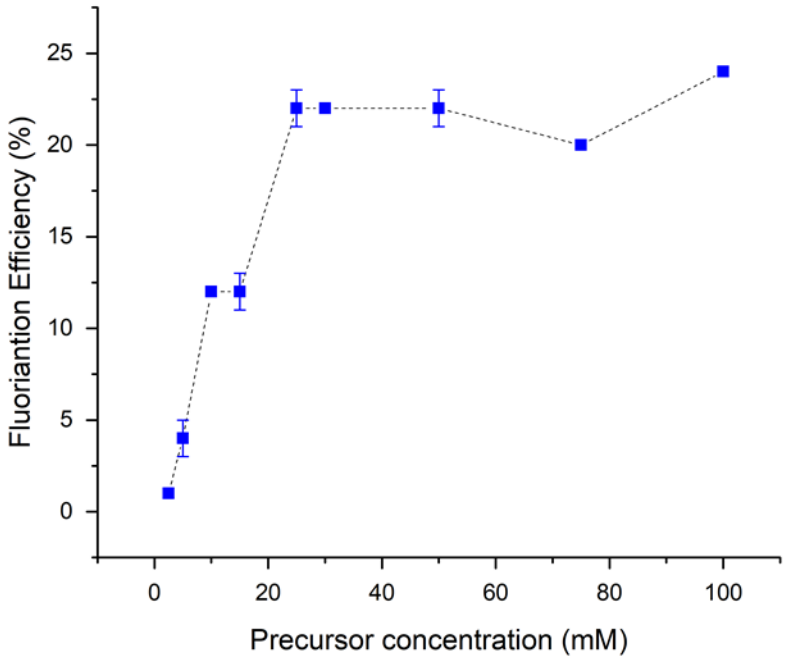

Figure 11. 3 Effect of precursor concentration on the fluorination efficiency of MMA precursor (n=1; spotting analysis was performed 2X).

Table 11. 2 Raw data showing collection efficiency (%), fluorination efficiency (%) and crude RCY (%) with changes in precursor concentration during the radiolabeling of MMA precursor (n=1; spotting analysis was performed 2X).

MMA precursor (mM)	Collection efficiency (%)	Fluorination efficiency (%)	Crude RCY (%)
2.5	81	1 ± 0	1 ± 0
5	50	4 ± 1	3 ± 0
10	78	12 ± 0	10 ± 0
15	86	12 ± 1	10 ± 1
25	87	22 ± 1	19 ± 1
30	91	22 ± 0	20 ± 0
50	91	22 ± 1	20 ± 1
75	90	20 ± 0	18 ± 0
100	88	24 ± 0	22 ± 0

The next parameter that was explored was the voltage, with values ranging from 1 V to 3 V vs 0 V for electrode cleaning (**Figure 11.4, Table 11.3**). Other parameters were: carbon electrodes, reaction time of 8 min, 30 mM TBAP, and 30 mM precursor. Radiofluorination was found to be low at the low voltages and gradually increased with the increase of voltage with the highest value (27%) at 2.2 V and steady decrease above 2.4 V. In addition, side product formation was observed at the high end of the voltage range with impurity abundances of 3%, 4%, 3%, and 3% at 2.4 V,

2.6 V, 2.8 V, and 3.0 V, respectively. Collection efficiency was above 85%, but collection efficiency above 100% was found at some wells and this may be due to potential dose calibrator measurements or manual error. The highest crude RCY was found at 2.4 V however side product was also found at this voltage, thus 2.2 V was chosen as the set parameter for the next experiments.

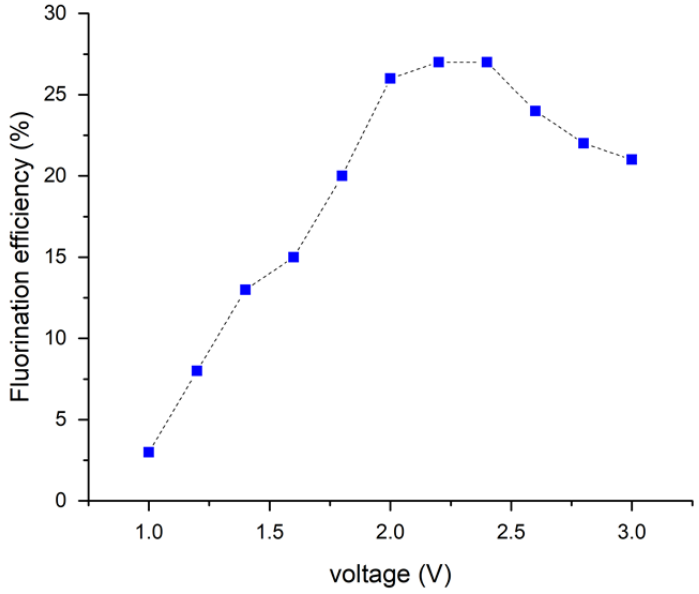

Figure 11. 4 Effect of voltage on the fluorination efficiency of MMA precursor (n=1).

Table 11. 3 Raw data showing collection efficiency (%), fluorination efficiency (%) and crude RCY (%) with changes on voltage during the radiolabeling of MMA precursor (n=1).

Voltage (V) vs 0 V	Collection efficiency (%)	Fluorination efficiency (%)	Crude RCY (%)
1.0	90	3	3
1.2	90	8	7
1.4	85	13	11
1.6	91	15	14
1.8	88	20	18
2.0	97	26	25
2.2	89	27	24
2.4	104	27	28*
2.6	112	24	27*
2.8	111	22	24*
3.0	103	21	22*

* Crude RCY may be overestimated due to the collection efficiency above 100%

It is important to notice that the previous work using HPLC vials for 1.5 mL reactions made use of PTFE stirring bar (1.7 mm) to ensure mixing of the solution during electrolysis(*309*). Unfortunately, a stirring bar could not be used in the microplate wells as the stir bar would scratch the electrodes. To induce stirring in the wells, we placed the well-plate adaptor on a shaker. Using the previous optimal parameters, i.e. 30 mM TBAP, 30 mM precursor, 8 min, 2.2 V vs 0V, and carbon electrodes, we varied the shaker settings (**Figure 11.5, Table 11.4**). Increasing the intensity of shaking improved the crude RCY, with the highest value (31%) occurring with the fast setting.

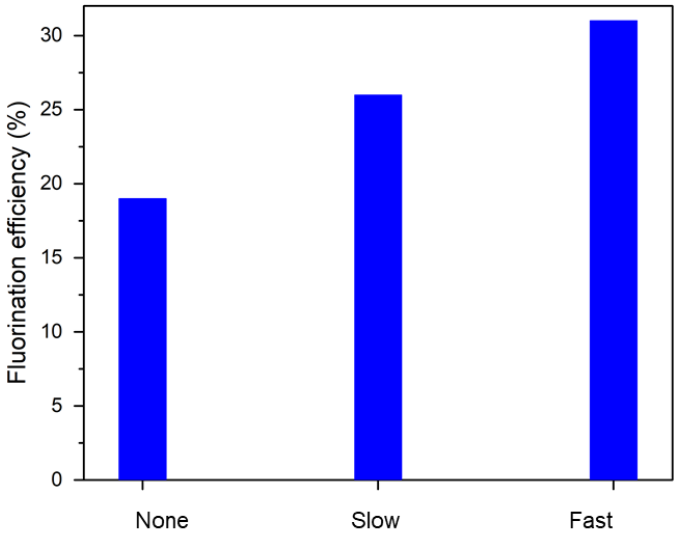

Figure 11. 5 Effect of shaker setting on the fluorination efficiency of MMA precursor (n=1)

Table 11. 4 Raw data showing collection efficiency (%), fluorination efficiency (%) and crude RCY (%) with changes on the shaker setting during the radiolabeling of MMA precursor (n=1).

Shaker setting	Collection efficiency (%)	Fluorination efficiency (%)	Crude RCY (%)
None	85	19	16
Slow	93	26	21
Fast	100	31	31

Previous reports showed the use of platinum electrodes with a silver reference electrode to be the better materials for the radiofluorination of thioether(*309*). Thus, we next compared the

influence of electrode material (**Table 11.5**). Other parameters were kept constant; 30 mM TBAP, 30 mM precursor, 8 min reaction time, and 2.2 V vs 0V. We found that the fluorination efficiency was higher using carbon electrodes (32%) vs the use of platinum electrodes (26%), and similarly the crude RCY values were 28% and 22%, respectively. Additionally, there was 14% side product formation using the platinum (Pt) electrodes and no side product with the carbon electrodes.

Table 11. 5 Electrode material effects on the electrochemical reactions.

Electrode material	Collection efficiency (%)	Fluorination efficiency (%)	Crude RCY (%)
Platinum	85	26	22
Carbon	90	32	28

Time of the reaction was the final parameter that was explored, in the range 4 – 60 min (**Figure 11.6, Table 11.6**). Other reaction parameters were kept constant; 30 mM TBAP, 30 mM precursor, 2.2 V vs. 0 V, carbon electrodes, and shaking set at high. We noticed that the fluorination efficiency increased with time, reaching its maximum at 45 min (55%) and decreased at 60 min to 30% due to side product formation. The highest crude RCY (47%) was found at 45 min. However, side product formation of 5% and 25% was observed at the 45 min and 60 min timepoints, respectively. Thus we chose 35 min as the optimal value.

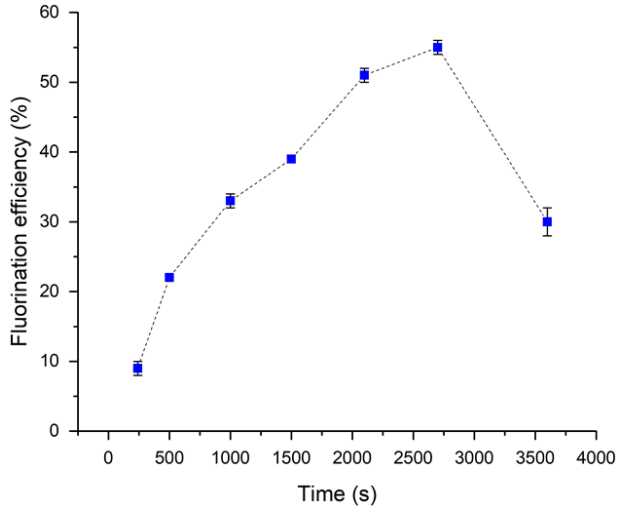

Figure 11. 6 Effect of reaction time on the fluorination efficiency of MMA precursor (n=1; spotting analysis was performed 2X).

Table 11. 6 Raw data showing collection efficiency (%), fluorination efficiency (%) and crude RCY (%) with changes in reaction time during the radiolabeling of MMA precursor (n=1; spotting analysis was performed 2X).

Reaction time (min)	Collection efficiency (%)	Fluorination efficiency (%)	Crude RCY (%)
4	88	9 ± 1	8
8	91	22 ± 0	20
16	87	33 ± 1	28
25	80	39 ± 0	31
35	31	51 ± 1	16*
45	86	55 ± 1	47
60	76	30 ± 2	23

*Low crude RCY due to low collection efficiency

11.3.2 Radiofluorination of methyl (ethylthio)acetate (MEA)

Based on the previous results with MMA, we set the initial concentration of TBAP and precursor at 30 mM, reaction time at 8 min, used carbon electrodes and set the shaker to the high setting. We initially explored the influence of voltage (in the range 1 V – 3 V vs. 0 V) (**Figure 11.7, Table 11.7**). We noticed a similar trend as MMA where the radiofluorination increased with increase of voltage, pleateauing at a value of 21% at 2.2V. Unlike MMA, this new precursor did not show any side product formation at the high voltages. Collection efficiency was above 95% for all wells with some above 100% that may be due to contamination of Eppendorf tube with crude product or dose calibrator sensitivity.

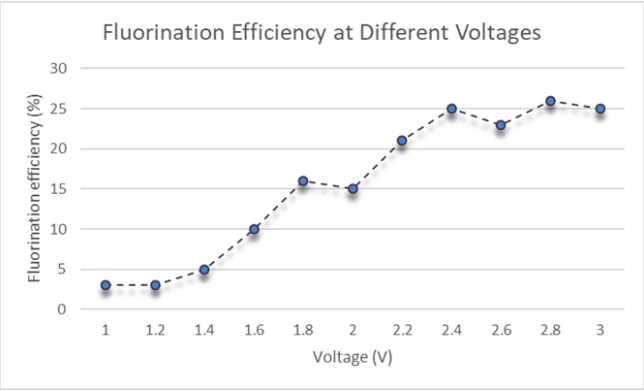

Figure 11. 7 Effect of voltage on the fluorination efficiency of MEA precursor (n=1).

Table 11. 7 Raw data showing collection efficiency (%), fluorination efficiency (%) and crude RCY (%) with changes on voltage during the radiolabeling of MEA precursor (n=1).

Voltage (V) vs 0 V	Collection efficiency (%)	Fluorination efficiency (%)	Crude RCY (%)
1.0	100	3	3
1.2	105	3	3*
1.4	105	5	6*
1.6	105	10	11*
1.8	101	16	17*
2.0	103	15	15*
2.2	103	21	21*
2.4	108	25	27*
2.6	99	23	23
2.8	98	26	26
3.0	99	25	25

* Crude RCY may be overestimated due to the collection efficiency above 100%

The next parameter that was explored was the TBAP concentration, in the range 2.5 mM to 100 mM (**Figure 11.8, Table 11.8**). Precursor concentration was kept at 30 mM, voltage at 2.2 V vs. 0 V, carbon electrode material, and fast setting of shaker for 8 min. Collection efficiency for all wells was equal or higher than 80%. Radiofluorination efficiency increased with base concentration, pleateauing at 40 mM TBAP and decreasing above 50-75 mM. We noticed side product formation when using high concentrations of base, i.e. 1%, 3%, to 6% with 50 mM, 75 mM, and 100 mM of TBAP, respectively. The optimal crude RCY was 20% using 40 mM of TBAP.

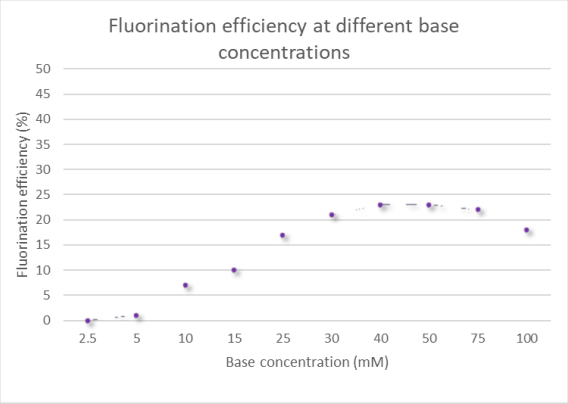

Figure 11. 8 Effect of TBAP concentration on the fluorination efficiency of MEA precursor (n=1).

Table 11. 8 Raw data showing collection efficiency (%), fluorination efficiency (%) and crude RCY (%) with changes in TBAP concentration during the radiolabeling of MEA precursor (n=1).

TBAP (mM)	Collection efficiency (%)	Fluorination efficiency (%)	Crude RCY (%)
2.5	91	0	0
5	93	1	1
10	85	7	6
15	87	10	9
25	86	17	15
30	86	21	18
40	87	23	20
50	89	23	20
75	80	22	17
100	86	18	16

The final parameter that was explored was the precursor concentration, ranging from 2.5 mM to 100 mM (**Figure 11.9, Table 11.9**). Other parameters were kept the same: TBAP concentration 40 mM, carbon electrodes, 8 min reaction time, and 2.2 V vs 0 V with the shaker set on the fast setting. Radiofluorination efficiency increased with precursor concentration and plateaued at 25 mM. As observed with MMA, side product was formed at low MEA precursor amounts which may be due to high base to precursor ratio. At MEA concentrations of 2.5, 5, 10, 15, and 25 mM, we noticed 3, 4, 6, 4, and 3% side product formation, respectively. The highest radiofluorination was found at 30 mM with 24% and crude RCY of 23%.

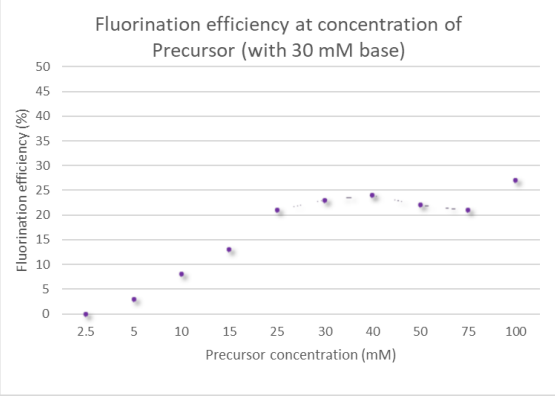

Figure 11. 9 Effect of precursor concentration on the fluorination efficiency of MEA precursor (n=1).

Table 11. 9 Raw data showing collection efficiency (%), fluorination efficiency (%) and crude RCY (%) with changes in precursor concentration during the radiolabeling of MEA precursor (n=1)

MEA precursor (mM)	Collection efficiency (%)	Fluorination efficiency (%)	Crude RCY (%)
2.5	95	0	0
5	96	3	3
10	97	8	8
15	97	13	12
25	105	21	22
30	99	24	23
40	95	23	22
50	89	22	20
75	85	21	18
100	88	27	24

11.4 Conclusion

In this study we briefly looked at the use of 96-well plate ELISA printed electrodes for the implementation of high throughput experimentation in electrochemical radiofluorination reactions. Advantages of this include the reduction in reagent consumption, the possibility to screen multiple conditions at once, the high repeatability of electrode geometry for each well (compared to hand-built cells with wire electrodes) and its commercial availability.

Carbon electrodes gave higher crude RCY than the platinum electrodes for MMA precursor, and generally the occurrence of side products was lower for carbon than platinum.

In the case of the radiofluorination of MMA the highest yield was found to be 51% with 1.6 V, 35 min, fast shaking, 30 mM TBAP, and 30 mM precursor. While this performance is lower than previously reported work (~90%) using HPLC vials containing 1.5 mL(*309*), the microwell format offered some advantages – namely the reaction time was reduced to 35 min vs 60 min and reactions occurred at room temperature instead of 70 °C. In the case of MEA precursor the highest crude RCY was found to be 23% using carbon electrodes, fast shaker setting, 8 min reaction time, 30 mM precursor, 40 mM TBAP, and 2.2 V. Further studies on electrode material and reaction time need to be performed to determine if the crude RCY can be further increased.

Overall, the system could be used to efficiency optimize the synthesis of electrochemical radiofluorination reactions, via generating detailed maps of the influence of reaction parameters on the synthesis performance.

Chapter 12: Outlook

As discussed in **Chapter 1** of this dissertation, many challenges surround radiopharmaceutical production for PET diagnostics, making it an expensive and complex process. Miniaturization may overcome these challenges, by enabling more compact, economic and efficient devices. Due to the reduction of shielding, physical footprint and reagent consumption, microfluidics can enable low-cost decentralized production of PET tracers, with the tracers produced on demand in imaging centers, instead of centralized large-batch production and distribution. Proof-of-concept microscale radiosynthesizer systems have been demonstrated, and though their use is not yet widespread, efforts are underway to further advance the technology and validate it for production of a wide variety of radiopharmaceuticals for research and clinical use.

To make use of this new technology, in **Chapter 2**, I showed that the use of multi array reaction sites in a single chip let to a strategy for the rapid optimization of [^{18}F]Fallypride synthesis and demonstrated efficient translation of macroscale synthesis procedures to microscale syntheses. Contamination tests confirmed the independence of reaction sites and reproducibility was demonstrated by performing replicate syntheses. Furthermore, the developed multi-reaction droplet radiosynthesis chip makes it practical to perform more comprehensive and robust studies of radiosynthesis conditions. Since the amount of precursor consumed per reaction is extremely small, and many reactions can be carried our using the same batch of radioisotope, the cost of optimization can be significantly lowered than for conventional setups.

A further advantage of the chip was that the reaction site matched exactly the single-reaction (“production”) radiochemistry system, enabling instant transition from optimization to routine production. In **Chapter 5**, I expanded this system from a single chip to a system in which 4 chips could be operated at once, allowing up to 64 reactions simultaneously, including multiple different heating profiles (temperatures or times) occurring at the same time. This technology facilitates

extensive synthesis optimization studies for new tracers in a short timeframe. The high-throughput methods I developed can be used to optimize the synthesis of new or existing tracers or compounds. With each reaction performed in a microdroplet, reagent consumption during the optimization process is minimized, and many reactions can be carried out in parallel from the same batch of radionuclide. Even though the operation of synthesis (like reagent loading and collecting) is manually performed using a pipette, our lab is currently developing a compact robotic system to automate those operations. With the robotic system, it is expected that the synthesis time can be further reduced, and operators can be relieved of tedious reagent and sample handling and can be better protected from radiation exposure. Such automated operation may also make it possible to do even larger numbers of experiments per day. In **Chapter 7,** I describe some approaches toward improving the synthesis and optimization of reactions involving volatile species, which can have high losses of radioactivity in the open droplet format. I designed a pre-concentration chip that allowed the [^{18}F]fluoride solution to be confined in a smaller area prior to adding [^{18}F]Flumazenil precursor. The chip achieved significantly improved fluorination efficiency and moderate improvement in collection efficiency of volatile reactions. This new approach could be applicable to isotope exchange reactions that are known to be volatile(*65*), and other volatile radiochemistry reactions(*136*). In addition, the concentration of [^{18}F]fluoride to a smaller area could help to reduce reagent consumption (e.g. solvent volume and precursor amounts) further and this could improve purification and simplify QC testing.

To support the use of such high-throughput reaction methods, I developed a technique for high-throughput radio-TLC analysis (**Chapter 3**). Cerenkov imaging in combination with parallel developing of multiple samples on a single TLC plate proved to be a practical method for rapid analysis. Compared to conventional methods, it provided significantly higher resolution, the ability to image multiple samples in parallel, and the ability to detect and quantify low-abundance impurities that were not discernable with conventional radio-TLC scanning. In the robotic system being developed for high-throughput optimization there will be a capability to automatically spot

samples onto TLC plates to further reduce the burden to the researcher. CLI imaging of TLC plates has broad applications for the analysis of radiotracers labeled with radionuclides that are positron emitters (F-18, Cu-64, Zr-89, I-124), betta emitters (e.g., I-131, Lu-177). Furthermore, this method could also be used for radiopharmaceuticals labeled with alpha emitters (e.g., Ac-225, Bi-213) that have applications in targeted radiotherapy.

Though microvolume radiosynthesis platforms are creating new possibilities to expand availability of diverse diagnostic radiopharmaceuticals at low cost, much work has been performed at lower activity scales. Using this this technology to prepare clinical doses requires scaling up to higher activity levels. Previous work on the increase of starting activity in microdroplets showed promising results. Recently, activity scale-up has been shown using a miniature trap and release process for the increase of activity on microdroplet reactions (e.g., up to 20 clinical doses of [^{18}F]Fallypride)(*30,47,62,71*). Another method that allowed the increase of activity on microdroplets was the dispensing and drying of relatively large amounts of activity by loading 30 µL droplets onto the chip, evaporating them, and repeating until the desired activity is concentrated on the chip (e.g., up to 2 clinical doses of [^{18}F]FET and [^{18}F]Florobetaben(*63*)). Subsequent reactions were performed in 10 µL volumes, utilizing 4 mm reactor droplet trap reactors(*63*). However, a decrease in overall performance was observed with increased activity scale. Many potential reasons for this decrease in observed yield could be due to: radiolytic degradation, stochiometric change in the precursor to contaminant [^{19}F]fluoride species, increased concentration of contaminant anionic impurities, increased concentration of any residual cationic impurities in the [^{18}F]fluoride solution introduced into the reactor. In **Chapter 6**, we present a method that may aid on the reduction of contaminants in the radioisotope source, which would otherwise interfere with the reaction. Preliminary results have demonstrated the ability to eliminate the impact of contaminants on reactions (performed at low activity scales but using large volumes of decayed radioisotope solution), and future work will focus on increasing

the activity scale to see if radiolysis and/or stoichiometric effects are also a limiting factor in scale-up. While more studies need to be conducted to study the effects of radiolysis and stoichiometry in high activity reactions, this method has already demonstrated that production yield can be improved with the removal of contaminants and it could enable clinical batches to be produced even at very low-yield reactions and increase the number of multi-patient batches to be produced.

Finally, in **Chapters 8-11** I described the development of electrochemical methods to radiolabel molecules. Electrochemical fluorination of organic compounds can be a powerful alternative technique for direct fluorination. Electrochemical oxidation can create an electron-poor carbon, potentially without the need for chemical modification, preparing the organic molecules for nucleophilic fluorination.(*243*,*266*) Fluorine atoms can be added to organic compounds in one step under mild conditions using electrochemistry, even for electron rich moieties such as aromatic and heteroaromatic rings, without the need to have leaving groups.(*267*,*249*). I showed the use of electrochemistry for the fluorination and radiofluorination of various thioether molecules, making it a potential method to be use in precursors that are particularly electron rich and hard to radiofluorinate using conventional methos. In addition, I combined the use of microfluidics and high throughput experimentation to accelerate the optimization process of electrochemical radiofluorination of thioethers. The advantages of this method was the reduction of reagents and parallel exploration of various reaction conditions. Since the method utilized a commercially available device, this could facilitate reproducibility of reaction conditions without the need to worry about the electrode configuration change during the experiment.

The increasing number of PET radiopharmaceuticals being developed to aid drug development and create new diagnostics has let to an increased need for radiosynthesis development and optimization. The use of microfluidics methods and high-throughput experimentation throughout this dissertation demonstrated rapid refinement and optimization of radiosynthesis protocols for existing radiopharmaceuticals, and translation of known macroscale protocols into droplet format. The presented methods could be further applied to optimization of

radiosynthesis novel radiopharmaceuticals, studies of novel labeling methods, and extended to therapeutic isotopes, while providing the means to safely manufacture batches of these compounds on demand with very little need of upfront capital cost.

References

1. Vallabhajosula S, Solnes L, Vallabhajosula B. A Broad Overview of Positron Emission Tomography Radiopharmaceuticals and Clinical Applications: What Is New? *Seminars in Nuclear Medicine*. 2011;41:246-264.

2. Cherry SR, James A. Sorenson, Michael E. Phelps. Physics in nuclear medicine. 4th ed. Philadelphia, PA, USA: Elsevier saunders; 2012.

3. Schulthess GK von, Veit-Haibach P. Workflow Considerations in PET/MR Imaging. *Journal of Nuclear Medicine*. 2014;55:19S-24S.

4. Dunphy MPS, Lewis JS. Radiopharmaceuticals in Preclinical and Clinical Development for Monitoring of Therapy with PET. *J Nucl Med*. 2009;50:106S-121S.

5. Matthews PM, Rabiner EA, Passchier J, Gunn RN. Positron emission tomography molecular imaging for drug development. *Br J Clin Pharmacol*. 2012;73:175-186.

6. Piel M, Vernaleken I, Rösch F. Positron Emission Tomography in CNS Drug Discovery and Drug Monitoring. *J Med Chem*. 2014;57:9232-9258.

7. glennroberts. Seeing More with PET Scans: Scientists Discover New Chemistry for Medical Images | Berkeley Lab. News Center. https://newscenter.lbl.gov/2017/07/27/new-chemistry-pet-scans-medical-imaging/.

8. Ametamey SM, Honer M, Schubiger PA. Molecular Imaging with PET. *Chem Rev*. 2008;108:1501-1516.

9. Guillaume M, Luxen A, Nebeling B, Argentini M, Clark JC, Pike VW. Recommendations for fluorine-18 production. *International Journal of Radiation Applications and Instrumentation Part A Applied Radiation and Isotopes*. 1991;42:749-762.

10. Jacobson O, Kiesewetter DO, Chen X. Fluorine-18 Radiochemistry, Labeling Strategies and Synthetic Routes. *Bioconjugate Chem*. 2015;26:1-18.

11. Kilbourn MR, Rodnick ME, Clark M. Production of Short Half-Life PET Radionuclides. In: Handbook of Radiopharmaceuticals. John Wiley & Sons, Ltd; 2020:45-69.

12. Brooks AF, Makaravage KJ, Wright J, Sanford MS, Scott PJH. Fluorine-18 Radiochemistry. In: Handbook of Radiopharmaceuticals. John Wiley & Sons, Ltd; 2020:251-289.

13. Wang J, van Dam RM. Economical Production of Radiopharmaceuticals for Preclinical Imaging Using Microdroplet Radiochemistry. In: Ossandon MR, Baker H, Rasooly A, eds. Biomedical Engineering Technologies: Volume 1. Methods in Molecular Biology. New York, NY: Springer US; 2022:813-828.

14. Collins J, Waldmann CM, Drake C, et al. Production of diverse PET probes with limited resources: 24 18F-labeled compounds prepared with a single radiosynthesizer. *Proceedings of the National Academy of Sciences*. 2017;114:11309-11314.

15. Kawai N, Miyake K, Yamamoto Y, Nishiyama Y, Tamiya T. 18F-FDG PET in the Diagnosis and Treatment of Primary Central Nervous System Lymphoma. *Biomed Res Int*. 2013;2013:247152.

16. Chassoux F, Artiges E, Semah F, et al. 18F-FDG-PET patterns of surgical success and failure in mesial temporal lobe epilepsy. *Neurology*. 2017;88:1045-1053.

17. Langen K-J, Galldiks N, Hattingen E, Shah NJ. Advances in neuro-oncology imaging. *Nat Rev Neurol*. 2017;13:279-289.

18. Parida GK, Roy SG, Kumar R. FDG-PET/CT in Skeletal Muscle: Pitfalls and Pathologies. *Seminars in Nuclear Medicine*. 2017;47:362-372.

19. Rice L, Bisdas S. The diagnostic value of FDG and amyloid PET in Alzheimer's disease—A systematic review. *European Journal of Radiology*. 2017;94:16-24.

20. Treglia G. Diagnostic Performance of 18F-FDG PET/CT in Infectious and Inflammatory Diseases according to Published Meta-Analyses. *Contrast Media & Molecular Imaging*. 2019;2019:e3018349.

21. Walker Z, Gandolfo F, Orini S, et al. Clinical utility of FDG PET in Parkinson's disease and atypical parkinsonism associated with dementia. *Eur J Nucl Med Mol Imaging*. 2018;45:1534-1545.

22. Treglia G, Sadeghi R, Del Sole A, Giovanella L. Diagnostic performance of PET/CT with tracers other than F-18-FDG in oncology: an evidence-based review. *Clin Transl Oncol*. 2014;16:770-775.

23. Keppler JS, Conti PS. A Cost Analysis of Positron Emission Tomography. *American Journal of Roentgenology*. 2001;177:31-40.

24. Rios A, Wang J, Chao PH, Dam RM van. A novel multi-reaction microdroplet platform for rapid radiochemistry optimization. *RSC Adv*. 2019;9:20370-20374.

25. Zhu S, Mosessian S, Kroeger K, et al. Transforming an Academic Radiochemistry Facility for Positron Emission Tomography Drug cGMP Compliance. *Mol Imaging Biol*. 2020;22:256-264.

26. Rensch C, Jackson A, Lindner S, et al. Microfluidics: A Groundbreaking Technology for PET Tracer Production? *Molecules*. 2013;18:7930-7956.

27. Pascali G, Matesic L. How Far Are We from Dose On Demand of Short-Lived Radiopharmaceuticals? In: Kuge Y, Shiga T, Tamaki N, eds. Perspectives on Nuclear Medicine for Molecular Diagnosis and Integrated Therapy. Springer Japan; 2016:79-92.

28. Knapp K-A, Nickels ML, Manning HC. The Current Role of Microfluidics in Radiofluorination Chemistry. *Mol Imaging Biol*. 2020;22:463-475.

29. Pascali G, Watts P, Salvadori PA. Microfluidics in radiopharmaceutical chemistry. *Nuclear Medicine and Biology*. 2013;40:776-787.

30. Keng PY, van Dam RM. Digital Microfluidics: A New Paradigm for Radiochemistry. *Mol Imag*. 2015;14:579-594.

31. Wang J, Chao PH, Hanet S, Dam RM van. Performing multi-step chemical reactions in microliter-sized droplets by leveraging a simple passive transport mechanism. *Lab Chip*. 2017;17:4342-4355.

32. Wang J, Chao PH, van Dam RM. Ultra-compact, automated microdroplet radiosynthesizer. *Lab Chip*. 2019:2415-2424.

33. Sergeev M, Lazari M, Morgia F, et al. Performing radiosynthesis in microvolumes to maximize molar activity of tracers for positron emission tomography. *Communications Chemistry*. 2018;1:10.

34. Hume SP, Gunn RN, Jones T. Pharmacological constraints associated with positron emission tomographic scanning of small laboratory animals. *European Journal of Nuclear Medicine and Molecular Imaging*. 1998;25:173-176.

35. Jagoda EM, Vaquero JJ, Seidel J, Green MV, Eckelman WC. Experiment assessment of mass effects in the rat: implications for small animal PET imaging. *Nuclear Medicine and Biology*. 2004;31:771-779.

36. Arima V, Watts P, Pascali G. Microfluidics in Planar Microchannels: Synthesis of Chemical Compounds On-Chip. In: Castillo-León J, Svendsen WE, eds. Lab-on-a-Chip Devices and Micro-Total Analysis Systems. Springer International Publishing; 2015:197-239.

37. Razzaq T, Kappe CO. Continuous Flow Organic Synthesis under High-Temperature/Pressure Conditions. *Chemistry – An Asian Journal*. 2010;5:1274-1289.

38. Wiles C, Watts P. Continuous Flow Reactors, a Tool for the Modern Synthetic Chemist. *Eur J Org Chem*. 2008;2008:1655-1671.

39. Liu Z, Schaap KS, Ballemans L, et al. Measurement of reaction kinetics of [177Lu]Lu-DOTA-TATE using a microfluidic system. *Dalton Trans*. 2017;46:14669-14676.

40. Pfaff S, Philippe C, Pichler V, Hacker M, Mitterhauser M, Wadsak W. Microfluidic 68 Ga-labeling: a proof of principle study. *Dalton Transactions*. 2018;47:5997-6004.

41. Wright BD, Whittenberg J, Desai A, et al. Microfluidic Preparation of a 89Zr-Labeled Trastuzumab Single-Patient Dose. *J Nucl Med*. 2016;57:747-752.

42. Zeng D, Desai AV, Ranganathan D, Wheeler TD, Kenis PJA, Reichert DE. Microfluidic radiolabeling of biomolecules with PET radiometals. *Nuclear Medicine and Biology*. 2013;40:42-51.

43. Bruton L, Scott PJH. Automated Synthesis Modules for PET Radiochemistry. In: Handbook of Radiopharmaceuticals. John Wiley & Sons, Ltd; 2020:437-456.

44. Saiki H, Iwata R, Nakanishi H, et al. Electrochemical concentration of no-carrier-added [18F]fluoride from [18O]water in a disposable microfluidic cell for radiosynthesis of 18F-labeled radiopharmaceuticals. *Applied Radiation and Isotopes*. 2010;68:1703-1708.

45. Wong R, Iwata R, Saiki H, Furumoto S, Ishikawa Y, Ozeki E. Reactivity of electrochemically concentrated anhydrous [18F]fluoride for microfluidic radiosynthesis of 18F-labeled compounds. *Applied Radiation and Isotopes*. 2012;70:193-199.

46. Iwata R, Terasaki K, Ishikawa Y, et al. A concentration-based microscale method for 18F-nucleophilic substitutions and its testing on the one-pot radiosynthesis of [18F]FET and [18F]fallypride. *Applied Radiation and Isotopes*. August 2020:109361.

47. Lebedev A, Miraghaie R, Kotta K, et al. Batch-reactor microfluidic device: first human use of a microfluidically produced PET radiotracer. *Lab Chip*. 2012;13:136-145.

48. Zhang X, Liu F, Knapp K-A, Nickels ML, Manning HC, Bellan LM. A simple microfluidic platform for rapid and efficient production of the radiotracer [18F]fallypride. *Lab Chip*. 2018;18:1369-1377.

49. Wang J, van Dam RM. High-Efficiency Production of Radiopharmaceuticals via Droplet Radiochemistry: A Review of Recent Progress. *Mol Imaging*. 2020;19:1-21.

50. Fiel SA, Yang H, Schaffer P, et al. Magnetic Droplet Microfluidics as a Platform for the Concentration of [18F]Fluoride and Radiosynthesis of Sulfonyl [18F]Fluoride. *ACS Appl Mater Interfaces*. 2015;7:12923-12929.

51. Lisova K, Chen BY, Wang J, Fong KM-M, Clark PM, van Dam RM. Rapid, efficient, and economical synthesis of PET tracers in a droplet microreactor: application to O-(2-[18F]fluoroethyl)-L-tyrosine ([18F]FET). *EJNMMI radiopharm chem*. 2019;5:1.

52. Wang J, Holloway T, Lisova K, Dam RM van. Green and efficient synthesis of the radiopharmaceutical [18F]FDOPA using a microdroplet reactor. *React Chem Eng*. December 2019.

53. Pascali G, Matesic L, Collier TL, et al. Optimization of nucleophilic 18F radiofluorinations using a microfluidic reaction approach. *Nat Protocols*. 2014;9:2017-2029.

54. Arima V, Pascali G, Lade O, et al. Radiochemistry on chip: towards dose-on-demand synthesis of PET radiopharmaceuticals. *Lab Chip*. 2013;13:2328-2336.

55. Matesic L, Kallinen A, Greguric I, Pascali G. Dose-on-demand production of diverse 18F-radiotracers for preclinical applications using a continuous flow microfluidic system. *Nuclear Medicine and Biology*. 2017;52:24-31.

56. Liu K, Lepin EJ, Wang M-W, et al. Microfluidic-Based 18F-Labeling of Biomolecules for Immuno–Positron Emission Tomography. *Mol Imaging*. 2011;10:168-176.

57. Chen Y-C, Liu K, Shen CK-F, van Dam RM. On-demand generation and mixing of liquid-in-gas slugs with digitally programmable composition and size. *J Micromech Microeng*. 2015;25:084006.

58. Iwata R, Pascali C, Terasaki K, Ishikawa Y, Furumoto S, Yanai K. Minimization of the amount of Kryptofix 222 - KHCO3 for applications to microscale 18F-radiolabeling. *Appl Radiat Isot*. 2017;125:113-118.

59. Laube M, Wodtke R, Kopka K, Kniess T, Pietzsch J. 18F-Chemistry in HPLC vials - a microliter scale radiofluorination approach. *Nuclear Medicine and Biology*. 2021;96-97:S61.

60. Lazari M, Irribarren J, Zhang S, van Dam RM. Understanding temperatures and pressures during short radiochemical reactions. *Applied Radiation and Isotopes*. 2016;108:82-91.

61. Rios A, Holloway TS, Chao PH, De Caro C, Okoro CC, van Dam RM. Microliter-scale reaction arrays for economical high-throughput experimentation in radiochemistry. *Sci Rep*. 2022;12:10263.

62. Wang J, Chao PH, Slavik R, van Dam RM. Multi-GBq production of the radiotracer [18F]fallypride in a droplet microreactor. *RSC Adv*. 2020;10:7828-7838.

63. Lisova K, Wang J, Hajagos TJ, et al. Economical droplet-based microfluidic production of [18F]FET and [18F]Florbetaben suitable for human use. *Sci Rep*. 2021;11:20636.

64. Lisova K, Wang J, Chao PH, van Dam RM. A simple and efficient automated microvolume radiosynthesis of [18F]Florbetaben. *EJNMMI Radiopharmacy and Chemistry*. 2020;5:30.

65. Lisova K, Sergeev M, Evans-Axelsson S, et al. Microscale radiosynthesis, preclinical imaging and dosimetry study of [18F]AMBF3-TATE: A potential PET tracer for clinical imaging of somatostatin receptors. *Nuclear Medicine and Biology*. 2018;61:36-44.

66. Sachinidis JI, Poniger S, Tochon-Danguy HJ. Automation for Optimised Production of Fluorine-18-Labelled Radiopharmaceuticals. *Current Radiopharmaceuticals*. 2010;3:248-253.

67. Keng PY, Esterby M, van Dam RM. Emerging Technologies for Decentralized Production of PET Tracers. In: Hsieh C-H, ed. Positron Emission Tomography - Current Clinical and Research Aspects. Rijeka, Croatia: InTech; 2012:153-182.

68. Boschi S, Lodi F, Malizia C, Cicoria G, Marengo M. Automation synthesis modules review. *Applied Radiation and Isotopes*. 2013;76:38-45.

69. Zhang X, Dunlow R, Blackman BN, Swenson RE. Optimization of 18F-syntheses using 19F-reagents at tracer-level concentrations and liquid chromatography/tandem mass spectrometry analysis: Improved synthesis of [18F]MDL100907. *Journal of Labelled Compounds and Radiopharmaceuticals*. 2018;61:427-437.

70. Audrain H. Positron Emission Tomography (PET) and Microfluidic Devices: A Breakthrough on the Microscale? *Angewandte Chemie International Edition*. 2007;46:1772-1775.

71. Elizarov AM, van Dam RM, Shin YS, et al. Design and Optimization of Coin-Shaped Microreactor Chips for PET Radiopharmaceutical Synthesis. *J Nucl Med*. 2010;51:282-287.

72. Iwata R, Pascali C, Terasaki K, Ishikawa Y, Furumoto S, Yanai K. Practical microscale one-pot radiosynthesis of 18F-labeled probes. *Journal of Labelled Compounds and Radiopharmaceuticals*. 2018;61:540-549.

73. Elsinga P, Todde S, Penuelas I, et al. Guidance on current good radiopharmacy practice (cGRPP) for the small-scale preparation of radiopharmaceuticals. *Eur J Nucl Med Mol Imaging*. 2010;37:1049-1062.

74. Siessmeier T, Zhou Y, Buchholz H-G, et al. Parametric Mapping of Binding in Human Brain of D2 Receptor Ligands of Different Affinities. *J Nucl Med*. 2005;46:964-972.

75. Vandehey NT, Moirano JM, Converse AK, et al. High-affinity dopamine D2/D3 PET radioligands 18F-fallypride and 11C-FLB457: A comparison of kinetics in extrastriatal regions using a multiple-injection protocol. *J Cereb Blood Flow Metab*. 2010;30:994-1007.

76. Rios A, Holloway TS, Wang J, Dam RM van. Optimization of Radiochemical Reactions using Droplet Arrays. *J Vis Exp*. 2021:e62056.

77. Dooraghi AA, Keng PY, Chen S, et al. Optimization of microfluidic PET tracer synthesis with Cerenkov imaging. *Analyst*. 2013;138:5654-5664.

78. Cho JS, Taschereau R, Olma S, et al. Cerenkov radiation imaging as a method for quantitative measurements of beta particles in a microfluidic chip. *Phys Med Biol*. 2009;54:6757-6771.

79. Chen S, Javed MR, Kim H-K, et al. Radiolabelling diverse positron emission tomography (PET) tracers using a single digital microfluidic reactor chip. *Lab Chip*. 2014;14:902-910.

80. Javed MR, Chen S, Lei J, et al. High yield and high specific activity synthesis of [18F]fallypride in a batch microfluidic reactor for micro-PET imaging. *Chem Commun*. 2014;50:1192-1194.

81. Lu S, Giamis AM, Pike VW. Synthesis of [18F]fallypride in a micro-reactor: rapid optimization and multiple-production in small doses for micro-PET studies. *Curr Radiopharm*. 2009;2:1-13.

82. Seok Moon B, Hyung Park J, Jin Lee H, et al. Highly efficient production of [18F]fallypride using small amounts of base concentration. *Applied Radiation and Isotopes*. 2010;68:2279-2284.

83. Chao PH, Lazari M, Hanet S, Narayanam MK, Murphy JM, van Dam RM. Automated concentration of [18F]fluoride into microliter volumes. *Applied Radiation and Isotopes*. 2018;141:138-148.

84. Akhrem AA, Kuznetsova AI. THIN-LAYER CHROMATOGRAPHY. *Russ Chem Rev*. 1963;32:366.

85. Zacharias P, Gather MC, Rojahn M, Nuyken O, Meerholz K. New Crosslinkable Hole Conductors for Blue-Phosphorescent Organic Light-Emitting Diodes. *Angewandte Chemie International Edition*. 2007;46:4388-4392.

86. Momiyama N, Torii H, Saito S, Yamamoto H. O-nitroso aldol synthesis: Catalytic enantioselective route to α-aminooxy carbonyl compounds via enamine intermediate. *PNAS*. 2004;101:5374-5378.

87. Skipski VP, Peterson RF, Barclay M. Quantitative analysis of phospholipids by thin-layer chromatography. *Biochem J*. 1964;90:374-378.

88. Waldmann CM, Gomez A, Marchis P, et al. An Automated Multidose Synthesis of the Potentiometric PET Probe 4-[^{18}F]Fluorobenzyl-Triphenylphosphonium ([^{18}F]FBnTP). *Mol Imaging Biol*. 2018;20:205-212.

89. Brom M, Franssen GM, Joosten L, Gotthardt M, Boerman OC. The effect of purification of Ga-68-labeled exendin on in vivo distribution. *EJNMMI Res*. 2016;6:65.

90. Leonard JP, Nowotnik DP, Neirinckx RD. Technetium-99m-d, 1-HM-PAO: a new radiopharmaceutical for imaging regional brain perfusion using SPECT--a comparison with iodine-123 HIPDM. *J Nucl Med*. 1986;27:1819-1823.

91. Madru R, Kjellman P, Olsson F, et al. 99mTc-labeled superparamagnetic iron oxide nanoparticles for multimodality SPECT/MRI of sentinel lymph nodes. *J Nucl Med*. 2012;53:459-463.

92. Price EW, Zeglis BM, Cawthray JF, Lewis JS, Adam MJ, Orvig C. What a Difference a Carbon Makes: H4octapa vs H4C3octapa, Ligands for In-111 and Lu-177 Radiochemistry. *Inorg Chem*. 2014;53:10412-10431.

93. Influence of cations on the complexation yield of DOTATATE with yttrium and lutetium: a perspective study for enhancing the 90Y and 177Lu labeling conditions. *Nuclear Medicine and Biology*. 2012;39:509-517.

94. Ha NS, Sadeghi S, van Dam RM. Recent Progress toward Microfluidic Quality Control Testing of Radiopharmaceuticals. *Micromachines*. 2017;8:337.

95. Ory D, Van den Brande J, de Groot T, et al. Retention of [18F]fluoride on reversed phase HPLC columns. *Journal of Pharmaceutical and Biomedical Analysis*. 2015;111:209-214.

96. Sherma J, DeGrandchamp D. Review of Advances in Planar Radiochromatography. *Journal of Liquid Chromatography & Related Technologies*. 2015;38:381-389.

97. Decristoforo C, Zaknun J, Kohler B, Oberladstaetter M, Riccabona G. The use of electronic autoradiography in radiopharmacy. *Nuclear Medicine and Biology*. 1997;24:361-365.

98. Jeon SJ, Kim KM, Lim I, Song K, Kim JG. Pixelated scintillator-based compact radio thin layer chromatography scanner for radiopharmaceuticals quality control. *J Inst*. 2017;12:T11003.

99. Othman N, Talib Y, Kamal WHBW. Imaging Scanner Usage in Radiochemical Purity Test. *Nuclear Technical Convention*. 2011.

100. Gillies JM, Prenant C, Chimon GN, et al. Microfluidic reactor for the radiosynthesis of PET radiotracers. *Applied Radiation and Isotopes*. 2006;64:325-332.

101. Fujibayashi Y, Cutler C, Anderson C, et al. Comparative studies of Cu-64-ATSM and C-11-Acetate in an acute myocardial infarction model: ex vivo imaging of hypoxia in rats. *Nuclear Medicine and Biology*. 1999;26:117-121.

102. von Guggenberg E, Penz B, Kemmler G, Virgolini I, Decristoforo C. Comparison of different methods for radiochemical purity testing of [99mTc-EDDA-HYNIC-D-Phe1,Tyr3]-Octreotide. *Applied Radiation and Isotopes*. 2006;64:194-200.

103. Savolainen H, Windhorst AD, Elsinga PH, et al. Evaluation of [18F]MC225 as a PET radiotracer for measuring P-glycoprotein function at the blood–brain barrier in rats: Kinetics, metabolism, and selectivity. *J Cereb Blood Flow Metab*. 2017;37:1286-1298.

104. Maneuski D, Giacomelli F, Lemaire C, et al. On the use of positron counting for radio-Assay in nuclear pharmaceutical production. *Applied Radiation and Isotopes*. 2017;125:9-14.

105. Cho JS, Taschereau R, Olma S, et al. Cerenkov radiation imaging as a method for quantitative measurements of beta particles in a microfluidic chip. *Physics in Medicine and Biology*. 2009;54:6757-6771.

106. Cho JS, Douraghy A, Olma S, et al. Čerenkov radiation imaging as a method for quantitative measurements of beta particles in a microfluidic chip. In: Proceedings of the IEEE Nuclear Science Symposium (NSS) Conference. ; 2008:4510-4515.

107. Mitchell GS, Gill RK, Boucher DL, Li C, Cherry SR. In vivo Cerenkov luminescence imaging: a new tool for molecular imaging. *Phil Trans R Soc A*. 2011;369:4605-4619.

108. Spinelli AE, D'Ambrosio D, Calderan L, Marengo M, Sbarbati A, Boschi F. Cerenkov radiation allows in vivo optical imaging of positron emitting radiotracers. *Phys Med Biol*. 2010;55:483.

109. Holland JP, Normand G, Ruggiero A, Lewis JS, Grimm J. Intraoperative Imaging of Positron Emission Tomographic Radiotracers Using Cerenkov Luminescence Emissions. *Mol Imaging*. 2011;10:7290.2010.00047.

110. Liu H, Carpenter CM, Jiang H, et al. Intraoperative Imaging of Tumors Using Cerenkov Luminescence Endoscopy: A Feasibility Experimental Study. *J Nucl Med*. 2012;53:1579-1584.

111. Park JC, An GI, Park S-I, et al. Luminescence imaging using radionuclides: a potential application in molecular imaging. *Nuclear Medicine and Biology*. 2011;38:321-329.

112. Spinelli AE, Gigliotti CR, Boschi F. Unified approach for bioluminescence, Cerenkov, β, X and γ rays imaging. *Biomed Opt Express, BOE*. 2015;6:2168-2180.

113. Ha YS, Lee W, Jung J-M, et al. Visualization and quantification of radiochemical purity by Cerenkov luminescence imaging. *Anal Chem*. 2018;90:8927-8935.

114. Fendler WP, Stuparu AD, Evans-Axelsson S, et al. Establishing 177Lu-PSMA-617 Radioligand Therapy in a Syngeneic Model of Murine Prostate Cancer. *J Nucl Med*. 2017;58:1786-1792.

115. Knowles SM, Tavare R, Zettlitz KA, et al. Applications of immunoPET: using 124I-anti-PSCA A11 minibody for imaging disease progression and response to therapy in mouse xenograft models of prostate cancer. *Clin Cancer Res*. October 2014:clincanres.1452.2014.

116. Baum RP, Kulkarni HR, Schuchardt C, et al. 177Lu-Labeled Prostate-Specific Membrane Antigen Radioligand Therapy of Metastatic Castration-Resistant Prostate Cancer: Safety and Efficacy. *J Nucl Med*. 2016;57:1006-1013.

117. Chatalic KLS, Konijnenberg M, Nonnekens J, et al. In Vivo Stabilization of a Gastrin-Releasing Peptide Receptor Antagonist Enhances PET Imaging and Radionuclide Therapy of Prostate Cancer in Preclinical Studies. *Theranostics*. 2016;6:104-117.

118. Kraeber-Bodéré F, Rousseau C, Bodet-Milin C, et al. Targeting, Toxicity, and Efficacy of 2-Step, Pretargeted Radioimmunotherapy Using a Chimeric Bispecific Antibody and 131I-Labeled Bivalent Hapten in a Phase I Optimization Clinical Trial. *J Nucl Med*. 2006;47:247-255.

119. Kratochwil C, Bruchertseifer F, Giesel FL, et al. 225Ac-PSMA-617 for PSMA-Targeted α-Radiation Therapy of Metastatic Castration-Resistant Prostate Cancer. *J Nucl Med*. 2016;57:1941-1944.

120. Ruggiero A, Holland JP, Lewis JS, Grimm J. Cerenkov luminescence imaging of medical isotopes. *J Nucl Med*. 2010;51:1123-1130.

121. Pandya DN, Hantgan R, Budzevich MM, et al. Preliminary Therapy Evaluation of 225Ac-DOTA-c(RGDyK) Demonstrates that Cerenkov Radiation Derived from 225Ac Daughter Decay Can Be Detected by Optical Imaging for In Vivo Tumor Visualization. *Theranostics*. 2016;6:698-709.

122. Hamacher K, Coenen HH. Efficient routine production of the 18F-labelled amino acid O-(2-[18F]fluoroethyl)-l-tyrosine. *Applied Radiation and Isotopes*. 2002;57:853-856.

123. Bourdier T, Greguric I, Roselt P, Jackson T, Faragalla J, Katsifis A. Fully automated one-pot radiosynthesis of O-(2-[18F]fluoroethyl)-l-tyrosine on the TracerLab FXFN module. *Nuclear Medicine and Biology*. 2011;38:645-651.

124. Banister S, Roeda D, Dolle F, Kassiou M. Fluorine-18 Chemistry for PET: A Concise Introduction. *Current Radiopharmaceuticals*. 2010;3:68-80.

125. Drugs@FDA: FDA-Approved Drugs. https://www.accessdata.fda.gov/scripts/cder/daf/.

126. Centre National de la Recherche Scientifique. ^{18}F-Database of Imaging Radiolabelled Compounds (DIRAC). ^{18}F-Database of Imaging Radiolabelled Compounds (DIRAC). http://www.iphc.cnrs.fr/dirac/.

127. Snyder L. Solvent selectivity in normal-phase TLC. *J Planar Chromatogr*. 2008;21:315-323.

128. Wang J, Rios A, Lisova K, Slavik R, Chatziioannou AF, van Dam RM. High-throughput radio-TLC analysis. *Nuclear Medicine and Biology*. 2020;82-83:41-48.

129. Lazari M, Quinn KM, Claggett SB, et al. ELIXYS - a fully automated, three-reactor high-pressure radiosynthesizer for development and routine production of diverse PET tracers. *EJNMMI Res*. 2013;3:52.

130. Inkster J a. H, Akurathi V, Sromek AW, Chen Y, Neumeyer JL, Packard AB. A non-anhydrous, minimally basic protocol for the simplification of nucleophilic 18 F-fluorination chemistry. *Scientific Reports*. 2020;10:6818 (9 pages).

131. Ismail R, Irribarren J, Javed MR, Machness A, van Dam M, Keng PY. Cationic imidazolium polymer monoliths for efficient solvent exchange, activation and fluorination on a continuous flow system. *RSC Advances*. 2014;4:25348-25356.

132. Wessmann SH, Henriksen G, Wester H-J. Cryptate mediated nucleophilic 18F-fluorination without azeotropic drying. *Nuklearmedizin*. 2012;51:1-8.

133. Bogni A, Laera L, Cucchi C, Iwata R, Seregni E, Pascali C. An improved automated one-pot synthesis of O-(2-[18F]fluoroethyl)-L-tyrosine ([18F]FET) based on a purification by cartridges. *Nuclear Medicine and Biology*. 2019;72-73:11-19.

134. Wang M-W, Yin D-Z, Zhang L, Zhou W, Wang Y-X. Remote-controlled module-assisted synthesis of O-(2-[18F]fluoroethyl)-L-tyrosine as tumor PET tracer using two different radiochemical routes. *Nuclear Science and Techniques*. 2006;17:148-153.

135. Wang H, Guo X, Jiang S, Tang G. Automated synthesis of [18F]Florbetaben as Alzheimer's disease imaging agent based on a synthesis module system. *Applied Radiation and Isotopes*. 2013;71:41-46.

136. Wang J, Holloway T, Lisova K, van Dam RM. Green and efficient synthesis of the radiopharmaceutical [18F]FDOPA using a microdroplet reactor. *React Chem Eng*. 2020;5:320-329.

137. Wang YX, Zhang L, Tang GH, Yin DZ. An improved enantioselective synthesis of no-carrier-added (NCA) 6-[18F]FLUORO-L-DOPA. *Journal of Labelled Compounds and Radiopharmaceuticals*. 2001;44:S866-S867.

138. Libert LC, Franci X, Plenevaux AR, et al. Production at the Curie Level of No-Carrier-Added 6-18F-Fluoro-l-Dopa. *J Nucl Med*. 2013;54:1154-1161.

139. Shen B, Ehrlichmann W, Uebele M, Machulla H-J, Reischl G. Automated synthesis of n.c.a. [18F]FDOPA via nucleophilic aromatic substitution with [18F]fluoride. *Applied Radiation and Isotopes*. 2009;67:1650-1653.

140. Li F, Hicks JW, Yu L, et al. Plasma radio-metabolite analysis of PET tracers for dynamic PET imaging: TLC and autoradiography. *EJNMMI Research*. 2020;10:141 (12 pages).

141. Stephenson NA, Holland JP, Kassenbrock A, et al. Iodonium Ylide Mediated Radiofluorination of 18F-FPEB and Validation for Human Use. *J Nucl Med*. 2015;56:489-492.

142. Lazari M, Collins J, Shen B, et al. Fully Automated Production of Diverse 18F-Labeled PET Tracers on the ELIXYS Multireactor Radiosynthesizer Without Hardware Modification. *J Nucl Med Technol*. 2014;42:203-210.

143. Nandy SK, Rajan MGR. Fully automated and simplified radiosynthesis of [18F]-3′-deoxy-3′-fluorothymidine using anhydro precursor and single neutral alumina column purification. *J Radioanal Nucl Chem*. 2009;283:741-748.

144. Lee SJ, Oh SJ, Chi DY, et al. Simple and highly efficient synthesis of 3′-deoxy-3′-[18F]fluorothymidine using nucleophilic fluorination catalyzed by protic solvent. *Eur J Nucl Med Mol Imaging*. 2007;34:1406-1409.

145. Vaulina D, Nasirzadeh M, Gomzina N. Automated radiosynthesis and purification of [18F]flumazenil with solid phase extraction. *Applied Radiation and Isotopes*. 2018;135:110-114.

146. Nasirzadeh M, Vaulina DD, Kuznetsova OF, Gomzina NA. A novel approach to the synthesis of [18F]flumazenil, a radioligand for PET imaging of central benzodiazepine receptors. *Russ Chem Bull*. 2016;65:794-800.

147. Ryzhikov NN, Gomzina NA, Fedorova OS, Vasil'ev DA, Kostikov AP, Krasikova RN. Preparation of [18F]Flumazenil, a Potential Radioligand for PET Imaging of Central Benzodiazepine Receptors, by Isotope Exchange. *Radiochemistry*. 2004;46:290-294.

148. Akula MR, Collier TL, Blevins DW, Kabalka GW, Osborne D. Sequential Preparation of [18F]FLT and [18F]FMISO Employing Advion NanoTek® Microfluidic Synthesis System. *Advances in Molecular Imaging*. 2019;9:53-59.

149. Zarganes-Tzitzikas T, Clemente GS, Elsinga PH, Dömling A. MCR Scaffolds Get Hotter with 18F-Labeling. *Molecules*. 2019;24:1327.

150. Russelli L, Martinelli J, De Rose F, et al. Room Temperature Al18F Labeling of 2-Aminomethylpiperidine-Based Chelators for PET Imaging. *ChemMedChem*. 2020;15:284-292.

151. Yu H-M, Chan C-H, Yang C-H, Hsia H-T, Wang M-H. Hexavalent lactoside labeled with [18F]AlF for PET imaging of asialoglycoprotein receptor. *Applied Radiation and Isotopes*. 2020;162:109199.

152. Shih I-H, Duan X-D, Kong F-L, et al. Automated Synthesis of 18F-Fluoropropoxytryptophan for Amino Acid Transporter System Imaging. Liao M-H, ed. *BioMed Research International*. 2014;2014:492545.

153. Ungersboeck J, Philippe C, Haeusler D, et al. Optimization of [11C]DASB-synthesis: Vessel-based and flow-through microreactor methods. *Applied Radiation and Isotopes*. 2012;70:2615-2620.

154. Koivula T, Laine J, Lipponen T, et al. Assessment of labelled products with different radioanalytical methods: study on 18F-fluorination reaction of 4-[18F]fluoro-N-[2-[1-(2-methoxyphenyl)-1-piperazinyl]ethyl-N-2-pyridinyl-benzamide (p-[18F]MPPF). *J Radioanal Nucl Chem*. 2010;286:841-846.

155. Johnson AR, Vitha MF. Chromatographic selectivity triangles. *Journal of Chromatography A*. 2011;1218:556-586.

156. Cardinale J, Martin R, Remde Y, et al. Procedures for the GMP-Compliant Production and Quality Control of [18F]PSMA-1007—A Next Generation Radiofluorinated Tracer for the Detection of Prostate Cancer. August 2017.

157. Wiegmann J. The chemistry of silica. Solubility, polymerization, colloid and surface properties, and biochemistry. Von RALPH K. ILER. New York/Chichester/Brisbane/Toronto: John Wiley & Sons 1979. XXIV, 866 S., Lwd., £ 39.50. *Acta Polymerica*. 1980;31:406-406.

158. Dalstein L, Potapova E, Tyrode E. The elusive silica/water interface: isolated silanols under water as revealed by vibrational sum frequency spectroscopy. *Physical Chemistry Chemical Physics*. 2017;19:10343-10349.

159. Eppard E, Homann T, de la Fuente A, Essler M, Rösch F. Optimization of Labeling PSMA ^{HBED} with Ethanol-Postprocessed ^{68} Ga and Its Quality Control Systems. *J Nucl Med*. 2017;58:432-437.

160. Jeong S, Park JY, Cha MG, et al. Highly robust and optimized conjugation of antibodies to nanoparticles using quantitatively validated protocols. *Nanoscale*. 2017;9:2548-2555.

161. Aggarwal R, Wei X, Kim W, et al. Heterogeneous Flare in Prostate-specific Membrane Antigen Positron Emission Tomography Tracer Uptake with Initiation of Androgen Pathway Blockade in Metastatic Prostate Cancer. *European Urology Oncology*. 2018;1:78-82.

162. Ma WW, Jacene H, Song D, et al. [18F]Fluorodeoxyglucose Positron Emission Tomography Correlates With Akt Pathway Activity but Is Not Predictive of Clinical Outcome During mTOR Inhibitor Therapy. *J Clin Oncol*. 2009;27:2697-2704.

163. Cherry SR. Fundamentals of Positron Emission Tomography and Applications in Preclinical Drug Development. *The Journal of Clinical Pharmacology*. 2001;41:482-491.

164. Seo YJ, Kang Y, Muench L, et al. Image-Guided Synthesis Reveals Potent Blood-Brain Barrier Permeable Histone Deacetylase Inhibitors. *ACS Chem Neurosci*. 2014;5:588-596.

165. Airas L, Nylund M, Rissanen E. Evaluation of Microglial Activation in Multiple Sclerosis Patients Using Positron Emission Tomography. *Front Neurol*. 2018;9.

166. Roelcke U, Wyss MT, Nowosielski M, et al. Amino acid positron emission tomography to monitor chemotherapy response and predict seizure control and progression-free survival in WHO grade II gliomas. *Neuro-Oncology*. 2016;18:744-751.

167. Wang YT, Edison P. Tau Imaging in Neurodegenerative Diseases Using Positron Emission Tomography. *Curr Neurol Neurosci Rep*. 2019;19:45.

168. Knapp K-A, Nickels ML, Manning HC. The Current Role of Microfluidics in Radiofluorination Chemistry. *Mol Imaging Biol*. September 2019.

169. Shevlin M. Practical High-Throughput Experimentation for Chemists. *ACS Med Chem Lett*. 2017;8:601-607.

170. Santanilla AB, Regalado EL, Pereira T, et al. Nanomole-scale high-throughput chemistry for the synthesis of complex molecules. *Science*. 2015;347:49-53.

171. Krska SW, DiRocco DA, Dreher SD, Shevlin M. The Evolution of Chemical High-Throughput Experimentation To Address Challenging Problems in Pharmaceutical Synthesis. *Acc Chem Res*. 2017;50:2976-2985.

172. Andersson JD, Matuskey D, Finnema SJ. Positron emission tomography imaging of the γ-aminobutyric acid system. *Neuroscience Letters*. 2019;691:35-43.

173. Mandap KS, Ido T, Kiyono Y, et al. Development of microwave-based automated nucleophilic [18F]fluorination system and its application to the production of [18F]flumazenil. *Nuclear Medicine and Biology*. 2009;36:403-409.

174. Massaweh G, Schirrmacher E, la Fougere C, et al. Improved work-up procedure for the production of [18F]flumazenil and first results of its use with a high-resolution research tomograph in human stroke. *Nuclear Medicine and Biology*. 2009;36:721-727.

175. Ryzhikov NN, Seneca N, Krasikova RN, et al. Preparation of highly specific radioactivity [18F]flumazenil and its evaluation in cynomolgus monkey by positron emission tomography. *Nuclear Medicine and Biology*. 2005;32:109-116.

176. Moon BS, Kil HS, Park JH, et al. Facile aromatic radiofluorination of [18F]flumazenil from diaryliodonium salts with evaluation of their stability and selectivity. *Org Biomol Chem*. 2011;9:8346-8355.

177. Gomzina NA, Zaitsev VV, Krasikova RN. Optimization of nucleophilic fluorination step in the synthesis of various compounds labelled with fluorine-18 for their use as pet radiotracers. *Journal of Labelled Compounds and Radiopharmaceuticals*. 2001;44:S895-S897.

178. Doi H, Goto M, Suzuki M. Pd0-Mediated Rapid C-[18F]Fluoromethylation by the Cross-Coupling Reaction of a [18F]Fluoromethyl Halide with an Arylboronic Acid Ester: Novel Method for the Synthesis of a 18F-Labeled Molecular Probe for Positron Emission Tomography. *BCSJ*. 2012;85:1233-1238.

179. Zarrad F, Zlatopolskiy BD, Krapf P, Zischler J, Neumaier B. A Practical Method for the Preparation of 18F-Labeled Aromatic Amino Acids from Nucleophilic [18F]Fluoride and Stannyl Precursors for Electrophilic Radiohalogenation. *Molecules*. 2017;22.

180. Simmons DA, James ML, Belichenko NP, et al. TSPO–PET imaging using [18F]PBR06 is a potential translatable biomarker for treatment response in Huntington's disease: preclinical evidence with the p75NTR ligand LM11A-31. *Hum Mol Genet*. 2018;27:2893-2912.

181. Wang M, Gao M, Miller KD, Zheng Q-H. Synthesis of [11C]PBR06 and [18F]PBR06 as agents for positron emission tomographic (PET) imaging of the translocator protein (TSPO). *Steroids*. 2011;76:1331-1340.

182. Zhang H, Xiao J, Zhou J, et al. 18F-PBR06 PET/CT imaging for evaluating atherosclerotic plaques linked to macrophage infiltration. *Nucl Med Commun*. 2019;40:370-376.

183. Timofeeva DS, Ofial AR, Mayr H. Kinetics of Electrophilic Fluorinations of Enamines and Carbanions: Comparison of the Fluorinating Power of N–F Reagents. *J Am Chem Soc*. 2018;140:11474-11486.

184. Cacace F, Speranza M, Wolf AP, Macgregor RR. Nucleophilic aromatic substitution; kinetics of fluorine-18 substitution reactions in polyfluorobenzenes. Isotopic exchange between 18F− and polyfluorobenzenes in dimethylsulfoxide. A kinetic study. *Journal of Fluorine Chemistry*. 1982;21:145-158.

185. Valera FE, Quaranta M, Moran A, et al. The Flow's the Thing…Or Is It? Assessing the Merits of Homogeneous Reactions in Flask and Flow. *Angewandte Chemie International Edition*. 2010;49:2478-2485.

186. Aroh KC, Jensen KF. Efficient kinetic experiments in continuous flow microreactors. *React Chem Eng*. 2018;3:94-101.

187. Chang C-W, Chiu C-H, Lin M-H, et al. GMP-compliant fully automated radiosynthesis of [18F]FEPPA for PET/MRI imaging of regional brain TSPO expression. *EJNMMI Res*. 2021;11:26.

188. Vignal N, Cisternino S, Rizzo-Padoin N, et al. [18F]FEPPA a TSPO Radioligand: Optimized Radiosynthesis and Evaluation as a PET Radiotracer for Brain Inflammation in a Peripheral LPS-Injected Mouse Model. *Molecules*. 2018;23:1375.

189. Berroterán-Infante N, Balber T, Fürlinger P, et al. [18F]FEPPA: Improved Automated Radiosynthesis, Binding Affinity, and Preliminary in Vitro Evaluation in Colorectal Cancer. *ACS Med Chem Lett*. 2018;9:177-181.

190. Vasdev N, Green DE, Vines DC, et al. Positron-Emission Tomography Imaging of the TSPO with [18F]FEPPA in a Preclinical Breast Cancer Model. *Cancer Biotherapy and Radiopharmaceuticals*. 2013;28:254-259.

191. Setiawan E, Wilson AA, Mizrahi R, et al. Role of Translocator Protein Density, a Marker of Neuroinflammation, in the Brain During Major Depressive Episodes. *JAMA Psychiatry*. 2015;72:268.

192. Dahl K, Garcia A, Stephenson NA, Vasdev N. “In-loop” 18F-fluorination: A proof-of-concept study. *Journal of Labelled Compounds and Radiopharmaceuticals*. 2019;62:292-297.

193. Gu Z, Taschereau R, Vu NT, et al. Performance Evaluation of G8, a High-Sensitivity Benchtop Preclinical PET/CT Tomograph. *Journal of Nuclear Medicine*. 2019;60:142-149.

194. Gu Z, Taschereau R, Vu NT, Prout DL, Lee J, Chatziioannou AF. Performance evaluation of HiPET, a high sensitivity and high resolution preclinical PET tomograph. *Phys Med Biol*. 2020;65:045009.

195. Jones J, Rios A, Chao P, Wang J, van Dam RM. High-throughput microdroplet radiochemistry platform to accelerate radiotracer development. In: Journal of Labelled Compounds & Radiopharmaceuticals. Vol 62. ; 2019:S350-S351.

196. Bowden GD, Pichler BJ, Maurer A. A Design of Experiments (DoE) Approach Accelerates the Optimization of Copper-Mediated 18 F-Fluorination Reactions of Arylstannanes. *Scientific Reports*. 2019;9:11370.

197. Calderwood S, Collier TL, Gouverneur V, Liang SH, Vasdev N. Synthesis of 18F-arenes from spirocyclic iodonium(III) ylides via continuous-flow microfluidics. *Journal of Fluorine Chemistry*. 2015;178:249-253.

198. Liang SH, Yokell DL, Jackson RN, et al. Microfluidic continuous-flow radiosynthesis of [18F]FPEB suitable for human PET imaging. *Med Chem Commun*. 2014;5:432-435.

199. Kelloff GJ, Krohn KA, Larson SM, et al. The Progress and Promise of Molecular Imaging Probes in Oncologic Drug Development. *Clin Cancer Res*. 2005;11:7967-7985.

200. Elizarov AM. Microreactors for radiopharmaceutical synthesis. *Lab Chip*. 2009;9:1326-1333.

201. Pascali G, Mazzone G, Saccomanni G, Manera C, Salvadori PA. Microfluidic approach for fast labeling optimization and dose-on-demand implementation. *Nuclear Medicine and Biology*. 2010;37:547-555.

202. Keng PY, Sergeev M, van Dam RM. Advantages of Radiochemistry in Microliter Volumes. In: Kuge Y, Shiga T, Tamaki N, eds. Perspectives on Nuclear Medicine for Molecular Diagnosis and Integrated Therapy. Springer Japan; 2016:93-111.

203. Búriová E, Macášek F, Melichar F, Kropáček M, Procházka L. Autoradiolysis of the 2-deoxy-2-[18F]fluoro-D-glucose radiopharmaceutical. *Journal of Radioanalytical and Nuclear Chemistry*. 2005;264:595-602.

204. Jacobson MS, Dankwart HR, Mahoney DW. Radiolysis of 2-[18F]fluoro-2-deoxy-d-glucose ([18F]FDG) and the role of ethanol and radioactive concentration. *Applied Radiation and Isotopes*. 2009;67:990-995.

205. Rensch C, Waengler B, Yaroshenko A, et al. Microfluidic reactor geometries for radiolysis reduction in radiopharmaceuticals. *Applied Radiation and Isotopes*. 2012;70:1691-1697.

206. Hess E, Takács S, Scholten B, Tárkányi F, Coenen HH, Qaim SM. Excitation function of the 18O(p,n)18F nuclear reaction from threshold up to 30 MeV. *Radiochimica Acta*. 2001;89:357-362.

207. Asti M, Grassi E, Sghedoni R, et al. Purification by ozonolysis of 18O enriched water after cyclotron irradiation and the utilization of the purified water for the production of [18F]-FDG (2-deoxy-2-[18F]-fluoro-d-glucose). *Applied Radiation and Isotopes*. 2007;65:831-835.

208. Kilian K, Chabecki B, Kiec J, et al. Synthesis, quality control and determination of metallic impurities in 18F-fludeoxyglucose production process. *Reports of Practical Oncology & Radiotherapy*. 2014;19:S22-S31.

209. Bowden L, León Vintró L, Mitchell PI, O'Donnell RG, Seymour AM, Duffy GJ. Radionuclide impurities in proton-irradiated [18O]H2O for the production of 18F−: Activities and distribution in the [18F]FDG synthesis process. *Applied Radiation and Isotopes*. 2009;67:248-255.

210. Allott L, Pieve CD, Turton DR, Smith G. A general [18F]AlF radiochemistry procedure on two automated synthesis platforms. *React Chem Eng*. 2017;2:68-74.

211. The aluminium-[18F]fluoride revolution: simple radiochemistry with a big impact for radiolabelled biomolecules | EJNMMI Radiopharmacy and Chemistry | Full Text. https://ejnmmipharmchem.springeropen.com/articles/10.1186/s41181-021-00141-0.

212. deMello AJ. Control and detection of chemical reactions in microfluidic systems. Nature. https://www.nature.com/articles/nature05062.

213. Elvira KS, i Solvas XC, Wootton RCR, deMello AJ. The past, present and potential for microfluidic reactor technology in chemical synthesis. *Nat Chem*. 2013;5:905-915.

214. Kaminski TS, Garstecki P. Controlled droplet microfluidic systems for multistep chemical and biological assays. *Chem Soc Rev*. August 2017.

215. Keng PY, Chen S, Ding H, et al. Micro-chemical synthesis of molecular probes on an electronic microfluidic device. *PNAS*. 2012;109:690-695.

216. Collins J, Waldmann CM, Drake C, et al. Production of diverse PET probes with limited resources: 24 ^{18}F-labeled compounds prepared with a single radiosynthesizer. *PNAS*. 2017;114:11309-11314.

217. Becherer A, Szabó M, Karanikas G, et al. Imaging of Advanced Neuroendocrine Tumors with 18F-FDOPA PET. *J Nucl Med*. 2004;45:1161-1167.

218. Fischman AJ. Role of [18F]-dopa–PET imaging in assessing movement disorders. *Radiologic Clinics of North America*. 2005;43:93-106.

219. Lu Y, Wang J, van Dam RM, Hsiao A. PHENYX – A flexible pipetting-based platform for automated microvolume radiochemistry. *Chemical Engineering Journal*. 2022;435:134983.

220. McDonald JC, Whitesides GM. Poly(dimethylsiloxane) as a Material for Fabricating Microfluidic Devices. *Acc Chem Res*. 2002;35:491-499.

221. J. Beulig R, Warias R, J. Heiland J, Ohla S, Zeitler K, Belder D. A droplet-chip/mass spectrometry approach to study organic synthesis at nanoliter scale. *Lab on a Chip*. 2017;17:1996-2002.

222. Lee JN, Park C, Whitesides GM. Solvent Compatibility of Poly(dimethylsiloxane)-Based Microfluidic Devices. *Anal Chem*. 2003;75:6544-6554.

223. W. Toepke M, J. Beebe D. PDMS absorption of small molecules and consequences in microfluidic applications. *Lab on a Chip*. 2006;6:1484-1486.

224. Camino G, Lomakin SM, Lazzari M. Polydimethylsiloxane thermal degradation Part 1. Kinetic aspects. *Polymer*. 2001;42:2395-2402.

225. Tucker B, Hermann M, Mainguy A, Oleschuk R. Hydrophobic/hydrophilic patterned surfaces for directed evaporative preconcentration. *Analyst*. 2020;145:643-650.

226. Uneyama K. Organofluorine Chemistry. John Wiley & Sons; 2008.

227. Bégué J-P, Bonnet-Delpon D. Bioorganic and Medicinal Chemistry of Fluorine | Wiley. Wiley.com. https://www.wiley.com/en-us/Bioorganic+and+Medicinal+Chemistry+of+Fluorine-p-9780470278307.

228. O'Hagan D. Fluorine in health care: Organofluorine containing blockbuster drugs. *Journal of Fluorine Chemistry*. 2010;131:1071-1081.

229. Purser S, Moore PR, Swallow S, Gouverneur V. Fluorine in medicinal chemistry. *Chem Soc Rev*. 2008;37:320-330.

230. Appendix: Approved Active Pharmaceutical Ingredients Containing Fluorine. In: Fluorine in Medicinal Chemistry and Chemical Biology. John Wiley & Sons, Ltd; 2009:525-526.

231. Hiyama T, Yamamoto H. Biologically Active Organofluorine Compounds. In: Hiyama T, Yamamoto H, eds. Organofluorine Compounds: Chemistry and Applications. Berlin, Heidelberg: Springer; 2000:137-182.

232. Villalba G, Ayres RU, Schroder H. Accounting for Fluorine: Production, Use, and Loss. *Journal of Industrial Ecology*. 2007;11:85-101.

233. Electrophilic fluorination at saturated sites - Chemical Communications (RSC Publishing). https://pubs.rsc.org/en/content/articlelanding/2000/cc/b001624l.

234. Rozen S. Elemental Fluorine: Not Only for Fluoroorganic Chemistry! *Acc Chem Res*. 1996;29:243-248.

235. Ghatora BK, Barton SJ, Foot PJS, Tate PM. The Effect of Direct Gas Fluorination on Medical Grade Poly(methyl methacrylate). *OJOPM*. 2014;04:74-83.

236. Krasikova R. PET Radiochemistry Automation: State of the Art and Future Trends in 18F-nucleophilic Fluorination. *Current Organic Chemistry*. 17:2097-2107.

237. Phelps ME. Positron emission tomography provides molecular imaging of biological processes. *PNAS*. 2000;97:9226-9233.

238. Lee E, Kamlet AS, Powers DC, et al. A fluoride-derived electrophilic late-stage fluorination reagent for PET imaging. *Science*. 2011;334:639-642.

239. Tredwell M, Gouverneur V. 18F labeling of arenes. *Angew Chem Int Ed Engl*. 2012;51:11426-11437.

240. Cole EL, Stewart MN, Littich R, Hoareau R, Scott PJH. Radiosyntheses using Fluorine-18: the Art and Science of Late Stage Fluorination. *Curr Top Med Chem*. 2014;14:875-900.

241. Fuchigami T, Shimojo M, Konno A, Nakagawa K. Electrolytic partial fluorination of organic compounds. 1. Regioselective anodic monofluorination of organosulfur compounds. *J Org Chem*. 1990;55:6074-6075.

242. Baizer MM, Lund H. Organic electrochemistry: an introduction and a guide. New York: M. Dekker; 1983.

243. Fuchigami T, Inagi S. Selective electrochemical fluorination of organic molecules and macromolecules in ionic liquids. *Chem Commun (Camb)*. 2011;47:10211-10223.

244. Prakash GKS, Olah GA. Synthetic methods and reactions. *Proc Indian Acad Sci (Chem Sci)*. 1988;100:143-185.

245. Brigaud T, Laurent A, Laurent E. OXIDATIVE FLUORINATION OF SULFIDES IN PRESENCE OF Et3N,3HF. *Phosphorus, Sulfur, and Silicon and the Related Elements*. 1991;59:153-156.

246. Meurs JHH, Eilenberg W. Oxidative fluorination in amine-hf mixturess. *Tetrahedron*. 1991;47:705-714.

247. Konno A, Nakagawa K, Fuchigami T. New mechanistic aspects of anodic monofluorination of halogenoalkyl and alkyl phenyl sulphides. *J Chem Soc, Chem Commun*. 1991:1027-1029.

248. Kim DW, Jeong H-J, Lim ST, Sohn M-H. Recent Trends in the Nucleophilic [(18)F]-radiolabeling Method with No-carrier-added [(18)F]fluoride. *Nucl Med Mol Imaging*. 2010;44:25-32.

249. He Q, Wang Y, Alfeazi I, Sadeghi S. Electrochemical nucleophilic synthesis of di-tert-butyl-(4-[18F]fluoro-1,2-phenylene)-dicarbonate. *Appl Radiat Isot*. 2014;92:52-57.

250. Reischl G, Kienzle GJ, Machulla H-J. Electrochemical radiofluorination: Labeling of benzene with [18F]fluoride by nucleophilic substitution. *Journal of Radioanalytical and Nuclear Chemistry*. 2002;254:409-411.

251. Superacid Chemistry, 2nd Edition | Wiley. Wiley.com. https://www.wiley.com/en-us/Superacid+Chemistry%2C+2nd+Edition-p-9780470421543.

252. Cyclotron Produced Radionuclides: Principles and Practice. https://www.iaea.org/publications/7849/cyclotron-produced-radionuclides-principles-and-practice.

253. Campbell MG, Mercier J, Genicot C, Gouverneur V, Hooker JM, Ritter T. Bridging the gaps in 18F PET tracer development. *Nat Chem*. 2016;9:1-3.

254. Tang P, Wang W, Ritter T. Deoxyfluorination of Phenols. *J Am Chem Soc*. 2011;133:11482-11484.

255. Lewandowski G, Meissner E, Milchert E. Special applications of fluorinated organic compounds. *J Hazard Mater*. 2006;136:385-391.

256. Champagne PA, Desroches J, Hamel J-D, Vandamme M, Paquin J-F. Monofluorination of Organic Compounds: 10 Years of Innovation. *Chem Rev*. 2015;115:9073-9174.

257. Gillis EP, Eastman KJ, Hill MD, Donnelly DJ, Meanwell NA. Applications of Fluorine in Medicinal Chemistry. *J Med Chem*. 2015;58:8315-8359.

258. Chambers RD, Parsons M, Sandford G, Bowden R. Electrophilic fluorination at saturated sites. *Chem Commun*. 2000:959-960.

259. Kohlhepp SV, Gulder T. Hypervalent iodine(III) fluorinations of alkenes and diazo compounds: new opportunities in fluorination chemistry. *Chem Soc Rev*. 2016;45:6270-6288.

260. Rotstein BH, Stephenson NA, Vasdev N, Liang SH. Spirocyclic hypervalent iodine(III)-mediated radiofluorination of non-activated and hindered aromatics. *Nat Commun*. 2014;5:4365.

261. Ichiishi N, Brooks AF, Topczewski JJ, Rodnick ME, Sanford MS, Scott PJH. Copper-catalyzed [18F]fluorination of (mesityl)(aryl)iodonium salts. *Org Lett*. 2014;16:3224-3227.

262. Furuya T, Kamlet AS, Ritter T. Catalysis for fluorination and trifluoromethylation. *Nature*. 2011;473:470-477.

263. Preshlock S, Tredwell M, Gouverneur V. (18)F-Labeling of Arenes and Heteroarenes for Applications in Positron Emission Tomography. *Chem Rev*. 2016;116:719-766.

264. Wiebe A, Gieshoff T, Möhle S, Rodrigo E, Zirbes M, Waldvogel SR. Electrifying Organic Synthesis. *Angew Chem Int Ed Engl*. 2018;57:5594-5619.

265. Möhle S, Zirbes M, Rodrigo E, Gieshoff T, Wiebe A, Waldvogel SR. Modern Electrochemical Aspects for the Synthesis of Value-Added Organic Products. *Angew Chem Int Ed Engl*. 2018;57:6018-6041.

266. Sawamura T, Takahashi K, Inagi S, Fuchigami T. Electrochemical Fluorination Using Alkali-Metal Fluorides. *Angewandte Chemie International Edition*. 2012;51:4413-4416.

267. Lebedev A, Jiao J, Lee J, et al. Radiochemistry on electrodes: Synthesis of an 18F-labelled and in vivo stable COX-2 inhibitor. Garg P, ed. *PLOS ONE*. 2017;12:e0176606.

268. Yoshida J, Suga S, Suzuki S, Kinomura N, Yamamoto A, Fujiwara K. Direct Oxidative Carbon−Carbon Bond Formation Using the “Cation Pool” Method. 1. Generation of Iminium Cation Pools and Their Reaction with Carbon Nucleophiles. *J Am Chem Soc*. 1999;121:9546-9549.

269. Fujie S, Matsumoto K, Suga S, Yoshida J. Thiofluorination of Carbon–Carbon Multiple Bonds Using Electrochemically Generated ArS(ArSSAr) $^{+}$ BF_4^{-}. *Chem Lett*. 2009;38:1186-1187.

270. Javed MR, Chen S, Lei J, et al. High yield and high specific activity synthesis of [18F]fallypride in a batch microfluidic reactor for micro-PET imaging. *Chem Commun*. 2014;50:1192-1194.

271. Leroux F, Jeschke P, Schlosser M. α-Fluorinated Ethers, Thioethers, and Amines: Anomerically Biased Species. *Chem Rev*. 2005;105:827-856.

272. Balandeh M, Waldmann C, Shirazi D, et al. Electrochemical Fluorination and Radiofluorination of Methyl(phenylthio)acetate Using Tetrabutylammonium Fluoride (TBAF). *J Electrochem Soc*. 2017;164:G99-G103.

273. Chen H, Hu Z, Zhang J, Liang G, Xu B. A modified fluoro-Pummerer reaction with DAST and NIS for synthesis of β-amino-α-fluoro-sulfides from corresponding β-amino-sulfides. *Tetrahedron*. 2015;71:2089-2094.

274. Waldmann CM, Lebedev A, Allison N, Sadeghi S. An automated synthesizer for electrochemical 18F-fluorination of organic compounds. *Appl Radiat Isot*. 2017;127:245-252.

275. Elsler B, Wiebe A, Schollmeyer D, Dyballa KM, Franke R, Waldvogel SR. Source of Selectivity in Oxidative Cross-Coupling of Aryls by Solvent Effect of 1,1,1,3,3,3-Hexafluoropropan-2-ol. *Chemistry – A European Journal*. 2015;21:12321-12325.

276. Kirste A, Nieger M, Malkowsky IM, Stecker F, Fischer A, Waldvogel SR. ortho-Selective Phenol-Coupling Reaction by Anodic Treatment on Boron-Doped Diamond Electrode Using Fluorinated Alcohols. *Chemistry – A European Journal*. 2009;15:2273-2277.

277. Waldvogel SR, Lips S, Selt M, Riehl B, Kampf CJ. Electrochemical Arylation Reaction. *Chem Rev*. 2018;118:6706-6765.

278. Colomer I, Chamberlain AER, Haughey MB, Donohoe TJ. Hexafluoroisopropanol as a highly versatile solvent. *Nat Rev Chem*. 2017;1:1-12.

279. Deng X, Rong J, Wang L, et al. Chemistry for Positron Emission Tomography: Recent Advances in 11C-, 18F-, 13N-, and 15O-Labeling Reactions. *Angewandte Chemie International Edition*. 2019;58:2580-2605.

280. Glaudemans AWJM, Enting RH, Heesters MAAM, et al. Value of 11C-methionine PET in imaging brain tumours and metastases. *Eur J Nucl Med Mol Imaging*. 2013;40:615-635.

281. Huang T, Tang G, Wang H, et al. Synthesis and preliminary biological evaluation of S-11C-methyl-d-cysteine as a new amino acid PET tracer for cancer imaging. *Amino Acids*. 2015;47:719-727.

282. Nuñez R, Macapinlac HA, Yeung HWD, et al. Combined 18F-FDG and 11C-methionine PET scans in patients with newly progressive metastatic prostate cancer. *J Nucl Med*. 2002;43:46-55.

283. Ilardi EA, Vitaku E, Njardarson JT. Data-Mining for Sulfur and Fluorine: An Evaluation of Pharmaceuticals To Reveal Opportunities for Drug Design and Discovery. *J Med Chem*. 2014;57:2832-2842.

284. Neal TR, Apana S, Berridge MS. Improved synthesis of [18F]fluoromethyl tosylate, a convenient reagent for radiofluoromethylations. *Journal of Labelled Compounds and Radiopharmaceuticals*. 2005;48:557-568.

285. Scott KA, Njardarson JT. Analysis of US FDA-Approved Drugs Containing Sulfur Atoms. *Top Curr Chem (Z)*. 2018;376:5.

286. Shinde GB, Mahale PK, Padaki SA, Niphade NC, Toche RB, Mathad VT. An efficient and safe process for the preparation of ticagrelor, a platelet aggregation inhibitor via resin-NO2 catalyzed formation of triazole ring. *SpringerPlus*. 2015;4:493.

287. Albizati KF, Babu S, Birchler A, et al. A synthesis of the HIV-protease inhibitor nelfinavir from d-tartaric acid. *Tetrahedron Letters*. 2001;42:6481-6485.

288. Meng Q, Zhao T, Kang D, Huang B, Zhan P, Liu X. The development of an effective synthetic route of lesinurad (RDEA594). *Chemistry Central Journal*. 2017;11:86.

289. Fuchigami T, Tajima T. Highly selective electrochemical fluorination of organic compounds in ionic liquids. *Journal of Fluorine Chemistry*. 2005;126:181-187.

290. Khan ZUH, Kong D, Chen Y, et al. Ionic liquids based fluorination of organic compounds using electrochemical method. *Journal of Industrial and Engineering Chemistry*. 2015;31:26-38.

291. Noel M, Suryanarayanan V, Chellammal S. A review of recent developments in the selective electrochemical fluorination of organic compounds. *Journal of Fluorine Chemistry*. 1997;83:31-40.

292. Dawood KM. Electrolytic fluorination of organic compounds. *Tetrahedron*. 2004;7:1435-1451.

293. Fuchigami T, Shimojo M, Konno A. Electrolytic Partial Fluorination of Organic Compounds. 17. Regiospecific Anodic Fluorination of Sulfides Bearing Electron-Withdrawing Substituents at the Position .alpha. to the Sulfur Atom. *J Org Chem*. 1995;60:3459-3464.

294. Hugenberg V, Haufe G. Fluoro-Pummerer rearrangement and analogous reactions. *Journal of Fluorine Chemistry*. 2012;143:238-262.

295. Bur SK, Padwa A. The Pummerer Reaction: Methodology and Strategy for the Synthesis of Heterocyclic Compounds. *Chem Rev*. 2004;104:2401-2432.

296. Wigman B, Lee W, Wei W, Houk KN, Nelson HM. Electrochemical Fluorination of Vinyl Boronates through Donor-Stabilized Vinyl Carbocation Intermediates**. *Angewandte Chemie International Edition*. 2022;61:e202113972.

297. Fuchigami T. Unique solvent effects on selective electrochemical fluorination of organic compounds. *Journal of Fluorine Chemistry*. 2007;128:311-316.

298. Hou Y, Fuchigami T. Electrolytic Partial Fluorination of Organic Compounds XL. Solvent Effects on Anodic Fluorination of Heterocyclic Sulfides. *J Electrochem Soc*. 2000;147:4567.

299. Jacobson O, Kiesewetter DO, Chen X. Fluorine-18 Radiochemistry, Labeling Strategies and Synthetic Routes. *Bioconjug Chem*. 2015;26:1-18.

300. Stang PJ, Anderson AG. Hammett and Taft substituent constants for the mesylate, tosylate, and triflate groups. *J Org Chem*. 1976;41:781-785.

301. Eberson L, Hartshorn MP, Persson O, Radner F. Making radical cations live longer. *Chem Commun*. 1996:2105-2112.

302. Eberson L, Hartshorn MP, Persson O. 1,1,1,3,3,3-Hexafluoropropan-2-ol as a solvent for the generation of highly persistent radical cations. *J Chem Soc, Perkin Trans 2*. 1995:1735-1744.

303. Shuklov IA, Dubrovina NV, Börner A. Fluorinated Alcohols as Solvents, Cosolvents and Additives in Homogeneous Catalysis. *Synthesis*. 2007;2007:2925-2943.

304. Shida N, Takenaka H, Gotou A, et al. Alkali Metal Fluorides in Fluorinated Alcohols: Fundamental Properties and Applications to Electrochemical Fluorination. *J Org Chem*. 2021;86:16128-16133.

305. Röckl JL, Dörr M, Waldvogel SR. Electrosynthesis 2.0 in 1,1,1,3,3,3-Hexafluoroisopropanol/Amine Mixtures. *ChemElectroChem*. 2020;7:3686-3694.

306. Collins J, Waldmann CM, Drake C, et al. Production of diverse PET probes with limited resources: 24 18F-labeled compounds prepared with a single radiosynthesizer. *Proceedings of the National Academy of Sciences*. 2017;114:11309-11314.

307. Balandeh M, Waldmann C, Shirazi D, et al. Electrochemical Fluorination and Radiofluorination of Methyl(phenylthio)acetate Using Tetrabutylammonium Fluoride (TBAF). *J Electrochem Soc*. 2017;164:G99-G103.

308. Balandeh M, Rios A, Allison N, et al. Electrochemical Flash Fluorination and Radiofluorination. *ChemElectroChem*. 2018;5:3353-3356.

309. Allison N, Balandeh M, Holloway T, et al. Electrochemical no-carrier-added radiofluorination of thioethers. *Journal of Fluorine Chemistry*. 2022;257-258:109988.

310. Aymard C, Bonaventura C, Henkens R, et al. High-Throughput Electrochemical Screening Assay for Free and Immobilized Oxidases: Electrochemiluminescence and Intermittent Pulse Amperometry. *ChemElectroChem*. 2017;4:957-966.

311. Abdellaoui S, Noiriel A, Henkens R, Bonaventura C, Blum LJ, Doumèche B. A 96-Well Electrochemical Method for the Screening of Enzymatic Activities. *Anal Chem*. 2013;85:3690-3697.

312. Park J, Park JS, Huang C-H, et al. An integrated magneto-electrochemical device for the rapid profiling of tumour extracellular vesicles from blood plasma. *Nat Biomed Eng*. 2021;5:678-689.

313. Pérez-Cruz F, Vazquez-Rodriguez S, Matos MJ, et al. Synthesis and Electrochemical and Biological Studies of Novel Coumarin–Chalcone Hybrid Compounds. *J Med Chem*. 2013;56:6136-6145.

314. Huang T, Tang G, Wang H, et al. Synthesis and preliminary biological evaluation of S-11C-methyl-d-cysteine as a new amino acid PET tracer for cancer imaging. *Amino Acids*. 2015;47:719-727.